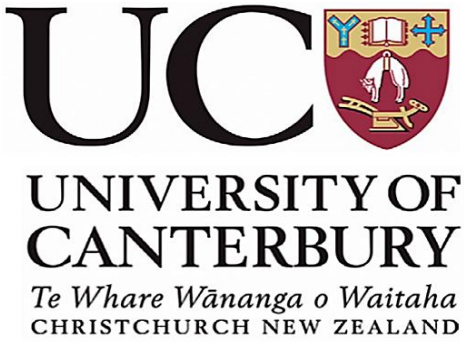

Optical and electrochemical properties of the periodically patterned photoanode

Maryam Shojaei

Department of Chemical and Process Engineering

University of Canterbury

Christchurch, New Zealand

July 2021

Acknowledgements

This work was carried out at the Department of Chemical and Process Engineering (CAPE) and at the Nanofabrication laboratory within the Department of Electrical and Computer Engineering, University of Canterbury, New Zealand, from April 2017 to July 2021. It was made feasible by financial support of University of Canterbury in the form of a UC Doctoral Scholarship and MacDiarmid institute in the form of Postgraduate Extension Scholarship, which are gratefully acknowledged.

The completion of this thesis would not have been possible without the continuous support and encouragement from several people, whom I wish to acknowledge here.

My deep gratitude goes first to my supervisory team. I would like to gratefully acknowledge my senior supervisor, Dr. Aaron Marshall, for his guidance and advice that formed the concept of this thesis and for his unfailing support and enthusiasm that powered me through my PhD journey. Secondly, I am very much indebted to my co-supervisor, Dr. Maan Alkaisi, for introducing me to the Nanofabrication laboratory, its facilities and people, and for his attitude to form a collaborative environment. I also would like to express my sincere gratitude to Dr. Paul Broady for his support and suggestions which formed the structure of this manuscript, and to Dr. Roger Reeves for offering access to his laboratory and sharing his knowledge.

I would like to specifically thank Glenn Wilson, Joanne Pollard, Rachel Rogers, Ranee Hearst, Leigh Richardson, Frank Weerts, Stephen Buezenburg, Graham Furniss, Graham Mitchell, David Rathgen, Rayleen Fredericks, Michael Sandridge, and Kun Zhao who helped me to navigate the practical and administrative part of research. I am also deeply thankful to Gary Turner and Helen Devereux for their abiding advice and assistance in the Nanofabrication laboratory, and to Robert McGregor for the skilled execution of vitreous designs.

I would like to express my sincere appreciation to my fellow PhD candidates who all have become close friends throughout my time in Christchurch. They introduced me to so many beautiful cultures from different parts of the world and surely proved friendship knows no borders. All those wonderful memories with many moments of laughter will stay with me forever. Special thanks to

Leatham Landon-Lane, Sam Nesbit, Maxime Savoie, Aran Warren, and Rodrigo Martinez Gazoni for their contribution to this project.

Most importantly, I would like to express my deepest appreciation to my family. There is not a proper word to show how much I am grateful for the endless kindness of my mother, Shahnaz, and my father, Mostafa who despite the long distances were present in every moment of my life and their ongoing trust strengthened my steps in each cross-section. My brothers Ali and Mohammad-Reza, and my sister Parisa deserve my deepest appreciation for their love and support.

Abstract

The integration of a photoelectrode into a redox flow battery (RFB) enables direct solar charging of the battery. The efficiency of a solar RFB depends on the number of photons that excite the electrons and lead to electron transfer reaction. The major obstacles during this process are poor light absorption by the photoelectrode, scattering/reflection losses, and rapid recombination of photo-generated charge carriers once they are generated within the semiconductors. This study addresses these limitations by investigation of the effects of patterning the geometry of nano-/micro-structures on the photoelectrode as a potential way to modify its optical, electrical and electrochemical properties.

The type of photoelectrode that is considered consists of a layer of TiO_2 on top of fluorine-doped tin oxide (FTO) coated glass. TiO_2 has attracted great interest due to its stability and large band gap (3.2 eV) that covers the redox potential of many species. However, this large band gap requires the absorption of high energy photons with a wavelength below 400 nm which is a small portion of the solar spectrum. Improved light harvesting of ultraviolet photons within the TiO_2 occurs by suppressing the different ways in which light is lost on the photoelectrode. These are 1) reflection from the surface, 2) absorption within the inactive layers, and 3) transmission through the photoactive layer.

Patterning a surface by a nano-sized structure reduces light reflection by causing a gradual change of refractive index from the air to the substrate. In addition, a periodic structure with a periodicity larger than the light wavelength diffracts the light into several beams. Light behaviour was studied on a glass substrate patterned by a periodic pyramidal nanostructure with a periodicity of 670 nm. The periodic structure was fabricated through a combination of laser interference lithography and nanoimprint lithography. The effect of surface patterning on light reflection and diffraction was evaluated using a numerical study based on the Finite-Difference Time-Domain method. The periodic structure reduced the light reflection over the whole wavelength range. At wavelengths smaller than the periodicity of the structure ($\lambda < 670$ nm), the light was diffracted into several beams, while at wavelengths higher than the periodicity ($\lambda > 670$ nm), the structure acted as a

homogenous medium with an equivalent refractive index without causing light diffraction. The effect of the optical behaviour of the structure on the photocatalytic activity of TiO_2 was probed experimentally through photodecomposition of methylene blue at λ=365 nm. The efficiency of methylene blue oxidation was higher on patterned substrate as a result of antireflection behaviour of the periodic structure and longer light path within the semiconductor material caused by diffraction.

The photo-generated charge carriers have a very short time to undergo the electron transfer reaction before charge recombination. Therefore, an effective photon absorption within the TiO_2 layer occurs at the vicinity of the electrode-electrolyte interface. This limits the thickness of the TiO_2 layer and the absorption of photons. This issue can be addressed by patterning the TiO_2 with a structure that provides a long dimension for light absorption, while it requires the charge carriers to pass a short distance to reach the acceptor species. This patterning will also influence the transport phenomena at the electrode-electrolyte interface. To separate the influence of patterning the electrode-electrolyte interface on the mass transport of redox species from its influence on the light/charge carrier behaviour within the photoactive layer, the mass transfer of redox species was investigated using cyclic voltammetry (both numerically and experimentally) on a patterned gold electrode in the presence of Fe^{2+}/Fe^{3+} redox species. It was observed that the effect of electrode-electrolyte structure on electrochemical performance depended on the size of the structure relative to the diffusion layer thickness. By reducing the diffusion layer thickness, the redox species concentration profile was affected by the structure. This resulted in a convergent mass transfer of redox species towards the electrode causing a nonuniform current density over the electrode surface, with it being greater at the tip of the structure and lower at the base.

Two approaches were employed to pattern the TiO_2 photoelectrode-electrolyte interface: 1) by direct fabrication of the pattern into the TiO_2 layer using imprint lithography, and 2) by coating the TiO_2 layer on a patterned FTO glass. Direct fabrication by imprint lithography used both a polymer-based and an alcohol-based paste to produce an upright pyramidal microstructure. Imprinting the polymer-based paste resulted in a higher throughput and more control over the final structure. However, annealing caused the polymer-based structure to greatly shrink. In order to coat TiO_2 onto the patterned FTO glass, a pattern containing micro-holes was fabricated into the FTO conductive layer by using photolithography followed by inductive coupled plasma etching.

Hydrothermal deposition was then used to grow TiO_2 nanorods on top of the FTO layer. Due to difficulties with reproducibility of the patterning of the TiO_2 layer by imprint lithography, the photoelectrochemical study of the patterned electrode was conducted only on the photoelectrode with a patterned FTO layer. The photoactivity of the patterned photoelectrode was studied during photo-oxidation of V^{4+} in a three-electrode setup during linear sweep voltammetry under chopped illumination. Patterning the FTO layer affected the photoelectrode by changing the light behaviour, the ohmic overpotential, the charge recombination rate, and the morphology of the TiO_2 layer. Overall, etching the FTO layer had a negative effect on the photoactivity of the fabricated electrodes, and an increase in the etched area resulted in a lower photocurrent.

The results showed that patterning technique can be a promising approach to enhance the photoactivity of an RFB photoelectrode. However, the presence of a nano-/micro-structured pattern can affect photoactivity of the photoelectrode in various ways. In order to obtain the maximum photoelectrochemical efficiency the combination of these effects must be considered.

Contents

Acknowledgements ..... **i**

Abstract ..... **iii**

1 Introduction **1**

1.1 Solar charging a redox flow battery using TiO_2 photoanode 1

1.2 Hypothesis 2

1.3 Thesis outline 3

2 Background information **5**

2.1 Renewable energy storage systems 5

2.2 Redox flow battery 7

2.3 The solar rechargeable battery 12

2.3.1 External and internal configurations 12

2.3.2 Photoelectrochemical cell/redox flow battery internal configuration 15

2.3.3 Band position and band bending 18

2.4 TiO_2 photoelectrode 20

2.5 Photocurrent and limiting factors 24

2.6 Characteristics of patterned photoelectrodes 27

2.6.1 Light behaviour on a patterned photoelectrode 28

2.6.2 Rate of electron transfer reaction on a patterned photoelectrode 35

2.7 Lithography techniques 36

2.8 Nanoimprint lithography 39

2.9 Llyod mirror laser interference lithography 40

3 Investigation into the effect of periodic nanopatterns on light harvesting 43

3.1 Introduction 43

3.2 Experimental methods 44

3.2.1 Nanoimprint lithography 44

3.2.2 Master mold preparation 46

3.2.3 Optical tests 53

3.3 Results and discussion 58

3.3.1 Characterisation 58

3.3.2 Optical behaviour 61

3.3.3 Photocatalytic study 77

3.4 Conclusion 79

4 The effect of electrode surface morphology on the electrochemical behaviour of a redox reaction 81

4.1 Introduction 81

4.2 Theory 82

4.2.1 Cyclic voltammetry 85

4.2.2 Cyclic voltammetry on a rough electrode 89

4.3 Experimental methods 90

4.3.1 Electrode preparation 90

4.3.2 Master mold preparation 91

4.3.3 Photomask preparation 93

4.3.4 Electrochemical studies 94

4.4 Results and discussion 96

4.4.1 Characterisation 96

4.4.2 Electrochemical behaviour 98

4.5 Conclusion 117

5 Patterning the photoelectrode-electrolyte interface and its effect on the photoactivity of a TiO_2 photoelectrode 120

5.1 Introduction 120

5.2 Experimental methods 121

5.2.1 Imprint lithography on TiO_2 polymer-based paste using a Si master mold 121

5.2.2 Imprint lithography on TiO_2 alcohol-based paste using a PDMS master mold 123

5.2.3 Patterning the FTO conductive layer 125

5.2.4 Hydrothermal synthesis of TiO_2 on patterned FTO 126

5.2.5 Testing the photoactivity of the photoelectrode 126

5.2.6 Resistivity of flat and patterned FTO measured using a four-point probe 127

5.3 Results and discussion 129

5.3.1 Characterisation of directly fabricated TiO_2 patterned substrates 129

5.3.2 Characterisation of patterned FTO coated with TiO_2 133

5.3.3 Photoelectrochemical behaviour of the patterned photoelectrode 136

5.4 Conclusion 141

6 Conclusion and recommendations 143

7 References 150

1 Introduction

1.1 Solar charging a redox flow battery using TiO_2 photoanode

Growing concern regarding climate change and the future energy crisis has caused human society to begin the transition to clean and renewable energy sources, among which solar energy is the most viable to meet the global energy demand [1]. However, renewable energy power generation suffers from intermittency issues, e.g. solar only generates power during daylight hours and wind turbines only generate power when the wind is blowing. To overcome this issue, rechargeable batteries can be used for power storage and to create a flexible and reliable electrical grid.

Great advances have been made in rechargeable batteries for electronic devices such as computers and mobile phones [2]. However, there are serious challenges associated with the scale-up of batteries for large-scale applications, including limited resources, restricted lifetime, and insufficient power [3–5]. Amongst various types of battery systems, redox flow batteries (RFBs) have several advantages such as safety, energy stability, acceptable operation and maintenance costs, and long lifetimes, and so RFBs are particularly suitable for large-scale electrical energy storage [6, 7]. An RFB utilises a pair of soluble redox couples in an electrolyte. In a redox flow battery, the electricity is stored by driving redox reactions in the electrolyte at each electrode. The charged electrolyte is stored in separate tanks and can be used on demand to produce electricity by reversing the redox reactions.

Because a redox flow battery can be easily coupled to a renewable energy power generator then in principle it is feasible to directly charge it with solar energy by utilizing photoelectrochemical reactions. It has been stated that: "*If a redox flow battery can be regenerated under solar illumination, it could lead to a significant breakthrough in the efficient and affordable storage of solar energy"* [8]. This idea of integrating a photoelectrode in the redox flow battery and configure it as a solar redox flow battery has been the focus of several recent studies [8–17], but this is still far from being a commercially viable option for large-scale solar energy conversion and storage.

These solar redox flow batteries can be improved by overcoming the limitations of the photoelectrodes where the solar energy is converted into stored chemical energy via photoelectrochemical reactions. All photoelectrodes have some limitations in common. These are:

1) Photoelectrodes only work at a specific wavelength range of light. Only photons with energy equal or higher than the band gap of the photoactive material excite the electron to drive the photochemical reaction.
2) Some light is lost due to reflection off the optical window of the photoelectrode.
3) Surface contamination of the optical window of the photoelectrode blocks the incident light.
4) Electron-hole recombination occurs after electron excitation.

Titanium dioxide (TiO_2) is a widely available, nontoxic, and highly efficient photoactive material that has attracted great interest for photoelectrochemical applications [18, 19]. However, due to its large band gap (3.2 eV [20]), it is only active in the UV range, which is less than 10% of the solar spectrum. While it is possible to address this issue by modifying the TiO_2 to make it more sensitive to visible light, this study focused on improving the photocatalytic efficiency of TiO_2 photoelectrodes in the UV spectrum by use of controlled nano-/micro-structures.

1.2 Hypothesis

It is proposed that the challenges described above can be overcome by patterning photoelectrodes with nano-/micro-structures. Such a patterning can greatly affect the physical behaviour of a photoelectrode [21–28].

This investigation examines whether surface patterning improves the optical and electrochemical behaviour of a TiO_2 photoelectrode in an RFB. An RFB photoelectrode consists of three layers: a glass base (optical window), a conductive layer, and a photoactive layer (Figure 1.1). It is hypothesised that surface patterning on each layer of the photoelectrode would affect the performance of the system in the following ways:

a) Patterning the optical window of the photoelectrode would reduce the photon loss by improving the antireflection behaviour of the glass substrate. It would also increase the probability of photon absorption by using diffraction effects to increase the path length of light within the absorbing layer.

b) Patterning the conductive layer would provide more conductive area and would enhance the flow of electrons and reduce the electrical resistance,

c) Patterning the interface of the electrode-electrolyte would enhance the electroactive surface area and mass transfer of redox ions present in the electrolyte.

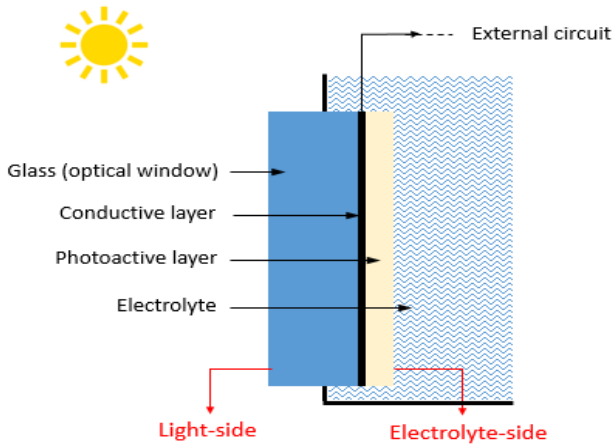

Figure 1.1. Schematic diagram of a solar RFB photoelectrode containing three layers: an optical window made of a transparent substrate such as glass, a conductive layer, and a photoactive layer.

1.3 Thesis outline

The focus of this work was to describe how patterning different layers of a TiO_2 photoelectrode could affect its photoelectrochemical behaviour within an RFB. This thesis is composed of 6 chapters. The successive thesis chapters are briefly summarised below.

Chapter 2 covers the background information about solar redox flow batteries and the current challenges of photoelectrodes. It introduces the fabrication techniques and breaks down the underlying theory behind the effect of nano-/micro-structured patterns on a solar RFB performance.

Chapter 3 highlights the effect of surface patterning on harvesting UV light within the TiO_2 layer. A periodic nanostructure was applied on the glass base of the photoelectrode. After describing the fabrication technique, numerical and experimental studies were used to elucidate the light behaviour within the photoelectrode.

Chapter 4 focuses on the effect of patterning on the electrochemical behaviour of the photoelectrode. To remove the light effect, a model system containing a patterned gold electrode was developed. Numerical and experimental methods were used to study how the geometrical properties of the electrode-electrolyte interface influences both the mass transport of redox species towards the electrode and the kinetics of electron transfer reaction.

Chapter 5 describes two different approaches to pattern the photoelectrode-electrolyte interface and evaluates three possible techniques that can be employed for this purpose. The various effects of patterning on a photoelectrode was illustrated and its net effect on photoelectrochemical behaviour of the patterned photoelectrode was studied in the presence of vanadium redox species.

Chapter 6 summarises the most significant findings of this work and puts them in context to each other. Suggestions are made for future investigations and their relevance to this field of study is discussed.

The size, periodicity, and the shape of the pattern applied on each layer of the photoelectrode was chosen according to the role of that layer and the simplicity of the fabrication. In addition, according to the main objectives of each part of the study, different synthesis methods were employed for the TiO_2 photoelectrode.

2 Background information

2.1 Renewable energy storage systems

Concerns are rapidly increasing about global warming and the lack of fuel sources to supply the growing human population. This has resulted in significant research focused on alternatives to fossil fuels and on energy carriers coupled to renewable energy sources [29–33]. Renewable energy that is sustainable, environmentally friendly, and found over wide geographical areas is available as solar [34], hydro [35], wind [36], geothermal [37], and biomass energies [38].

Utilisation of most of these renewable energy resources is limited by geography and the ecological impacts. Solar energy is the most promising alternative for fossil fuels because of its availability over a wide geographical area and its accessibility to individual people. However, because of the intermittent nature of solar energy, there needs to be a way to store and release it on demand [39]. The goal of a fully renewable energy source is achievable if the technology of storage and subsequent release of the energy can compete with fossil fuels in terms of cost [40].

Solar energy storage technologies that are available for large-scale applications can be divided into four types: thermal, mechanical, chemical, and electrochemical. Thermal storage through the change of the temperature and phase of a material is a suitable method for on-site storage. An example of mechanical energy storage which can be coupled to solar energy is pumped hydro-electric, and this has the largest storage capacity that is commercially available. While this storage technology has low material and maintenance costs, there is the obvious limitation of requiring sites of a suitable geography. Solar energy can be stored as chemical energy through driving a chemical reaction. An example of this approach is the electrolytic cell in which the system must be continuously fed with new reactants. Electrochemical storage systems (rechargeable batteries) are based on using solar energy to drive an electrochemical reaction between a photoactive material and another substance. This method is the most promising for the integration of solar energy due to desirable features such as pollution-free operation, flexible power and energy characteristics, low maintenance, and reasonable operation cost [3, 34, 40–43]. The most popular rechargeable batteries are lithium-ion batteries [44], lead-acid [45], sodium-sulfur (Na-S) [46], nickel-metal

hydride (Ni-MH) batteries [47], and redox flow batteries (RFB) [48]. The main characteristics of each battery is presented in Table 2.1.

Table 2.1. Major characteristics of different types of batteries [49–52]

Technology	**Energy density (W h/kg)**	**Battery voltage (V)**	**Efficiency %**	**Usage life**	**Response time**	**Discharge time (h)**	**Capital cost ($/kW h)**	**Operation temperature (°C)**
Nickel-metal hydride batteries	90-110	1.35	70-90	>5	-	>1	-	-30 to 70
Lead-acid batteries	25-50	2	75-85	2-3	ms	1	130	18 to 45
Sodium sulphur	150-240	1.78-2.07	85-90	10-15	s	1	550	300 to 350
Li-ion batteries	100-200	2.5-5.00	95	5-6	ms	1	600	20 to 65
Redox flow batteries	10-50	1.26	85	5-15	ms	1-10	900	5 to 45

To evaluate a battery two main factors of power quality and energy management are considered [49]. The advantages and disadvantages of the most common batteries are presented in Table 2.2.

Table 2.2. Advantages and disadvantages of different types of batteries [50, 53]

Battery type	Advantages	Disadvantages
Ni-MH	- Long cycle life - High energy density - High-temperature capability - Good charge retention - Rapid recharge capability - Sealed maintenance-free design - Environmentally acceptable and recyclable materials	- Relatively high cost (compared with lead–acid batteries) - Decreased performance at low temperature - Nickel-cadmium type contains toxic material
Lead-acid	- Low capital cost - Adjustable various sizes and designs - High battery voltage - High recyclability of battery components	- Short cycle life - Low energy-to-volume ratio - Irreversible polarisation of electrodes (sulfation generation after long-term storage in a discharged condition) -Toxic materials and environmental issues
Na-S	- Long cycle life - High energy density - Pulse power capability - High self-discharge resistance	- High working temperature - High cost - Chemical handling
Li-ion	- Long cycle life - High energy and power density - Low maintenance fee - Broad operation temperature range - Long shelf life - Rapid charge capability	- Relatively high cost - Poor high-temperature performance - Requirement of protective circuitry
RFB	- Long cycle life - High safety - Low operation cost and maintenance - Capability of deep discharge - High round trip efficiencies - Acceptable costs for large-scale energy storage - Scalable - Flexible design - Long lifetime	- Requirement of large space - Relatively low energy density - Chemical handling

2.2 Redox flow battery

RFBs are considered as one of the most promising technologies for stationary energy storage. RFBs have many advantages over other types of rechargeable batteries, such as high energy storage capacity, scalability and flexibility, low cost, long operation lifetime, high round-trip efficiency, high depth of discharge, and low environmental impact. RFBs can be adjusted for wide

ranges of operational powers and discharge times, which makes them ideal options for electricity generation using renewable sources [54].

RFBs are designed to store and release electrical energy through the oxidation and reduction reaction between two redox couples without consuming the ions [49, 55]. An RFB consists of several cells in series or parallel. Each cell is made of two half-cells that are separated by an ion conducting membrane. A schematic diagram of an RFB is presented in Figure 2.1. In each half-cell, the electrode is in contact with an electrolyte containing redox species. During the charge and discharge process, the redox species undergo the electron transfer reaction at the surface of the electrode. The charged and discharged electrolytes are stored in two separate tanks and pumped continuously through the cells. A membrane prevents the electrolyte in each half-cell from freely mixing, while it allows the transport of charge carriers to maintain electrical neutrality and to complete the electrical circuit.

During the discharge process, an electrolyte containing the redox species is pumped through the electrode chambers. When the energy of the electrons in the electrode are at a higher level than the lowest unoccupied molecular orbital of the acceptor ions, the electron transfer reaction occurs between the active sites of the electrode and redox species [56]. The energy of the electrons can be modulated by applying voltage to the electrode using an external power source. The general reaction in RFBs for each half-cell is as follows:

Negative*

$$A^{n+} + xe^- \underset{discharge}{\overset{charge}{\rightleftharpoons}} A^{(n-x)+} \qquad (n > x)$$

Positive

$$B^{m+} \underset{discharge}{\overset{charge}{\rightleftharpoons}} B^{(m+y)+} + e^-$$

* The negative electrode is the cathode during charging and is the anode during discharging.

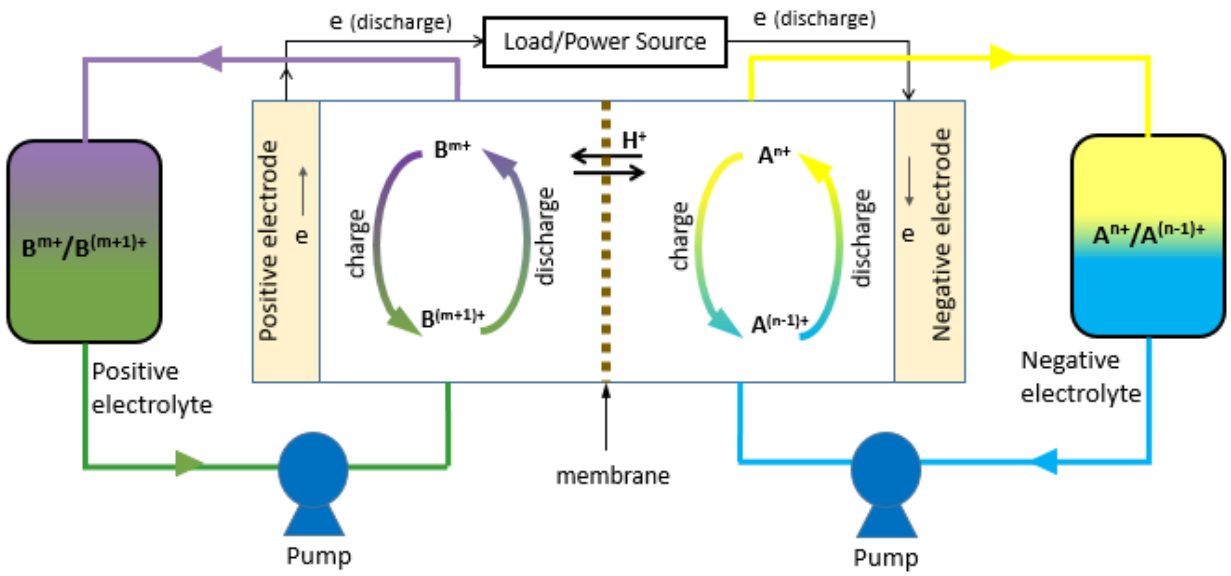

Figure 2.1. Schematic diagram of a redox flow battery: positive and negative half-cells are separated by an ion exchange membrane, and negative and positive electrolytes containing the redox species are stored in external tanks and are continuously circulated through the system using pumps.

Through the charging process, a power source is utilised to reverse the electrochemical reaction and to drive the electrons to the negative half-cell via an external circuit. In RFBs, the system storage capacity is determined by the redox couple concentration and the electrolyte volume, while the system power is set by the stack size and the arrangement of cells within the stack. Hence, the power and the output stored energy can be adjusted independently, and this provides more flexibility in setting up a RFB based on the desired design [57–60].

The RFB electrolyte consists of redox ions and a supporting electrolyte. The supporting electrolyte is a dissolved salt that helps to decrease the solution resistance, balances the charge, and completes the electrical circuit for the electron transfer. The supporting electrolyte is chemically and electrochemically inert in the conditions of the process in order to eliminate the deleterious /undesirable electrode processes [58, 59]. High concentration of supporting electrolyte enhances the conductivity of the solution, however, the supporting electrolyte is kept at low concentration to prevent it from affecting the electroactive species behaviour and the chemical reaction [61]. In

an RFB, self-discharge could occur due to crossover of the electrolyte through the membrane/separator or by losing the electrolyte due to the evaporation. Storing electrolyte in air-tight tanks prevents evaporation and guarantees its very long shelf life [62]. The problem caused by cross contamination of redox species through the ion exchange membrane can be eliminated by using similar ions in both half-cells [63–69]. This was first proposed by Skyllas-Kazacos *et al.* who suggested that an all-vanadium RFB would remove the crossover problem associated with the use of an iron/chromium RFB [65].

RFBs are classified based on the redox species used to store the energy. Various soluble species have been investigated as redox couples, for instance: iron/chromium [70], polysulfide/bromide [71], all-vanadium [72], zinc/bromine [73], zinc/cerium [58], all-lead [59], and all-iron [66]. The characteristics of these systems are described in Table 2.3.

In an RFB, the electrochemical reaction occurs at the surface of the electrode; therefore, the surface chemistry and morphology of the electrode have strong influence on the redox reaction. The electrode is inert and the redox couple does not react with the electrode and does not transfer across the electrode-electrolyte interface [54]. A suitable photoelectrode has a high surface area, appropriate porosity, low electronic resistance, stability in the electrolyte, and high electrochemical activity to enable high current-density operation [74].

Table 2.3. The chemistry of commonly used redox flow batteries

RFB system	Reaction	E°_{cell} vs. SHE	Electrolyte	Advantages	Disadvantages
Iron/chromium [75, 76]	$Fe^{2+} \rightleftarrows Fe^{3+} + e^-$ $Cr^{3+} + e^- \rightleftarrows Cr^{2+}$	1.17	HCl HCl	- Reasonable surface over-potential value at a certain current	- Efficiency and capacity loss due to ions cross over - Slow kinetics of chromium redox couple - Low open circuit potential
Polysulfide/ bromide [77]	$2S_2^{2-} \rightleftarrows S_4^{2-} + 2e^-$ $3Br^- \rightleftarrows Br_3^- + 2e^-$	1.35	NaS_2 NaBr	- Abundant and inexpensive redox species - Highly soluble redox ions	- Efficiency and capacity loss due to ions cross over
All-vanadium [54]	$V^{2+} \rightleftarrows V^{3+} + e^-$ $VO_2^+ + e^- \rightleftarrows VO^{2+}$	1.26	H_2SO_4 H_2SO_4	- Ions cross over does not cause capacity loss - Possibility to regenerate the proper form of redox ions	- Efficiency loss due to ions crossover - Low vanadium solubility
Zinc/bromine [78–80]	$Zn \rightleftarrows Zn^{2+} + 2e^-$ $Br_2 + 2e^- \rightleftarrows 2Br^-$	1.8	$ZnBr_2$ $ZnBr_2$	- High energy density and reaction kinetics of bromine	- Efficiency and capacity loss due to ions cross over -Toxicity of bromine - Production of highly corroding/complexing HBr
Zinc/cerium [58, 81]	$Zn \rightleftarrows Zn^{2+} + 2e^-$ $2Ce^{4+} + 2e^- \rightleftarrows 2Ce^{3+}$	2.4	CH_3SO_3H CH_3SO_3H	- High cell potential	- Low electrolyte conductivity, stability - Slow kinetics of Ce redox reaction - Low diffusivity of Ce(III) - Opposite effect of pH on solubility of Ce(III) and Ce(IV)
All-lead [82]	$Pb^{2+} + 2H_2O \rightleftarrows PbO_2 + 4H^+ + 2e^-$ $Pb^{2+} + 2e^- \rightleftarrows Pb$	1.6	CH_3SO_3H CH_3SO_3H	- Ions cross over does not cause capacity loss	- Short circle problem due to the material growth across the separator gap
All-iron [83–85]	$Fe^{2+} \rightleftarrows Fe^{3+} + e^-$ $Fe^{2+} + 2e^- \rightleftarrows Fe$	1.21	HCl HCl	- Ions cross over does not cause capacity loss - Non-hazardous and inexpensive material	- Precise pH control is required - Low overall cell voltage - H_2 generation problem

2.3 The solar rechargeable battery

2.3.1 External and internal configurations

Currently, solar energy can be stored by coupling photovoltaic cells with rechargeable batteries through external wiring (Figure 2.2-a). A photovoltaic cell consists of n-type and p-type semiconductors to convert the solar energy into electricity but does not have the capability of energy storage [86]. Gibson *et al.* used a high efficiency crystalline and amorphous silicon photovoltaic module to recharge lithium-ion battery modules. The system had an overall efficiency of 14.5% for conversion of solar energy to electrical energy stored in the battery (the photovoltaic system efficiency of nearly 15%, and a battery charging efficiency of approximately 100%) [87]. In another study, Gibson and Kelly charged a nickel metal hydride battery using a photovoltaic cell, achieving a solar-to-electricity efficiency of 11.7-15.6 % [88]. Urbain *et al.* combined a high photovoltage cell with an all-vanadium continuous-flow battery and reported energy efficiency of up to 77.5% for a complete charge-discharge process and an overall solar-to-electricity efficiency of 10.46% [89]. Many other studies have been made on optimal battery charging using photovoltaic panels [90–93]. These batteries can be used for short or long-term storage for different applications, such as portable electronic equipment, electrical vehicles, and aerospace [94, 95].

External configuration of the rechargeable battery and photovoltaic modules has two problems. First, it enlarges the volume and weight of the entire device and results in the additional cost of external hardware. Secondly, the out-put of these systems not only depends on the battery conversion efficiency, but also on the behaviour of the photovoltaic modules [41, 96].

The internal integration of photoelectrodes into rechargeable batteries is a potential solution to this issue. This approach forms a compact photo-rechargeable system in which a photoelectrode induces a redox reaction within the battery, and the same device provides both power conversion and energy storage (Figure 2.2-b) [10, 96, 97]. Integrating the energy conversion with the energy storage into one device simplifies the entire system, reduces the internal resistance, improves the space efficiency and the volume energy density, and results in a stable load base. However, the development of these systems has been slowed down by device complexity, conversion efficiency inferiority, and links between the power to energy sizing [41]. Additionally, rechargeable batteries contain various types of active materials in the organic, aqueous and organic/aqueous systems.

Therefore, the internal integration of photoelectrodes into rechargeable batteries needs highly compatibility of the chemistry and potential energy of each part [41]. Table 2.4 presents the characteristics of some recent solar rechargeable batteries based on internal integration of the photoelectrode.

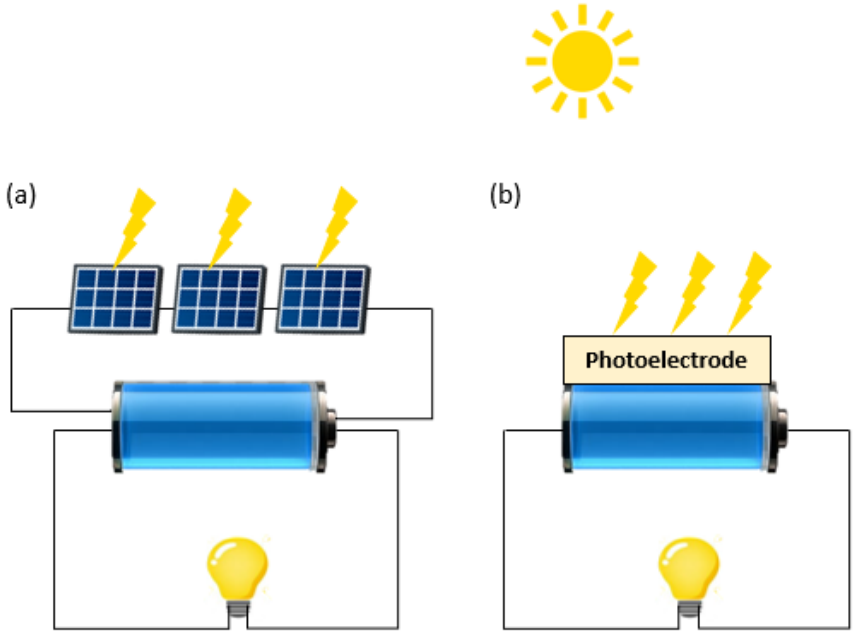

Figure 2.2. Schematic diagram of solar rechargeable batteries: (a) external configuration where photovoltaic cells are coupled with a rechargeable battery through external wiring (b) internal configuration where a photoelectrode is integrated into a rechargeable battery and induces a redox reaction.

Table 2.4. Characteristics of various rechargeable batteries with internal integration of photoelectrodes

Type	**Photoactive material**	**Active material in anode/cathode**	**Capacity**	**Number of cycles (capacity retention/ change of photo-assisted charging voltage)**	**Energy efficiency***	**Ref.**
Li-ion	Dye sensitised TiO_2	TiO_2/$LiCoO_2$	–	3 (~100% capacity retention)	0.82 %	[98]
	$LiFePO_4$/ N719 dye	Li/$LiFePO_4$	340 mAh/g	15 (~100% capacity retention)	0.06-0.08 %	[99]
	TiO_2	Li/$LiFePO_4$	137 mAh/g	10 (~97% capacity retention)	–	[100]
Li-O_2	Dye sensitised electrode	Li/O_2	–	4 (2.72 V→3.1 V)	–	[101]
	Dye sensitised electrode/ C_3N_4	Li/O_2	600 mAh/g	70 (1.96 V→2.35 V)	–	[102]
Li-S	Pt-modified CdS	Li/S	792 mAh/g	10 (92.5% capacity retention)	–	[103]
Li-I RFB	Dye sensitised electrode	Li/I	32600 mAh/L	25 (2.91 V→ 2.93 V)	–	[14]
	α-Fe_2O_3	Li/I	192	22 (~99% capacity retention)	–	[104]
All-vanadium RFB	TiO_2	Vanadium	0.0042 μmol/h VO^{2+} conversion rate	–	12 %	[105]
	α-Fe_2O_3	Anthraquinon compound/ K_4FeCN_6	–	–	0.05-0.08 %	[106]
	Dual silicon	Anthraquinon compound/HBr	730 mAh/L	10 (98% capacity retention)	3.2 %	[107]
	Silicon solar cell	Anthraquinon/ benzoquinone compounds	3500 mAh/L	–	1.7 %	[108]
	Dye sensitised electrode	Li_2WO_4/LiI	19.5 mAh/L	10 (98.6% capacity retention)	–	[48]
	Dye sensitised electrode	Hydrogen storage alloy/LiI	26.7 mAh/g	20 (88% capacity retention)	<1 %	[109]
	Dye sensitised electrode	Na_2S_4/NaI	240 Ah/cm^2	10 (78% capacity retention)	1.7 %	[110]
	TiO_2	Na_2S/NaI	110 mAh/g	20 (90% capacity retention)	–	[111]

* Photoelectric conversion and storage efficiency

2.3.2 Photoelectrochemical cell/redox flow battery internal configuration

Many studies have investigated the feasibility of rechargeable solar RFBs [8, 9, 11, 105, 112, 113]. In a solar RFB, the driving force for the electrochemical reaction is the capture of the energy of photons [92]. For this purpose, a photoactive electrode is integrated into the RFB to configure the RFB as a photoelectrochemical cell (Figure 2.3). The oxidation (or reduction, or both) of the redox species is performed within the battery by the direct action of light.

A photoelectrode is made of a semiconductor material. Semiconductors possess discrete electronic states, which means there is no available energy level between their valence band (the highest energy configuration that is occupied by electrons) and conduction band (the lowest unoccupied energy level where the electrons have higher mobility). The energy difference between the conduction and valence bands is termed the bandgap energy (Eg) and determines the minimum energy that is required for electron excitation. By absorbing photons with an energy equal or higher than the band gap energy, the electrons are excited from their valence band to the conduction band [114]. If the electrode is in contact with any other material with a different Fermi level (i.e. the level at which the probability of occupancy of states with electrons is 1/2 (at $T > 0$) [115]), such as a redox couple, then charge transfer occurs across the junction, and solar energy is converted to chemical energy. The principle of the photoelectrochemical reaction is elaborated in the next section.

A solar RFB can be configured as a photoanode/normal cathode, a photocathode/normal anode, or a photoanode/photocathode. For a photoanode/cathode, the photoanode would be an n-type semiconductor. In an n-type photoelectrode, the holes migrate to the semiconductor surface to oxidise the redox species in the vicinity of the electrode-electrolyte interface, and the excited electrons move towards the cathode through an external circuit. In a p-type photoelectrode, the excited electrons reduce the redox species and the holes combine with the electrons from the external circuit. The concept of n-type and p-type photoelectrodes is clarified in Figure 2.4.

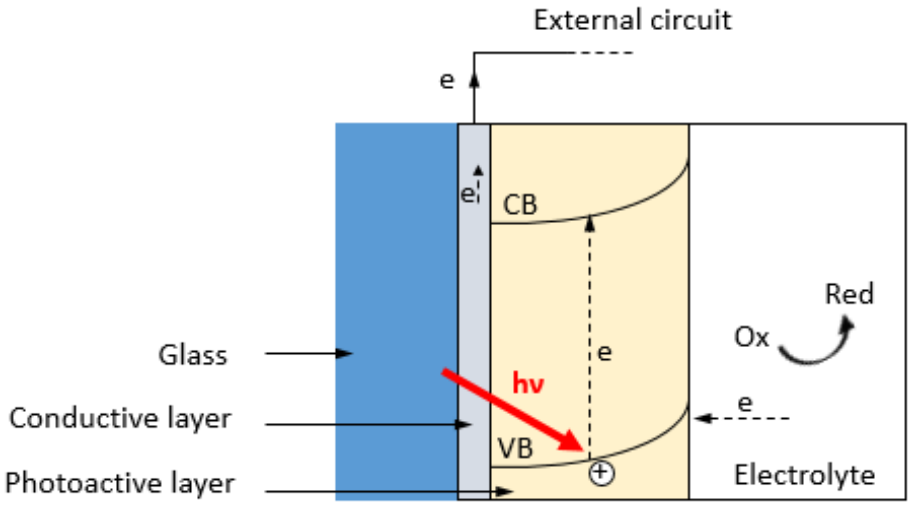

Figure 2.3: Principle of the photoelectrochemical process (VB = valence band, CB = conduction band, Ox = oxidant, Red = reductant): upon photon absorption the semiconductor's electrons are excited from VB to CB, and the generated charges participate in the electron transfer reaction with the redox species (Ox and Red) present in the electrolyte.

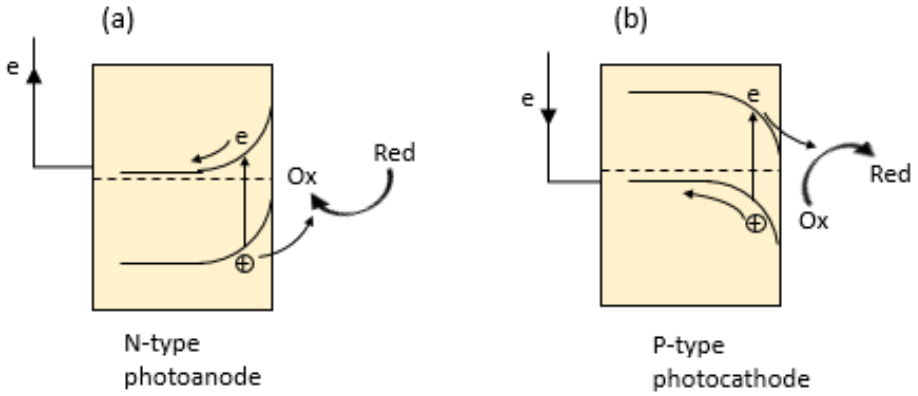

Figure 2.4: The concept and energy level of (a) n-type photoanode, where the generated holes oxidise the redox species, (b) p-type photocathode, where the generated electrons reduce the redox species [116].

Figure 2.5 presents a schematic diagram of a vanadium solar RFB in which an n-type photoanode is integrated into the positive half-cell, while the negative half-cell is the same as that of a normal RFB. The general reaction in each half-cell of this configuration is as follows:

Negative $$VO^{2+} + 2H^{+} + e^{-} \underset{discharge}{\overset{charge}{\rightleftharpoons}} V^{3+} + H_2O$$

Positive $$VO^{2+} + H_2O \underset{discharge}{\overset{charge}{\rightleftharpoons}} VO_2^{+} + 2H^{+} + e^{-}$$

The generated holes oxidise the redox species close to the electrode-electrolyte interface, and the electrons migrate towards the cathode through an external circuit. The positive charge carriers that are produced through the oxidation reaction move towards the negative half-cell through the membrane to react with the electrons and maintain the electrical balance in the system. The electrical energy is produced on demand by reversing the reactions and discharging the electrolyte.

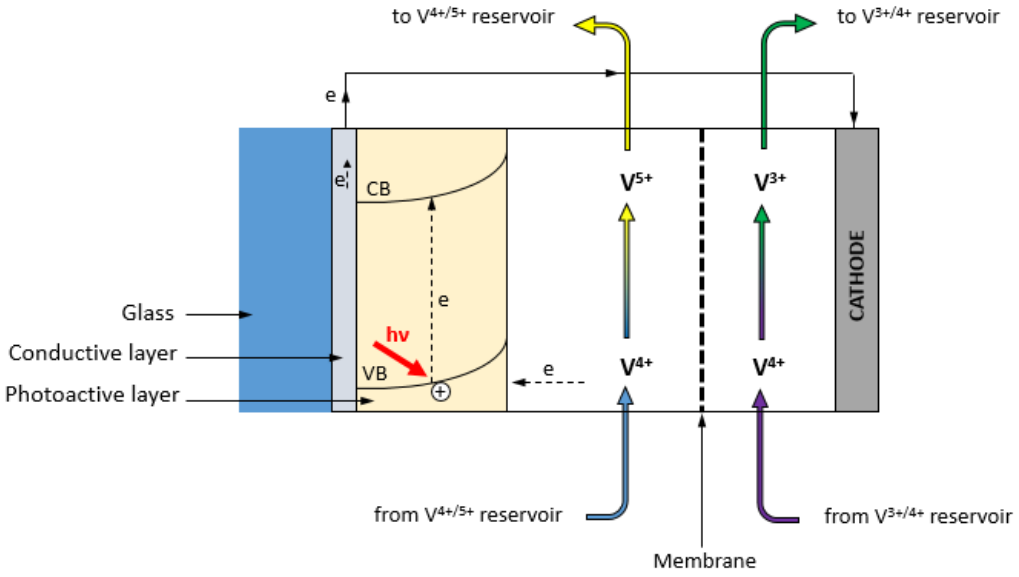

Figure 2.5: Schematic diagram of an all-vanadium solar RFB with an n-type photoelectrode (VB = valence band, CB = conduction band): the excited electrons move towards the cathode through an external circuit to reduce V^{4+} to V^{3+}, and the holes oxidise V^{4+} to V^{5+} on the photoanode.

2.3.3 Band position and band bending

The photoactive material is a semiconductor with an appropriate band gap. The ability of the photoelectrode to undergo the charge transfer process depends on the band energy position of the semiconductor and the redox potential levels of the adsorbate species. For the electron transfer reaction, the potential level of the acceptor species is required to be more positive than the conduction band potential of the semiconductor, while the potential level of the donor species needs to be more negative than the valence band edge of the semiconductor [117]. For redox couples with the potential slightly more positive than the conduction band edge, cathodic processes are possible, whereas anodic processes are kinetically hindered [118].

The band positions of various semiconductor materials with respect to the standard potentials of the V^{2+}/V^{3+} and VO^{2+}/VO_2^{+} redox couples (Figure 2.6).

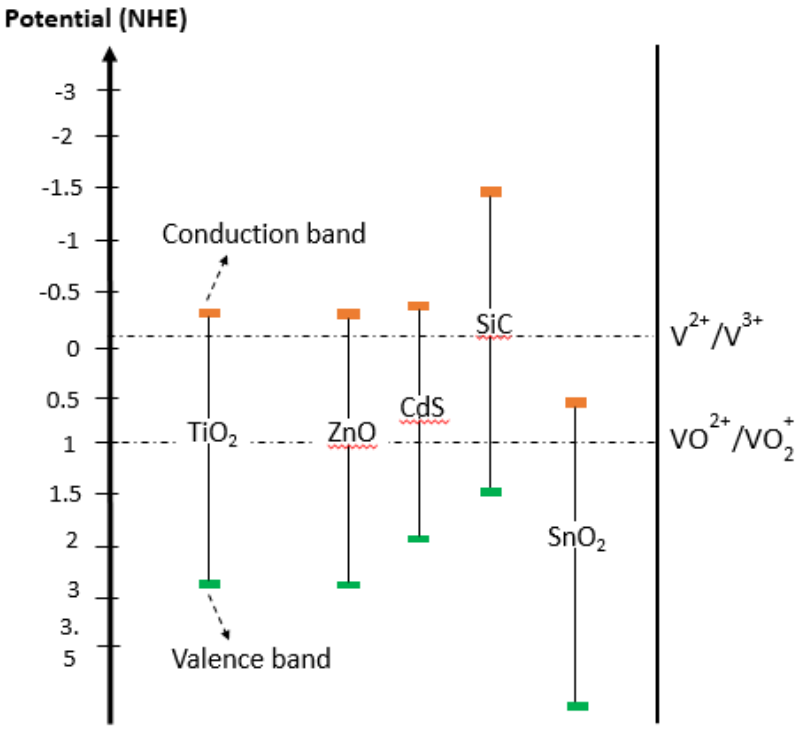

Figure 2.6: Band positions of various semiconductor materials with respect to the standard potentials of the V^{2+}/V^{3+} and VO^{2+}/VO_2^{+} redox couples.

When the semiconductor is in contact with an electrolyte, electric current initially flows across the semiconductor-electrolyte interface. As the electrons transfer from the semiconductor, the holes stay behind and form a positive space charge. This results in an electric field near the surface of the semiconductor which causes the separation of excited electron-hole pairs. The charge transfer to the semiconductor surface continues until the electric field becomes too strong for bulk electrons to cross [56, 59, 74]. At this point, the Fermi level of the semiconductor electrons is equal to the redox potential of the electrolyte and a dynamic equilibrium is obtained. The charge transfer across the interface changes the charge distribution and forms a space charge layer on each side of the interface. At the electrolyte-side this region is known as the double layer. At the semiconductor-side, the charge distribution changes the semiconductor energy offset and results in band bending near the junction. The band bending depends on the position of the semiconductor Fermi level (E_f) with respect to the redox potential. Figure 2.7 presents a schematic view of the electronic energy levels at the interface between an n-type semiconductor and an electrolyte. The flat band corresponds to the case in which semiconductor Fermi level is equal to the electrolyte redox potential and the semiconductor contains a uniform charge distribution (Figure 2.7-a). The existence of a positive charge on the interface increases the concentration of electrons in the vicinity of the interface and forms a space charge layer. This is called an accumulation layer. In this case, the bands of the semiconductor bend down toward the surface as a result of the decrease of electron potential energy (Figure 2.7-b). When negative charges accumulate at the interface, the electron concentration decreases near the surface of the semiconductor. As a result, a depletion layer forms in the space charge layer and the bands bend upward toward the surface (Figure 2.7-c). With more electron depletion, the Fermi level falls below the intrinsic level and the surface region of the semiconductor appears to be p-type while the bulk still exhibits n-type behaviour. This space charge layer is called an inversion layer (Figure 2.7-d) [117, 119].

Changing the voltage of the semiconductor by using a potentiostat causes the semiconductor and redox couple Fermi levels to separate, and hence the level of band bending owing to electron depletion in the semiconductor will change depending on the applied voltage. At the voltage that there is no band bending or charge depletion, the semiconductor is at its flat-band potential [120].

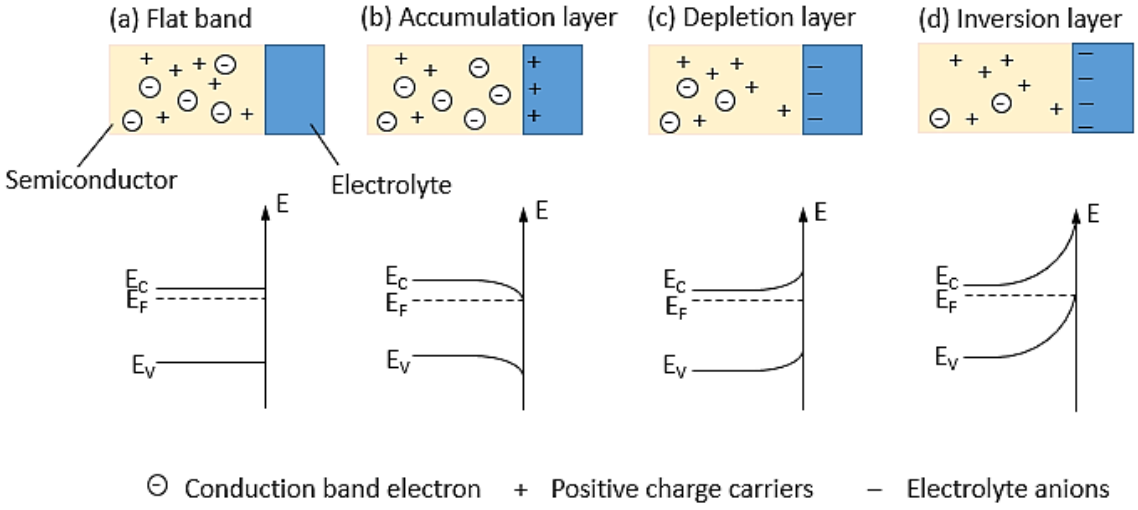

Figure 2.7: n-type semiconductor-solution interface (E_v = valence band energy level, E_c = conduction band energy level, E_f = Fermi level): a) flat band, where no space charge layer exists, b) accumulation layer, where excess electrons have been injected into the semiconductor, c) depletion layer, where electrons moved from the semiconductor to the electrolyte, d) inversion layer, where the number of electrons is depleted below their intrinsic level rendering the semiconductor p-type at the surface [119].

2.4 TiO_2 photoelectrode

The TiO_2 photoelectrode in solar RFB consists a layer of TiO_2 coated on a conductive layer on top of a glass base. The conductive layer has a high transparency to maximise the amount of light reaching the photoactive layer [121, 122]. The most commonly used transparent conductive layer is indium-doped tin oxide (ITO), which has relatively high optical transparency and superior conductivity. However, many groups are working to find a suitable replacement for ITO due to its scarcity, high price, and toxicity [123]. Fluorine-doped tin oxide (FTO) is a low-cost alternative that has attracted high attention due to several advantages. Apart from its low resistivity and high optical transmittance, it adheres strongly to the substrate, is resistant to physical etching, and has high thermal and chemical stability [123–127].

TiO_2 structure

TiO_2 is a semiconductor material that is widely used for different applications due to several advantages, such as suitable valence band and conduction band positions, long-term stability, non-toxicity, and strong oxidising power. It has three polymorphs, rutile, which is the stable phase, and anatase and brookite which are the metastable phases [20]. Brookite is difficult to be synthesised and therefore has rarely been used as a photocatalyst. Anatase has a larger band gap (3.2 eV) than that of rutile (3.0 eV) and therefore, it has lower absorbance ability for solar light. However, it displays much higher photocatalytic activity than rutile [117, 128, 129]. The high photoactivity of anatase is related to its structure, crystallite size, specific surface areas, and pore structure. Anatase has a higher surface adsorption capacity for hydroxyl groups and a lower charge carrier recombination rate than rutile [130, 131]. On the other hand, rutile has a larger grain size and lower specific surface areas causing volume recombination of charges [132, 133] and also a worse surface adsorption capacity [134, 135]. In addition, the lifetime of photogenerated electrons and holes in anatase is about an order of magnitude larger than that of photogenerated electrons and holes in rutile. As a result, the photoexcited electrons and holes in anatase have greater chance to participate in surface chemical reactions [128].

Mixtures of both phases of TiO_2 exhibit higher photoactivity as well as effective degradation in comparison with pure anatase or rutile catalysts [132]. A typical TiO_2 powder used in photoelectrochemical cells is Degussa P-25 which is composed of 75% anatase and 25% of rutile with particle size of 25 nm diameter. It is a cheap and easily processed powder, with a high surface area. It has a high photocatalytic activity that some researchers believe is due to the synergistic effect of the mixed anatase and rutile [136]. However, it is also suggested that the high photoactivity of Degussa P25 is partially due to high crystallinity and a minor Fe^{3+}doping, but mainly is derived from its anatase phase [133].

Film formation

TiO_2 photoelectrodes can be made using a variety of methods for film formation, such as: thermal or anodic oxidation of titanium, electron beam evaporation, ion sputtering, chemical vapour deposition, sol-gel, and mechanical deposition of a TiO_2 nanoparticle slurry using doctor blading, screen printing, or airbrush spray deposition. Solvothermal (in a non-aqueous solvent) and

hydrothermal (in water) processes are simple routes to obtain TiO_2 nanotube/nanorod with high length-to-diameter ratio for large scale production. They involve dissolving TiO_2 or its precursor in a solvent (organic or aqueous) followed by use of an autoclave in which the nanosized crystallised TiO_2 nanotubes/nanorods form under high temperature and pressure [137].

Anodic oxidation includes immobilising the TiO_2 powder from a solution containing Ti precursor chemicals, or a suspension of pre-synthesised powder, followed by densification using thermal treatment [138]. This method enables production of ordered TiO_2 nanotubes with high length-to-diameter ratio [139].

Electron beam evaporation can be applied to form a thin film of TiO_2 (deposition rate < 0.2 nm/s) [140, 141]. It uses an electron beam to focus a large amount of energy onto the source material. Conventional electron beam evaporation results in a porous film of TiO_2 with a refractive index of 1.9, which is lower than the refractive index of the bulk. Hence, TiO_2 films are commonly prepared by ion beam assisted electron beam evaporation. In this technique, atoms deposited on the substrate get more energy from ion bombardment, resulting in the formation of a more compact structure with higher refractive index [142].

Ion sputtering also forms a thin film of TiO_2 (deposition rate < 1 nm/s) [143, 144]. This method is based on low-energy ion bombardment of a metallic target [145].

Chemical vapor deposition enables low temperature formation of a thin film of TiO_2 (deposition rate < 1 nm/s). In this technique, chemical reaction is activated by surface heating of the titanium precursor. The activated gas phase molecule is absorbed on a surface and then decomposed to produce TiO_2 [146, 147]. The composition and structure of the deposited compounds can be easily controlled by choice of the deposition condition [148].

The sol-gel method involves the evolution of inorganic networks by the formation of a colloidal suspension (sol) and gelation of this to form a network in a continuous liquid phase (gel). The precursor consists of a metal or metalloid element surrounded by various ligands [149]. This technique is used to produce sub-micron TiO_2 spheres by controlling the hydrolysis and condensation reactions. It allows the possibility of widely varying the film properties by changing the composition of the solution [150].

Doctor blading consists of the deposition of a viscous slurry, which is spread on a substrate by use of a blade. The thickness of the TiO_2 film can be adjusted by the distance between the substrate and the blade [151, 152]. This method is easy to perform and has a high throughput. However, it is difficult to reproduce precisely the same film. Also, a binding agent needs to be used to make a viscous slurry and that can diminish the electrical conductivity of the film [153].

Screen printing is very similar to doctor blading technique. The only difference is that a mask (mesh) is placed on the substrate and by moving the blade, the slurry is deposited on the substrate through the openings of the mask [154–156].

Airbrush spray deposition uses a colloidal solution of TiO_2 which is sprayed over a surface. To obtain the maximum homogeneity in the final TiO_2 film, the slurry solution must be atomised [157].

After deposition of the TiO_2 film, it is usually annealed at 450°C. Annealing allows the TiO_2 particles to interconnect and form a network. Annealing increases the grain size and reduces the resistivity of the films which results in enhanced electron transport [158]. The resistivity of the film decreases with increasing annealing temperature [159]. During annealing the heating rate impacts the surface roughness of the TiO_2 film. Surfaces of films prepared at low annealing rates (1°C/min) are smoother and more homogeneous. In contrast, a sudden increase of temperature leads to decreased coalescence of the particles which increases roughness of the film [160].

TiO_2 patterning

The main challenge of a TiO_2 photoelectrode is the high band gap of TiO_2 (3.2 eV). This limits its activity to just the UV range, which is less than 10% of the solar spectrum. As a result, various techniques have been employed to enhance the photoactivity of the TiO_2 for different applications. Some focus on expanding the active spectral rage of TiO_2 (e.g. to the visible spectrum). These include: doping TiO_2 with metallic and non-metallic species [161, 162, 171, 172, 163–170], reducing TiO_x photocatalysts [173–177], introducing intermediate band gap by compositing TiO_2 with semiconductors having lower band gap energy (e.g. CdS particles) [178–181], sensitizing of TiO_2 with dyes (e.g. thionine) [182–184], and doping TiO_2 with upconversion luminescence agent [185, 186]. Alternatively, patterning is an approach that can be used to improve the photoactivity

of TiO_2 in the UV spectrum. This can improve the photoanode-electrolyte interface and enhance the wettability of the photo-anode active materials by the electrolyte providing more active sites for the electron transfer reaction. It also provides the advantages of convergent diffusion of redox ion [187], increased path length of photons close to the solution interface, shorter charge carrier path [188], and low charge recombination [189]. In a research, by patterning a geometry of micropillars on the TiO_2 surface in a DSSC, the power conversion efficiency was improved from 4.05% to 5.33%. This was stable in a prolonged aging test (2000 h at 50 °C) during which it maintained 96% of its initial value [21].

Several approaches have been applied to pattern the TiO_2 layer. One technique is using photolithography to form a pattern containing an array of pillars or holes in a negative photoresist followed by deposition of a TiO_2 layer on the surface by electron beam evaporation, sputtering, or screen-printing. SU-8 is the most common photoresist used for this purpose, as it enables the formation of a thick layer with a high thermal and chemical stability that resists the consecutive steps [25]. Calcination of the substrate at 450°C burns the photoresist and leaves an array of holes in or pillars out of the TiO_2. An inverse opal structure can be fabricated using microsphere lithography. This method uses a suspension of polymeric spherical beads (e.g. polystyrene) which are deposited on the substrate by various methods such as spin-coating, or dip coating. The voids of polystyrene opals are then filled by infiltration of TiO_2 using a colloidal solution of TiO_2 or a solution of titanium precursor (sol-gel) [190–193]. Imprint lithography can be used to fabricate a variety of patterns into a TiO_2 paste followed by curing the TiO_2 layer using heat or UV light [21, 22, 194–196]. Hydrothermal growth of TiO_2 is an efficient method to fabricate dense oriented/disoriented single-crystalline/polycrystalline TiO_2 nanorods with a wide range of lengths up to 10 μm [197–200].

2.5 Photocurrent and limiting factors

The photocurrent is simply the net rate of electron transfer between the photoelectrode and the redox species in the electrolyte when driven by solar energy. To excite the electrons to the conduction band, the photon energy must be at least equal to the band gap energy of the photoactive

material. This implies that every photoelectrode is active only in a specific range of light wavelengths. The maximum wavelength to excite the electrons to the conduction band can be calculated using Planck-Einstein equation (Eq. 2.1).

$$E = h\nu = {}^{hc}/_{\lambda} \qquad \text{Eq. 2.1}$$

Where:
E is energy,
h is Planck's constant,
v is light frequency,
c is the speed of light,
λ is light wavelength.

In order to harvest more photons with appropriate wavelength, the light loss on the photoelectrode must be minimised. There are various factors that limit photon harvesting in the semiconductor layer (Figure 2.8):

- Reflection from the outer surface of the optical window
- Surface contamination on the optical window that blocks the light path
- Light absorption within the inactive layer or in the photoactive layer away from the electrode-electrolyte interface
- Light transmission through the photoactive layer

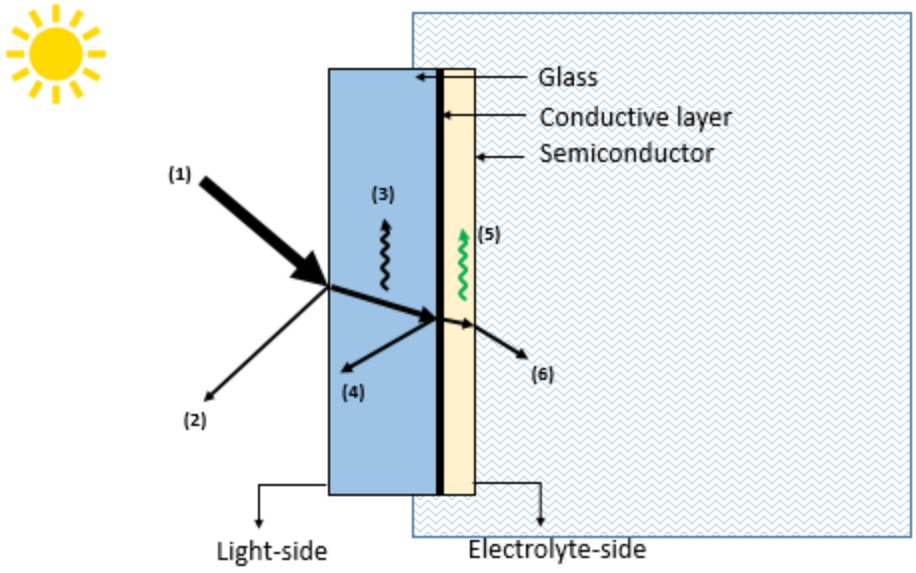

Figure 2.8: The paths taken by photons incident on a RFB photoelectrode: (1) incident light, (2) reflection from outer surface of the photoelectrode, (3) ineffective light absorption within the substrate, (4) back reflection from inner layers, (5) effective photon absorption causing excitation of electrons, (6) transmission through the photoactive layer

When photons are absorbed, the resulting electron-hole excitation does not necessarily lead to electron transfer reactions. The photoactivity of the semiconductor layer is restricted by factors that cause high recombination rates, such as short hole diffusion length and short carrier lifetime. Studies on the time scale of charge transfer reaction suggest that photocatalytic reactions could be completed within μs to ms after the generation of the electron-hole pair, while the charge recombination process is relatively fast and takes a few μs [201–203]. The excited charges can follow several recombination pathways (Figure 2.9). The separated electron and hole pairs move randomly to the surface of the semiconductor and, on their way, might recombine with the opposite charge carriers on the bulk semiconductor (pathway 1). The charges that get to the surface might either recombine with charge carriers at the surface trapping sites (pathway 2) or react with the redox species at the interface (pathway 3). The bulk recombination can be minimised by reducing the distance for charge carriers to reach acceptor species. Hence, for an effective charge transfer reaction, absorption of photons must occur close to the semiconductor-electrolyte interface at the space charge layer.

The electron exchange with the redox couple is in competition with electron-hole recombination. Therefore, the number of available redox couples at the interface and their speed of reaction with the available charges affects the electron-hole recombination rate [203–205]. In other words, the charge recombination rate is a function of redox species mass transfer rate and the electron transfer reaction kinetics.

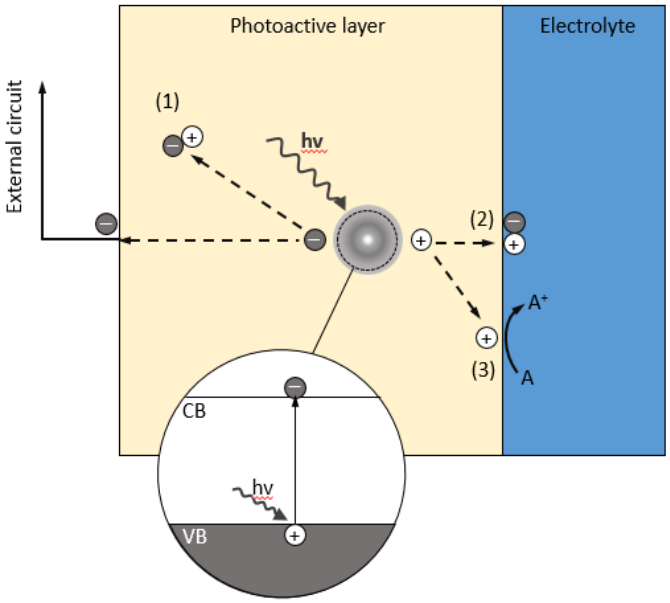

Figure 2.9. The possible pathways for excited electron-hole pairs on an n-type semiconductor: (1) bulk recombination, (2) surface recombination, (3) electron travelling through an external circuit and hole participating in the redox reaction.

2.6 Characteristics of patterned photoelectrodes

Apart from the inherent kinetics of the photocatalytic reaction, the efficiency of the RFB photoelectrode depends on the number of photons absorbed in the semiconductor layer and the rate of charge transfer to the redox species. The fabrication of photoanodes with strong light-harvesting ability, low charge recombination, and optimal interface with the electrolyte is a key

challenge in photoelectrochemical devices. Patterning each layer of the photoelectrode can affect its photoactivity in different ways.

2.6.1 Light behaviour on a patterned photoelectrode

The incident light on a photoelectrode can take several paths. Some reflects from the photoelectrode, some is absorbed within each layer, and the remainder is transmitted through the photoelectrode. Improvements in light harvesting increase the amount of light absorbed within the photoactive layer.

The presence of a nano-/micro-structured pattern in the light path affects light behaviour in several ways. Changing the surface geometry of a substrate changes the light reflectivity and refractivity and, consequently, the absorption of photons within the photoactive layer. In addition, photoelectrodes placed outdoors are always at risk of being fouled by dust and other contaminants which block the light path. Surface roughness on the optical window of a photoelectrode reduces the surface contamination rate by improving its self-cleaning behaviour during rainfall.

An improvement in light absorption in the photoactive layer can be achieved by increasing the amount of photoactive material. However, there is a thickness limitation as increasing the charge carrier path length boosts the volume charge recombination. Therefore, a favourable structure for a semiconductor is one that provides a long dimension for light absorption but a short distance for charge carriers to reach acceptor species [34]. A high–aspect ratio nanorod array is an example of such an structure in which light travels along the axis of each rod to be absorbed by the semiconductor while the carriers move radially along the short dimension to be collected as electricity [188].

Antireflection behaviour

The application of regular and random nanostructures as an antireflection coating has been widely studied for various optoelectronic devices [206, 207, 216–221, 208–215].

Light reflection occurs due to the change of light velocity when it reaches a substance with different refractive index. Small differences between the refractive indexes of two media cause less light reflection [222]. Light reflection is typically minimised by creating a nanoscale roughness on a surface which produces a gradual change of refractive index between two media [223] (Figure 2.10). Periodic arrays with a periodicity less than the light wavelength (sub-wavelength structures) behave as homogenous media [224–226]. In these arrangements, the spacing between the elements is small enough to suppress light diffraction caused by their periodicity, and light interacts with the whole pattern rather than interacting with each spot [227–230]. Currently, subwavelength structures are extensively employed to synthesise a wide range of refractive indexes [231].

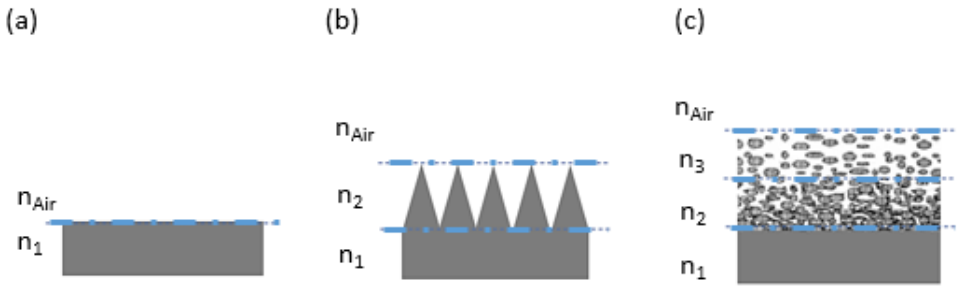

Figure 2.10. Schematic illustration of refractive index (n) increase from air to the substrate for: (a) plane substrate, (b) periodic subwavelength structure, (c) porous layers. Gradual change of refractive indexes reduces the light reflection from a to c.

The effective refractive index of a subwavelength structure depends on the light wavelength and the geometrical properties of the structure [218, 219]. The geometrical properties (Figure 2.11) are defined by pitch (periodicity), filling ratio (base diameter-to-pitch), and aspect ratio (height-to-base diameter). In a periodic structure, a large material filling ratio reduces light reflection from an open basal area, and a higher aspect ratio enables a more gradual and continuous refractive index change from air to the substrate. However, fabrication of very tall and continuous structures is technically challenging and economically inefficient [232]. Many investigations have focused on the antireflection behaviour of nanostructured gratings with different geometries, such as moth-

eye [233–235], inverted pyramids [236], pyramids [237], nanopencils [232], nanorods [238, 239], nanopillars [240], nanocones [217, 241], and inverted nanocones [230, 236, 242]. Pyramidal nanostructure is one of the features that was highly effective in antireflection [236, 237, 243]. The geometry of this structure causes a very gradual change of refractive index profile from air to the substrate, and the sharp tip of pyramids minimises top surface reflection and improves light transmission down to the base.

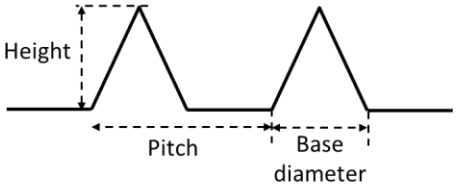

Figure 2.11. Geometrical properties of a subwavelength structure: Material filling ratio = $\frac{\text{Base diameter}}{\text{Pitch}}$, Aspect ratio= $\frac{\text{Height}}{\text{Base diameter}}$

Diffraction grating

Light scatters when it passes through the junction of two media with different refractive indexes. This changes the light path length through the photoactive material and affects photon absorption [27, 28, 244]. Variation of light path length and absorption depth with respect to the semiconductor-electrolyte interface and the space charge layer affects the electron transfer rate (Figure 2.12).

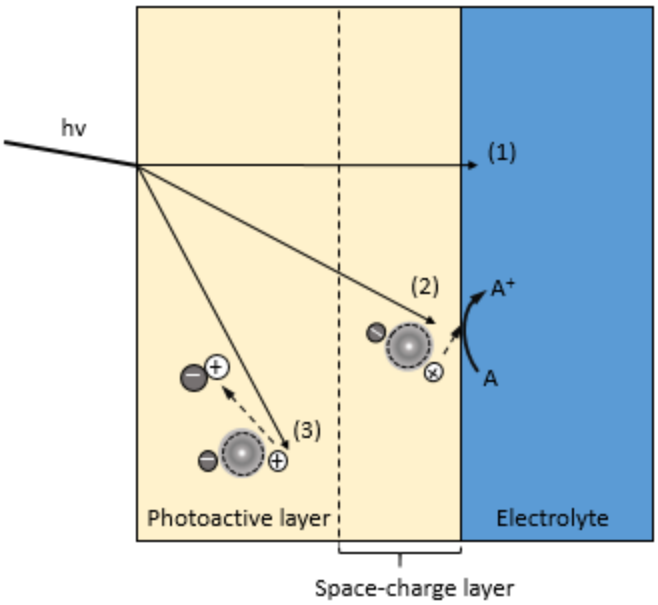

Figure 2.12: The effect of light path length on loss of photons; arrow length represents absorption depth: (1) transmitted light when photon absorption depth is larger than semiconductor thickness, (2) photon absorption in the space charge layer resulting in an electron transfer reaction, (3) photon absorption outside the space charge layer resulting in electron-hole recombination.

Periodic structure with elements separated by a distance comparable to the wavelength of light diffracts the light into several reflecting/transmitting beams that travel in different directions [245]. Figure 2.13 shows two beams of a monochromatic light with wavelength of λ incident at some angle α upon a grating with a pitch of d. In the wavefront *A*, the two incident beams are in the same phase. The difference in the path length of two incident light rays is seen to be $d \sin\alpha + d \sin\beta$. Upon diffraction, if the difference in the path lengths of the two rays is an integral number of wavelengths (Eq. 2.2), the beams are in phase at the wavefront *B* and interfere constructively. At all other angles the wavelets originating from the surface will interfere destructively. As a result, there will be several discrete angles at which the condition for constructive interference is satisfied, and the light is reflected (or/and transmitted) into discrete directions (Figure 2.14) [246].

$$d \sin\alpha + d \sin\beta = m\lambda \qquad \text{Eq. 2.2}$$

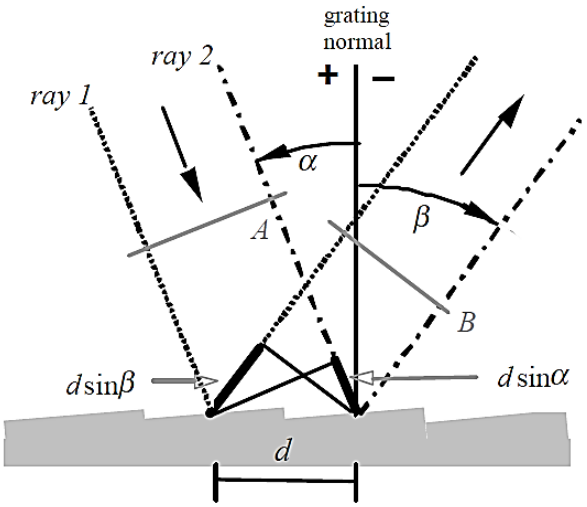

Figure 2.13. A monochromatic light of wavelength λ incident at an angle α and diffracted by a grating with the pitch of d at set of angles [246].

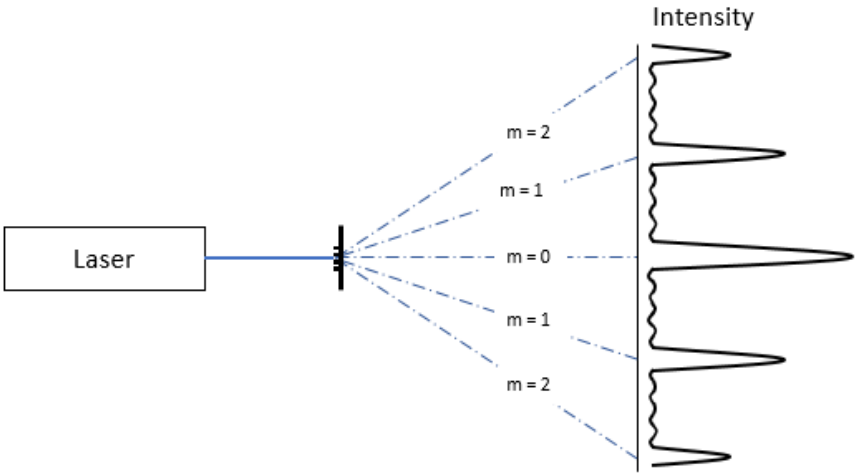

Figure 2.14. Diffraction maxima created by a periodic grating and the beam intensity of each diffraction order (m).

The angular location of the principal intensity maxima when light of wavelength λ is diffracted from a grating of pitch d is derived from the following equation [246, 247]:

$$sin\,\theta_m = \frac{m\lambda}{nd} \pm sin\,\alpha \qquad \text{Eq. 2.3}$$

Where:
λ is the wavelength of light in the air ($n \sim 1$),
n is the refractive index of the medium,
d is the pitch of structure,
α is the angle of incidence,
m is the order of diffracted ray called the order of maximum.

The grating equation reveals that only those spectral orders for which $|m\lambda/d| < 2$ can exist. For $\lambda/d << 1$, a large number of diffraction order exists and the case m = 0 leads to $\beta = -\alpha$ [246].

Self-cleaning behaviour

The surface contamination on the optical window of solar panels blocks the incident light and reduces the system's efficiency. This issue is addressed by improving the self-cleaning behaviour of the optical window of the photoelectrode [236–238, 248–254].

The term self-cleaning refers to super-hydrophilicity or super-hydrophobicity of the surfaces. This causes water to effectively wash the surface during rainfall. With a super-hydrophilic surface, water spreads out and forms a thin film that washes away the dust. In contrast, a super-hydrophobic surface minimises the solid-liquid contact area between water droplets and the surface. The consequence is that spherical water droplets roll off the surface whilst picking up dust particles [255].

Surface roughness improves self-cleaning behaviour by making hydrophilic surfaces super-hydrophilic and hydrophobic surfaces super-hydrophobic [256, 257]. This phenomenon is known as lotus behaviour (Figure 2.15).

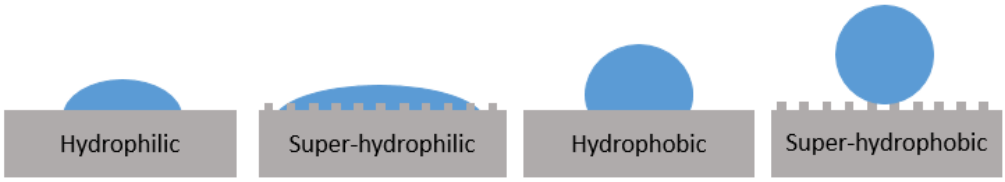

Figure 2.15: The effect of surface roughness on hydrophilicity and hydrophobicity of solid materials.

Self-cleaning behaviour of a surface can be evaluated by measuring its wetting properties. Contact angle measurements are often used for this [258]. The sessile drop method is a popular approach, in which a liquid droplet is placed on the solid surface and a measurement made of the angle between this and the tangent at the drop boundary (Figure 2.16). If the deposited drop stops spreading over the surface, the equilibrium contact angle is given by Young's equation:

$$\gamma_{SV} = \gamma_{LV}\, cos\theta_c + \gamma_{SL} \qquad \text{Eq. 2.4}$$

Where

θ_c is the equilibrium contact angle,

γ_{SL}, γ_{SV}, and γ_{LV} are solid-liquid, solid-vapor and liquid-vapor interfacial tensions.

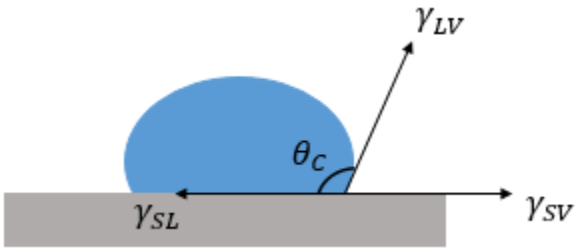

Figure 2.16. Schematic illustration of the contact angle formed by a sessile drop on a solid surface, θc is the contact angle and γ_{SL}, γ_{LV}, γ_{SV} are surface tensions between the three phases.

2.6.2 Rate of electron transfer reaction on a patterned photoelectrode

The electron transfer from the photoelectrode to the redox species is in competition with the charge recombination within the semiconductor layer. Patterning the electrode-electrolyte interface can affect the charge recombination by reducing the distance that charge carriers pass to get to the redox species and increasing the number of available redox species at the electrode surface.

The morphology of the electrode-electrolyte interface defines the available electroactive surface area (EASA) for the reactants. Texturing the surface of the electrode by nano-/micro-structures increases its surface area to volume ratio. However, there is a limitation in size reduction as an increased surface area to volume ratio is associated with more crystalline defects and this would favour charge recombination [259, 260]. Surface patterning is another approach to enhance the surface to volume ratio of the material. This improves the number of active sites of the semiconductor and allows electrolyte penetration into the whole thickness of the semiconductor layer [261, 262]. Furthermore, surface irregularities on the semiconductor-electrolyte interface serve as charge carrier traps and help to suppress recombination. This increases the lifetime of the separated electron and hole to above a fraction of a nanosecond [117, 263, 264].

The morphology of the electrode-electrolyte interface can also affect the redox species concentration profile in the solution (Figure 2.17). Radial diffusion to the edges of the structure contributes significantly to the overall diffusion. It has been shown that in a micro-structured electrode, the spacing between the elements affects the generated current, and the back diffusion of products to the neighbouring elements contributes to the efficiency of the system [187].

The enhanced EASA and mass transport improves the sensitivity of the electrode and reduces the impedance [265–267]. Due to these favourable characteristics, many researches have been conducted to fabricate nano-/micro-patterned electrodes for a variety of applications such as energy conversion and storage systems [268–271], sensors [272, 273], and electro-synthesis [274].

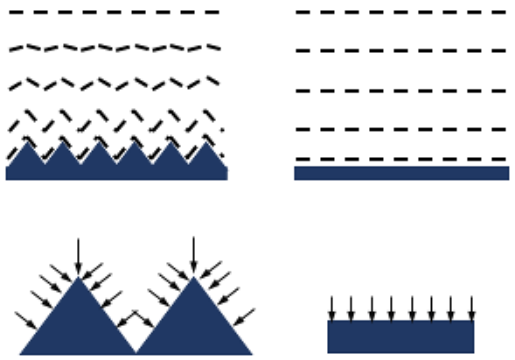

Figure 2.17. Surface morphology effect on redox reactant concentration profile in the solution (dashed lines represent the points with equal concentration in the diffusion layer, and vectors show the species flux towards the electrode surface).

2.7 Lithography techniques

Fabrication of nano-/micro-structures has contributed greatly to the improvement of technologies such as integrated circuits and microchips [45-56], and high-sensitivity, high-resolution sensing systems [275, 276]. Patterning the surface of the photoelectrode with nano-/micro-structures is a promising technique to modify its optical and electrochemical properties [113]. By utilizing patterning technologies developed in the last three decades, this approach could easily be scaled up for manufacturing industrial devices [277–281].

Fabrication usually consists of two steps: a) lithography which results in a patterned resist (a polymeric mixture that is formulated for a given lithography technology) film coated on top of a functional material, b) techniques such as etching which transfer the pattern from the resist to the top of the functional material.

Lithography produces precise and complex two-dimensional or three-dimensional structures that range in size from a few nanometres up to tens of millimetres. Lithographic printing of the pattern in the resist can be performed mechanically, chemically, or by using radiation (photons, electrons, or ions). The pattern can either be fabricated directly on the functional substrate or be transferred to the functional substrate through a mask [282]. The resist that is used for lithography has to be sensitive to the imaging radiation and withstand the etching (or other pattern transfer) step whilst

also having some tolerance to process variability such as exposure level. The sensitivity of a resist is usually expressed as the dose in millijoules per centimetre squared that brings about the required response to the developer.

Lithography techniques are diverse, of which seven are briefly described below and in Table 2.5.

1) Electron beam lithography forms a pattern by focusing a beam of ions on the resist and blanking the beam at appropriate intervals. This method is used to fabricate structures with ultra-high resolution (less than 10 nm wide). However, it is slow, and this limits the throughput which makes it inappropriate for mass production.

2) Focused ion beam lithography uses a beam of ions to create a pattern across a surface, enabling the fabrication of high-resolution structures. Due to the problem of shot noise in the beam, its application is limited to features with sizes greater than 100 nm [283].

3) Photolithography patterns a thin layer of photosensitive resist (photoresist) over a substrate by exposing it to UV light through a mask (an opaque, patternable film on top of a transparent substrate such as glass). In the exposed area, the polymer chains of photoresist break down and become soluble in a chemical solution called developer. Removing the exposed photoresist in a developer forms the desired pattern into this layer [284–287].

4) Laser interference lithography [221, 288] uses two laser beams from the same source which coincide on the surface of the substrate, and their intensity and phase correlations form a pattern of dark and bright spots on a photoresist layer. The final pattern is obtained by developing the exposed photoresist.

5) Nanoimprint lithography [238, 289] is a mechanical approach that fabricates a pattern by stamping a mold (template) into a resist.

6) Nanosphere lithography involves submerging the substrate in a nanosphere suspension (such as polystyrene beads suspended in a solvent) and then a self-assembled hexagonal-close-packed monolayer of nanospheres is formed by evaporation of the solvent. This layer is used as a lithography mask to grow a nanostructure through deposition of the desired material [290, 291].

7) Block copolymer lithography is a chemical technique in which the pattern forms through self-assembly of a monolayer of molecules on the local surface during thermal or solvent annealing. This method offers an attractive alternative patterning technology as self-assembly can occur on length scales from a few to hundreds of nanometres [280, 292]. Reactive ion etching is commonly used to transfer the self-assembled block polymer pattern into a functional material [293].

Table 2.5: Specifications of the major lithography techniques

Lithography technique	**Minimum feature size**	**Throughput**	**Limitation**	**Ref.**
Electron beam lithography	< 5 nm	Very low (8 h for a chip pattern)	- Slow - High cost	[294]
Focused ion beam lithography	20 nm	Very low	- Slow - High cost	[295]
Photolithography	2-3 µm	Very high (60 wafers/h)	- Limited resolution - Precise control of positions is required	[282, 296]
Laser interference lithography	> 50 nm	High	- Complexity - Only for periodic structures - Features' size is limited by the light wavelength	[297, 298]
Nanoimprint lithography	6-40 nm	High (> 5 wafers/h)	- Achieving an imprinted layer with a uniform thickness is challenging	[299]
Nanosphere lithography	>100 nm	High	- Only for a limited range of shape and spacing - Size limitation due to increasing polydispersity by reducing the particles' diameter	[300]
Block copolymer lithography	< 10 nm	Low	- Complexity - Block-block interaction, - Temperature-dependant	[293]

2.8 Nanoimprint lithography

Nanoimprint lithography was first proposed in 1995 by Chou *et al*. [301]. In this method (Figure 2.18), a mold that contains the inverse of the desired feature is stamped into a thin layer of polymeric material on the substrate to replicate the pattern through mechanical deformation. The curing process depends on the type of polymeric material. Thermoplastic polymers are heated whilst photo-polymers are exposed to UV radiation [242, 283]. The mold is then peeled off and anisotropic etching is used to remove the residual resist from the compressed area. The patterned polymeric layer can be used as: (a) a mask for dry etching if the imprinted polymer is resistant enough, (b) a mold to fabricate an upright structure, or (c) a functional substrate assuming the polymer has a required functionality such as a conductivity and optical response.

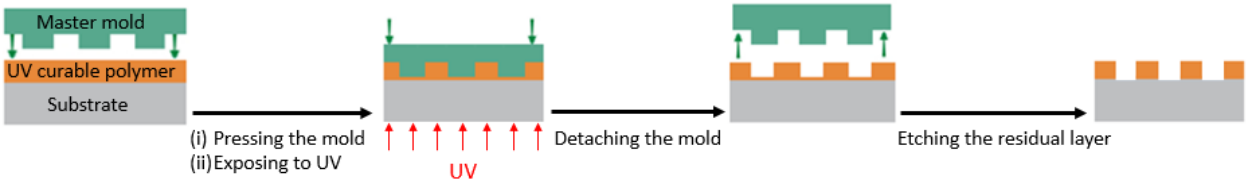

Figure 2.18: Process flow diagram of the nanoimprint lithography method; the pattern is transferred from a master mold to a UV curable polymer coated on a substrate.

Nanoimprint lithography has many advantages over other lithography techniques. The resolution of nanoimprinting is not limited by the factors that limit the other techniques, such as wave diffraction, scattering and interference in a resist, and back scattering from the substrate. Therefore, it has the potential to create patterns with sizes ranging from several micrometers to sub-25 nm over a large area with a high-throughput and low-cost [234, 302]. Furthermore, it enables an accurate reproduction of original mold patterns while maintaining smooth vertical sidewalls in the imprint resist.

Despite the simplicity of this approach, nanoimprinting has its own challenges. Direct contact between the mask and the wafer makes the technology susceptible to more defects. Any residue of resist or dirt on the mold reduces the quality of the pattern. The mold is exposed to heating and

cooling cycles and high pressure which reduces its lifetime. It is very common for the mold to be damaged during the demolding step. An anti-sticking layer coated on the mold prevents this but must be renewed after a number of prints. The number of cycles that an anti-sticking layer can survive before being renewed depends on the stability of this layer when exposed to operational conditions such as mechanical stresses and high temperatures. It also depends on the strength of chemical binding to the master mold [303]. The time required for stamp cleaning and replacement, alignment, and coating with an anti-sticking layer reduces the throughput [282].

2.9 Llyod mirror laser interference lithography

Interference lithography uses a coherent laser split into two or more beams which recombine at a substrate at different angles of incidence. The overlap of the intensities and phases of the beams creates a pattern of dark and bright spots on the substrate (Figure 2.19) [304]. The interference of two, three and four beams would respectively form 1, 2 and 3 dimensional structures [288]. The angles of incidence of the beams can be used to control the periodicity of the pattern. When interference involves two beams then the periodicity of the pattern is obtained by the following equation:

$$P = \frac{\lambda}{\sin\theta_1 + \sin\theta_2} \qquad \text{Eq. 2.5}$$

Where:

P is the pattern periodicity,

λ is the beam's wavelength,

θ_1, θ_2 are the angle of incidence corresponding to each beam.

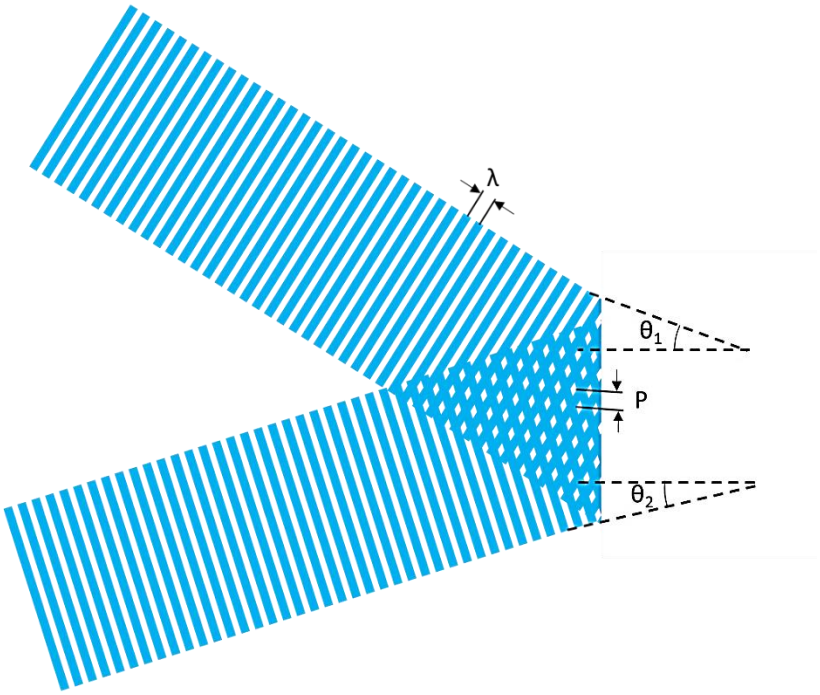

Figure 2.19. The overlap of two similar beams with a wavelength of λ but with different phases (different angle of incidence of θ_1 and θ_2) creates a pattern of dark and bright spots with the periodicity of P, where $P = \frac{\lambda}{\sin\theta_1 + \sin\theta_2}$.

The pattern can be recorded on a photosensitive material. In this case, the laser wavelength is chosen based on the sensitivity and absorption of the surface. The laser can be pulsed or continuous, however, the beams must interfere in their coherence length. In order to optimise interference, the beams' polarisation vector must be in the same direction. Patterns with high resolution can be obtained by using a Lloyd's Mirror Interferometer (Figure 2.20) to split the laser beam [288]. A Lloyd's mirror interferometer creates a diverging beam by using a laser with a long coherent Gaussian beam which passes through a lens and a pinhole. Some of the light directly hits the substrate, and some reflects from the mirror, which is perpendicular to the substrate. The beam centre is aligned at the intersection of the mirror and the substrate ($\alpha_1 = \alpha_2$) to have beams with equal intensity. At the substrate, both of the beams have the same angle of incidence which is equivalent to the angle of rotation of the stage. Therefore, to calculate the periodicity of the structure, Eq. 2.5 is simplified as follows:

$$P = \frac{\lambda}{2 \sin \theta} \qquad \text{Eq. 2.6}$$

Where:

P is the periodicity of the pattern (pitch),

λ is the wavelength of the beam,

θ is the angle of incidence which is equivalent to the angle of rotation of the stage.

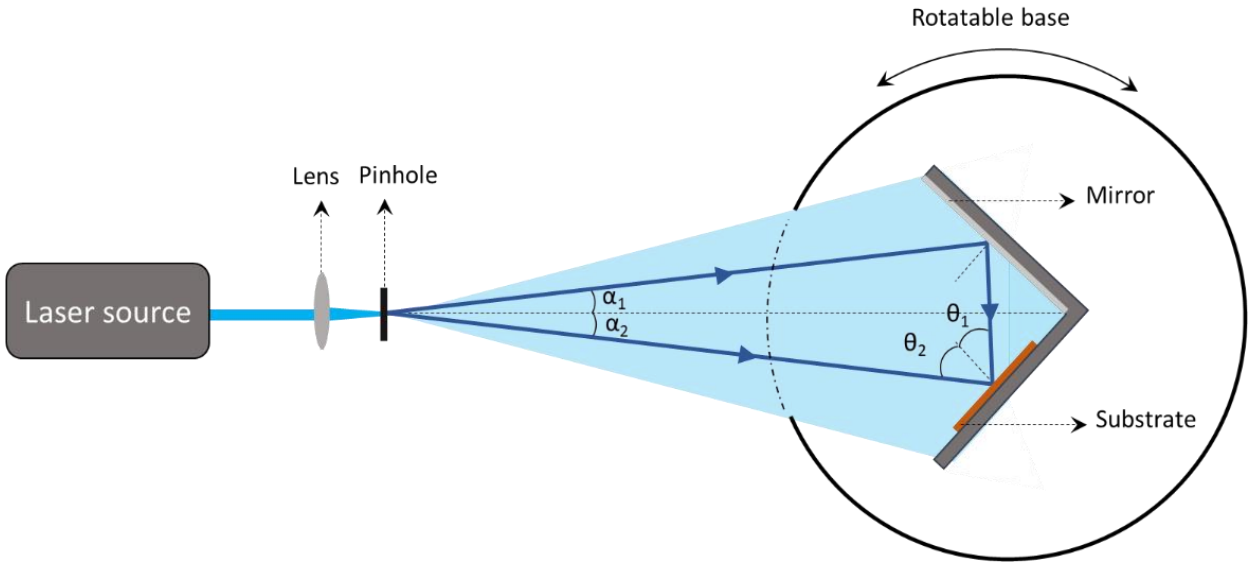

Figure 2.20. Schematic diagram of Lloyd's mirror interferometer; the laser beam is split into two coherent beams using a lens and a pinhole. One beam travels directly to the substrate, and the other hits a mirror and reflects to the substrate. The two beams, which are in different phases, interfere with each other at the substrate and form a periodic pattern of spots which are light (where the interference is constructive) and dark (where the interference is destructive). The mirror and the substrate are placed on a rotatable base that enables control of the periodicity of the pattern by adjusting the incidence angle of beams [304].

3 Investigation into the effect of periodic nanopatterns on light harvesting

3.1 Introduction

The photoactivity of a semiconductor material is highly dependent on the performance of harvesting photons within the semiconductor layer. In some applications, a specific range of wavelengths of light is preferable, and efforts are made to improve the light harvesting in that specific range. Light harvesting is improved by reducing the number of photons that are lost due to: 1) reflection from the surface, 2) absorption within inactive layers, and 3) transmission through the photoactive layer. This chapter describes an investigation into the effects of a periodically patterned optical window on the harvesting of UV light in a TiO_2 layer.

Surface roughness reduces light reflection by causing a gradual change of refractive index between two media [223]. Periodic structures with a periodicity less than the wavelength of incident light have been employed widely as a coating to reduce the reflection of specific ranges of wavelength for different applications, such as solar cells [216, 217, 305], and imaging lenses [306, 307]. It has been shown that fabricating a subwavelength structure on the surface of a Si wafer results in 80% less light reflection in a wavelength range of $400 - 800$ nm [308]. Furthermore, the nanoscale roughness caused by subwavelength structures improves the self-cleaning behaviour of the surface by boosting the surface hydrophobicity or hydrophilicity. This reduces surface contamination that would otherwise block the light path [309, 310].

Photons with an absorption length greater than the thickness of the photoactive layer are transmitted through the layer without being absorbed [311]. Therefore, increasing the light path length within the photoactive layer would improve light absorption. This reduces the required thickness of photoactive layer and as a result, lowers the bulk charge recombination [312]. One approach to lengthen the path of photons and reduce light transmission is to use a back-reflector scattering layer coated on top of the photoactive layer [313]. Another approach is to apply diffraction gratings to manipulate the light path within the photoactive layer. Diffraction gratings change the light propagation direction from normal to oblique and prolong the path of the incident

light in the active layer [19, 314–316]. In addition, upon diffraction, some photons would travel within the photoactive layer at an angle higher than the critical angle which would result in their reflection back into this layer [317].

In this study, a periodic structure of nanopyramids with a periodicity of 670 nm was fabricated from a transparent UV curable polymer coated on the bare side of a fluorine-doped tin-oxide (FTO) coated glass substrate by nanoimprint lithography. The effect of the fabricated structure on light behaviour was evaluated by measuring the total transmission along with a numerical study based on the Finite-Difference Time-Domain (FDTD) method using a software package called Lumerical. Then, the conductive side of the patterned and flat FTO glass substrates was coated by a layer of TiO_2 to study the effect of the patterned optical window on photoactivity of TiO_2 through photodecomposition of methylene blue (MB). MB is a cationic organic dye which has a redox potential located within the energy gap range of TiO_2, and its photodecomposition on TiO_2 has been widely investigated [318–326].

3.2 Experimental methods

3.2.1 Nanoimprint lithography

Nanoimprint lithography was used to transfer a pyramidal nanoarray structure from a Si master mold onto a thin layer of UV curable polymer. Ormostamp is a commercial UV curable hybrid polymer with a refractive index of 1.516, that is highly transparent to UV and visible light. It has high thermal and mechanical stability and anti-adhesive properties that make it an appropriate candidate for imprinting. Ormostamp was coated onto the bare side of a commercially available FTO glass (TEC 10, Ossila) substrate and was patterned by stamping a Si master mold containing an array of inverted nanopyramids.

Prior to imprinting, the FTO glass substrate was cleaned by acetone, methanol, and isopropyl alcohol in an ultrasonic bath for 10 min each. After rinsing with deionised (DI) water and drying with nitrogen gas, the substrate was exposed to further cleaning using O_2 plasma for 10 min. To improve the adhesion of Ormostamp to the glass substrate, an adhesion promoter called

Ormoprime08 was spin-coated onto the substrate at a speed of 4000 rpm for 1 min. Then, to enhance the adhesion between the glass and the Ormoprime08, the substrate was soft baked on a hot plate at 200°C for 30 min before cooling down to room temperature. A Si master mold containing an array of inverted nanopyramids was prepared as explained in section 3.2.2. The master mold was cleaned using acetone, methanol, and isopropanol in an ultrasonic bath for 10 min each. To improve the demolding capabilities of the Si master mold, an anti-sticking layer was coated on its surface by vapor deposition of a silane (trichloro(*1H, 1H, 2H, 2H*-perfluorooctyl)silane) inside a vacuum desiccator. The substrate was left to react at room temperature for 2 hours and then was baked in an oven at 90°C for 1 h.

A small droplet of Ormostamp was placed on the bare side of a 1 cm^2 FTO glass substrate. By pressing the Si master mold on the droplet, the Ormostamp flowed and conformed to the mold [237]. To stamp the mold onto the substrate, a vacuum was used to enhance the homogeneity of the polymer and to prevent formation of air bubbles (Figure 3.1). The Ormostamp was then exposed to UV light through the glass substrate with an exposure dose of 1000 mJ/cm^2 using a Karl Suss mask aligner system.

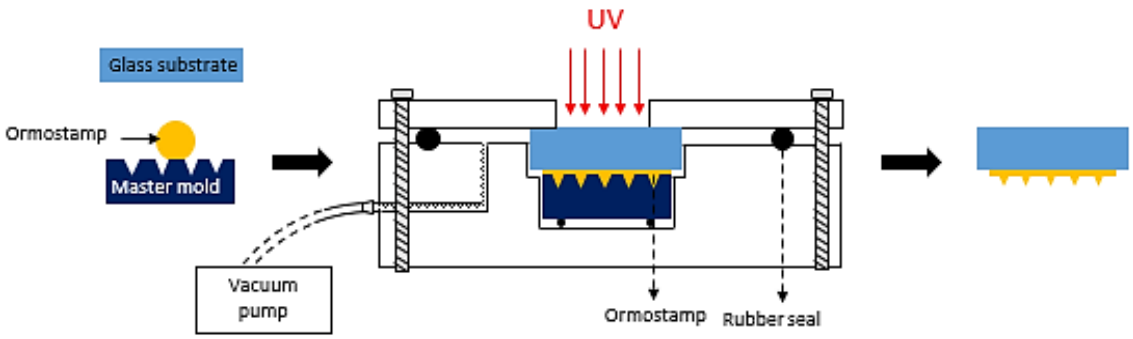

Figure 3.1. The sample holder designed for the nanoimprint lithography. Application of a vacuum provided the appropriate pressure for Ormostamp to flow and conform to the Si master mold. The Ormostamp layer is exposed to UV light through the glass substrate.

3.2.2 Master mold preparation

The master mold substrate was a single side polished, Czochralski (CZ) grown, 350 μm thick, boron doped p-type silicon wafer with (100) crystal orientation.

To remove metal and organic contaminants the Si wafer was cleaned by immersion in a mixture of H_2SO_4 and H_2O_2 (3:1 by volume) for 10 minutes and then rinsed with DI water. The wafer was then dipped into dilute hydrofluoric acid in DI water (1:10 by volume) for 10 seconds to remove the naturally formed silicon oxide layer. Finally, it was rinsed with DI water and blown dry with nitrogen gas.

To prepare a Si master mold containing an array of inverted nanopyramids, the wafer was coated by a layer of photoresist material, and laser interference lithography (LIL) was employed to record an initial pattern on this layer. The high reflectivity of the Si wafer interferes with LIL, so to counter this, an anti-reflection layer (AZ BARLi II) was applied under the photoresist layer. AZ BARLi II is a bottom antireflective layer coating for highly reflective surfaces designed to work with positive photoresists[‡]. The pattern was transferred to the Si wafer through a multi-step etching process. At the final step, the inverted pyramidal structure was formed by KOH wet etching. Below are described the wafer preparation and the etching processes.

Preparation of the Si wafer

After cleaning, the Si wafer was coated with four layers (Figure 3.2), each of which played a specific role:

1. A 100 nm thick SiO_2 layer was used as a hard mask for Si during KOH etching. The SiO_2 layer was formed by thermal oxidation at 1000˚C for 12 minutes. The schematic diagram of the resistance heated quartz tube furnace used for SiO_2 growth is shown in Figure 3.3. O_2 gas was bubbled through the water at 95˚C into the oxidation tube to perform the oxidation in a wet oxygen environment based on the chemical reaction given by:

[‡] Positive photoresist is a type of photoresist in which the exposed part is soluble in a suitable solvent (in this case alkaline solution is used to remove the exposed part).

$$Si_{(s)} + 2H_2O_{(v)} \rightarrow SiO_{2(s)} + 2H_2$$

2. To prevent formation of an undesired optical reflection from the Si surface during LIL, an antireflection coating was added to the SiO_2 layer. For this purpose, AZ BARLi II was spin-coated at 2250 rpm for 60 s and baked on a hot plate at 200˚C for 60 s.
3. A 50 nm SiO_2 layer was deposited on top of AZ BARLi II using vacuum thermal evaporation. This layer made the subsequent ion etching much easier and solved the selectivity problem between photoresist and AZ BARLi II during O_2 plasma etching.
4. The commercially available i-line[§] positive photoresist (AZMiR 701) was used to record the periodic fringe pattern during LIL. To improve adhesion between the SiO_2 layer and the photoresist, AZMiR 701 was spin-coated immediately after spin-coating hexamethyldisilazane (HMDS). Spin-coating the undiluted AZMiR 701 resist produces a layer with a thickness greater than the 200-400 nm that was required for this study. Therefore, the concentrated AZMiR 701 photoresist was diluted with PGMEA (1-methoxy-2-propyl-acetate) at a ratio of 1:3 by volume and was coated onto the substrate at spinning speed of 3000 rpm for 60 s. The substrate was subsequently baked on a hot plate at 90°C for 60 s. The wafer was cut into 1×1 cm samples to be used for LIL.

[§] An i-line photoresist is a general purpose, multi-wavelength resist designed to cover a wide range of film thicknesses (1–10 μm) with a single coat process.

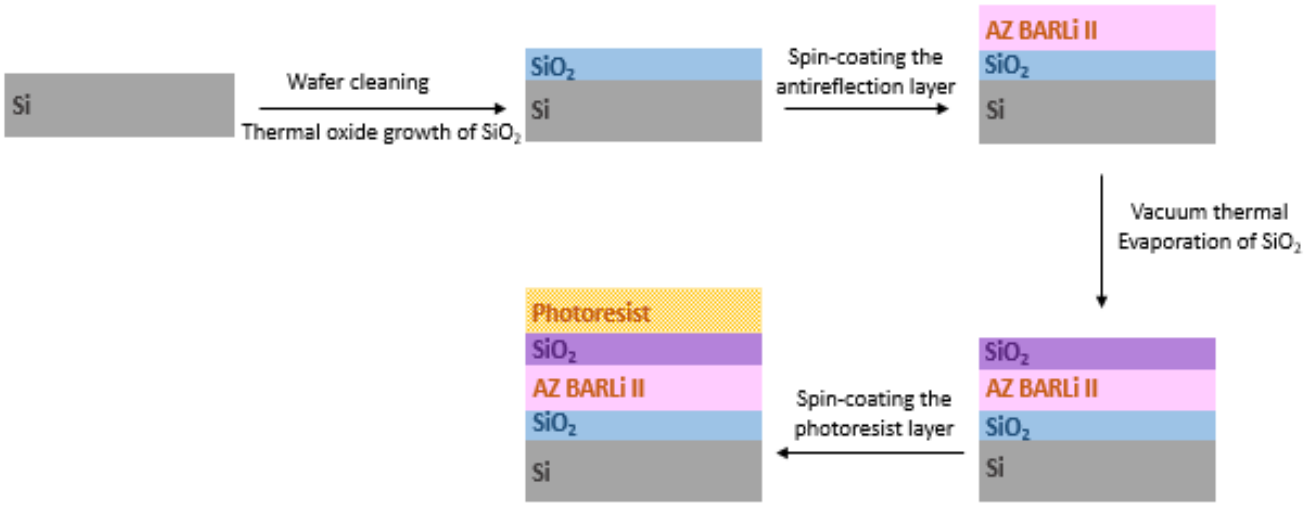

Figure 3.2. Si wafer preparation for LIL and consecutive etching processes which were used to fabricate an inverted pyramidal structure into the Si wafer. The layers are: 1) the photoresist layer to record the initial pattern, 2) SiO_2 layer for low selectivity between photoresist and AZ BARLi II during the developing process, 3) AZ BARLi II as an antireflection coating to prevent the high reflectivity of Si interfering with LIL, 4) SiO_2 as a hard mask for KOH etching of Si wafer.

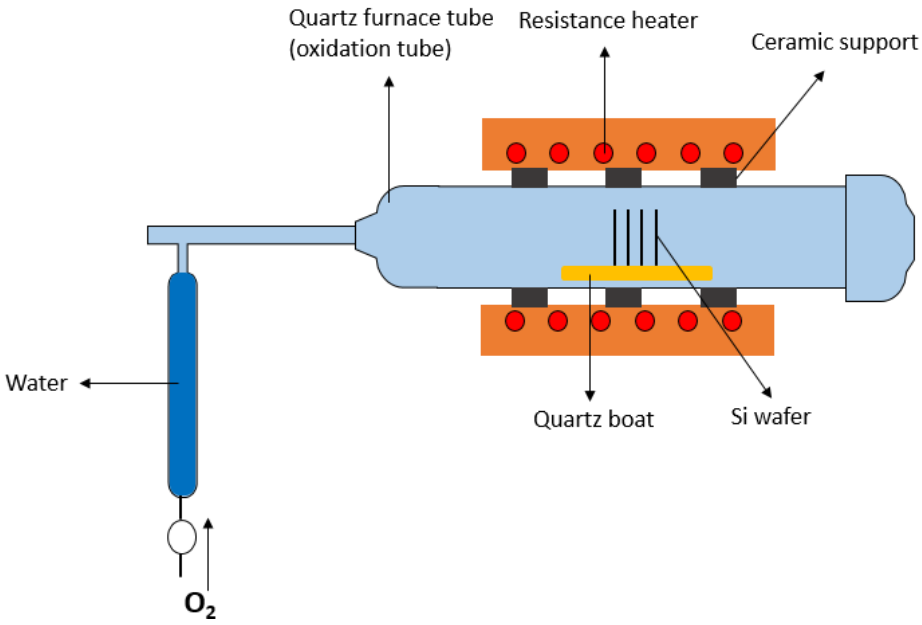

Figure 3.3. Schematic diagram of the resistance heated quartz tube furnace used to grow SiO_2 layer on Si wafer: O_2 passes through water and flows to the furnace tube to oxidise Si in a wet environment.

Laser interference lithography

A Lloyd's mirror interference system was used to create an initial pattern on the photoresist layer. A 50 mW He Cd laser with a coherence length of 30 cm at 325 nm was employed as a light source. A commercial spatial filter consists of a UV objective lens with a focal length of 5.77 mm and a 5μm diameter pinhole was used to remove the high frequency noise from the beam to achieve a clean Gaussian profile and to create a diverging beam. A UV-enhanced aluminium coated mirror was used due to its enhanced reflectance in the UV region over a broad range of angles. The complete optical setup was built on an actively damped table in order to prevent vibrations which could affect the interference pattern. The centre of the substrate and mirror assembly was located on the optical axis, and the angle of incidence was adjusted to 13.25 degrees. To record the initial pattern, two coherent beams were superimposed onto the photoresist and created a series of parallel lines through 80 s UV light exposure. Then, the substrate was rotated by 90 degrees and another set of interference lines was put on the photoresist. The intersection of these lines gave a series of dark and light spots (e.g. Figure 3.4). The exposed part of the photoresist was removed by immersing the substrate into diluted AZ 326 MIF developer solution for 30 s. A short O_2 plasma etching was performed to remove any residual photoresist at the bottom of the holes (power=100 W, time=10 s, pressure= 100 mTorr). The photoresist layer patterned with an array of holes (Figure 3.5) was used as a hard mask for the next etching step.

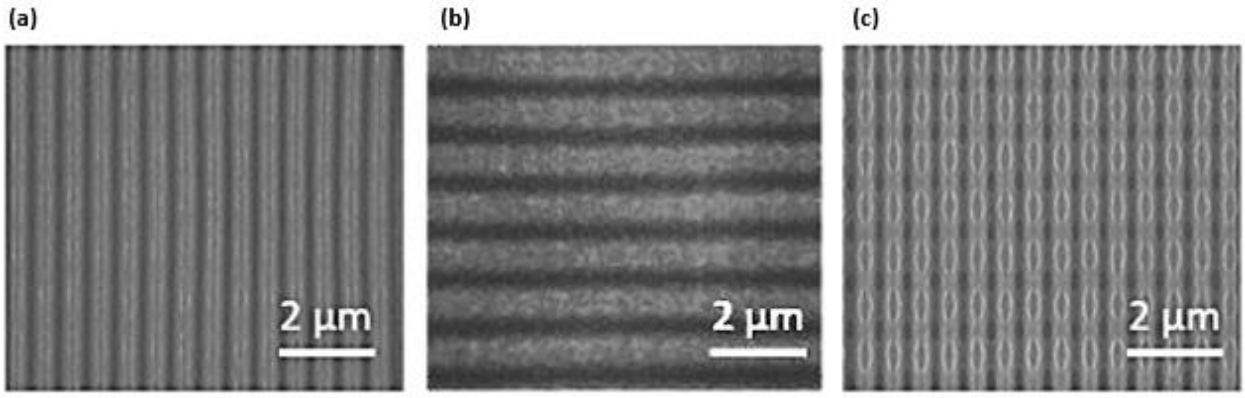

Figure 3.4. SEM images of the patterns recorded on a photoresist material by use of LIL: (a) vertical and (b) horizontal series of parallel lines, (c) series of dark and light spots produced by overlap of lines (a) and (b) [327].

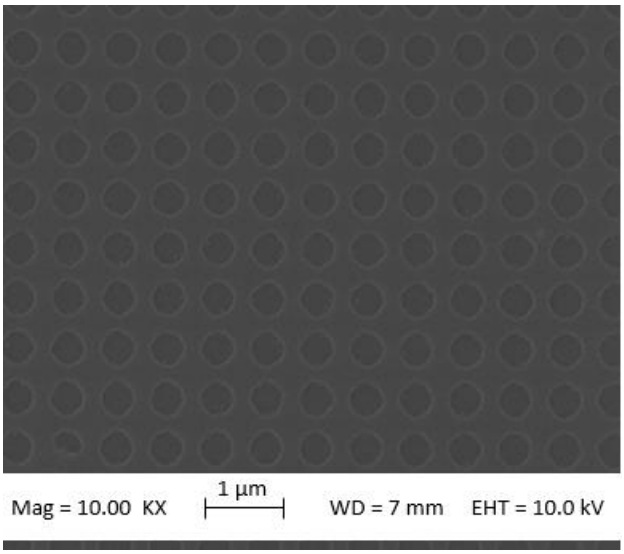

Figure 3.5. SEM image of the nanoholes fabricated into the photoresist layer through LIL after developing the exposed photoresist at magnification of 1000X.

Pattern transfer

The pattern transfer to underlying layers occurred through consecutive etching steps. To etch each layer, the top layer played the role of a hard mask. The sequence of etching process (Figure 3.6) was as follows:

1. CHF_3/Ar plasma etching fabricated a pattern of holes into the SiO_2 interlayer while the resist pattern produced by LIL served as the etching mask (time =1.5 min, power = 150 W, pressure = 100 mTorr).
2. O_2 plasma etching (power = 100 W, time = 13.5 s, pressure = 100 mTorr) transferred the pattern into AZ BARLi II.
3. CHF_3/Ar plasma etching transferred the pattern into the thermal SiO_2 bottom layer (power = 150 W, T = 300 K, pressure = 100 mTorr, t = 3.5 min).
4. The pattern transfer to the Si layer used KOH wet etching which is elaborated in the next section.

Pyramids formation by Si anisotropic wet etching

The pyramidal structure was formed by anisotropic wet etching (Step (e) in Figure 3.6). A Si wafer is a single-crystal material and allows very high anisotropic etching. The etching rate depends on the crystal planes that are exposed to the etchant. This is related to the number of back bonds that must be broken at each crystal plane. To etch the (111) plane of a Si crystal, more back bonds must be broken and therefore, the etch rate of the (111) plane is significantly lower than that of other planes [328]. Anisotropic properties of silicon cause various structural shapes to form during etching, depending on the solution composition [329]. KOH forms an inverted pyramidal structure in a (100) oriented Si substrate with an angle of 54.7° between (100) and (111) planes (Figure 3.7) [330].

The etching rate of a Si wafer is dependent on the concentration and temperature of the etchant solution [331]. Wet etching was performed in 30 wt.% KOH diluted in DI water at 80°C for 170 s, while SiO_2 was used as a hard mask. The etching rates of the SiO_2 layer and the (100) and (110) planes of the Si wafer measured under this condition were as follows:

Table 3.1. Etching rate of Si and SiO_2 in a 30 wt.% solution of KOH at 80°C

	Etching rate (μm/min)
Si (100)	1.2
Si (110)	2
SiO_2	0.4

The SiO_2 residue was removed by immersing the samples in buffered HF (6:1 volume ratio of NH_4F solution to 49% HF) for 3 min. The samples were then washed with DI water and dried with N_2.

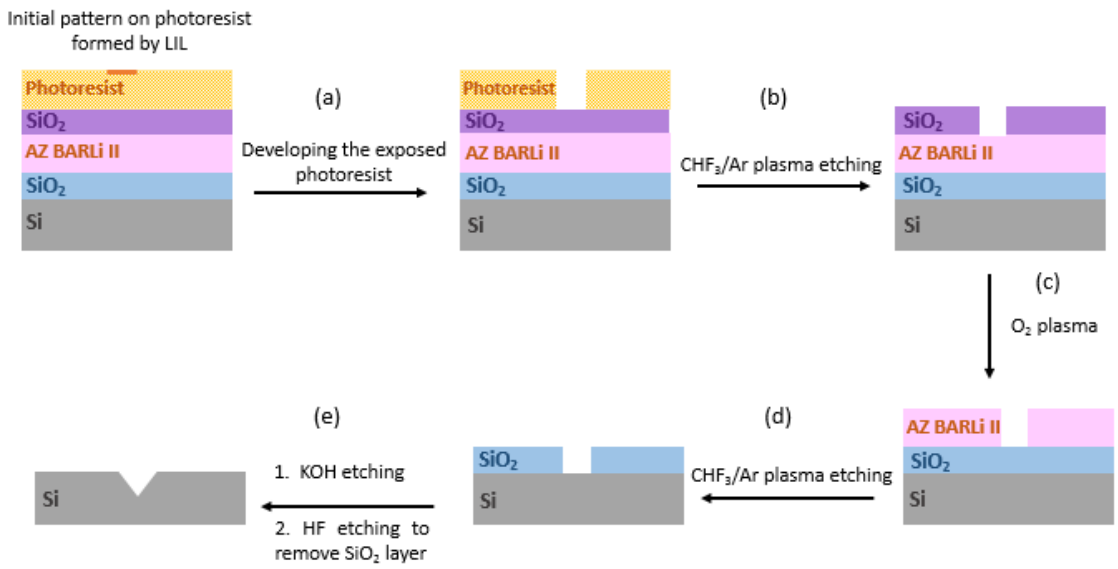

Figure 3.6. Fabrication of a Si master mold containing inverted pyramidal structure. The initial pattern was formed on the photoresist layer using LIL. This pattern was transferred to the Si wafer through a multi-step etching process. During etching each layer, the top layer acted as a hard mask. The etching steps included (a) development of the photoresist layer, (b) CHF_3/Ar plasma etching of the SiO_2 layer, (c) O_2 plasma etching of AZ BARLi II, (d) CH_3/Ar etching of the SiO_2 layer, (e) KOH etching to form the pyramidal structure in the Si wafer. The residue of SiO_2 was removed by HF etching.

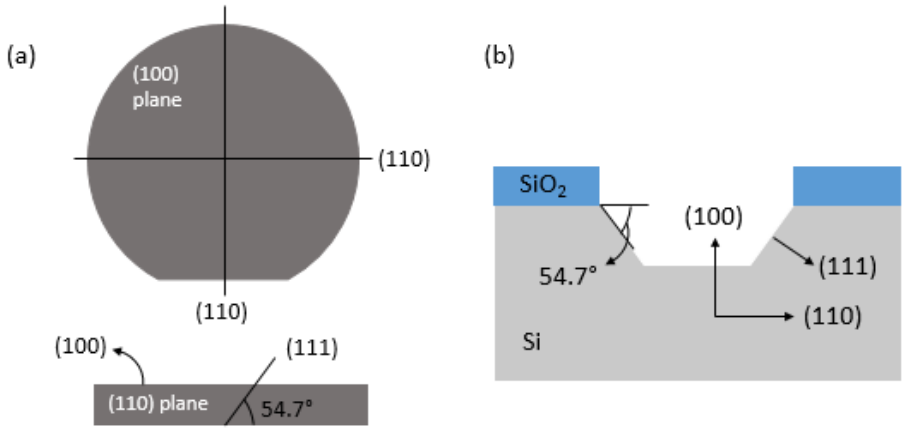

Figure 3.7. (a) Orientation of crystal planes in a Si (100) wafer; the flat edge on the Si wafer indicates orientation along (110), (b) pyramidal shape formation during anisotropic wet etching on a Si (100) wafer using KOH etchant.

3.2.3 Optical tests

The antireflection behaviour of the fabricated pattern was studied by measuring the light transmission while laser light (λ=325 nm) with an intensity of 30 mW/cm^2 illuminated the substrate. The detector was placed as close as possible to the sample to enable it to capture the total transmitted light including the scattered part (Figure 3.8).

To observe the effect of periodic pattern on light diffraction, laser light with wavelengths of 325 nm, 532 nm, and 633 nm illuminated the substrate, and the diffraction maxima were recorded on a plane 5 cm away from the other side of the substrate (Figure 3.9).

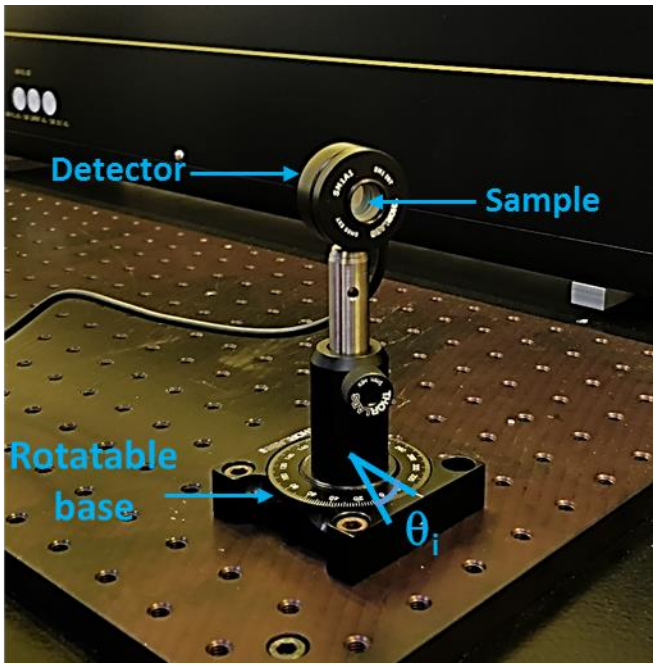

Figure 3.8. Experimental setup to measure light transmission. The detector was placed as close as possible to the sample to capture the total transmission including the scattered part. In order to measure the effect of angle of incidence, the sample holder was placed on a rotatable base.

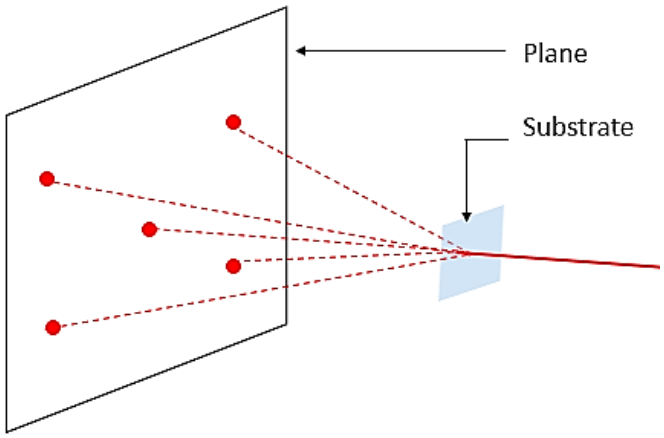

Figure 3.9. Schematic diagram of the setup used to record the diffraction maxima. Glass substrate containing periodic structure split and diffracted the incident light into several beams. The beams were recorded on a plane placed 5 cm away from the substrate.

Photocatalytic test

The effect of the fabricated periodic structure on the photocatalytic behaviour of TiO_2 was evaluated through the decomposition of MB. The mechanistic scheme leading to the photodecomposition of MB is as follows [318, 319]:

Photon absorption excites TiO_2 electrons to the conduction band:

$$TiO_2 + (hv) \rightarrow h^+_{VB} + e^-_{CB}$$

The energised electrons can either recombine with the holes (and then release the absorbed energy as heat) or the electron-hole pairs can react with electron acceptors/donors adsorbed on the surface of the TiO_2. In the latter case, the electrons reduce the oxygen molecules dissolved in the solution and form superoxide ions:

$$O_2 + e^-_{CB} \rightarrow O^-_2$$

The holes also react with water and form hydroxyl radicals. The hydroxyl radicals oxidise the MB molecules:

$H_2O + h_{VB}^+ \rightarrow H^+ + OH^\bullet$

$MB + OH^\bullet \rightarrow MB^+ + OH^-$ (degradation product)

Superoxide ions can also react with protons and form a hydrogen peroxide intermediate. This reaction is followed by the decomposition of hydrogen peroxide and formation of more hydroxyl radical. MB oxidises by reacting with the hydroxyl radicals:

$O_2^- + H^+ \rightarrow HO_2$

$2HO_2 \rightarrow H_2O_2 + O_2$

$H_2O_2 + e^- \rightarrow OH^\bullet + OH^-$

$MB + OH^\bullet \rightarrow MB^+ + OH^-$ (degradation product)

TiO_2 photo-holes do not directly react with MB since MB is cationic and not an electron donor [319]. During the experiments, MB decomposition through the path of superoxide ions was prevented by using Ar gas to purge O_2 from the solution.

The solution becomes colourless due to the decomposition of MB molecules. The rate of colour change of the solution is an indicator of the efficiency of the photocatalytic reaction. The concentration of MB is calculated by measuring the optical absorptivity of the solution and using Beer-Lambert law that relates the quantity of absorbed light through a medium to the concentration of absorbing species and the path length of the beam in the absorbing medium (Eq. 3.1) [325]:

$$A = \varepsilon bc \qquad \text{Eq. 3.1}$$

Where:

A is the absorbance,

ε is the molar absorptivity (L mol^{-1} cm^{-1}),

c is the concentration,

b is the path length of the beam in the absorbing medium.

MB has a pronounced absorption maximum at 664 nm and an absorption coefficient (ε) of 95000 L mol^{-1} cm^{-1} [332]. The UV-vis absorption spectra of MB solutions at different concentrations is illustrated in Figure 3.10.

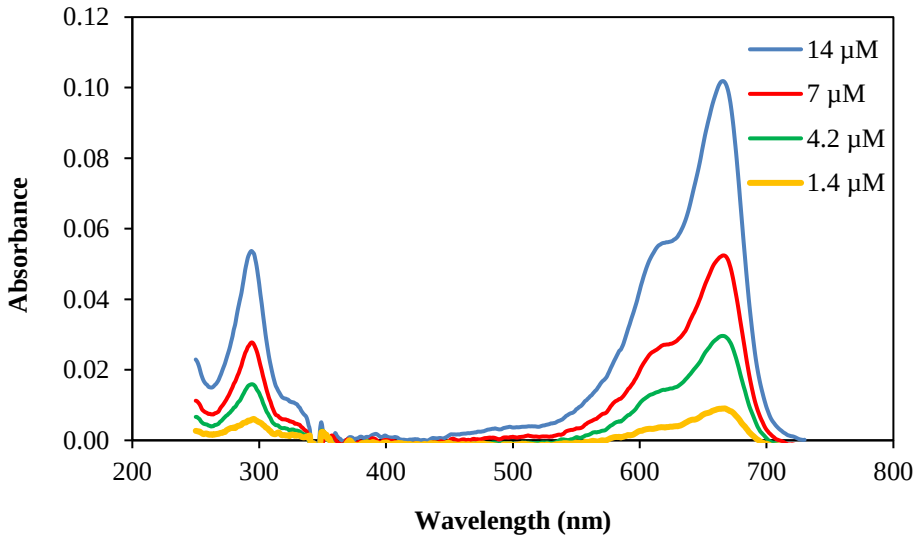

Figure 3.10. UV-vis absorption spectra of solutions at different concentrations of MB.

Previous research on photodegradation of MB on TiO_2 powder showed a pseudo-first order kinetics depending on the concentration of both MB and TiO_2 [333]:

$$-r_{MB} = -\frac{dC_{MB}}{dt} = kC_{MB}C_{cat} \qquad \text{Eq. 3.2}$$

Where:

r_{MB} is the photodegradation reaction rate,

k is the rate constant,

t is time,

C_{MB} and C_{cat} are the concentrations of MB and the photocatalyst (in this case TiO_2), respectively.

For the case where TiO_2 concentration is constant the rate equation can be stated with an apparent rate constant as follows:

$$-r_{MB} = -\frac{dC_{MB}}{dt} = k_{app}C_{MB} \quad \text{Eq. 3.3}$$

$$k_{app} = kC_{cat} \quad \text{Eq. 3.4}$$

Based on the pseudo-first order kinetics, at a constant light intensity, the concentration of MB changes based on the following equation:

$$-ln\frac{C_{MB}}{C_{MB(t=0)}} = k_{app}t \quad \text{Eq. 3.5}$$

The effect of light harvesting on photocatalytic behaviour of TiO_2 was evaluated through photodecomposition of MB on TiO_2. This is a standard model reaction, which is often used to quantify the photocatalytic behaviour of TiO_2 materials [318–324, 326]. Two sets of substrates, with and without the periodic pattern, were coated by a layer of TiO_2. To enhance the surface adsorption of TiO_2 particles, substrates were cleaned by ultrasonication in acetone, methanol and isopropanol for 15 minutes each. Further cleaning was achieved using O_2 plasma asher for 10 minutes. A solution containing 0.2 M TiO_2 (Degussa P25) and 0.037 M titanium tetraisopropoxide in isopropanol was sprayed on the substrate at a rate of 1 ml/min for 2 min while the substrate temperature was fixed at 90°C. The TiO_2 layer was not annealed due to relatively low thermal resistivity of the UV curable polymer.

The coated substrate with an active area of 1 cm^2 (2 ± 0.05 mg TiO_2) was immersed into MB solution (Figure 3.11) and was illuminated by a collimated LED light at a wavelength of 365 nm (M365LP1, Thorlabs). The light intensity was measured using a thermal surface absorber sensor (S401C, Thorlabs). The solution was continuously stirred in order to have a uniform concentration of MB throughout. To establish an adsorption-desorption equilibrium, the solution was stirred for

30 min before illumination while Ar gas was used to purge O_2 from the solution. During the experiment, Ar gas was continuously flowing over the top of the solution to suppress MB oxidation by O_2. The concentration of MB before and after photodecomposition was assessed by measuring light absorbance of the solution using a VWR UV-1600PC spectrophotometer.

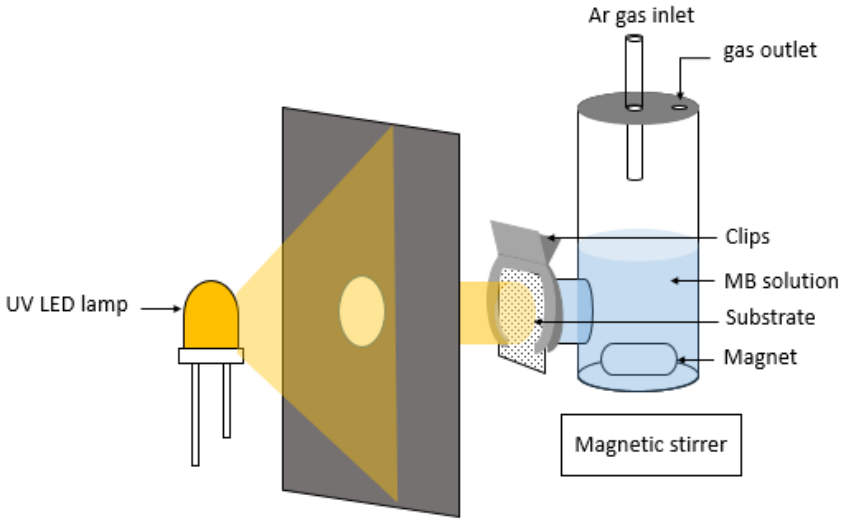

Figure 3.11. Schematic diagram of the setup used for photodecomposition of MB. A plane with a hole on the light path narrowed down the light beam. 1 cm^2 of the photoactive material was in contact with the solution. MB solution was continuously stirred and Ar gas was continuously passed over the top of the solution to prevent MB oxidation by O_2.

3.3 Results and discussion

3.3.1 Characterisation

Surface morphology of the Si master mold is illustrated using SEM imaging (Figure 3.12) and AFM analysis (Figure 3.13). The structure contained a periodic pyramidal array with a width of 490 nm, height of 345 nm, and pitch of 670 nm.

A successful transfer of pyramidal structure onto the glass surface was verified by SEM and AFM images (Figures 3.14 and 3.15).

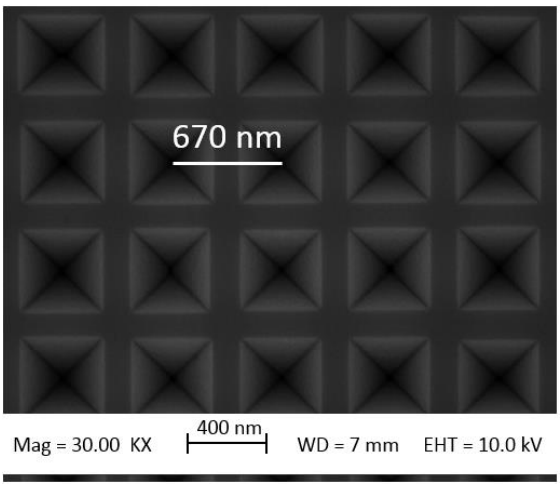

Figure 3.12. SEM image of the Si master mold containing inverted pyramidal arrays with a periodicity of 670 nm.

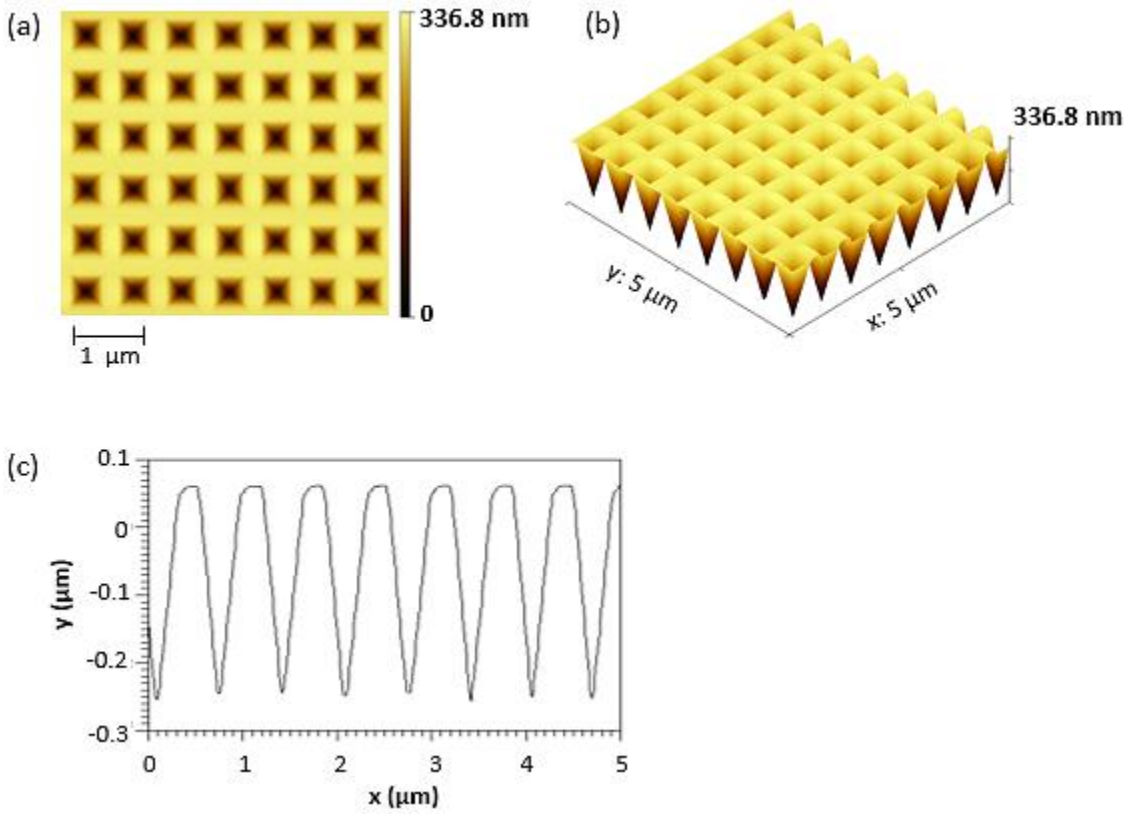

Figure 3.13. AFM image of the Si master mold containing inverted pyramidal arrays: (a) 2D view, (b) 3D view, (c) cross-sectional trace.

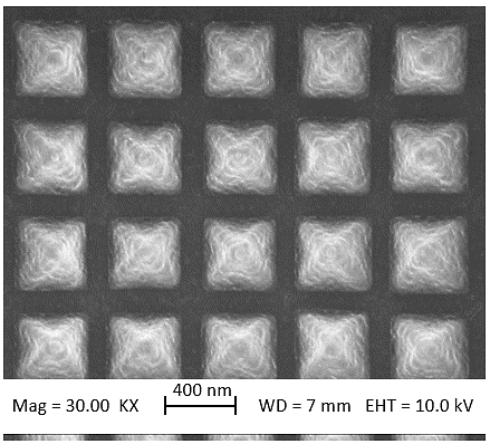

Figure 3.14. SEM image of the periodic pyramidal nanostructure fabricated into the Ormostamp layer on top of a glass substrate.

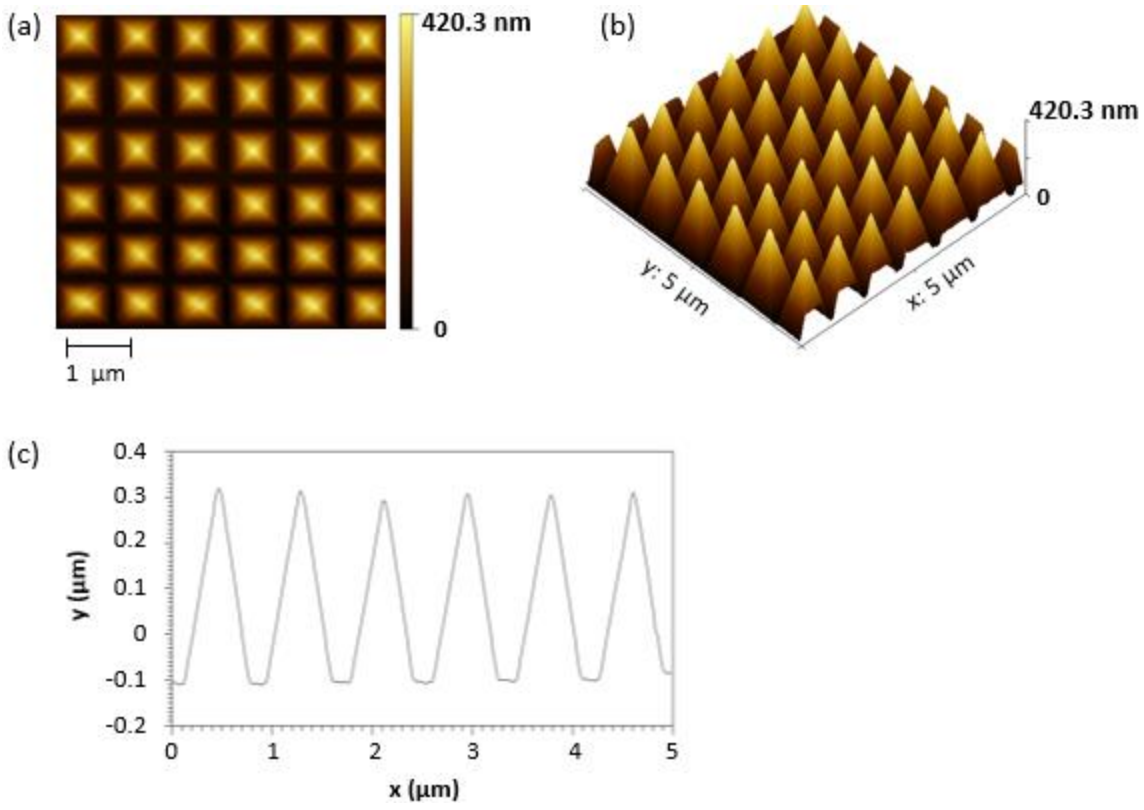

Figure 3.15. AFM image of periodic pyramidal nanostructure fabricated into the Ormostamp layer on top of a glass substrate: (a) 2D view, (b) 3D view, (c) cross-sectional trace.

3.3.2 Optical behaviour

Numerical study

FDTD Lumerical software package was used to numerically simulate the light behaviour on flat and patterned glass, FTO glass, and TiO_2-coated FTO glass substrates. Figure 3.16 shows the perspective and XZ views of the simulated patterned glass substrate in the Lumerical software environment. The part of the system that is periodically repeated (enclosed by the brown rectangle) was chosen for the FDTD simulation. The applied boundary conditions were as follows:

1) Along the direction of the wave propagation (z axis) where there is no light reflection in the boundaries, the perfectly matched layers (PML) were set as the boundary condition.
2) At normal angle of incidence, both the structure and the electromagnetic fields are periodic and symmetric, therefore the symmetric boundary condition was used in x and y directions to minimise the simulation time. The type of symmetric boundary condition is determined by the direction of the electric and magnetic fields. The electric field polarisation of the source shown by the blue arrow indicates that the boundaries in x direction is parallel to the electric field and is perpendicular to the magnetic field. Hence, antisymmetric boundary condition was applied in x direction. The opposite case happens for the boundaries in y direction, and the symmetric boundary condition was applied in these boundaries.
3) When the periodic structure is illuminated by a plane wave propagating at an angle, there will be a phase difference between each period of the device, and the electromagnetic field is not periodic. In this case, Bloch boundary condition was set in both x and y directions for a plane wave with a single frequency.

The simulated data was recorded using monitors that were placed at different positions ((3) for the light reflection, (4) for the light transmitted through the nanostructure, and (5) for total light transmission). The glass substrate was 1.1 mm thick, however, to reduce the computational time the glass thickness reduced to 1 micron. Therefore, in the numerical result the light absorption in the glass substrate is essentially not considered.

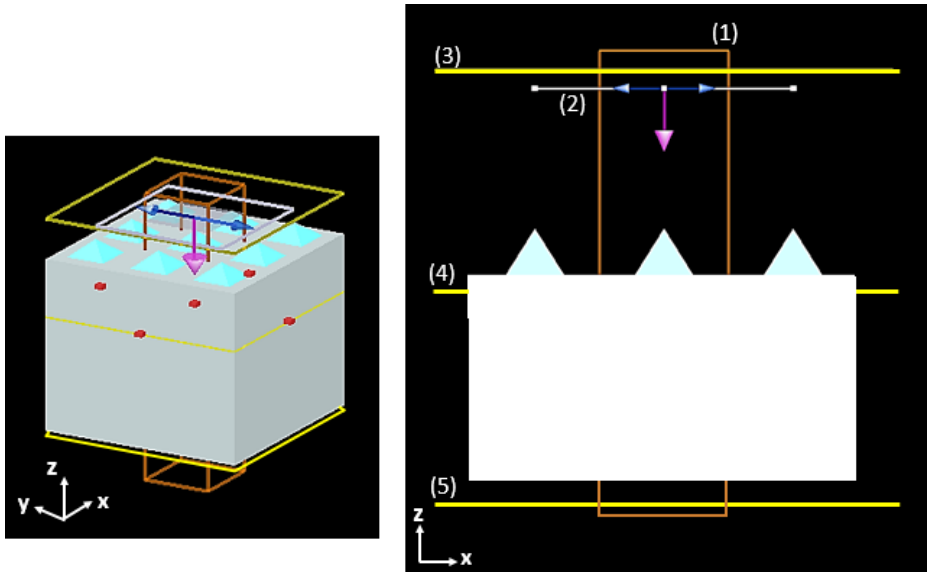

Figure 3.16. 3D and 2D views of the simulated glass substrate patterned by periodic pyramidal nanostructures in the Lumerical software environment; (1) is the simulated system, (2) is the light source, (3) is the reflection monitor, (4) is the in-glass transmission monitor to record light transmitted through the nanostructure, (5) is the transmission monitor to record the total light transmitted through the substrate.

The magnitude of the electric field of the incident light into the patterned glass was analysed at a wavelength of 250 nm by placing a virtual monitor ((4) in Figure 3.16) at the base of the pyramidal patterns (Figure 3.17). These simulations clearly show that the substrate immediately under the tip of the pyramidal structure was subjected to a much higher electric field strength than the basal areas of the pattern. This suggests that the fabricated structure was successful in reducing light reflection.

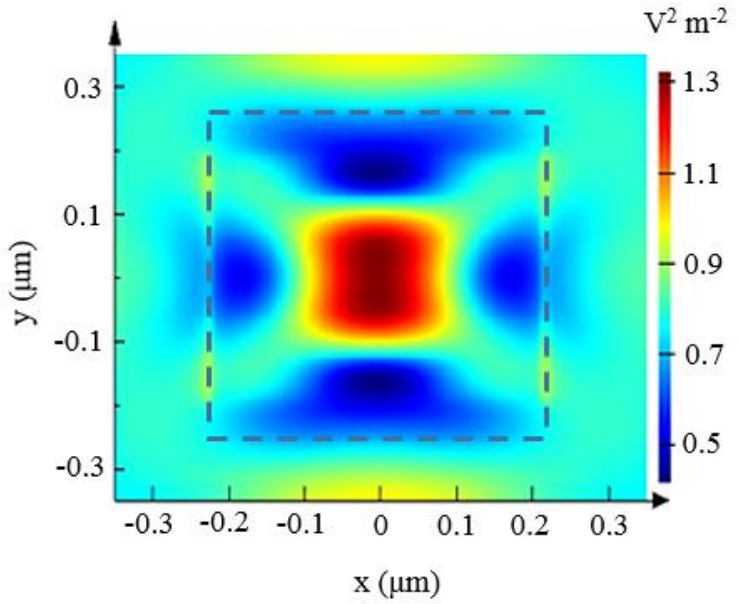

Figure 3.17. FDTD analysis of the electric field distribution recorded at the base of a pyramidal structure (shown by a dashed square) while UV light (λ=250 nm) illuminated the substrate at a normal angle of incidence.

Simulation results (Figure 3.18) showed that light reflection and transmission on flat glass is not wavelength dependent, and almost 96% of light passes through the structure. The presence of periodic nanostructure caused a very slight improvement in light transmission. On the patterned glass, a sudden increase of transmitted light is observed for wavelengths larger than the structure's periodicity where the grating acts as a subwavelength structure. The subwavelength structure resulted in less than 1% light reflection.

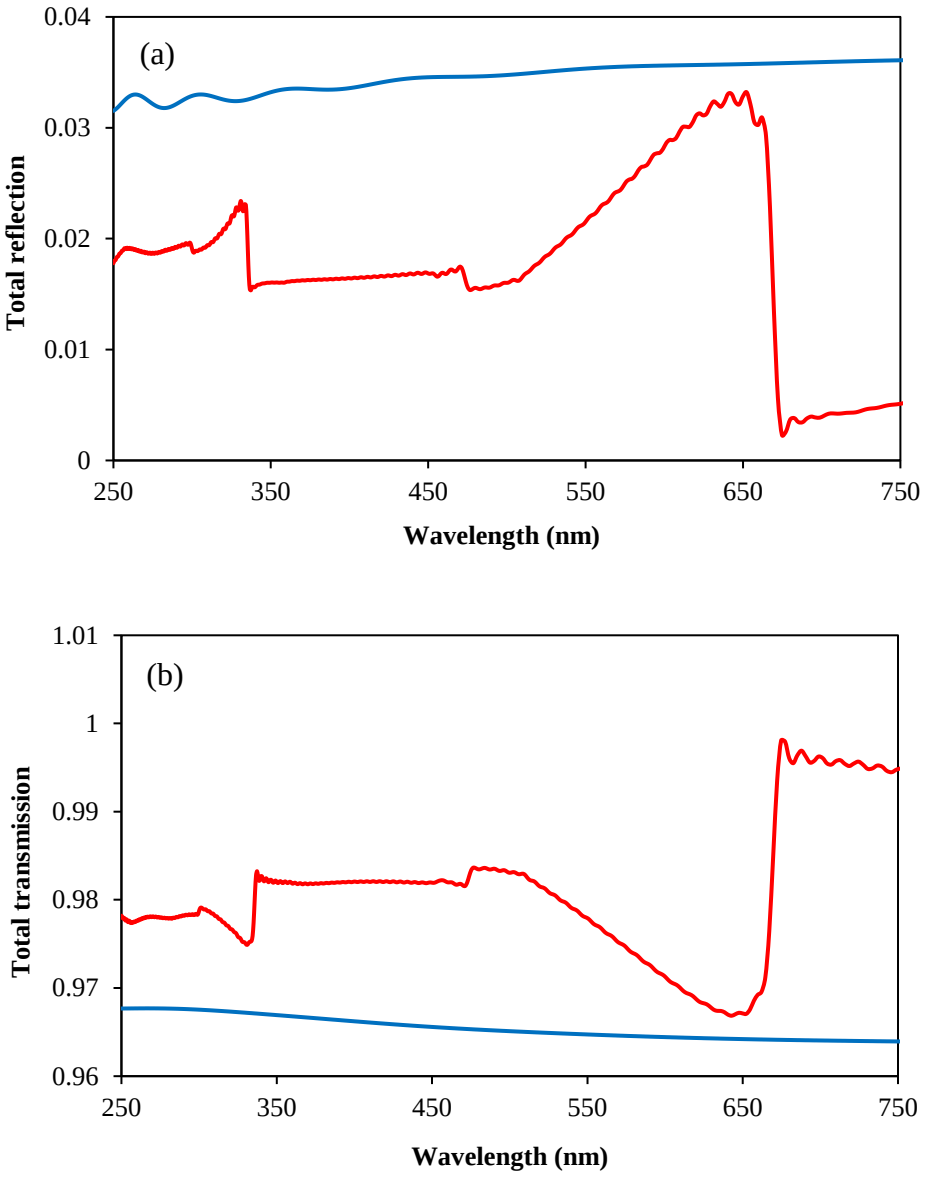

Figure 3.18. Simulated light reflectance (a) and transmittance (b) on patterned (—) and flat (—) glass substrates with a thickness of 1μm for plane waves at different wavelengths propagating at normal angle of incidence. The light illuminates the flat/patterned side of the glass.

The periodical structure split and diffracted the incident light into several beams that passed through the glass substrate at different angles (Figure 3.19). Some of these beams do not appear in Figure 3.20 which illustrates the transmission spectra after passing through the glass. When a beam reaches the surface of a substrate with lower refractive index ($n_1 > n_2$) at an angle of incidence

higher than its critical angle ($\theta_c = \arcsin(n_2/n_1)$), it does not pass through the surface but is reflected back into the substrate. The critical angle of the glass-to-air interface is 41.8 degrees and if light propagates at an angle higher than this then internal reflection occurs as shown in Figure 3.21.

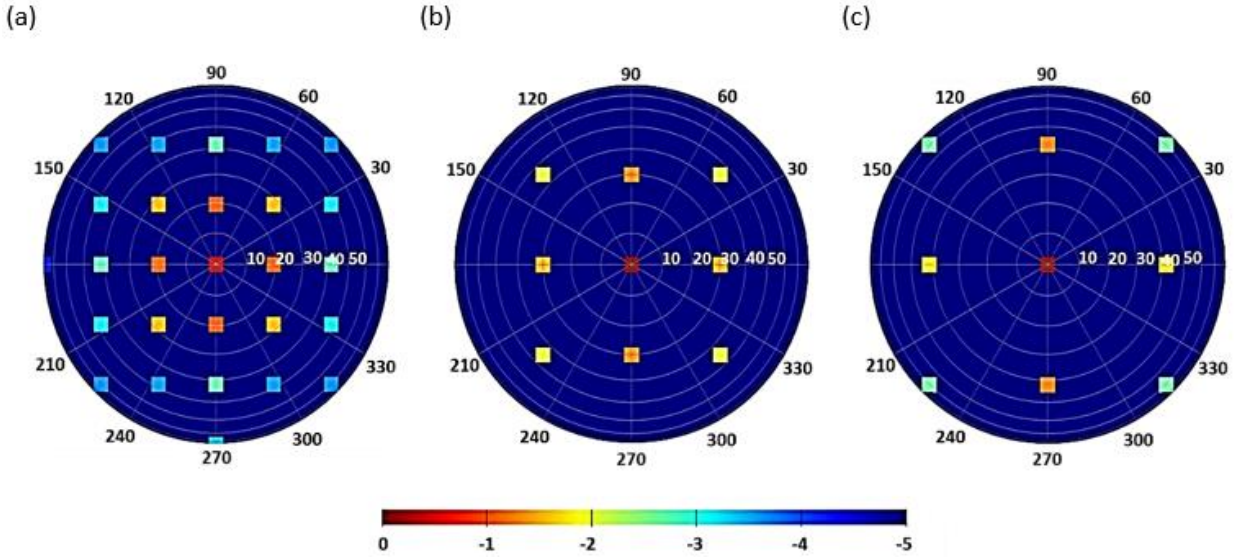

Figure 3.19. Simulated diffraction order of light after passing through a pyramidal structure (at monitor (4) in Figure 3.16) at wavelengths of: (a) 325 nm, (b) 532 nm, (c) 633 nm. The position of each beam is shown by its diffraction angle. The colour bar represents the diffraction efficiency in a natural logarithmic scale.

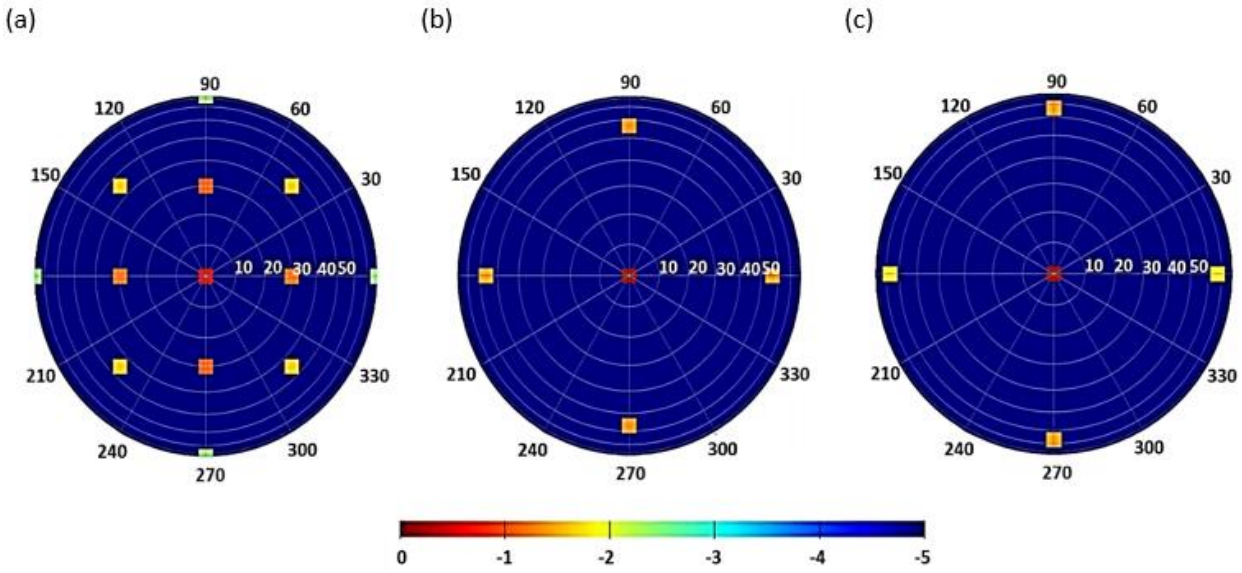

Figure 3.20. Simulated diffraction order of light after passing through the patterned glass (at monitor (5) in Figure 3.16) at wavelengths of: (a) 325 nm, (b) 532 nm, (c) 633 nm. The position of each beam is shown by its diffraction angle. The colour bar represents the diffraction efficiency in a natural logarithmic scale.

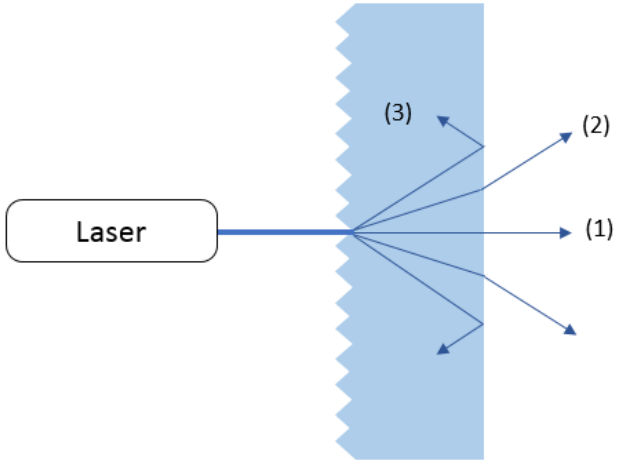

Figure 3.21. The behaviour of diffracted beams within a substrate: (1) direct transmission, (2) beams with an angle lower than the critical angle of the substrate would scatter, (3) beams with an angle higher than the critical angle of the substrate reflect back into the substrate.

The periodic structure acts as a dispersive optical component, and except for the specular order (zeroth-order diffraction maximum), the direction of each diffracted beam depends on the wavelength. By increasing the wavelength, the angle of diffracted orders increases until the higher order beam disappears. This leads to a redistribution of energy between the propagating orders [247]. A change in number of diffraction maxima is caused by increasing the wavelength (Figure 3.22). By using Eq. 2.3 at normal angle of incidence (Eq. 3.6), the wavelength at which a diffraction maximum disappears can be calculated.

$$sin\,\theta_m = \frac{m\lambda}{nd} \qquad \text{Eq. 3.6}$$

A maximum order of *m* is disappeared when $\theta_m = 90$ degrees. By applying the refractive index of the substrate (*n*) and the periodicity of the pattern (*d*), the wavelength at which the maximum order of *m* does not exit the substrate is:

$$\lambda = \frac{nd}{m} \qquad \text{Eq. 3.7}$$

In a two-dimensional Cartesian system, where the position of the diffraction maxima is defined by two values (x' and y' as shown in Figure 3.23), *m* is calculated by:

$$m = \sqrt{x'^2 + y'^2} \qquad \text{Eq. 3.8}$$

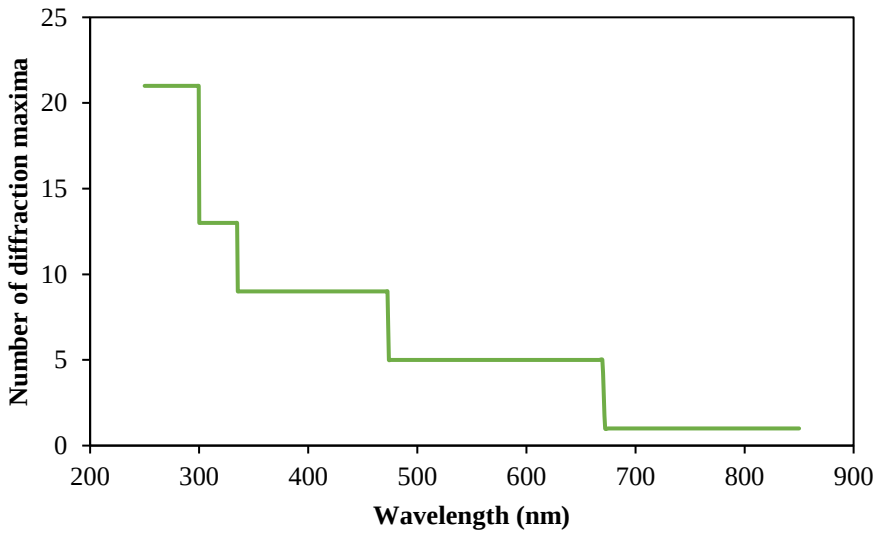

Figure 3.22. Simulation of the number of diffraction maxima transmitting through the glass substrate at different wavelengths. Diffraction maximum with the order of m disappears at a wavelength of $\lambda = \frac{nd}{m}$.

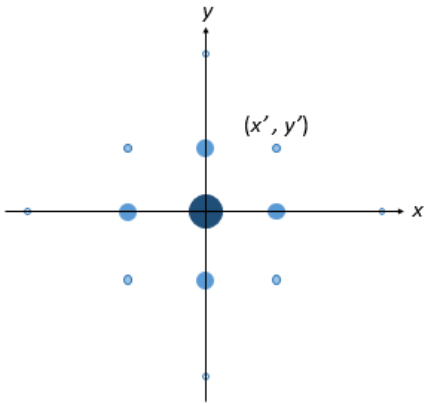

Figure 3.23. Diffracted maxima in a two-dimensional Cartesian system. The order of each maxima (m) is defined by its position according to $m = \sqrt{x'^2 + y'^2}$.

The diffraction maximum of m = (0,1) changes in direction at increasing wavelengths (Figure 3.24). The beam's angle is changed as the beam travels from the glass substrate to the air. This occurs due to change of light speed that is described by Snell's law. At wavelengths greater than 670 nm, the only propagation is from the zeroth-order maximum (direct transmission).

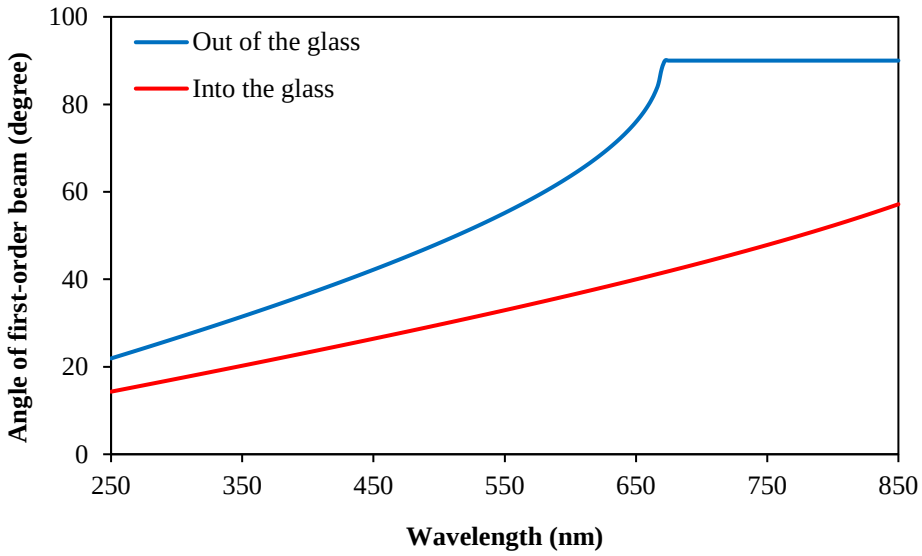

Figure 3.24. The angle of diffraction maximum of *m* = (0,1) after passing through the grating (into the glass) and after transmission through the glass (out of the glass).

The presence of FTO and TiO_2 layers on the glass substrate changes the light behaviour. Figure 3.25 shows the XZ views of the simulated patterned glass substrate coated by FTO and FTO-TiO_2 in a Lumerical software environment. In addition to the monitors recording the total reflection (3) and transmission (4), a vertical monitor (5) was recording the light behaviour as it passed through the substrate.

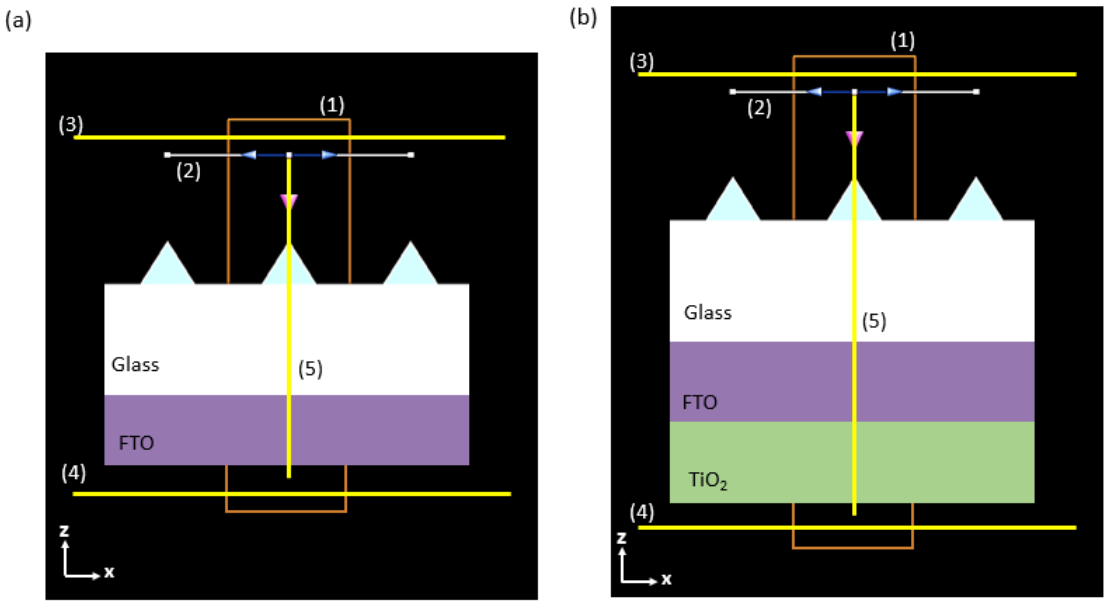

Figure 3.25. XZ views of the simulated glass substrate patterned by periodic pyramidal nanostructure coated by (a) FTO, and (b) FTO-TiO_2 in the Lumerical software environment; (1) is the simulated system, (2) is the light source, (3) is the reflection monitor, (4) is the transmission monitor, and (5) is the cross-sectional monitor to track the light behaviour within the system.

Light behaviour was studied when a 700 nm-thick layer of FTO was placed on flat and patterned glass substrates (Figure 3.26). The refractive index of FTO for light wavelengths less than 580 nm was defined by Eq. 3.9 [334]:

$$n = \left(1 + \lambda^2/(0.370\,\lambda^2 - 0.0105)\right)^{0.5} \qquad \text{Eq. 3.9}$$

Due to the change of refractive index from glass to FTO, some light was reflected from the glass-FTO interface and, therefore, the total reflection was higher than that of the bare glass substrate in Figure 3.18-a. The light reflected from the surfaces of FTO and glass were in different phases which, at some wavelengths, resulted in destructive interference, leading to the broad peaks in reflection and transmission trends.

Light behaviour was also simulated for an FTO glass coated with a continuous film of TiO_2 with a thickness of 600 nm (Figure 3.27). TiO_2 refractive index was defined as a function of light wavelength presented by Siefke *et al.* [335]. The reflection from TiO_2-FTO interface also

interfered with the reflection from the glass surface and the glass-FTO interface. This increased the fluctuation of light reflection by changing the wavelength. Due to the large band gap, TiO_2 absorbed all the UV light.

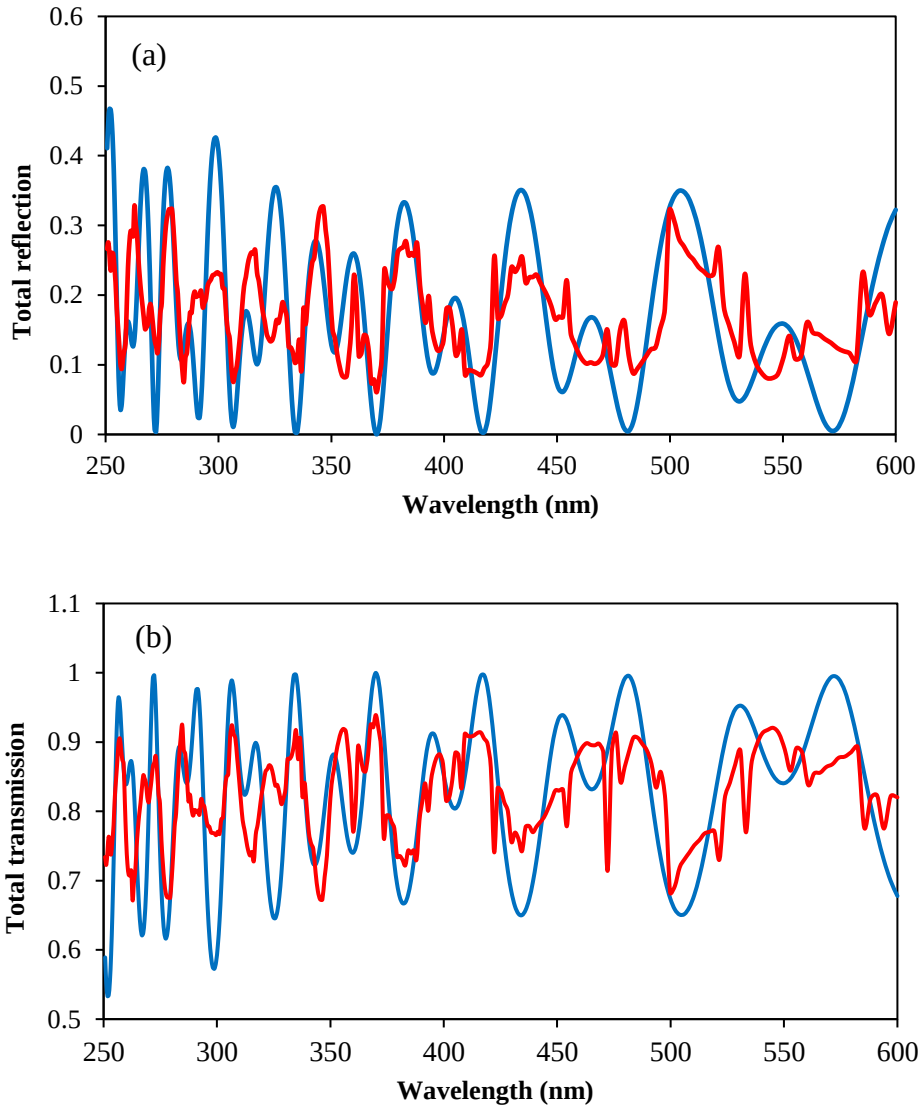

Figure 3.26. Simulated light reflectance (a) and transmittance (b) on patterned (—) and flat (—) FTO glass substrates for plane waves at different wavelengths propagating at normal angle of incidence. Each substrate consisted of 1 µm-thick glass coated by 700 nm-thick layer of FTO. The light illuminated the flat/patterned side of the glass that is uncoated. The light reflected from the surfaces of FTO and glass were in different phases which, at some wavelengths, resulted in destructive interference, leading to the broad peaks in reflection and transmission trends.

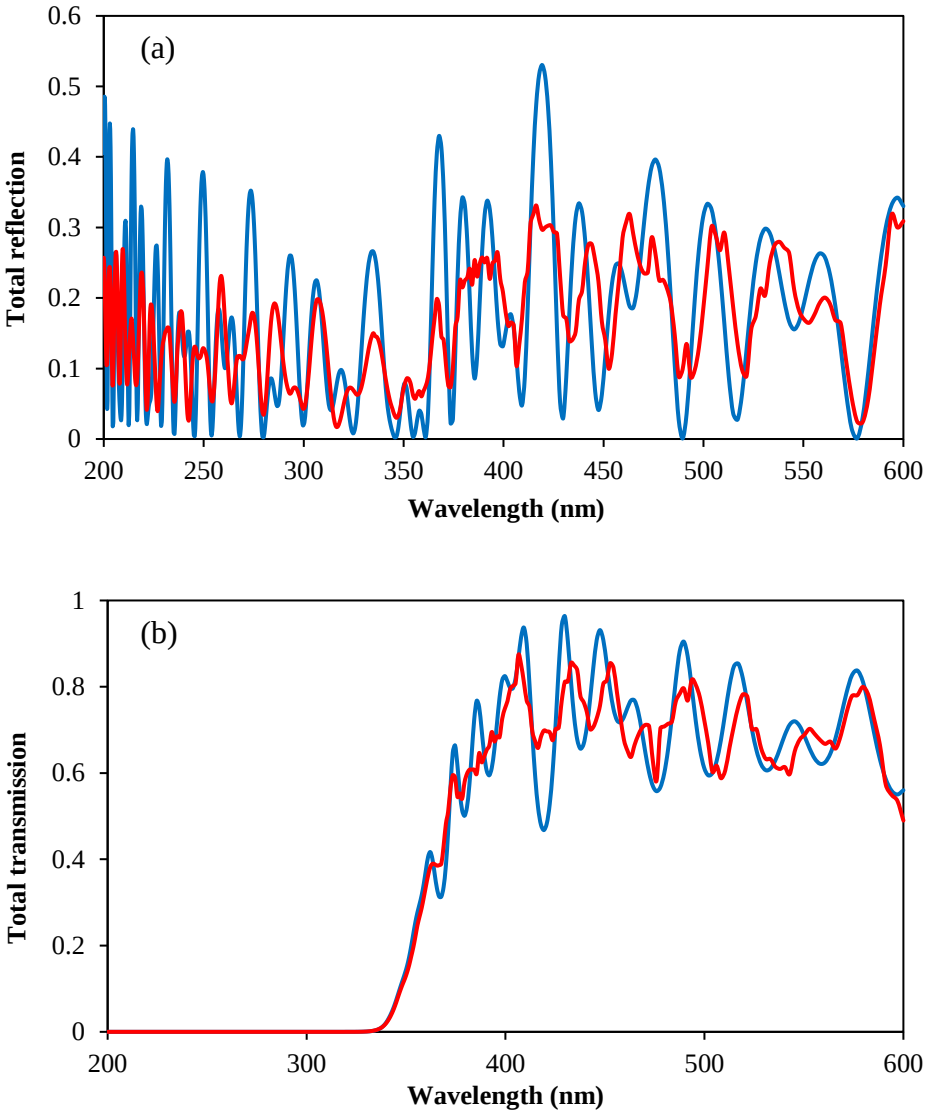

Figure 3.27. Simulated light reflectance (a) and transmittance (b) on patterned (—) and flat (—) FTO glass substrate coated by TiO_2 for plane waves at different wavelengths propagating at normal angle of incidence. Each substrate consists of 1 µm-thick glass coated by 700 nm-thick layer of FTO, and then 600-nm thick layer of TiO_2. The light illuminates the flat/patterned side of the glass that is uncoated.

The magnitude of the electric field along the light path within the flat and patterned substrates (glass-FTO and glass-FTO-TiO_2) was analysed at a wavelength of 250 nm by placing a virtual monitor((5) in Figure 3.25) across the Z axis (Figure 3.28). The presence of pyramidal structure reduced the light reflection and therefore higher light intensity was observed within the glass layer.

However, much light was lost by reflection from the glass-FTO interface. All the light transmitted through the FTO layer was absorbed at the FTO-TiO_2 layer (Figure 3.28-c and d). However, in a real scenario, the TiO_2 layer consists of a porous structure made of many particles that, depending on their size and distribution, scatter the light in different directions. Therefore, effective light absorption occurs over a range of distances from the FTO-TiO_2 interface.

The main purpose of patterning the photoelectrode is to maximise light absorption within the photoactive layer (TiO_2) by minimising light loss that occurs due to light reflection from the interfaces and light absorption within the inactive layers (FTO glass). The application of anti-reflection coating at each interface (the air-glass, the glass-FTO, and the FTO-TiO_2) could have a significant effect on light harvesting within the photoactive TiO_2 layer. However, the effect of a fabricated pattern on diffraction and on increasing the light path within an inactive layer does not favour the photoelectrochemical reaction. Therefore, a trade-off between lower light reflection and higher light absorption should be considered before deciding to pattern the surface of an inactive layer.

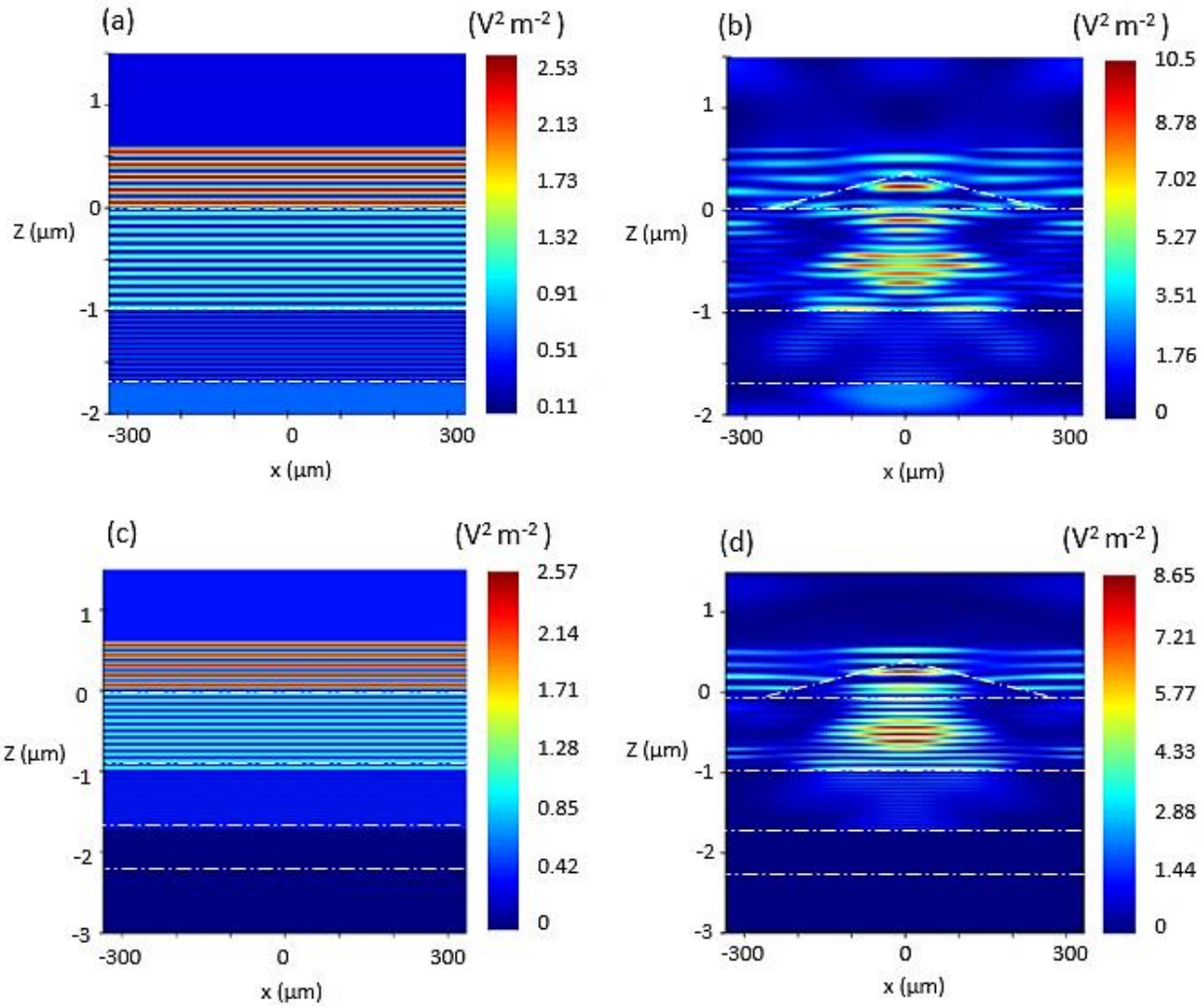

Figure 2.28. A cross-section of electric field intensity along the light path while UV light (λ=250 nm) illuminated the substrate at a normal angle of incidence: (a) and (b) are respectively flat and patterned FTO glass, (c) and (d) are are respectively flat and patterned FTO glass coated with TiO_2. Glass thickness = 1µm, FTO thickness = 700 nm, TiO_2 thickness = 600 nm. The coordination of layers on z axis are: glass: -1 to 0, FTO: -1 to -1.7, and TiO_2: -1.7 to -2.3. The light source is at z = 0.5. The base of the pyramid is at z = 0 and its tip is at z = 0.345. The interfaces are shown with dashed lines.

Experimental study

A laser light (λ=325 nm) with an intensity of 30 mW/cm^2 was used to study the antireflection behaviour of the fabricated nanostructures. The intensity of the light transmitted through the flat

and patterned FTO glass was measured whilst the light propagated at different angles of incidence (Figure 3.29). A portion of the illuminated light was absorbed by the substrate and was released as thermal energy, and some part of light was lost due to the reflection. The remaining light transmitted through the substrate was measured. Increasing the angle of incidence enhanced light reflection from the substrate. The transmitted light intensity of patterned FTO glass was almost 5% higher than that of flat FTO glass at a normal angle of incidence, which agrees well with the simulation results in Figure 3.26-b. This increase can be explained only by antireflection behaviour of the fabricated structure. Although the simulation results (Figure 3.26-b) show a higher transmission (about 80%) through both flat and patterned substrates than the experimental results (about 20%), the thickness of the simulated substrates was much less than the real samples and the numerical results did not include the effect of light absorption within the glass layer.

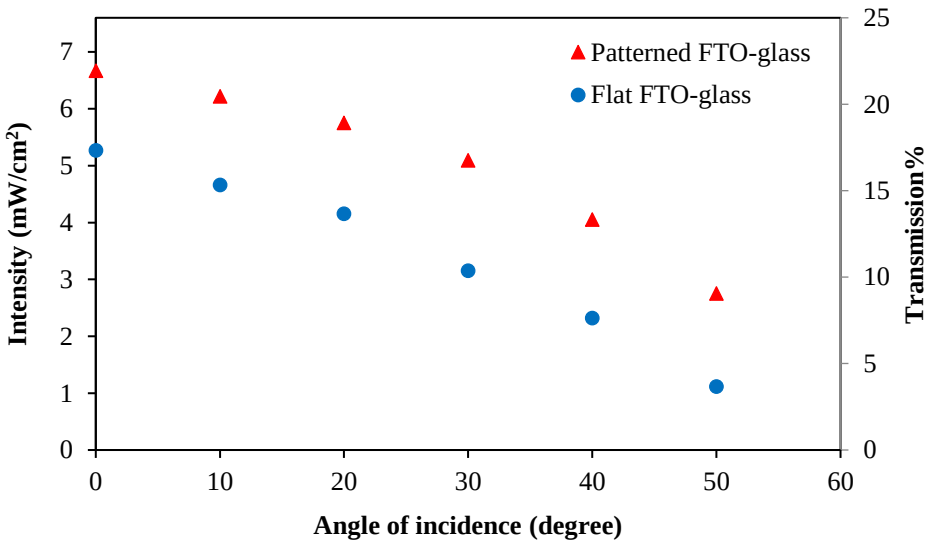

Figure 3.29. The intensity and the percentage of the light transmitted through flat and patterned FTO glass when illuminated by laser light (λ=325 nm) with an intensity of 30 mW/cm^2 propagating at different angles of incidence.

The patterned substrate propagated different diffraction maxima when light at different wavelengths (325 nm, 532 nm, and 633 nm) was used at normal angle of incidence (Figure 3.30).

The intensity of each diffraction order maxima was measured for the 325 nm laser light illuminating the substrate at normal angle of incidence (Figure 3.31). The zeroth-order beam had the highest intensity, and the intensity of the beams reduced with distance from the central beam.

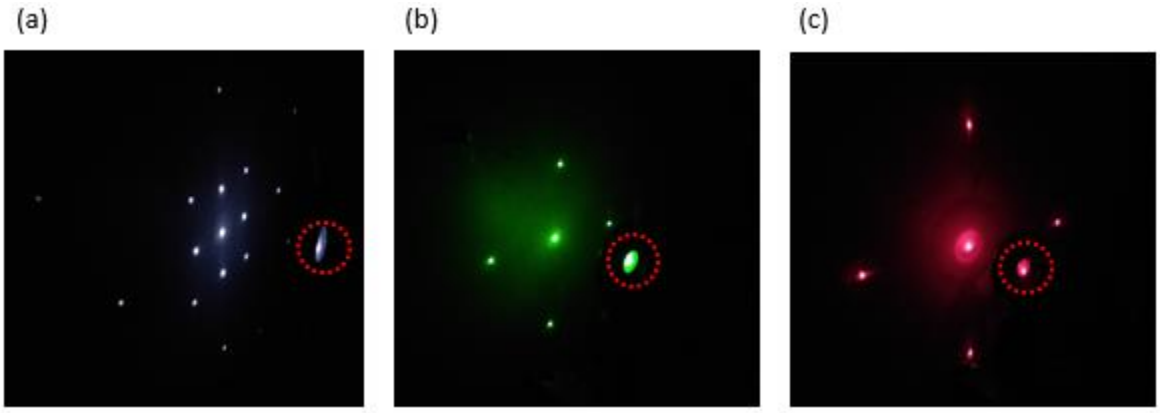

Figure 3.30. Diffracted maxima when the patterned glass was illuminated by laser light at wavelengths of (a) 325 nm, (b) 532 nm, (c) 633 nm. The sample is specified with a dashed circle, and the screen with the diffraction spots is at an angle to the image.

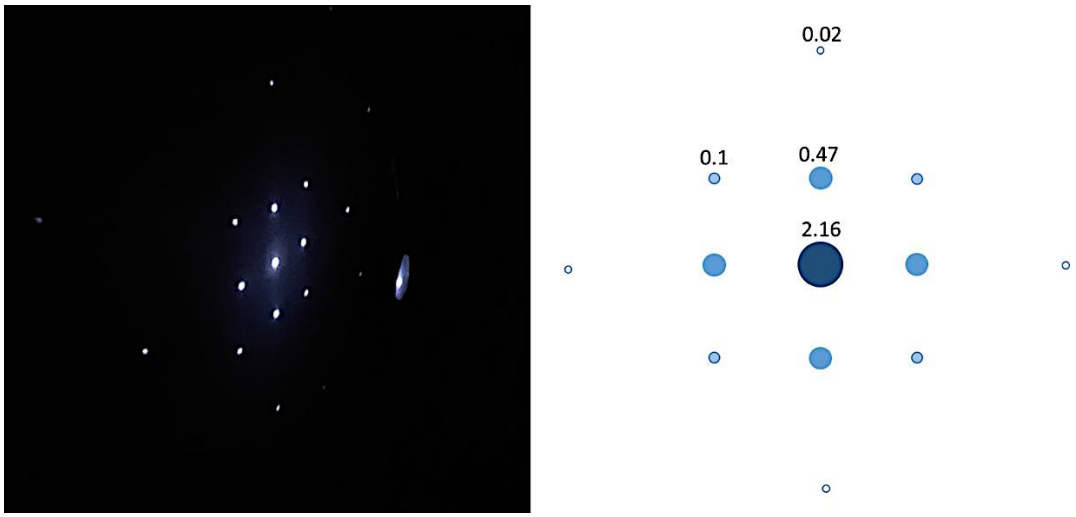

Figure 3.31. The intensity of diffraction orders (mW/cm^2) when the periodic grating was illuminated by laser light (λ=325 nm) at an intensity of 30 mW/cm^2.

The patterned glass coated by TiO_2 was illuminated by laser light at the intensity of 532 nm and 633 nm. TiO_2 layer was highly dispersive and scattered the light in every direction. Due to the high amount of scattering, it was not possible to accurately quantify spatial distribution of the intensity of transmitted light. The wavelength of 325 nm was not tested as the substrate could reflect the light in every direction and caused a safety issue.

3.3.3 Photocatalytic study

To evaluate the rate of MB photodecomposition on patterned and flat substrates, the samples were immersed in a 14 µM solution of MB and were illuminated by UV light (λ=365 nm) with an intensity of 130 mW/cm^2. The experiment was repeated three times on three sets of patterned and flat substrates. A linear change of MB concentration occurred over time (Figure 3.32). This suggested that the oxidation of MB was independent of the MB concentration. This can occur when there is enough MB at the active sites of the substrate to react with the generated charges, and therefore, the reaction rate only depends on the light intensity. If the concentration of MB is not enough to react with the generated charges, this condition would not apply and the reaction rate would be a function of MB concentration [333]. The rate constants of 0.0109 mol L^{-1} s^{-1} and 0.0191 mol L^{-1} s^{-1} were obtained for flat and patterned substrates, respectively, which means the rate of photodecomposition of MB on patterned substrate is 1.75 times greater than that on a flat substrate. As shown by Eq. 3.2, the apparent rate constant of MB is a function of TiO_2 concentration and, therefore, the excited electron-hole pairs through photon absorption. The presence of a nanostructure pattern not only increased the light transmission by 5% but also affected the light path length and light scattering within the photoactive TiO_2 layer. The combination of these effects resulted in higher electron-hole excitation and a faster photodecomposition of MB on patterned substrate. The effect of light diffraction could not be evaluated because TiO_2 particles scatter the light in different directions and affect the path lengths of photons.

The dependency of the photooxidation of MB on the light intensity was evaluated by exposing the substrates to UV light (λ=365 nm) at different intensities and measuring the concentration of oxidised MB after 3 hours (Figure 3.33). It can be seen that the concentration of oxidised MB

changed linearly with increase in light intensity, for example, doubling the light intensity doubled the concentration of oxidised MB.

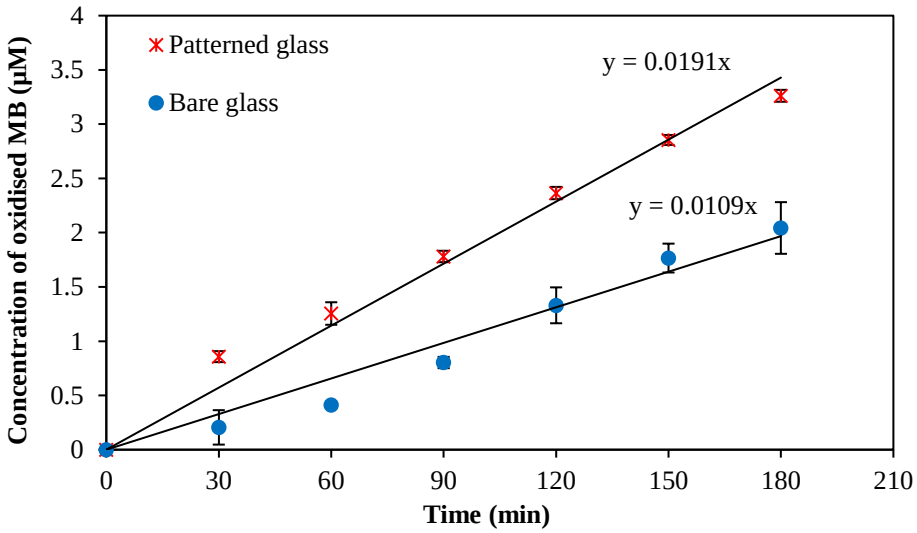

Figure 3.32. Concentration of oxidised MB on TiO_2 for patterned and flat glass substrates over time while they were illuminated by UV light (λ=365 nm) at an intensity of 130 mW/cm^2.

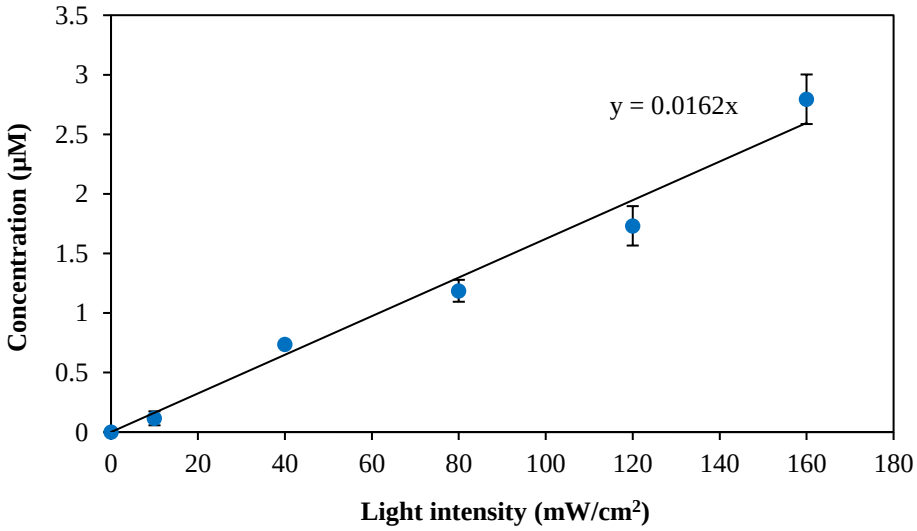

Figure 3.33. The concentration of oxidised MB after 3 h while UV light (λ = 365 nm) at different intensities illuminated the substrate. There was a linear increase in the photoactivity of the TiO_2 layer with increase in the intensity of the incident light.

3.4 Conclusion

Light behaviour was studied on a glass substrate patterned by a periodic pyramidal nanostructure with a periodicity of 670 nm. The pyramidal structure was initially fabricated on a Si wafer using a combination of LIL and KOH wet etching and was then transferred to a glass-like UV curable polymer coated on the bare side of an FTO glass substrate using nanoimprint lithography.

The fabricated structure affected light behaviour in two ways: 1) causing a gradual change in the refractive index from air to the substrate and reducing the reflection, and 2) splitting the light and diffracting it into several beams. These two effects were elucidated in a numerical study using the FDTD method. Light diffraction occurred at wavelengths smaller than the periodicity of the structure ($\lambda < 670$ nm). The change in the number of diffracted maxima and their direction at different wavelengths were studied numerically. Increasing the periodicity of the structure increased the number of diffraction maxima and caused more change in the light path. At light wavelengths higher than the periodicity ($\lambda > 670$ nm), the structure acted as a homogenous medium without causing light diffraction. At the whole wavelength range, the fabricated structure reduced the light reflection from the glass surface by causing a gradual change of refractive index from the air to the substrate. Higher antireflection behaviour was observed at wavelengths higher than the periodicity of the structure. The presence of FTO and TiO_2 layers on the glass substrate changed the light behaviour. Due to the change of refractive index, some light was lost by reflection from each interface. Simulating the electric field distribution over the pyramidal structure showed it had a very high intensity at the top of the pyramids and the structure reduced the light reflection. However, it also scattered the light and increased the light path, which consequently increased light absorption. As the main goal is to maximise light harvesting within the photoactive layer (in this case TiO_2), patterning the inactive layer requires a trade-off between reduced light reflection and increased light absorption.

The effect of a fabricated structure on light reflection was measured by illuminating the substrate by a monochromatic and coherent UV light at wavelength of 325 nm and measuring the light transmission. The periodic structure reduced the light reflection by 5%.

To study the effect of a patterned optical window on TiO_2 photoactivity, the patterned FTO glass was coated by a layer of TiO_2. The photoactivity of TiO_2 was assessed by measuring photodecomposition of MB at a wavelength of 365 nm. The rate of MB photodecomposition on the patterned substrate was 1.75 times higher than that on the flat substrate. This difference was due to reduced light reflection and prolongation of the path of photons within the TiO_2 layer. The path length was affected by light diffraction caused by the periodic structure and by light scattering from the surface of the TiO_2 particles. However, the effect of light diffraction and scattering could not be distinguished.

4 The effect of electrode surface morphology on the electrochemical behaviour of a redox reaction

4.1 Introduction

In a solar redox flow battery, the redox reaction occurs at the electrode-electrolyte interface. The interfacial characteristics of the electrode, such as the presence of various crystal faces, kink sites, and the micro-/meso-scale roughness affect this electrochemical reaction [336, 337]. Electrodes generally have a nonplanar surface, and flat electrodes, even after polishing, have some surface roughness as a result of the manufacturing process. An electrode can also be roughened deliberately in a number of ways, such as scratching [266], electrodeposition [338], electrochemical roughening [339–342], etching [343], and lithography [344]. In a solar redox flow battery (RFB), the characteristics of the electrode-electrolyte interface affect the photon path length/scattering properties, the mass transport of redox species to the electrode, and the electroactive surface area. Hence, a rational development of electrodes requires knowledge of surface structure−activity relationships.

Several studies have described the electrochemical response of rough electrodes using the theory of disordered fractals [345–352]. This provides a general description of the interfacial energy and mass exchange at the surface of the electrode. However, most rough electrodes only approximate fractal characteristics. The electrochemical response of rough electrodes can also be modelled using an interfacial structure with a regular and ordered pattern of well-defined geometry [353–357]. Regular structures provide an opportunity for an analytical study of the relationship between diffusion and the geometrical properties of the electrode's surface.

In this part of the study, an electrode containing a well-defined and regular pyramidal micro-array was used as a model of a rough electrode in order to study the effect of the electrode's surface roughness on the rate of the electron transfer reaction. On this path, this chapter covers two main goals:

1) understanding the mass transport of redox species over a pyramidal structure,

2) understand how the complex mass transfer behaviour at a patterned (rough) electrode influences cyclic voltammetry (CV), which is the standard approach for measuring kinetics.

To prepare the electrode, a pyramidal structure was fabricated over a glass substrate using a combination of photolithography and nanoimprint lithography and this was then coated with a 120 nm thick layer of gold. The electrochemical response of the patterned gold was studied using CV in the presence of an iron redox couple, with a numerical simulation applied to elucidate the mass transport behaviour of the redox species near the electrode surface.

4.2 Theory

Electrochemistry relates the flow of electrons to chemical changes. This process consists of two steps: 1) electron exchange between the electrode and the reactant, and 2) reactant/product transport (often by diffusion) to/from the electrode surface. The overall redox reaction rate and hence the measured current is defined by the rate of these steps – with the slowest of the two processes controlling the overall rate.

During the electrochemical process, shifting the electrode potential away from the equilibrium potential will cause the redox species at the electrode surface to undergo the electron transfer reaction which results in a concentration gradient in the electrolyte solution. The redox species diffuse from the bulk solution towards the electrode according to Fick's second law (Eq. 4.1), neglecting the mass transport of redox ions due to migration and convection:

$$N_i = D_i \frac{\partial C_i}{\partial x} \qquad \text{Eq. 4.1}$$

Where:

N_i is the diffusion flux,

D_i is component *i* diffusion coefficient,

C_i is component *i* concentration,

x is position.

The electrochemical reaction proceeds only if the consumed species are replaced by redox species from the bulk solution. The relative magnitude of electron transfer rate and redox species mass transfer rate defines the concentration of redox couple at the electrode surface. For an applied potential, if the system has enough time to reach a thermodynamic equilibrium, the concentrations of redox species at the electrode surface are described by the Nernst equation (Eq. 4.2):

$$E = E_f^0 - \frac{RT}{nF} \ln\left(\frac{C_{Re}}{C_{Ox}}\right) \qquad \text{Eq. 4.2}$$

Where:

E and E_f^0 are respectively the applied electrode potential and the formal reduction potential of the redox couple,

C_{Re} and C_{Ox} are the concentration of the reduced and oxidised form of redox couple in the bulk solution,

R is the universal gas constant,

T is the temperature,

n is the number of electrons transferred in the reaction,

F is the Faraday constant.

The volume of the solution in which the concentration is affected by the electrode is called the diffusion layer. In the absence of convection, the diffusion layer thickness is a function of diffusion coefficient and time and can be estimated using Eq. 4.3:

$$\delta = \sqrt{2Dt} \qquad \text{Eq. 4.3}$$

Where:

δ is the diffusion layer thickness,

D is the diffusion coefficient of the redox ion,

t is time.

By increasing the time of the electrochemical process, the diffusion layer grows into the bulk solution. However, when the thickness of the diffusion layer is sufficiently large, the chaotic motion of eddies prevents further thickening of this layer. Therefore, within a distance from the electrode, due to the microscopic mixing processes in the solution, the concentration of each solute is at its initial bulk value. The thickness of the diffusion layer is reduced if there is macroscopic convection within the electrolyte, for instance due to a density gradient within the solution or a forced hydrodynamic regime (such as a rotating disk electrode, flow channel systems, vibrations, and movement of air near the cell). The diffusion layer thickness can be accurately calculated from the concentration profiles. Another widely-used concept to approximate the diffusion layer thickness is the Nernst diffusion layer. This is defined as the distance at which a linear concentration profile with a gradient equal to the concentration gradient at the electrode surface takes its bulk value (Figure 4.1) [358]. The Nernst diffusion layer thickness in a typical electrochemical solution is of the order of a few hundred micrometers [359, 360].

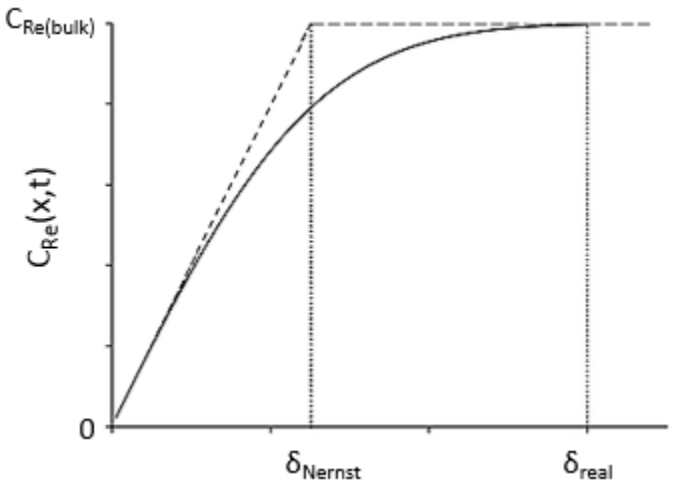

Figure 4.1. The real diffusion layer thickness (δ_{real}) corresponding to the real concentration profile (——) and the Nernst diffusion layer thickness (δ_{Nernst}) corresponding to a linear concentration profile (- - -) with the constant gradient equal to the concentration gradient at the electrode surface.

4.2.1 Cyclic voltammetry

CV is a well-known technique to monitor redox behaviour of chemical species within a wide potential range. It relies on recording the current while the potential is swept cyclically between two limits with a constant rate, called potential sweep rate (Figure 4.2). Applying potential provides the driving force for an electrochemical reaction. The redox ions at the electrode-electrolyte interface participate in the electron transfer reaction, and as a result, the electrons flow through the external circuit. By increasing the potential, the reductant concentration is depleted near the electrode, with the current controlled by either the diffusion of reductant from the bulk solution or the electron transfer rate (Figure 4.2-c). During the scan, the diffusion layer thickness grows throughout the scan, and this in turn slows down delivery (mass transfer) of the reductant to the electrode surface. The maximum current (peak) is observed at the potential at which the reductant mass transfer is highest.

In CV, the anodic and cathodic peak current and the difference between peak potentials (peak separation) provide information about the kinetics of electron transfer reaction and redox species mass transport rate [361]. In this regard, CV has been used extensively to study the effect of surface morphology on the electrochemical reaction.

During a CV process, the potential sweep rate defines the thickness of the diffusion layer at each potential [362]. By increasing the potential sweep rate, the diffusion layer has less time to extend into the solution and hence the diffusion layer becomes thinner.

The reversibility state of the CV process is defined by competition between the electron transfer reaction rate and the potential sweep rate. In this regard, three states of the reaction can occur; it can be reversible, quasi-reversible or irreversible.

Reversible CV occurs when the electron transfer rate is higher than the potential sweep rate. In this case, at each potential, the electron transfer reaction has enough time to reach a thermodynamic equilibrium, and the redox species concentration at the electrode surface is given by the Nernst equation. In the reversible condition, the overall reaction rate is limited by redox species mass transfer rate. As a result, CV analysis does not lead to any information about the kinetics of the

electron transfer reaction [362]. In this state, the separation of cathodic and anodic peak potentials is about 59/n mV, where n is the number of electrons transferred in the reaction [363].

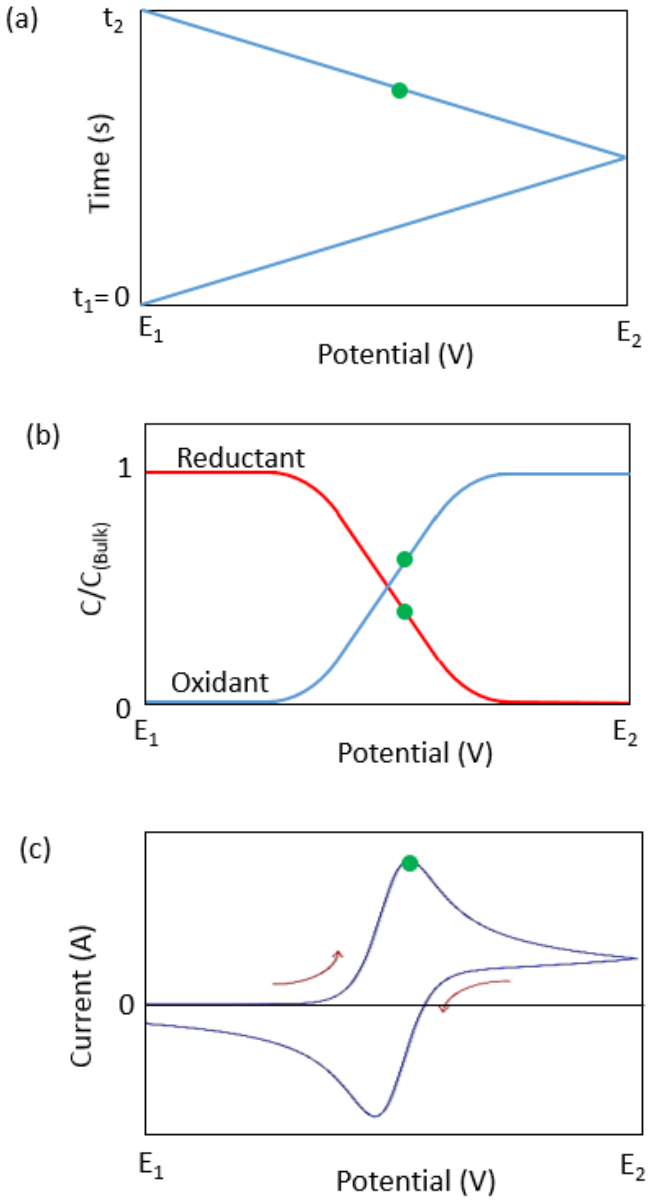

Figure 4.2. System change during cyclic voltammetry: (a) potential is swept cyclically between two limits with a constant rate, (b) the reductant and oxidant concentration at the electrode surface at each potential, (c) the current recorded at each potential. The green point on each graph represents the condition at which the maximum current was obtained.

By increasing the potential sweep rate, the diffusion layer has less time to extend into the bulk solution, and redox species mass transfer rate to and from the electrode is increased. At a certain redox species mass transfer rate, the rate of the electron transfer is not enough to maintain the equilibrium at each potential. In this state, which is called quasi-reversible, both the oxidation and reduction reactions contribute to the electron transfer reaction, and the concentration at the electrode surface changes based on the following equation [364]:

$$t > 0, x = 0, D_o \left(\frac{\partial C_o}{\partial x}\right) = k_f C_o - k_r C_R \qquad \text{Eq. 4.4}$$

Where:

C_O and C_R are respectively oxidant and reductant concentration,

k_f and k_r are the heterogeneous electron transfer rate constant of forward and reverse reactions,

other parameters have their usual meanings.

The electron transfer kinetics depend on the rate constants (k_f and k_r) which, assuming Butler-Volmer type kinetic behaviour, depend on the overpotential applied to the electrodes:

$$k_f = k^{\circ} \exp\left(\frac{-\alpha n F}{RT}\left(E - E_f^0\right)\right) \qquad \text{Eq. 4.5}$$

$$k_r = k^{\circ} \exp\left(\frac{(1-\alpha) n F}{RT}\left(E - E_f^0\right)\right) \qquad \text{Eq. 4.6}$$

Where:

k° is the standard rate constant,

α is the charge transfer coefficient,

n is the number of electrons transferred during the oxidation and reduction reactions,

F is the Faraday constant,

$E - E_f^0$ is the difference between the cell potential and the formal potential known as the activation overpotential,

other parameters have their usual meanings.

The net electron transfer rate at a surface can be calculated using the Butler-Volmer equation [365]:

$$i = FAk^{\circ}\left(C_R exp\left(\frac{-\alpha nF(E-E_f^0)}{RT}\right) - C_O exp\left(\frac{(1-\alpha)nF(E-E_f^0)}{RT}\right)\right) \quad \text{Eq. 4.7}$$

Where:

i is the current,

A is the surface area of the electrode.

In quasi-reversible state, the electrochemical reaction is limited by the kinetics of the electron transfer reaction, and the separation of peak potentials can be a measure of the standard rate constant. In this case, the cathodic and anodic peak occurs later, and the peak separation would be higher than 59/n mV. Nicholson has shown a theoretical correlation between peak separations and standard rate constant at a specific potential scan rate (Eq. 4.8 and Eq. 4.9) [361]. However, Nicholson method is applied for a one-dimensional diffusion of redox species towards a planar electrode. Accurate use of the Nicholson method requires the CV to be recorded at multiple sweep rates.

$$\psi = \left(\frac{D_{Fe^{3+}}}{D_{Fe^{2+}}}\right)^{\alpha/2} \times k_s\left(\frac{R \times T}{z \times F \times D_{Fe^{3+}} \times dE/dt}\right) \quad \text{Eq. 4.8}$$

$$\psi = (-0.6288 + 0.0021\left(E_p^a - E_p^c\right))/(1 - 0.017\left(E_p^a - E_p^c\right)) \quad \text{Eq. 4.9}$$

In the irreversible state, the electron transfer reaction is in a static equilibrium and the cathodic peak does not appear in the CV. In this condition, the concentration of redox species at the electrode surface is given by:

$$t > 0, x = 0, D_o\left(\frac{\partial C_o}{\partial x}\right) = kC_o \quad \text{Eq. 4.10}$$

$$k = k^{\circ} \exp\left(\frac{-\alpha n F}{RT}\left(E - E_f^0\right)\right) \qquad \text{Eq. 4.11}$$

In the irreversible state, the theoretical approach is very complex and numerical analysis is required to study the electrochemical properties.

As the reversibility state of the CV depends on the potential sweep rate, it is common for a fast reaction to show non-reversible behaviour at higher sweep rates [364].

4.2.2 Cyclic voltammetry on a rough electrode

Surface morphology of a non-planar electrode can affect the electron transfer reaction in two ways: 1) changing the electroactive surface area (EASA) of the electrode, 2) changing the concentration profile of the redox species in the electrolyte solution. During CV, at low potential sweep rate, when the diffusion layer thickness is much larger than the scale of roughness, the effect of electrode's surface structure on the concentration profile is insignificant. Also, if the reaction is in reversible state and is limited by mass transfer rate, the EASA does not affect the CV. Therefore, under the reversible state, when the diffusion layer thickness is much higher than the scale of the roughness on the electrode surface, CV does not provide any information regarding the electrode's surface morphology.

In the quasi-reversible region, the electron transfer reaction does not have enough time to reach a dynamic equilibrium. The electrochemical reaction is limited by the kinetics of electron transfer. Therefore, the parameters that affect the rate of the electron transfer reaction (such as the EASA of the electrode and mass transfer rate of the redox species) change the peak separation. Increasing the potential sweep rate reduces the size of diffusion layer thickness relative to the scale of the structure on the electrode's surface and, as a consequence, the electrode's surface morphology changes the concentration profile. In the quasi-reversible state, larger EASA improves the electrochemical reaction rate. Therefore, the peak separation of a rough electrode is different from that of a perfectly flat electrode at the same potential sweep rate. For a non-planar electrode in the quasi-reversible state where the diffusion layer thickness is large enough to neglect the effect of

surface roughness on mass transfer rate, the following is the relationship between the apparent rate constant estimated through CV and the electron transfer standard rate constant [366]:

$$k_{app} = \Psi k^{\circ} \qquad \text{Eq. 4.12}$$

Where:

k_{app} is the apparent rate constant measured through CV,

and Ψ is the roughness factor and is defined as:

$$\Psi = \frac{\text{Electroactive area}}{\text{Substrate area}} \qquad \text{Eq. 4.13}$$

4.3 Experimental methods

The effect of the electrode's geometrical feature on the electrochemical reaction rate was investigated through numerical and experimental study of CV in the presence of Fe^{2+}/Fe^{3+} redox couple.

4.3.1 Electrode preparation

The side of the electrode in contact with the electrolyte was patterned with a periodic pyramidal microstructure. The structure was fabricated into a layer of UV curable polymer on top of a glass substrate using imprint lithography as described in section 2.3.1. Electron beam evaporation was utilised to coat the pyramidal structure with a 120 nm layer of gold as an electrically conductive material.

A Si master mold containing an array of inverted pyramids was utilised for imprint lithography. To prepare the master mold, photolithography was employed to record an initial pattern on the photoresist layer coated on the Si wafer, and the pattern was transferred to the Si wafer using a multi-step etching process.

4.3.2 Master mold preparation

The first stage in photolithography was to put a layer of photoresist over a commercial 100 nm SiO_2 coated Si wafer. The Si wafer was cleaned by sonication in acetone, methanol, and isopropyl alcohol for 10 min each. Then, it was rinsed with deionised (DI) water and blown with nitrogen gas. Further cleaning was achieved by use of an O_2 plasma asher for 10 min. Hexamethyldisilazane (HMDS) was immediately spin-coated on the substrate at a speed of 4000 rpm for 30 s to improve the adhesion between the photoresist and SiO_2 layer. A layer of positive photoresist of AZ1518 was immediately spin-coated at spinning speed of 4000 rpm for 60 s. The wafer was then soft baked on a hot plate at 90°C for 1 min.

To transfer the pattern to the photoresist, 405 nm UV light with an exposure dose of 55 mJ/cm^2 was used to illuminate the Si wafer through the photomask using a Karl Suss mask aligner system. The photomask preparation process is elaborated in the next section. The exposed photoresist was removed by immersing the wafer in AZ 326 MIF developer for 1 min. The developer was thoroughly rinsed with DI water to ensure there was no residue left on the surface that would interfere with the subsequent etching steps. Then, the Si wafer was post-baked on a hot plate at 120°C for 6 min. The pattern was transferred to the SiO_2 layer by immersing the wafer in 40% buffered HF (6:1 volume ratio of NH_4F solution to 49% HF) for 80 s (etching rate of SiO_2 in buffered HF is about 80 nm/min), while the photoresist worked as a mask for the SiO_2 layer. To remove the photoresist layer, the wafer was sonicated in acetone, methanol, and isopropyl alcohol for 10 min each, and then rinsed with DI water. The inverted pyramidal structure on a Si (100) substrate was fabricated by wet etching in 30% KOH solution at 80°C for 255 sec (etching rate of Si (100) in KOH at 80°C is about 1.2 μm/min). The etching steps to fabricate the inverted pyramidal structure into the Si wafer is presented schematically in Figure 4.3. The microscopic image of the Si wafer after each etching step is shown in Figure 4.4.

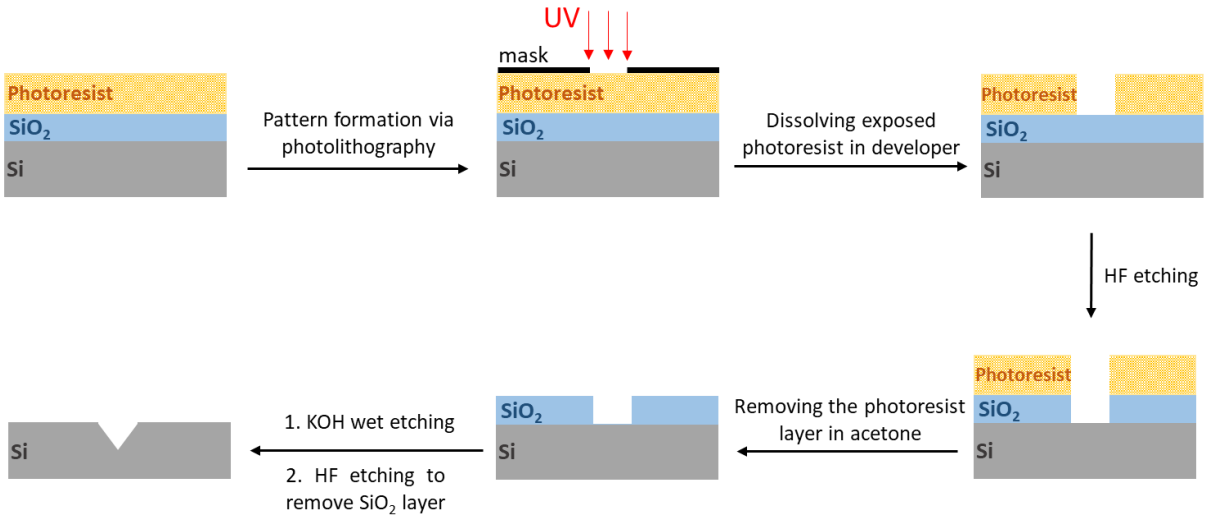

Figure 4.3. Schematic diagram of Si master mold preparation. The initial pattern was recorded on the photoresist layer using photolithography and was transferred to the Si layer through a multi-step etching process. For each layer, the layer above it worked as a hard mask. KOH etching was used to produce the pyramidal structure in the Si wafer.

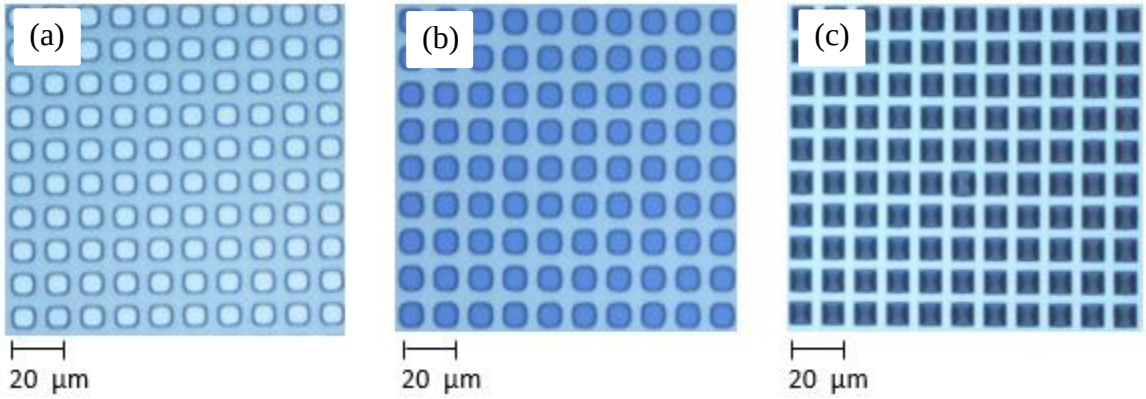

Figure 4.4. Images of the Si wafer at each step in preparation of the Si master mold: (a) the exposed photoresist was dissolved in developer, (b) the pattern was transferred to the SiO_2 layer by etching with buffered HF solution, (c) the pyramidal structure was etched into the Si wafer using KOH.

4.3.3 Photomask preparation

The photomask used in photolithography was a chrome metal on soda lime glass plate containing a periodic array of square-shaped openings of 7×7 μm and pitch of 14 μm. This pattern was designed by L-edit software and was written on a 4 inches chrome-coated glass (4x4x .060 SL LRC 10M 1518 5k, Nanofilm) using a Heidleburg micro PG laser mask writer equipped with a laser of 405 nm wavelength. The commercial chrome glass that was used for this purpose contained a layer of a positive-tone photoresist (AZ1518). During mask writing, the photoresist was exposed by light. The exposed photoresist was dissolved by immersing in AZ 326 MIF developer for 40 s. Then, the chrome layer was etched for 45 s in a solution of 0.3 M ammonium cerium (IV) nitrate and 0.15 M perchloric acid in DI water. After rinsing with DI water, the photoresist was removed by 30 min sonication in acetone. A schematic diagram of the photomask preparation process is shown in Figure 4.5, and a microscopic image of the prepared photomask is presented in Figure 4.6.

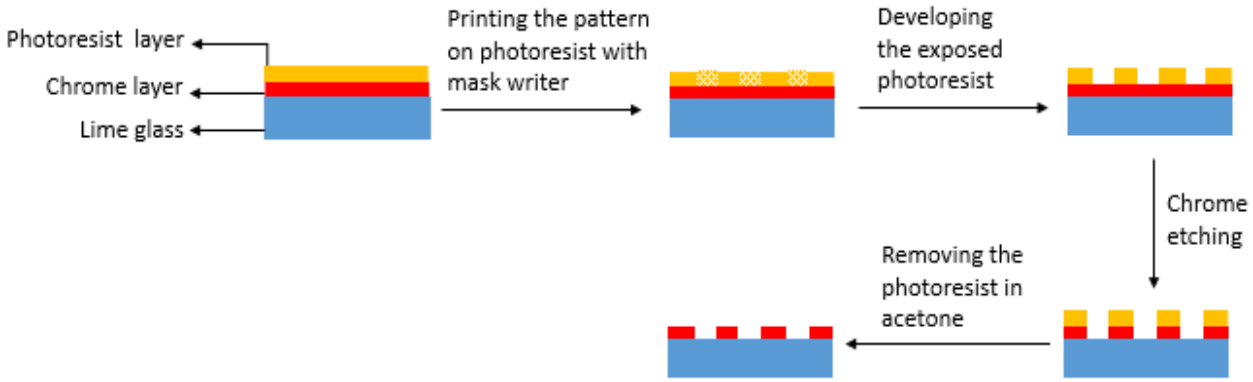

Figure 4.5. Preparation of a photomask containing an array of square-shaped openings. The initial pattern was printed on the photoresist layer using a mask writer. After developing the photoresist, it acts as a hard mask for the chrome layer during the etching process, after which, the photoresist layer is dissolved in acetone.

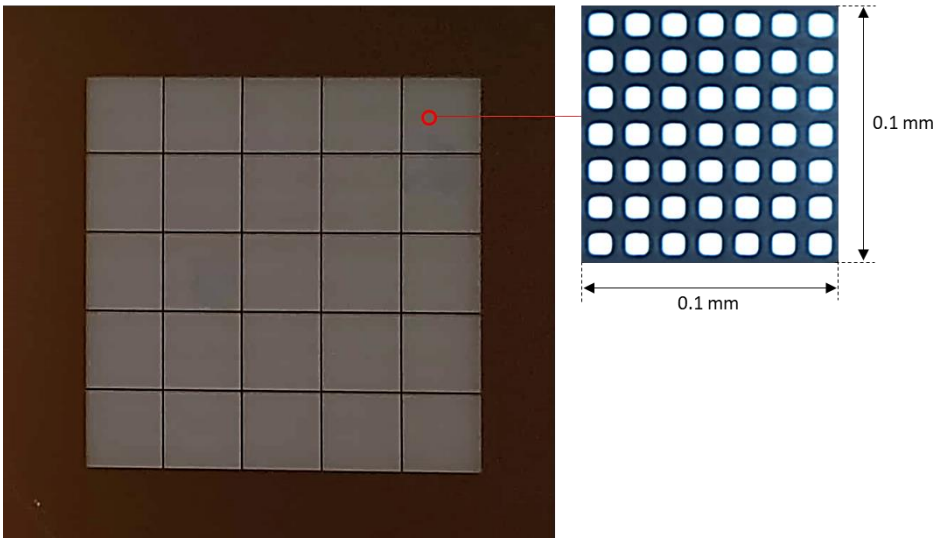

Figure 4.6. An image of the photomask used in photolithography and a microscopic image of its pattern which consists of an array of square-shaped openings (each being 7×7 μm and with a pitch of 14 μm).

4.3.4 Electrochemical studies

The CVs of the gold-coated patterned electrode were compared with those of a flat electrode. The flat electrode was a glass substrate coated with a 120 nm layer of gold using electron beam evaporation. All experiments were conducted at least in duplicate. The electrochemical cell (Figure 4.7) was a three-electrode setup including a working electrode (1×1 cm), a Pt counter electrode, and an Ag|AgCl reference electrode. Inlets at the top of the cell were used to introduce the working electrode, Pt counter electrode, reference electrode, and gas line port for argon purging of electrolyte solutions.

To measure the patterned electrode's EASA, CV was carried out in an aqueous solution of 0.5 M sulfuric acid. The potential limits were set to prevent the onset of hydrogen and oxygen evolution. Before starting the process, dissolved oxygen was purged from the electrolyte solution by bubbling argon through the gas inlet. During measurement, CV was performed in a static solution, argon was no longer bubbled through the electrolyte, but was released above the surface. Before recording the CV, the electrode surface was first brought into a reproducible state by applying a few fast potential scans that resulted in electrochemical surface cleaning. The potential was

scanned from 0 to 1.7 V vs. Ag|AgCl, at a sweep rate of 0.1 Vs^{-1}. The CV scan starts at the estimated open circuit potential of 0.5 V vs. Ag|AgCl.

The electrochemical behaviour of the electrodes was studied in the presence of a Fe^{2+}/Fe^{3+} redox couple. Only Fe^{2+} species were initially present in the electrolyte. An electrolyte containing 1 mM Fe^{2+} in 0.5 M H_2SO_4 was prepared by using iron (II) sulphate heptahydrate as the precursor. Prior to the CV scan, the electrolyte was purged by Ar gas to remove the dissolved O_2, and during CV Ar gas was released on top of the electrolyte. Before measurements, the electrode surface was electrochemically cleaned by running a few fast voltammetry cycles. The potential was swept at different rates between the limits of 0 V and 1V vs. Ag|AgCl.

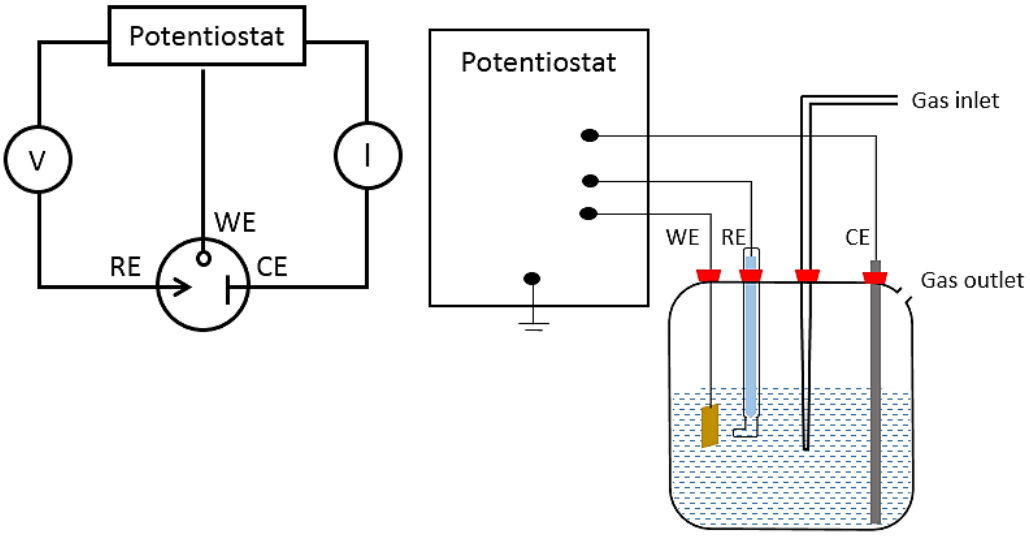

Figure 4.7. Schematic diagram of a three-electrode cell including the working electrode (WE), reference electrode (RE), counter electrode (CE), and a gas inlet for the purge of oxygen using Ar. Potentiostat injects the current into the cell through the counter electrode, while maintaining a constant potential difference between the working and reference electrodes. No current passes through the reference electrode; it has a constant potential which is used to as a reference to measure the potential of working electrode.

4.4 Results and discussion

4.4.1 Characterisation

The size and morphology of the Si master mold containing an inverted pyramidal microarray is determined using SEM (Figure 4.8) and AFM (Figure 4.9). The gold-coated pyramids fabricated in this work were found by SEM (Figure 4.10) to be consistent in shape, with a height of 5 µm, a width of 7 µm, and a periodicity of 14 µm.

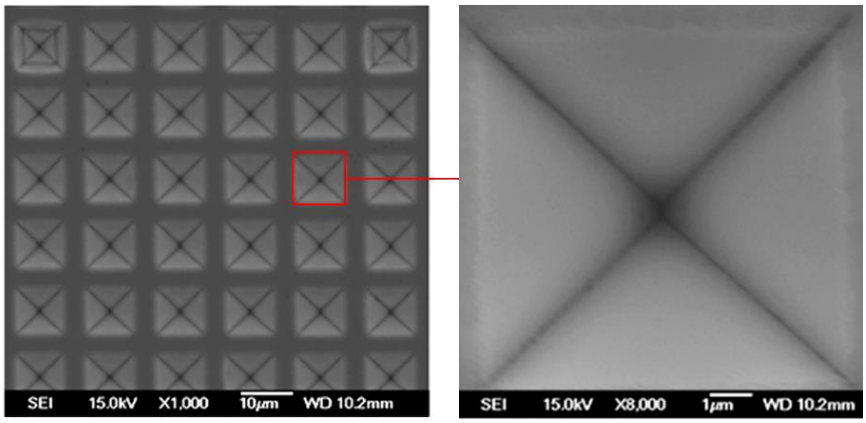

Figure 4.8. SEM image of the Si master mold containing an inverted pyramidal microarray at magnifications of 1000X and 8000X.

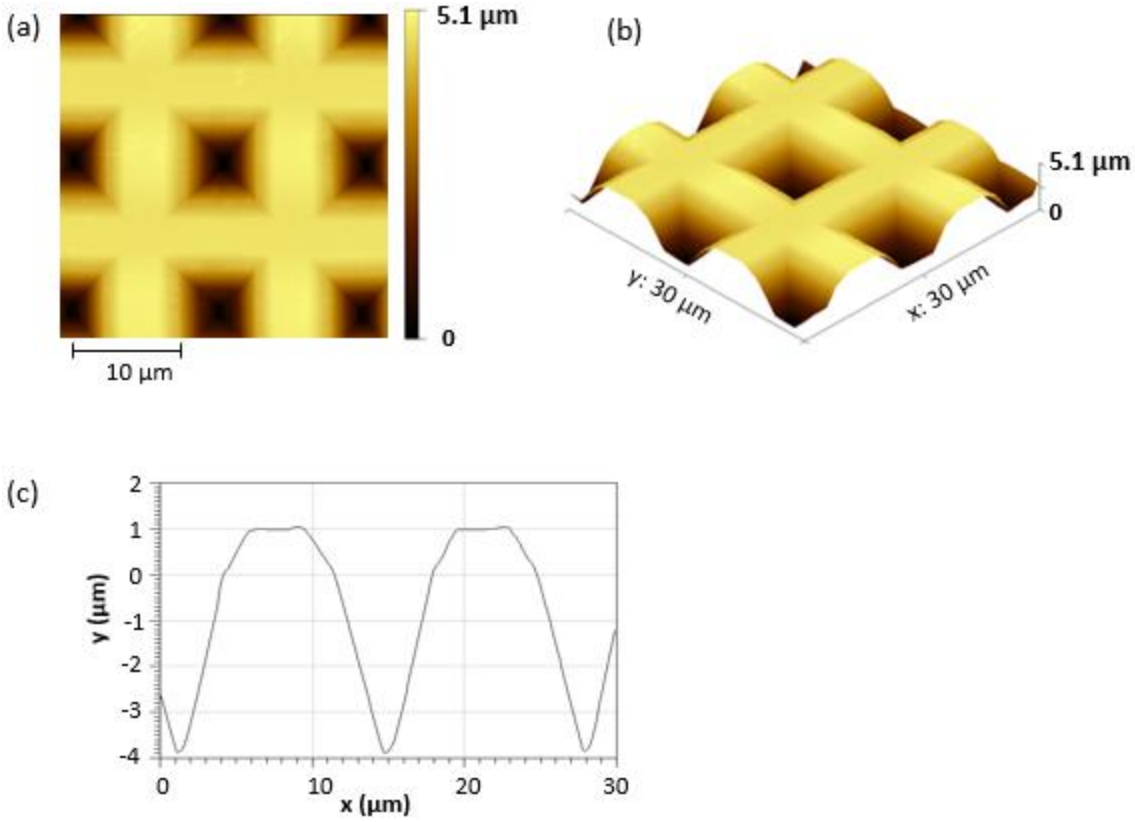

Figure 4.9. AFM image of the Si master mold containing an inverted pyramidal microarray: (a) 2D view, (b) 3D view, (c) cross-sectional trace.

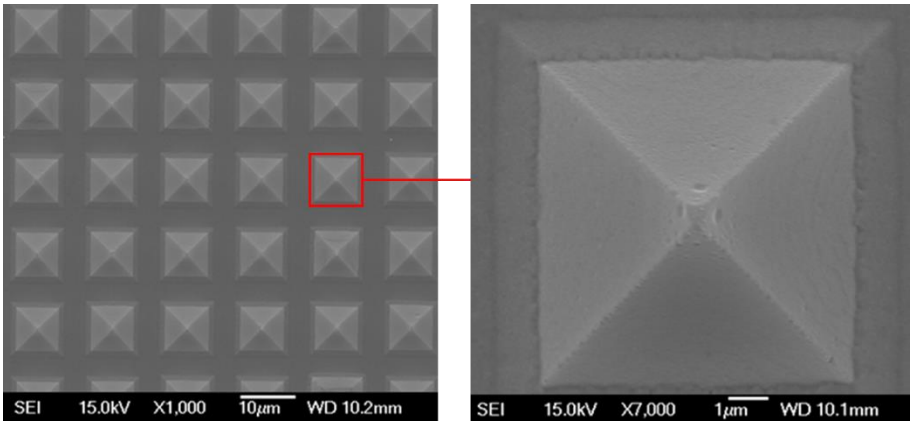

Figure 4.10. SEM image of a gold electrode patterned by an upright pyramidal microarray. The pattern was fabricated into an Ormostamp layer coated on top of a glass substrate and was coated by a 120 nm layer of gold.

4.4.2 Electrochemical behaviour

Experimental measurement of roughness factor

CV of gold has well defined regions that have been well explained previously [367]. These regions were observed in CV scan of the gold-coated flat and patterned electrodes (Figure 4.11). As the potential was scanned during the anodic sweep, the gold oxide started to form at around 1.1 V vs. Ag|AgCl. In the cathodic sweep, the gold oxide reduced to metallic gold below 1 V vs. Ag|AgCl. The area under the reduction peak in the plotted CV (shaded area in Figure 4.11) is equivalent to the charge required to fully reduce the gold oxide surface of the fabricated electrode to a metallic gold surface. By measuring this value and by considering the charge of 400 μC/cm^2 as that necessary to form a single monolayer of AuO on the Au (100) face [368], the EASA and roughness factor of the fabricated electrodes can be estimated. Using this method, the roughness factor of gold-coated flat and patterned electrodes was found to be 1.93 and 3.26, respectively. The roughness of the flat electrode corresponded to only the nanoscale irregularities of the gold coating, while on the patterned electrode the roughness was caused by both the nanoscale irregularities of the gold coating and the microscale pyramidal structure.

EASA of an electrode can also be estimated by measuring the electrode's double layer capacity. In the double layer region, the current results from the charging of the electrode's double layer at the electrode-electrolyte interface based on Eq. 4.14 and depends on the EASA of the electrode.

$$j = Cv \qquad \text{Eq. 4.14}$$

Where:
j is the current density,
C is the capacitance,
v is the scan rate.

For both flat and patterned electrodes, CVs at different potential sweep rates were recorded in the region where no significant faradic reaction occurred (Figure 4.12), and the current was plotted versus potential sweep rate as shown in Figure 4.13. The slope of the interpolated line is equivalent

to the double layer capacity of the electrode. With a double layer capacity of 20 µF/cm^2 for a perfectly smooth gold electrode [369], the calculated roughness factors were 1.520 for the gold-coated flat electrode and 3.175 for the gold-coated patterned electrode.

The roughness factors obtained from the two methods agreed pretty well (1.93 vs. 1.52 for the flat, and 3.26 vs. 3.175 for the patterned electrode). The regular structure of the pyramids made it possible to calculate the geometric area of the patterned electrode. The pyramidal structure provided 1.19 times more surface area than the flat electrode, whereas the experimental results showed that the surface area of the patterned electrode was 1.69–2.08 times greater. This suggests that the effect of patterning on the roughness factor is not only because of the microscale structure but is mostly due to the nanoscale roughness formed during gold deposition. On the patterned electrode, the gold layer was deposited onto the Ormostamp layer, while on the flat electrode, it was coated onto a glass substrate. This could be the reason of higher nanoscale roughness on the patterned electrode.

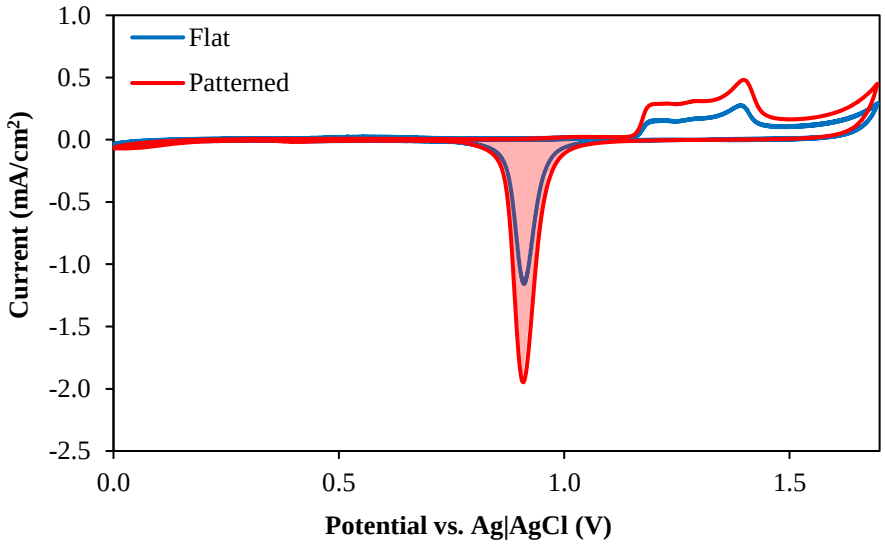

Figure 4.11. CV scan of gold-coated flat and patterned electrodes in an electrolyte solution of 0.5 M H_2SO_4 recorded at a potential sweep rate of 0.1 V s^{-1}. The shaded area represents the charge required for full reduction of gold oxide at the surface of the patterned electrode. By measuring the integrated area under the reduction peak a roughness factor of 1.93 and 3.26 was obtained for flat and patterned electrodes, respectively.

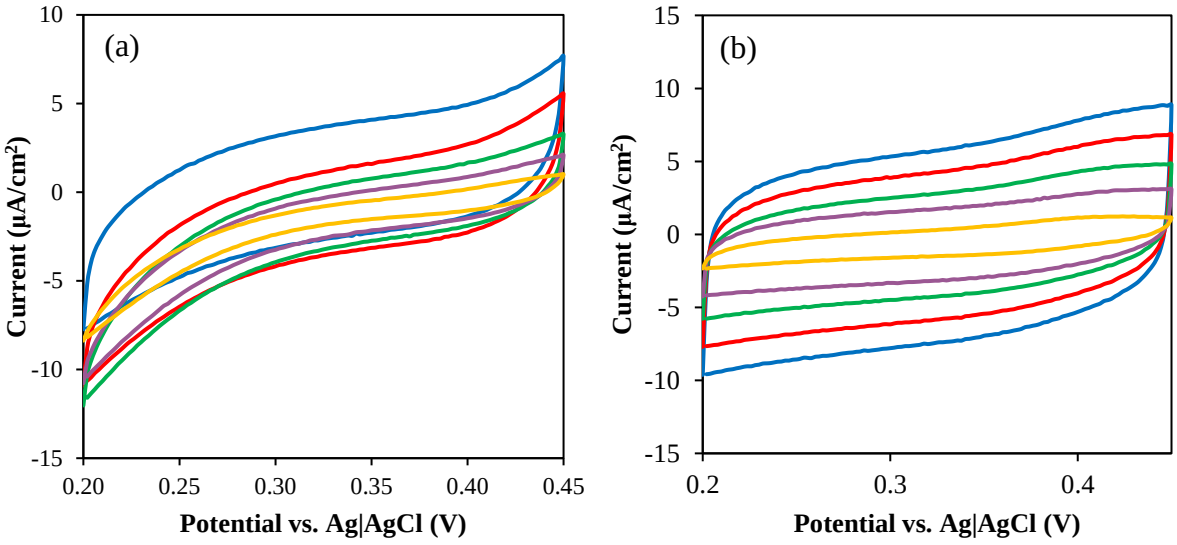

Figure 4.12. CV scan of 1×1 cm gold-coated (a) flat and (b) patterned electrodes in contact with an electrolyte solution of 0.5 M H_2SO_4 in the double-layer region at different potential sweep rates: 0.02, 0.4, 0.06, 0.08, and 0.1 V s^{-1}.

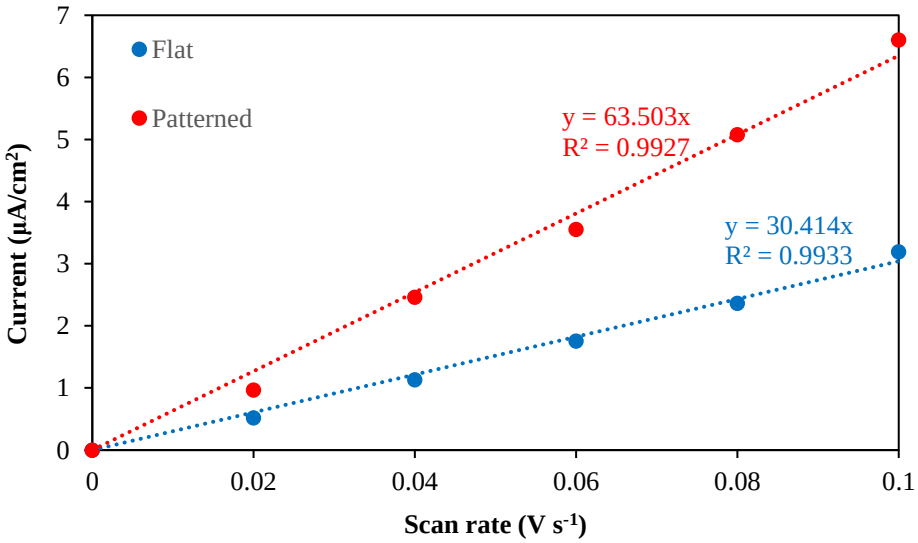

Figure 4.13. Current value in the double-layer region as a function of scan rate for 1×1 cm gold-coated flat and patterned electrodes in an electrolyte solution of 0.5 M H_2SO_4. The slope of each plot represents the double layer capacitance of each electrode.

Numerical study

Numerical simulations based on finite elements analysis were conducted using COMSOL software in order to study the CV of gold electrode patterned with upright pyramidal structure in the presence of Fe^{2+}. The results were compared with that of a flat electrode.

The simulation system was defined for part of the pattern that is periodically repeated. A schematic diagram of the simulated system including the applied boundary conditions is presented in Figure 4.14. The defined parameters and boundary conditions used in the numerical simulation are presented in Table 4.1 and Table 4.2, respectively. Only Fe^{2+} was initially present in the solution. By sweeping the potential, the redox species near the electrode's surface participate in the electron transfer reaction and create a concentration gradient within the solution. The electron transfer reaction at the surface of an electrode is described by the Butler-Volmer equation which relates the current density to the electrode's potential as follows:

$$j_{loc} = nFk_0 \left(C_{Fe^{2+}} \exp\left(\frac{(n-\alpha)F(E-E^{\circ})}{RT}\right) - C_{Fe^{3+}} \exp\left(-\frac{\alpha F(E-E^{\circ})}{RT}\right)\right) \qquad \text{Eq. 4.15}$$

Where:
J_{loc} is the local current density,
and the other parameters have their usual meanings.

Fick's second law was used to calculate the rate of mass transfer to and from the electrode surface, assuming the mass transfer due to convection and migration is negligible. The bulk position (Table 4.1) is defined as a product of the diffusion layer thickness calculated by Eq. 4.3. While the bulk position must be at a distance from the electrode's surface where the solution's concentration is not affected by the electrode, a very high distance would increase the size of the system and the computational time.

Table 4.1. Defined parameters used for numerical simulation

Parameter	Value
bulk position	$H = 3\times\sqrt{2\, D_{Fe^{3+}}\times\lvert V_2-V_1\rvert/\nu}$
Fe^{2+} diffusion coefficient	$D_{Fe^{2+}} = 6.13\times10^{-6}$ [cm^2/s] [370]
Fe^{3+} diffusion coefficient	$D_{Fe^{3+}} = 5.28\times10^{-6}$ [cm^2/s] [370]
Fe^{2+} initial concentration	$C_{Fe^{2+}}$ =1 [mmol/L]
Fe^{3+} initial concentration	$C_{Fe^{3+}}$ = 0 [mmol/L]
standard rate constant	k° = 0.0448 [cm/s]
double layer capacitance	C_{DL} = 0.2 [F/m^2]
formal potential	E_f = 0.47 [V]
temperature	T = 298 [K]
charge transfer coefficient	$\alpha = 0.5$
potential sweep rate	ν
initial potential	V_1
final potential	V_2

Table 4.2. Defined boundary conditions used for numerical simulation

Boundary	Condition
Electrode Surface	Butler-Volmer equation
Bulk solution	$C_{Fe^{2+}}$ =1 [mmol/L]; $C_{Fe^{3+}}$ = 0 [mmol/L]
Sides of system	$\frac{\partial^2 C_{Fe^{2+}}}{\partial x^2}=0$; $\frac{\partial^2 C_{Fe^{3+}}}{\partial x^2}=0$

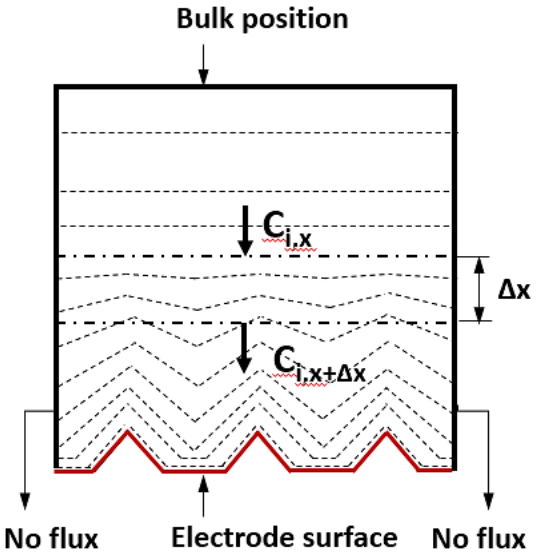

Figure 4.14. Schematic diagram of the simulated system: due to the concentration gradient, the redox species (C_i) diffuse from the bulk solution towards the electrode to participate in the electron transfer reaction at the surface of the electrode. Mass transfer occurs within the system and there is no flux from outside the boundaries.

Mesh optimisation

In the finite element analysis, the size and type of the mesh plays an important role in defining the accuracy of the results and calculation time. Generally, the denser the mesh, the greater the simulation time, which is unnecessary if changes in the physical properties are minimal in well-meshed regions. Hence, there is a trade-off between the time of calculation and the accuracy of the result. The optimum meshing was chosen by running the simulation at high potential sweep rates which are more sensitive to the mesh structure due to steep variation of physical properties.

For the flat electrode, three types of swept, distributed swept, and tetrahedral meshes were tested by observing how these mesh types influenced the peak current density during simulated CV. A sweep rate of 10 V s^{-1} was chosen for the comparison as this creates the thinnest diffusion layer which in turn is most sensitive to the mesh type. The swept mesh creates hexahedral elements which start at a source boundary and sweep along to a destination boundary distributed uniformly along the system. In distributed swept mesh, the size of the elements grows at a constant rate over the geometry to create a denser mesh in the domain with high variation of physical properties.

Tetrahedral mesh is well suited for complex-shaped geometries requiring a varying element size as it creates an unstructured mesh with irregular connectivity. It forms very small elements in tight spaces and very large elements in more open spaces without creating problems in the solution algorithms. The effect of meshing on the current density and the final meshing structure (distributed swept mesh) that were chosen for numerical study of a flat electrode are presented in Figure 4.15. The distributed swept mesh with 300 elements automatically distributed within the system provides a reasonable accuracy over a wide range of mesh size. For a mesh size smaller than 1 µm, similar results were observed for all type of meshes.

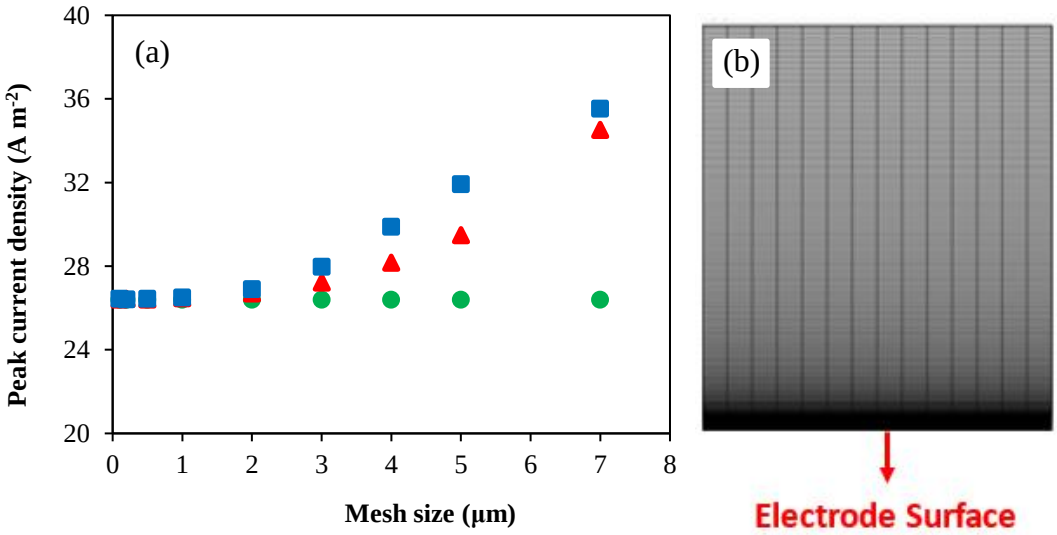

Figure 4.15. (a) the effect of mesh sizes of three mesh types (swept ■, distributed swept ●, and tetrahedral ▲) on the peak current density of a flat electrode at potential sweep rate of 10 V s^{-1}, (b) A 2D image of a distributed swept mesh that was used for numerical studies.

Due to the specific geometry of the patterned electrode, tetrahedral mesh is automatically chosen by COMSOL. In the tetrahedral mesh, the shape of the elements and the angles between them provide a great chance of reaching more accurate results at the sharp tip of the electrode. The effect of tetrahedral mesh size on the current density of the patterned electrode was studied at potential sweep rate of 10 V s^{-1} (Figure 4.16). For mesh sizes below 1 µm, the size of the mesh had negligible

influence on the calculated CVs. Hence, a mesh size of 0.5 µm was chosen for further calculations. However, using this size of mesh caused the calculation time to be increased drastically. To reduce the calculation time, the system was divided into two mesh domains by using a partition: a) tetrahedral mesh for the domain close to the electrode where the physical properties of the system are affected by the surface geometry of the electrode, b) distributed swept mesh for the domain in which surface geometry does not affect the concentration gradient. The patterned electrode's meshing structure is shown in Figure 4.17-a and the effect of partition distance from the electrode is presented in Figure 4.17-b. For further numerical studies on the patterned electrode, a partition was placed at a distance of 10 µm from the electrode's base in order to separate two domains, one of a tetrahedral mesh with a size of 0.5 µm, and a second of a distributed swept mesh containing 300 automatically distributed elements.

The accuracy of the results using this mesh structure was tested by comparing the numerical and experimental CV of flat and patterned electrodes at a potential sweep rate of 0.5 V s^{-1} (Figure 4.18).

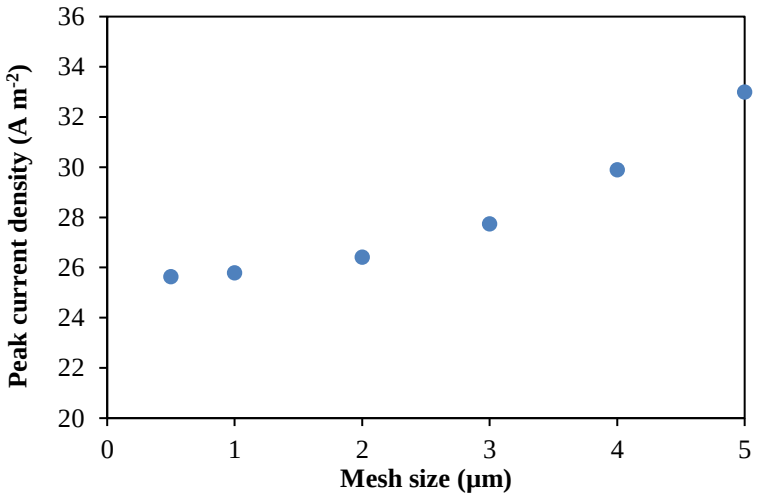

Figure 4.16. The effect of tetrahedral mesh size on the current density of a patterned electrode at a potential sweep rate of 10 V s^{-1}.

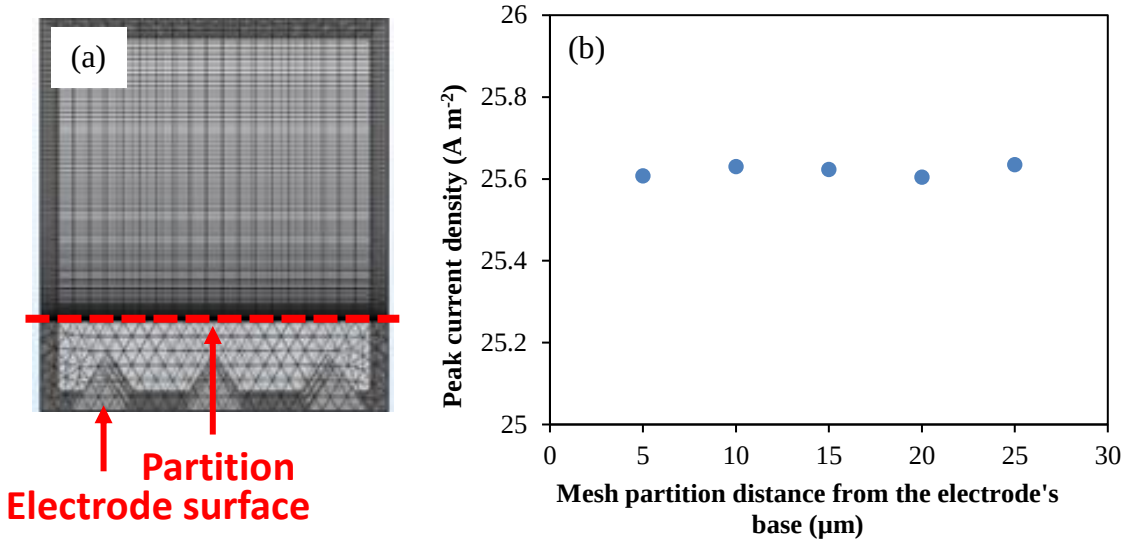

Figure 4.17. (a) An image of the mesh structure used for the patterned electrode (the system is divided into two mesh domains by using a partition), and (b) the effect of mesh partition distance from the base of the electrode on the peak current density.

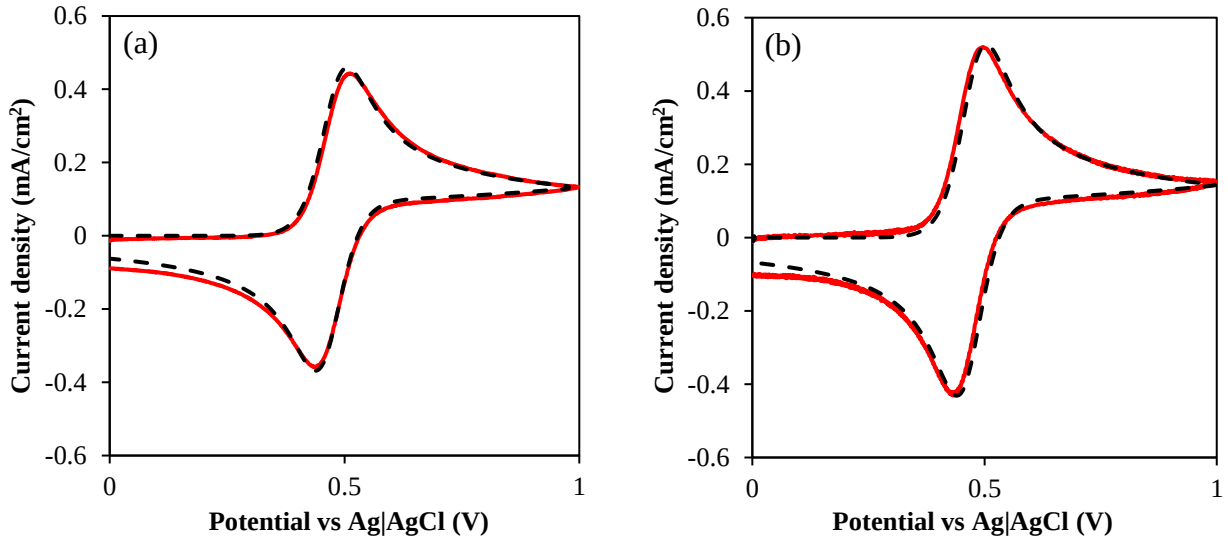

Figure 4.18. Numerical (- - -) and experimental (——) CV (first cycle) of (a) flat and (b) patterned electrode in an electrolyte containing 1 mM Fe^{2+} at potential sweep rate of 0.5 V s^{-1}.

Numerical and experimental study of surface roughness effect on electrochemical reaction

In CV, the peak separation is defined by kinetics of the electron transfer reaction relative to the rate of redox species mass transfer. On a patterned electrode, changing the potential sweep rate changes the concentration profile over the system and therefore affects the mass transfer rate and the availability of the EASA. As a result, the peak separation varies with potential sweep rate. The change of peak separation by potential sweep rate was measured for flat and patterned electrodes (Figure 4.19). As expected, at low potential sweep rate (thick diffusion layer) for a reversible electron transfer reaction, peak separation of flat and patterned electrodes was the same, and the CV did not give any information regarding the electrode's EASA. However, due to higher EASA on the patterned electrode, the transition from a reversible to a quasi-reversible state occurred at a higher potential sweep rate. In a quasi-reversible CV, because of higher EASA of the patterned electrode, the kinetics of the electron transfer reaction dominated the mass transfer at a lower potential, therefore, the peak separation of the patterned electrode was smaller than that of the flat electrode.

At very high potential sweep rates, the behaviour of the patterned electrode came close to that of the flat electrode (explained later in this section). By visualising the concentration profile of the redox species on the patterned electrode (Figure 4.20), it can be observed that the maximum difference between the flat and patterned electrode occurred at the potential sweep rates that caused a convergent diffusion of redox species towards the pyramids.

The sensitivity of the system to environmental noise at very low potential sweep rates, and high double layer overpotential at very high potential sweep rates caused the deviation of experimental results from those of the numerical simulation.

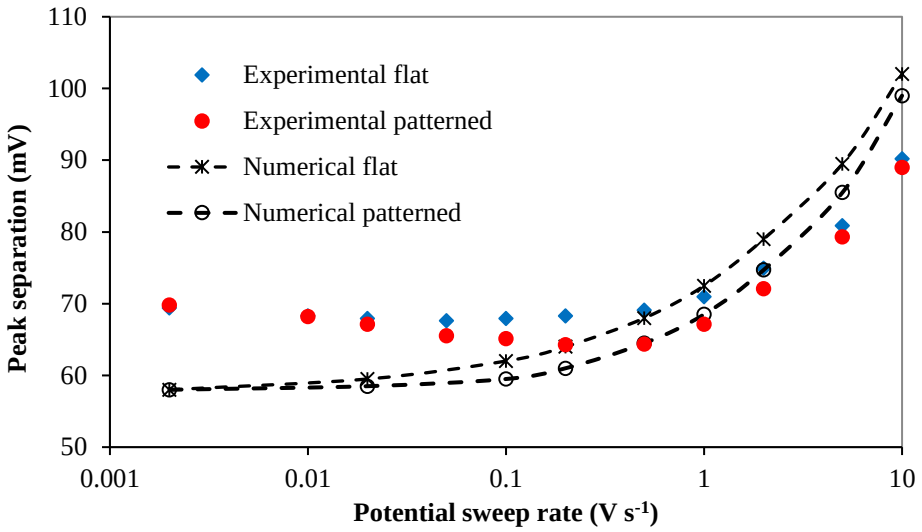

Figure 4.19. Numerical and experimental peak separation of the CV of flat and patterned electrodes at different potential sweep rates.

The concentration profile of the patterned electrode at peak potential was simulated at potential sweep rates of 0.002, 0.5, 1, and 10 V s^{-1} (Figure 4.20). Depending on the potential sweep rates, four different case of diffusion were observed. At very low sweep rate, when the diffusion layer thickness was much larger than the structure's scale, there was a small concentration gradient from the base to the top of the pyramid, and the redox species diffusional area was equal to the electrode's projected area. Therefore, a perpendicular diffusion of redox species occurred through the system, which was similar to the diffusion towards a flat electrode with an EASA equal to the electrode's projected area (Figure 4.20-a). When the diffusion layer thickness was small enough, the electrode's surface structure affected the redox species concentration profile (Figure 4.20-b). In this case, the diffusional area was larger than the electrode's projected area. The redox species diffusion was convergent towards each pyramid and overlapped with that of neighbouring pyramids. Higher potential sweep rate reduced the overlap of the concentration profile of each pyramid (Figure 4.20-c). When there was no overlap in the concentration profile of each pyramid, the redox species diffusion was perpendicular to the surface of each pyramid with a diffusional area equal to the EASA (Figure 4.20-d). This shows that at super-high potential sweep rates, the patterned electrode would be expected to behave as a flat electrode with a larger area than calculated from a 2D projection.

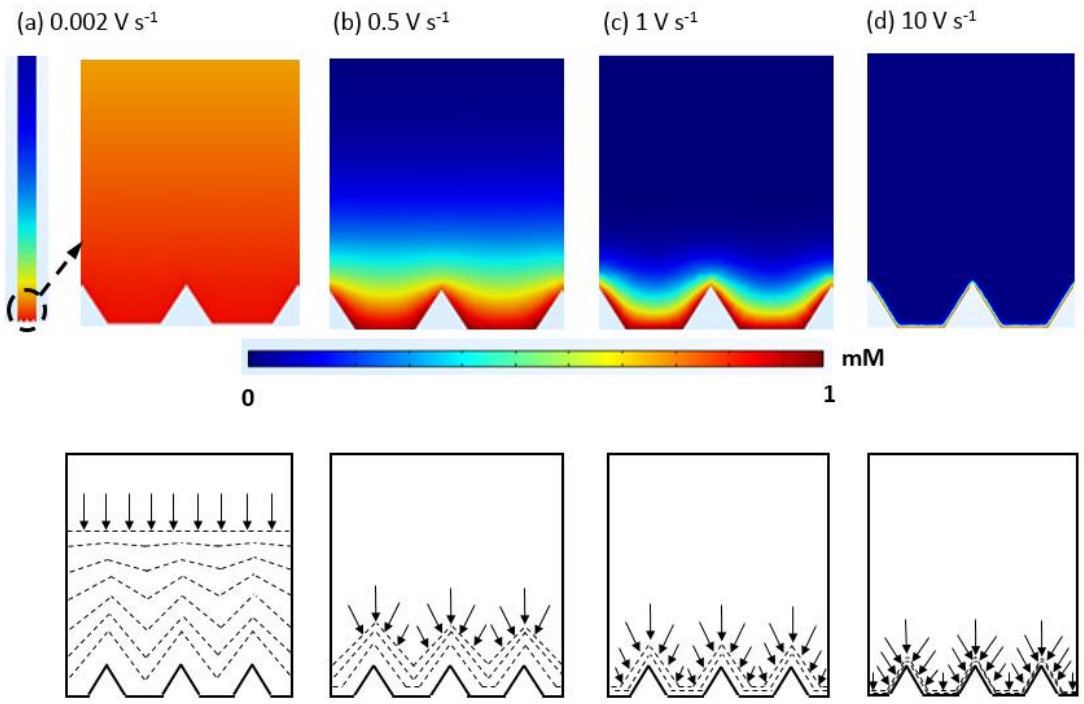

Figure 4.20. Concentration profile of the pyramidal pattern at the peak potential of the simulated CV at potential sweep rates of: (a) 0.002 V s^{-1}, (b) 0.5 V s^{-1}, (c) 1 V s^{-1}, (d) 10 V s^{-1}. For each case, the contour diagram shows the regions with equal concentration (dashed lines) and the direction of redox species diffusion (arrows).

The CVs of patterned and flat electrodes were simulated at a super-high potential sweep rate of 50 V s^{-1}, while the current densities were normalised by the electroactive surface area of each electrode (Figure 4.21). The patterned electrode showed a slightly higher peak current and slightly smaller peak potential than that of a flat electrode. The reason can be explained by plotting the local current density of the patterned electrode at the peak potential (Figure 4.22). The current density was uniform over the patterned electrode except at the tip of the pyramid and along the edge of the base. At the tip, the convergent mass transport of the redox species caused a high current density (akin to the high mass transport to a micro hemi-spherical or microdisc electrode), while at the edge of the base the current density was almost zero as a result of divergent mass transport. The behaviour of the tip and base edge through the CV affected the average of local current density at the surface of the electrode (Figure 4.23). In comparison to the base edge, the tip of the pyramid caused a higher peak which occurred at higher overpotentials. At the base of the electrode, the divergent mass transport of the redox species lowered the current density and causes

the peak current to occur at potentials closer to the reversible potential. This divergent mass transport is similar to that seen for thin-layer electrolyte systems where the peak separation can be much smaller than 59/n mV [371].

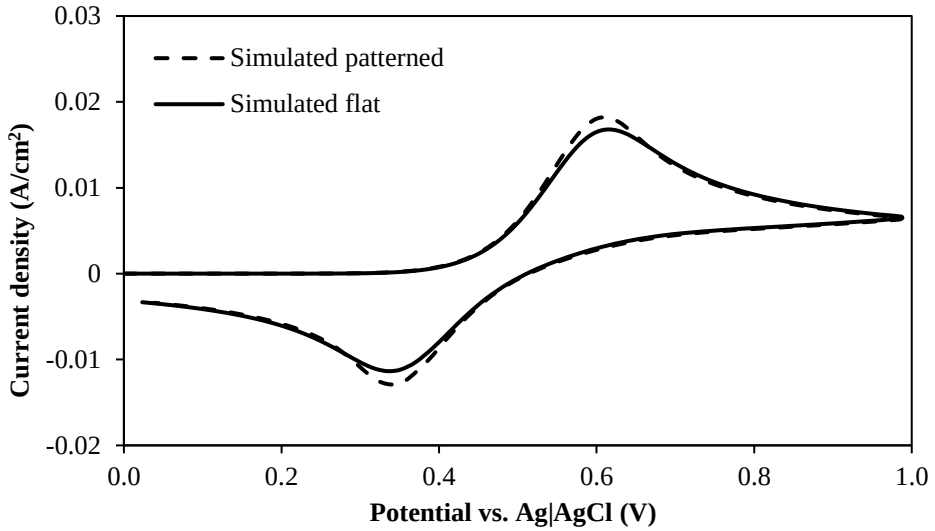

Figure 4.21. Simulated CV of a pyramidal patterned and a flat electrode at potential sweep rate of 50 V s^{-1}. The current was normalised by EASA of each electrode.

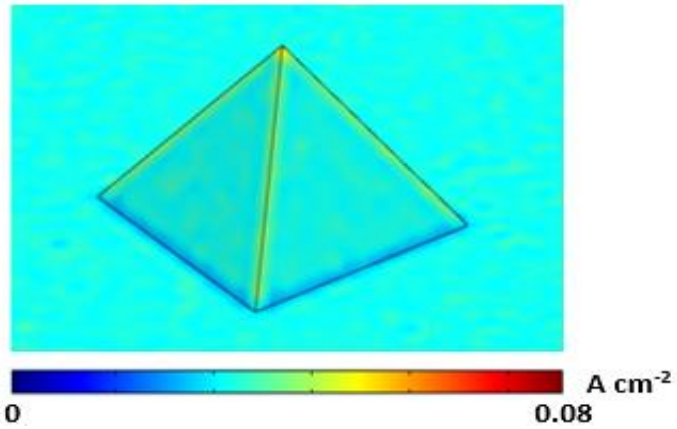

Figure 4.22. The local current density of the pyramidal structure at the peak potential of the simulated CV at potential sweep rate of 50 V s^{-1}; At the tip of the pyramid, the convergent mass transport of the redox species caused a high current density, while at the base edge of pyramids the current density was almost zero as a result of divergent mass transport.

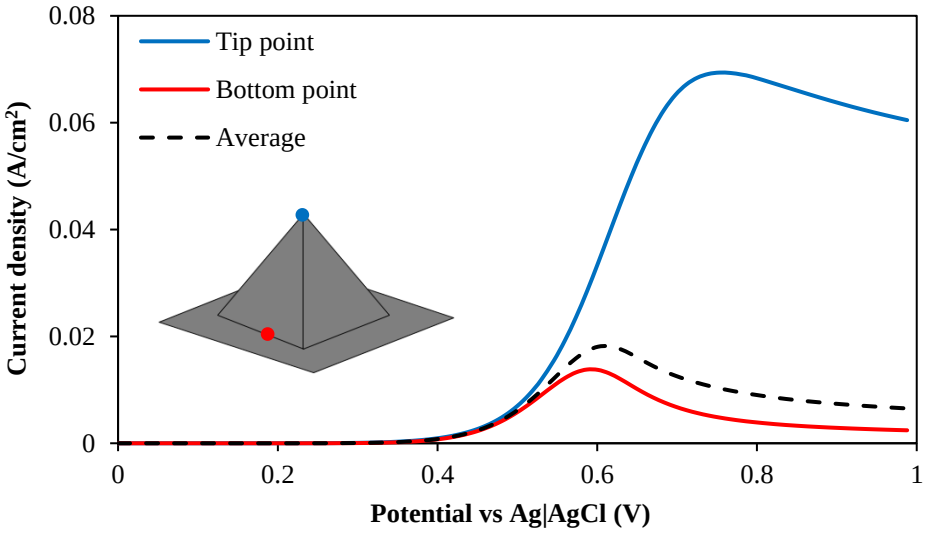

Figure 4.23. The current density at the tip and the base edge of the pyramid and the average current density over the patterned electrode during the simulated CV at potential sweep rate of 50 V s^{-1}. In comparison to the base edge, the tip of the pyramid caused a higher peak which occurred at higher potential.

To confirm that the behaviour of rough electrodes is identical to that of flat electrodes when the sweep rate is high enough that the diffusion layer follows the electrode morphology, a "rough" electrode with smooth features was simulated at 50 V s^{-1} (Figure 4.24). The shape of the roughness was designed to eliminate the divergent and convergent diffusion of redox species to the surface of the electrode. The normal diffusion towards the surface resulted in a uniform concentration profile over the surface of the electrode. In this case, the CV of the patterned electrode, while the current density was normalised by the EASA, was exactly the same as that of a flat electrode (Figure 4.25).

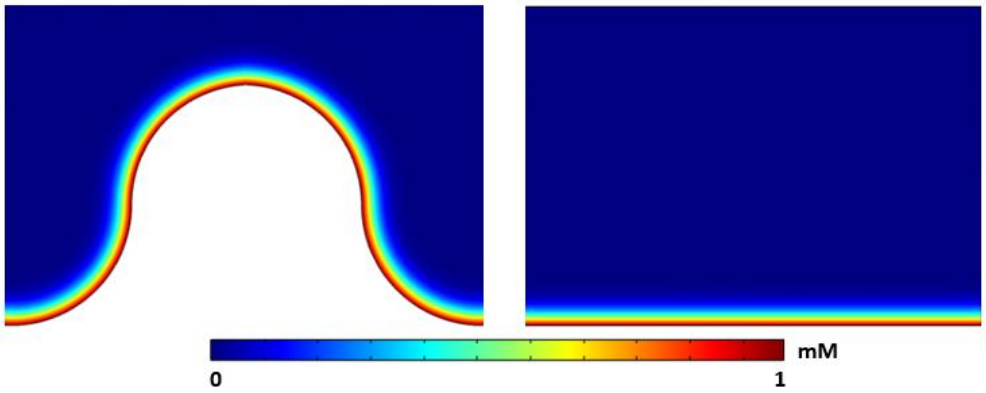

Figure 4.24. The concentration profile of a round and a flat electrode at the peak potential during the simulated CV at potential sweep rate of 50 V s^{-1}. The uniform concentration profile over the round structure caused a normal diffusion of redox species towards the electrode surface.

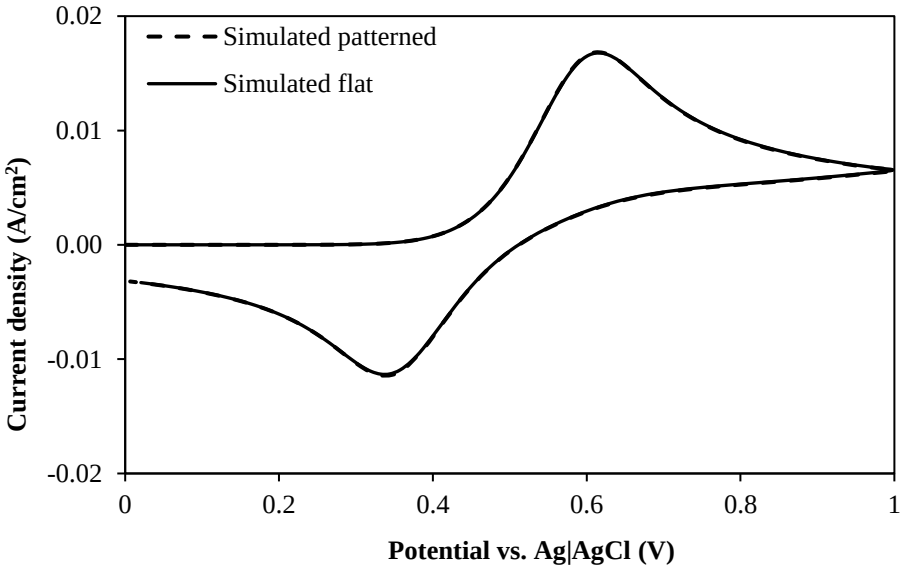

Figure 4.25. Simulated CV of a round and a flat electrode at potential sweep rate of 50 V s^{-1}. The current was normalised by EASA of each electrode.

Surface roughness scale

An electrode's roughness is defined as roughness factor which relates the scale of roughness to the EASA. However, structures with the same roughness factor can have different scales of roughness (Figure 4.26).

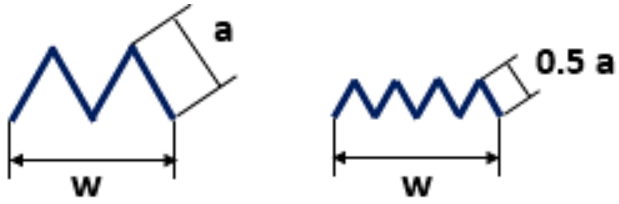

Figure 4.26. Two structures with the same roughness factor (EASA), but with different scales of roughness.

Apart from changing the electrode's EASA, surface roughness affects the concentration profile of the redox species in the electrolyte solution. To focus on the effect of surface roughness scale on redox species mass transfer, the CVs of the patterns with the same EASA (roughness factor) but different scales were numerically modelled in a 2D environment. The concentration profile of three different structures at the peak potential of the simulated CV at potential sweep rate of 1 V s^{-1} is shown in Figure 4.27. When the size of the structure is much smaller than the diffusion layer thickness, the diffusional area is equal to the electrode's projected area. This is similar to a case where CV is run at a slow potential sweep rate. By increasing the scale of the structure, surface roughness had more effect on the redox species concentration profile. This showed that the redox species concentration profile depended on the relative scale of the structure to the diffusion layer thickness [357].

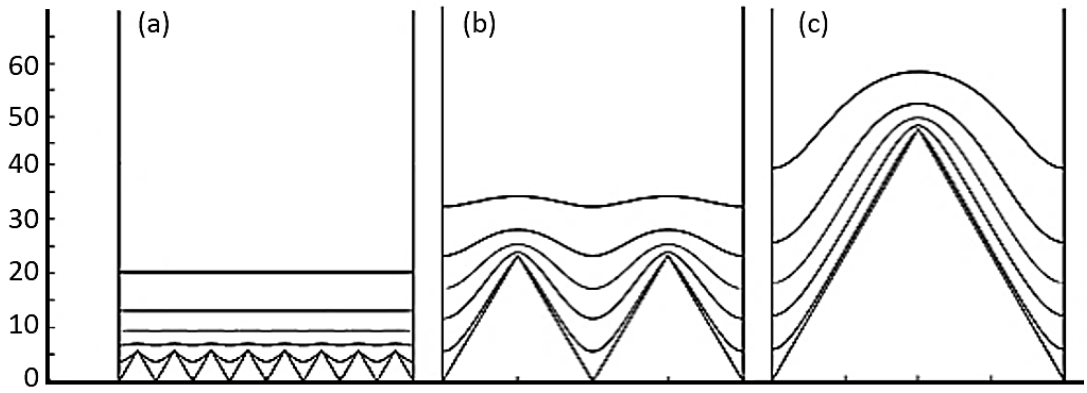

Figure 4.27. Concentration profile at the peak potential of the simulated CV of three electrodes of different sizes but the same EASA at the potential sweep rate of 1V s^{-1}. By increasing the structure's scale from (a) to (c) the surface roughness had increasing effect on the concentration profile of the redox species.

The anodic scan of CV at the potential sweep rate of 1 V s^{-1} was simulated for structures with different heights (Figure 4.28). Due to convergent diffusion, the rate of redox species mass transfer towards the electrode increased according to the height of the structure and resulted in higher current.

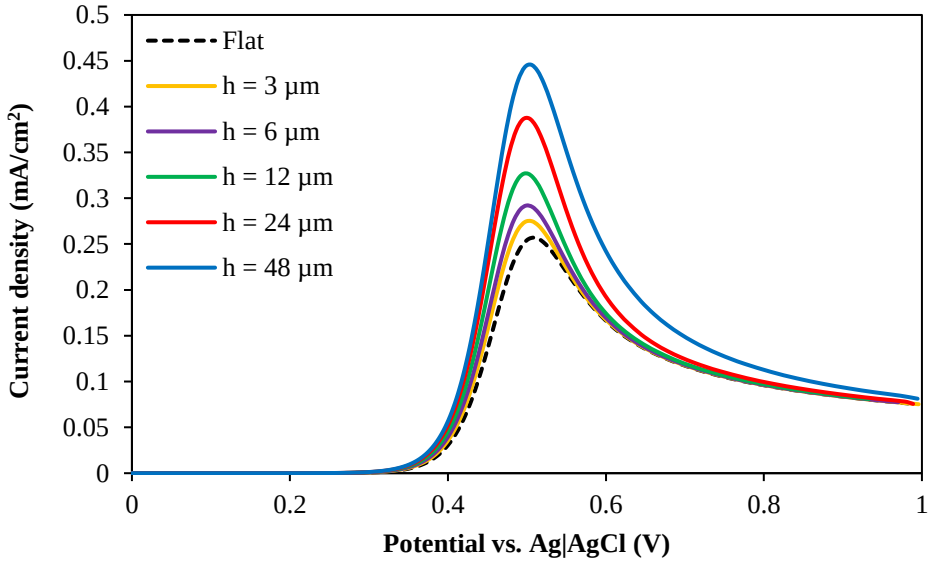

Figure 4.28. The anodic current of simulated CV for electrodes with different scale of structures (h = height of the structure) at potential sweep rate of 1 V s^{-1}.

The change of peak separation by potential sweep rate was measured for each structure (Figure 4.29-a) and was compared with that of a flat electrode (Figure 4.29-b). On a patterned electrode, the area through which the redox species diffuse changes as a function of distance away from the electrode surface. Close to the electrode surface, the diffusional area is large and approaches the true surface area of the electrode, and as a result the flux of the redox species decreases. In this case, the behaviour of the patterned electrode was not uniform along the surface. For example, on a pyramidal structure, the tip of the pyramid was exposed to a high mass transfer of redox species due to convergent diffusion, while the base edges received a small mass transfer. For a small-scale structure (e.g. h = 3 µm), increasing the potential sweep rate caused the peak separation to increase continuously due to lower diffusion layer thickness and higher mass transport of redox species (Figure 4.29-a). In contrast, for a large-scale structure (e.g. h = 24 µm) an increase in the potential sweep rate resulted in a change from a reducing to an increasing peak separation. Using h = 24 µm at potential sweep rate of 0.002 V s^{-1} as an example, the rate in which the diffusional area was changing through the diffusion layer thickness was higher than for a smaller structure, therefore, the electron transfer reaction was limited by the redox species mass transport at lower potential causing a smaller peak separation. By increasing the potential sweep rate up to 10 V s^{-1}, the redox species had even less time to reach the base of the structure, and therefore the peak separation decreased. At sweep rates higher than 10 V s^{-1}, the change of diffusional area along the diffusion layer was lower, and redox species could reach the base of the electrode faster. This resulted in the electron transfer reaction being limited by redox species mass transport at higher potential causing a larger peak separation. Ultimately, at a very high potential sweep rate of 10 V s^{-1}, the whole surface of the electrode was uniformly engaged in the reaction (Figures 4.21 and 4.22) and the structure behaved almost as a flat electrode with an extended EASA.

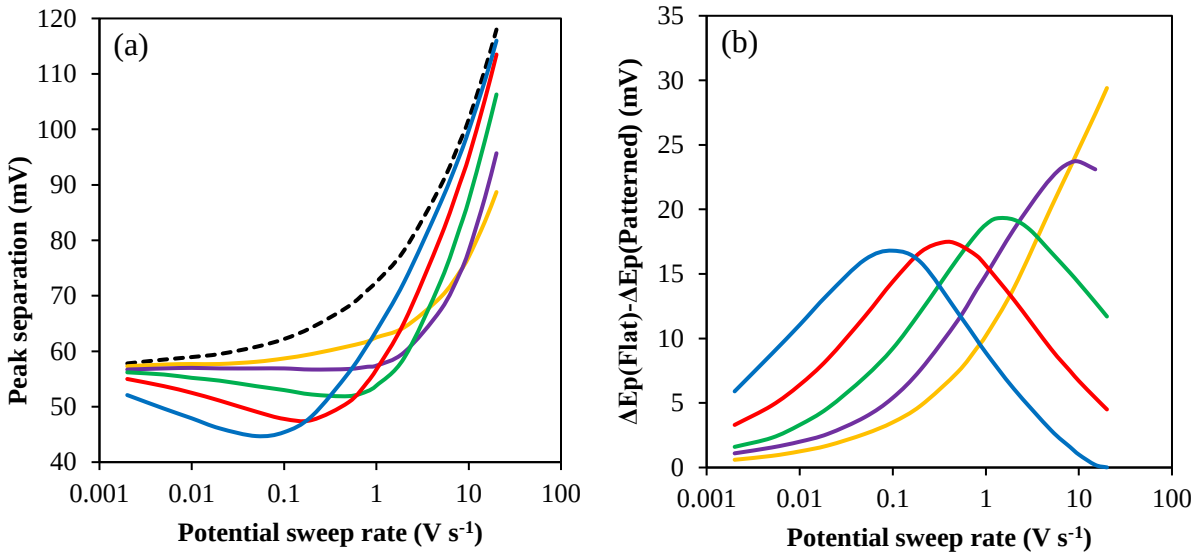

Figure 4.29. (a) The peak separation of patterned structure and (b) the deviation from that of a flat electrode at different potential sweep rates for structures with different sizes (h = height of the structure):
h = 3 µm, h = 6 µm, h = 12 µm, h = 24 µm, h = 48 µm.

The patterned electrode's behaviour at different potential sweep rates depended on the relative magnitude of the diffusion layer thickness to the scale of roughness. To get a better understanding, the peak separation of each structure at a different ratio of height to diffusion layer thickness and its deviation from that of a flat electrode were measured (Figure 4.30). The diffusion layer thickness was approximated by using (Eq. 4.3). At high ratios, the surface roughness had more effect on the electrochemical reaction and there was higher deviation from the flat electrode. However, regardless of the structure's scale, there was a turning point after which the behaviour of a patterned electrode started to approach that of a flat electrode. For all the structures, the turning point occurred at the same ratio (h/δ =0.25).

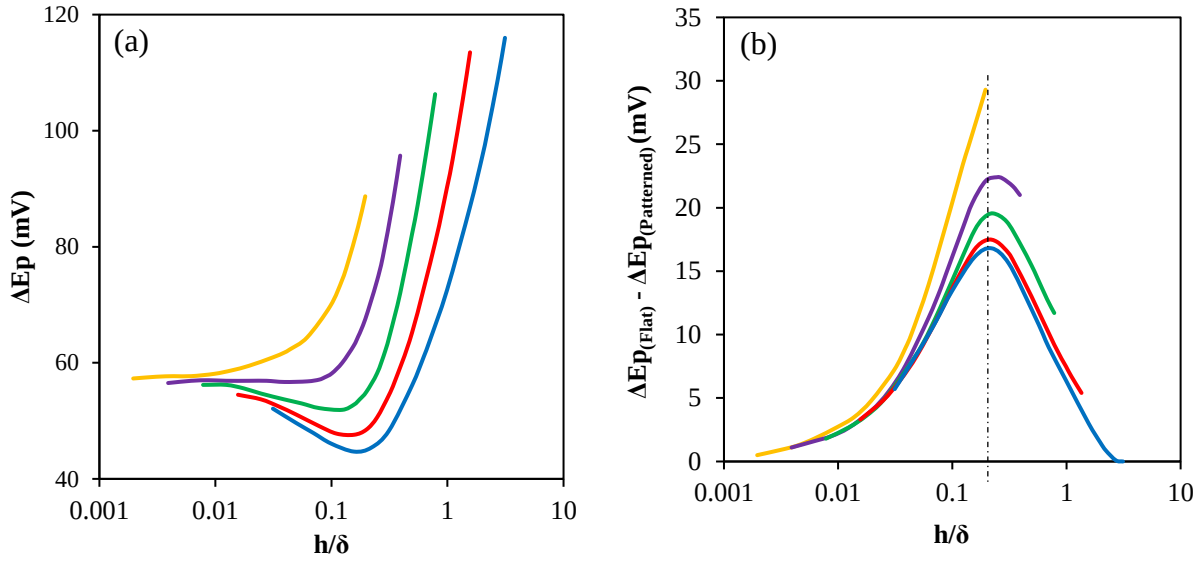

Figure 4.30. (a) The peak separation of patterned structure and (b) the deviation from that of a flat electrode at different ratios of the structure's height (h) to diffusion layer thickness (δ) for structures of different sizes: h = 3 µm, h = 6 µm, h = 12 µm, h = 24 µm, h = 48 µm.

4.5 Conclusion

This part of the study investigated the effect of an electrode's surface morphology on the mass transport behaviour of redox species and how this affected the cyclic voltammetric response. The surface roughness of the electrode was modelled as a regular structure to enable numerical as well as experimental studies. The patterned electrode was prepared by fabricating a periodic pyramidal microstructure (height 5 µm, width 7 µm, periodicity 14 µm) into a UV curable polymer using lithography, and then coating the structure with a 120 nm layer of gold as a conductive layer. The electrochemical behaviour of the patterned electrode was compared with that of a gold-coated flat electrode.

Although the geometrical surface area of the patterned electrode was only 19% higher than the flat electrode, it provided 70% higher EASA than the flat electrode. This suggests that the pyramidal structure affected the nanoscale roughness formed during the gold coating using electron beam evaporation.

The effect of electrode's surface roughness on the electron transfer reaction was studied using CV technique in the presence of 1 mM Fe^{2+}. Along with the experimental results, the CV of the electrodes were analysed using a finite element method (COMSOL software). The simulation was carried out with optimised meshing structure to enhance the accuracy of the results and reduce the calculation time. However, deviation from experimental results was observed due to experimental error such as sensitivity of the system to environmental noise at very low potential sweep rates, and high double layer overpotential at very high potential sweep rates.

The peak separation of a cyclic voltammogram can be used as an estimation for the electrode's EASA. In the reversible state, the peak separation of a patterned electrode is equal to that of a flat electrode (59/n mV) and the CV does not give any information regarding the electrode's surface roughness. The low sweep rate CV on a structure with low roughness results in a reversible condition, and even a 1 μm roughness caused by very poor polishing can give a CV similar to that of a flat electrode.

In quasi-reversible state, surface roughness affected the electron transfer reaction by providing more EASA and changing the redox species mass transfer. The tips of the structure play an important role, as they cause convergent mass transport, and hence much higher current density. If the tips can also enhance the rate of the electron transfer reaction on a photocatalyst, then maximising the number of tips could be a way to promote a photoelectrochemical reaction. However, the tips need to be sufficiently distant from each other to promote convergent mass transport. The enhanced mass transport on a rough electrode can be useful while measuring the rate constant of a fast reaction, which is currently measured by use of micro-disc electrodes [372, 373].

The effect of surface roughness on redox species mass transfer was studied by simulating the CV of structures with different sizes but the same EASA. Surface roughness causes the diffusional area to change within the diffusion layer according to the distance from the electrode; it becomes larger closer to the electrode's surface. In the quasi-reversible state, the change of diffusional area within the diffusion layer causes a nonuniform current density over the electrode surface with it being greater at the tip of the structure and lower at the base. The change in diffusional area is greater when larger structures are used. When the potential sweep rate is high and the whole diffusion layer is affected by the structure, the structure's base would be more accessible for the

redox species. At very high potential sweep rate, the behaviour of a patterned electrode becomes very close to that of a flat electrode with an extended area.

The effect of surface roughness depends on the thickness of the diffusion layer relative to the scale of roughness. To get a better understanding, measurements were made of the peak separation of each structure at different ratios of height to diffusion layer thickness, and of their deviation from that of a flat electrode. At high ratios, the surface roughness had more effect on the electrochemical reaction, and higher deviation from the flat electrode was observed. However, regardless of the structure's scale, there was a potential sweep rate above which the behaviour of a patterned electrode started to approach that of a flat electrode. For all structures, this turning point occurred at the same ratio ($h/\delta = 0.25$). This result could be useful in optimisation of the shape and scale of a rough electrode.

5 Patterning the photoelectrode-electrolyte interface and its effect on the photoactivity of a TiO_2 photoelectrode

5.1 Introduction

The photoelectrode-electrolyte interface of a TiO_2 photoelectrode can be patterned either by fabrication of a structure into the TiO_2 or by coating TiO_2 onto a patterned conductive glass. Various methods to pattern the TiO_2 film have been elaborated in section 2.6. To make a pattern conductive glass, one approach is to deposit the transparent conductive layer on a patterned glass substrate. In previous research [1-3], a patterned glass substrate has been coated with fluorine-doped tin-oxide (FTO) using spray pyrolysis, and then coated with a semiconducting material. The FTO conductive layer can also be patterned by etching/deposition through a hard mask [24, 374–378]. The patterned FTO layer contributes to efficient light harvesting and increases the effective electrode surface area [24, 374, 375, 379–381].

This chapter focuses on patterning the TiO_2 photoelectrode-electrolyte interface by 1) direct fabrication of the pattern into the TiO_2 layer using imprint lithography, and 2) coating a patterned FTO layer with TiO_2 (Figure 5.1). Two methods were used for the direct fabrication of an upright pyramidal microstructure: 1) imprinting a polymer-based paste using a Si master mold, and 2) imprinting an alcohol-based paste using a PDMS master mold. In order to coat TiO_2 onto the patterned FTO glass, a pattern containing micro-holes was fabricated into the FTO conductive layer by using photolithography followed by inductive coupled plasma (ICP) etching. The patterned FTO layer was then coated by TiO_2 using the hydrothermal method. In this method, a micro-hole structure was chosen due to the simplicity of the fabrication process.

The photoelectrochemical behaviour of the patterned photoanode was studied in the presence of a vanadium redox couple, and the results were compared with that of a flat electrode. Due to difficulties with reproducibility of the patterning of the TiO_2 layer by imprint lithography, the photoelectrochemical study of the patterned electrode was conducted only on the photoelectrode with a patterned FTO layer.

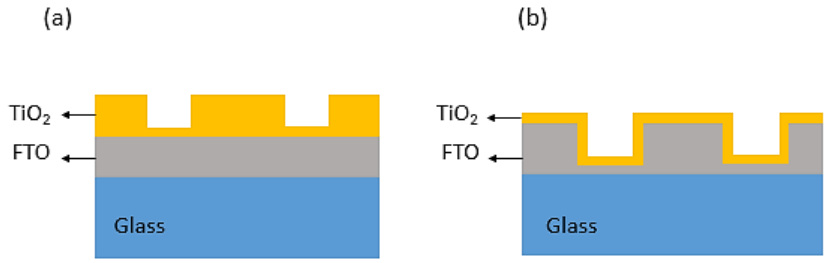

Figure 5.1. Schematic diagram of patterning the TiO_2 photoelectrode-electrolyte interface by (a) direct fabrication of the pattern into the TiO_2 layer, and (b) coating a patterned FTO layer with TiO_2.

5.2 Experimental methods

5.2.1 Imprint lithography on TiO_2 polymer-based paste using a Si master mold

A polymer-based paste was prepared by dispersing commercial TiO_2 powder (P25, Degussa) into a UV curable polymer (Ormostamp). To prepare a paste containing 10 vol% TiO_2 nanoparticles (density of 4.26 g/cm^3), 0.71 g TiO_2 was dispersed in 5 ml isopropanol using 15 min sonication at room temperature. 1 ml dichloromethane was then added to the suspension. 1.5 ml polymer was added to the mixture and the solution was stirred on a hot plate at 50°C until the solvents evaporated.

Imprint lithography was used to transfer a periodic pyramidal microstructure to the TiO_2 paste coated on the conductive side of a commercially available FTO glass (TEC 10, Ossila). For this purpose, a Si master mold containing inverted pyramidal structure with a height and periodicity of 5 µm was prepared as described in section 4.3.2.

The FTO glass substrate was cleaned by successive washing in acetone, methanol, and isopropyl alcohol in an ultrasonic bath. After rinsing with deionised (DI) water and drying with N_2 gas, the substrate was cleaned further using an O_2 plasma asher for 10 min. A small droplet of the paste was placed on top of the master mold and imprinting lithography was performed as described in section 3.2.1. The polymer was cured by exposing the substrate to 405 nm UV light at a dose of 900 mJ/cm^2 using a Karl Suss mask aligner system. UV exposure caused the polymer molecules to link between the TiO_2 particles. This enabled detachment of the Si master mold without

deformation of the structure. The substrate was then heat-treated in the air at 450°C for 3 h at a heating rate of 1°C/min. This heat treatment burned off the polymer and annealed the TiO_2.

Challenges

For KOH etching on a Si wafer, SiO_2 can be used as a hard mask due to the high selectivity of the etchant (refer to section 4.3.2). This works well for etching patterns with small details, but when this approach is used to etch large patterns, the long etching time resulted in undercutting at the SiO_2-Si interface and detachment of the SiO_2 mask. The initial pattern in this study contained squares with a spacing of 5 µm. By considering the etching rate of Si (110), this periodicity is relatively small for the time required to etch pyramids with a height of 5 µm. Therefore, the etching time had to be precisely calculated, and all the steps before KOH etching had to be done perfectly in order to prevent from any interference with the calculated time. In order to achieve this, after developing the exposed photoresist, the substrate was rinsed enough to remove any residue of photoresist, and enough time was provided for HF etching to remove all the SiO_2 layer within the square-shaped openings. This ensured that KOH etching time was not prolonged due to residue of photoresist or SiO_2. To enhance the resistance of photoresist to a longer period of HF etching, it was post-baked for 6 min.

Another factor that can interfere with the calculated etching time is the alignment of photomask edges with crystallographic directions of Si during photolithography. This plays an important role in defining the final fabricated structure [382]. Figure 5.2 illustrates how the alignment of the photo mask during photolithography can affect the shape and arrangement of the fabricated structure. Misalignment of the photomask increases the width of pyramids and reduces the distance between them. This causes total removal of the Si under the SiO_2 layer.

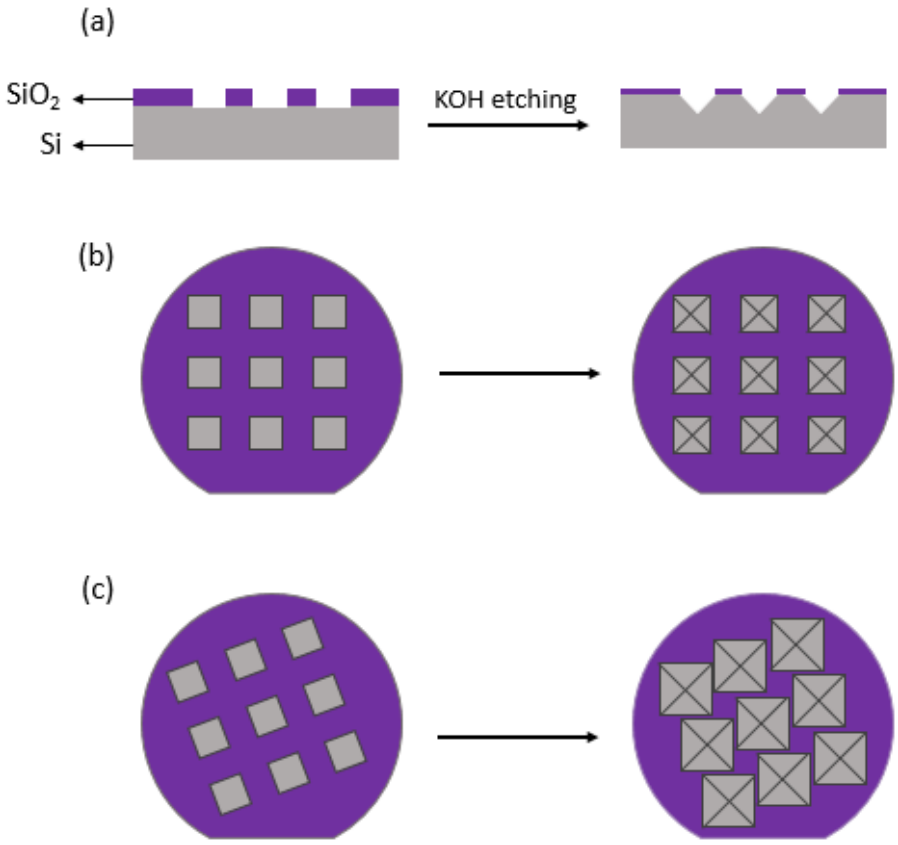

Figure 5.2. Schematic images of the pyramidal structure fabricated into Si wafer after KOH etching: (a) cross-section of the wafer, (b) photomask well-aligned with the Si wafer crystallography, (c) photomask not well-aligned with the Si wafer crystallography. The flat edge on the Si wafer indicates orientation along Si (110).

5.2.2 Imprint lithography on TiO_2 alcohol-based paste using a PDMS master mold

An alcohol-based TiO_2 paste was made by dispersing TiO_2 nanoparticles (P25, Degussa) into α-terpineol. A paste containing 30 vol% TiO_2 was coated on the conductive side of an FTO glass substrate and was patterned by an upright pyramidal structure using imprint lithography. A gas permeable PDMS master mold was used to let the alcohol evaporate.

A double-casting process (Figure 5.3) was used to replicate a PDMS master mold from a Si master mold identical to the one used in section 5.2.1. An anti-sticking layer was coated onto the Si master mold by vapor deposition of a silane (trichloro(*1H, 1H, 2H, 2H*-perfluorooctyl)silane) inside a vacuum desiccator. A mixture containing Sylgard™ 184 A and 184 B with a ratio of 10 to 1 (by

weight) was degassed in a vacuum desiccator for 20 min to remove the air bubbles. It was then poured onto the Si master mold and again degassed. The solution was cured on a hotplate at 80°C for 2 hours and then peeled off. This PDMS layer contained an array of upright pyramids and was used as a mold for the second PDMS casting to form a PDMS layer with inverted pyramidal structure identical to those on the Si master mold. To prevent PDMS-to-PDMS adhesion and to facilitate the demolding process, the PDMS mold was placed in silane vapor in a desiccator for 3 h. Due to the strong hydrophobicity of the PDMS surface, prior to applying the anti-sticking layer, the surface of the PDMS mold was activated by oxygen plasma asher. This promoted silane bonding to the surface [194, 383, 384]. After silane deposition, a PDMS mixture with a ratio of 10 to 1 (by weight) was degassed and then poured on the PDMS mold. This layer was cured, peeled off and cut into 1×1 cm pieces which were then used in patterning the TiO_2 paste.

TiO_2 paste was prepared by the method of Ito *et al.* [154]. 1 ml acetic acid and 1 ml DI water was added to 6 g TiO_2 followed by grinding in a mortar for 5 min. Adsorption of acetic acid on the surface of TiO_2 prevented aggregation of particles. Additionally, because of the presence of water, the surface of TiO_2 was covered by hydroxides which improved the connection between TiO_2 particles and the FTO surface. Three successive 1 ml aliquots of ethanol were then added to the mixture with grinding for 5 min after each addition. The mixture was transferred to a beaker by flushing with additional ethanol and was then sonicated for 15 min at room temperature. 20 mg α-terpineol was added, and the solution was placed on a hot plate at 70°C to remove the ethanol.

The paste was dispersed onto an FTO glass substrate by doctor blading, and the PDMS master mold was gently pressed on it to let the paste fill the pattern by capillary action. To dry the paste, the substrate was heated to 90°C at a rate of 1°C/min and was left at this temperature for 2 h. Heating needed to be slow to prevent bubble formation in the structure. After drying, the PDMS master mold was detached and the substrate was sintered in air at 450°C for 2 h with a heating rate of 1°C/min.

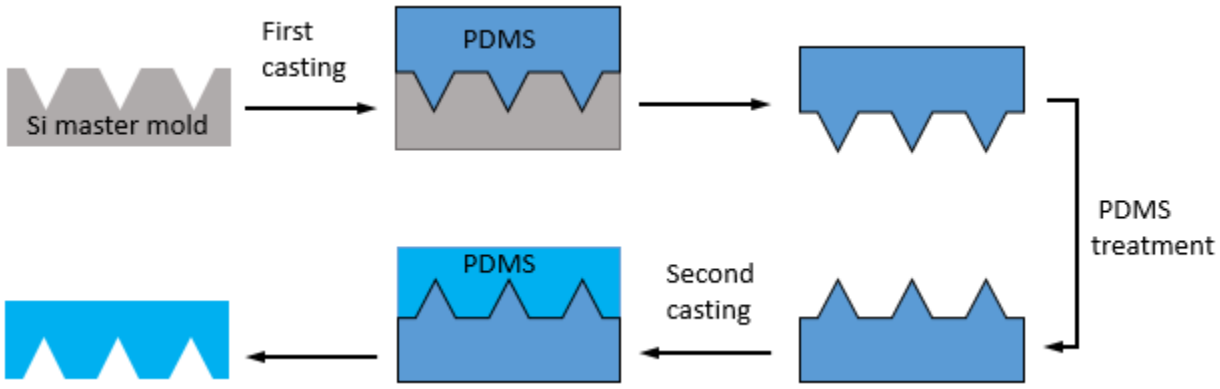

Figure 5.3. Double casting process to fabricate a PDMS master mold containing an inverted pyramidal structure: a Si master mold containing an inverted pyramidal structure was used as a template for the first casting process to form a PDMS layer patterned by an upright pyramidal structure. The surface of this layer was treated and then used as the template for the second casting process.

5.2.3 Patterning the FTO conductive layer

A periodic microstructure was fabricated by photolithography onto the FTO layer of a commercially available FTO glass substrate (600 nm FTO). The FTO glass substrate was cleaned by sonication for 10 min in each of acetone, methanol and isopropanol. It was then rinsed with DI water and blown with N_2 gas. Further cleaning was achieved by use of O_2 plasma asher for 10 min. Hexamethyldisilazane (HMDS) was immediately spin-coated on the substrate at 3000 rpm for 30 s. This layer was used to improve the adhesion between the FTO and the photoresist. A layer of positive photoresist consisting of AZ 1518 was then immediately spin-coated onto the HMDS at 3000 rpm for 60s. The substrate was then soft baked at 90°C for 60 s. The photoresist was exposed to 405 nm UV light at 110 mJ/cm^2 through a chrome mask containing an array of square-shaped openings of 5×5 µm and pitch of 10 µm. The chrome mask was prepared as described in section 4.3.3. The substrate was immersed in AZ 326 MIF developer for 60 s. The exposed part of the photoresist was dissolved leaving an array of holes in this layer. The substrate was then baked on a hot plate at 110°C for 6 min.

The FTO layer was patterned using inductively coupled plasma etching in the presence of Ar gas. During etching, the patterned photoresist acted as a hard mask for the FTO layer. The Ar flow rate was 20 cm^3/min at a pressure of 5 mbar. The high frequency and ICP power were set at 100 W and

1000 W respectively. Etching was at a rate of 240 nm/min for AZ 1518 and 70 nm/min for FTO. After etching, the photoresist layer was lifted off by sonication in acetone for 30 min. This procedure was also tried for AZ 12XT-20PL photoresist (coated at a spinning speed of 4000 rpm for 60 s) as the hard mask, and an etching rate of 65 nm/min was obtained. Due to the similarity of etching rates of FTO and AZ 12XT-20PL, the thickness of the photoresist needed to be greater than the depth of pattern in the substrate.

5.2.4 Hydrothermal synthesis of TiO_2 on patterned FTO

A 1.5 µm layer of TiO_2 was coated on a patterned FTO substrate using hydrothermal deposition. First, the patterned FTO glass substrate was cleaned by sonication for 10 min in each of acetone, methanol, and isopropanol followed by rinsing with DI water and drying under N_2 flow. The substrate was placed in a 25 ml Teflon liner on a larger custom Teflon base. 5.5 ml toluene and 3.5 ml HCl were added into the liner. The liner was transferred to a glovebox where 10 ml $Ti(OBu)_4$ was added to the mixture. The liner was sealed in an autoclave and then placed in an oven at 180°C for 2 h. The autoclave was cooled to room temperature and the substrate was then thoroughly washed with ethanol and dried in air. The TiO_2 layer was calcined in a tube furnace at 450°C for 2 h with a ramp rate of 4°C/min.

5.2.5 Testing the photoactivity of the photoelectrode

The photoelectrochemical efficiency of the fabricated photoelectrode was evaluated in the presence of vanadium in a three-electrode setup (Figure 5.4). The cell consisted of two chambers that were separated by a Nafion 115 membrane. In the negative half-cell, 1 cm^2 of the photoelectrode was in contact with an electrolyte solution of 0.1 M vanadyl sulfate in 0.5 M sulfuric acid, and in the positive half-cell, the Pt counter electrode was in contact with 0.5 M sulfuric acid. The electrolyte was stirred for 30 min before illumination while Ar gas was used to purge O_2 from the solution. During the experiment, Ar gas was continuously flowing over the top of the solution to prevent O_2 from interfering with the redox reaction. The photoelectrode was illuminated using a solar simulator (xenon lamp with AM 1.5 filter) at 100 mW/cm^2. An electro-

mechanical shutter controlled by the potentiostat was placed between the light source and the cell to create chopped illumination; it was closed for 20 s and opened for 20 s repeatedly. Linear sweep voltammetry was conducted at a potential sweep rate of 0.5 mV s^{-1} between potentials of 0 to 0.7 V vs. Ag|AgCl, and the cell current was measured under chopped light conditions.

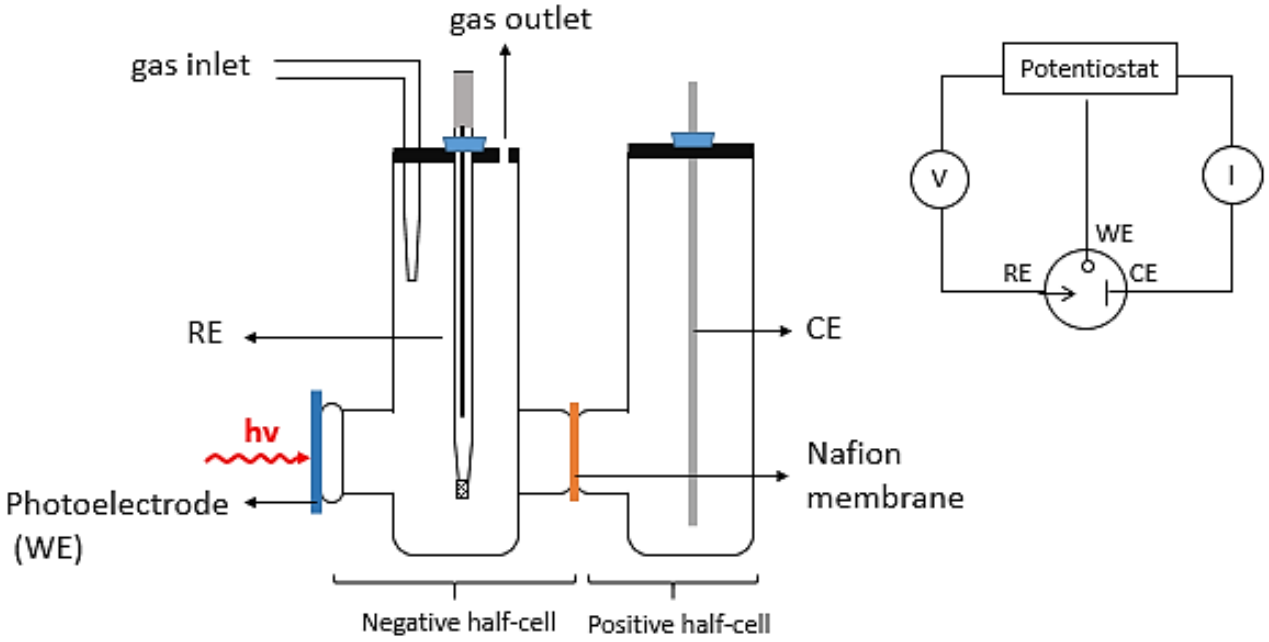

Figure 5.4. The three-electrode setup used for the photoelectrochemistry test, and a diagram showing the connection of the electrodes to the potentiostat; WE = working electrode, RE = reference electrode, CE = counter electrode. The photoactive layer of the photoelectrode (TiO_2) is in contact with the electrolyte, and the glass side of the photoelectrode is illuminated.

5.2.6 Resistivity of flat and patterned FTO measured using a four-point probe

Before coating the TiO_2 layer, the sheet-resistivities of the FTO substrates were measured using the four-point probe method. In this technique, four sharp probes contact the surface of the FTO layer at points that lie in a straight line and are equally spaced (Figure 5.5). Current is passed through the two outer points, and the potential is measured between the inner pair. The four-point probe device was connected to a potentiostat and the current was recorded at different potentials during a linear sweep voltammetry with a potential sweep rate of 0.1 V s^{-1}. In order to use the

potentiostat in a four-point probe technique, the outer probes were connected to Working and Counter leads, which carried the current, and the inner probes were connected to Working Sense and Reference leads, which measured the potential. By using a four-point probe device and running the linear sweep voltammetry the current was measured at different potentials. When the thickness of the conductive layer is much smaller than the probe spacing (s), the sheet resistivity is calculated by the following equation (Eq. 5.1) [385]:

$$R_s = \frac{\rho}{t} = \frac{\pi}{ln\,2}\left(\frac{V}{I}\right) \qquad \text{Eq. 5.1}$$

Where:

R_s is the sheet resistivity (Ω/square),

ρ is the sheet resistivity (Ω.m),

t is the conductive film thickness,

and the other parameters have their usual meaning.

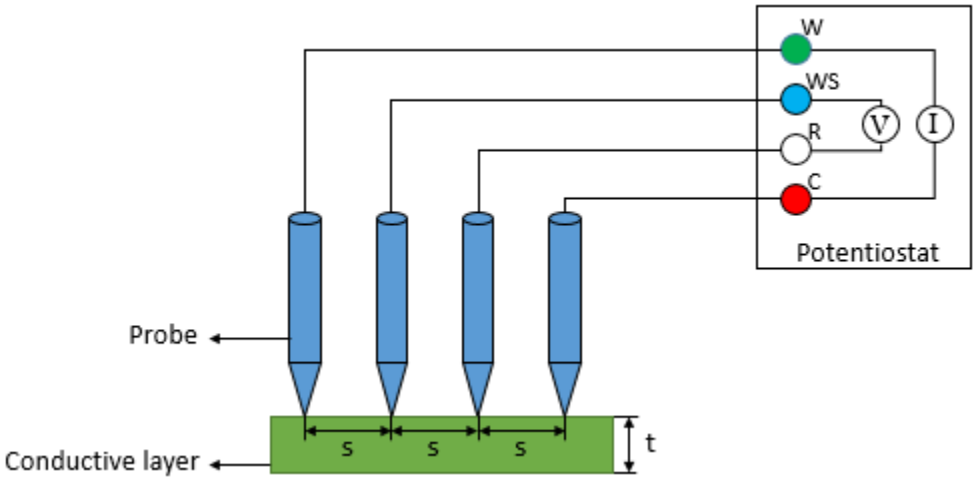

Figure 5.5. Schematic diagram of a four-point probe connected to a potentiostat and used to measure the resistivity of a conductive layer with a thickness of t. The four-point probe consisted of 4 sharp probes that were in a straight line and equally spaced (s). The outer probes were connected to Working (W) and Counter (C) leads, which carry the current, and the inner probes were connected to Working Sense (WS) and Reference (R) leads, which measured the potential.

5.3 Results and discussion

5.3.1 Characterisation of directly fabricated TiO_2 patterned substrates

SEM images showed the effect of photomask alignment with the crystallographic direction of the Si wafer during UV exposure (Figure 5.6). Misalignment between the photomask and the crystallographic direction of the Si wafer (Figure 5.6-a) reduced the distance between the squares. In this configuration, KOH had enough time to remove the whole Si underlying the SiO_2 layer before formation of a full pyramid. In the absence of SiO_2, the Si was removed uniformly from all over the surface and the inverted pyramids did not form. However, upright pyramids appeared when the edges of the neighbouring squares touched. Successful fabrication of a Si master mold containing an array of inverted pyramids (Figure 5.6-b) occurred when the photomask was aligned with the Si wafer crystallographic orientation.

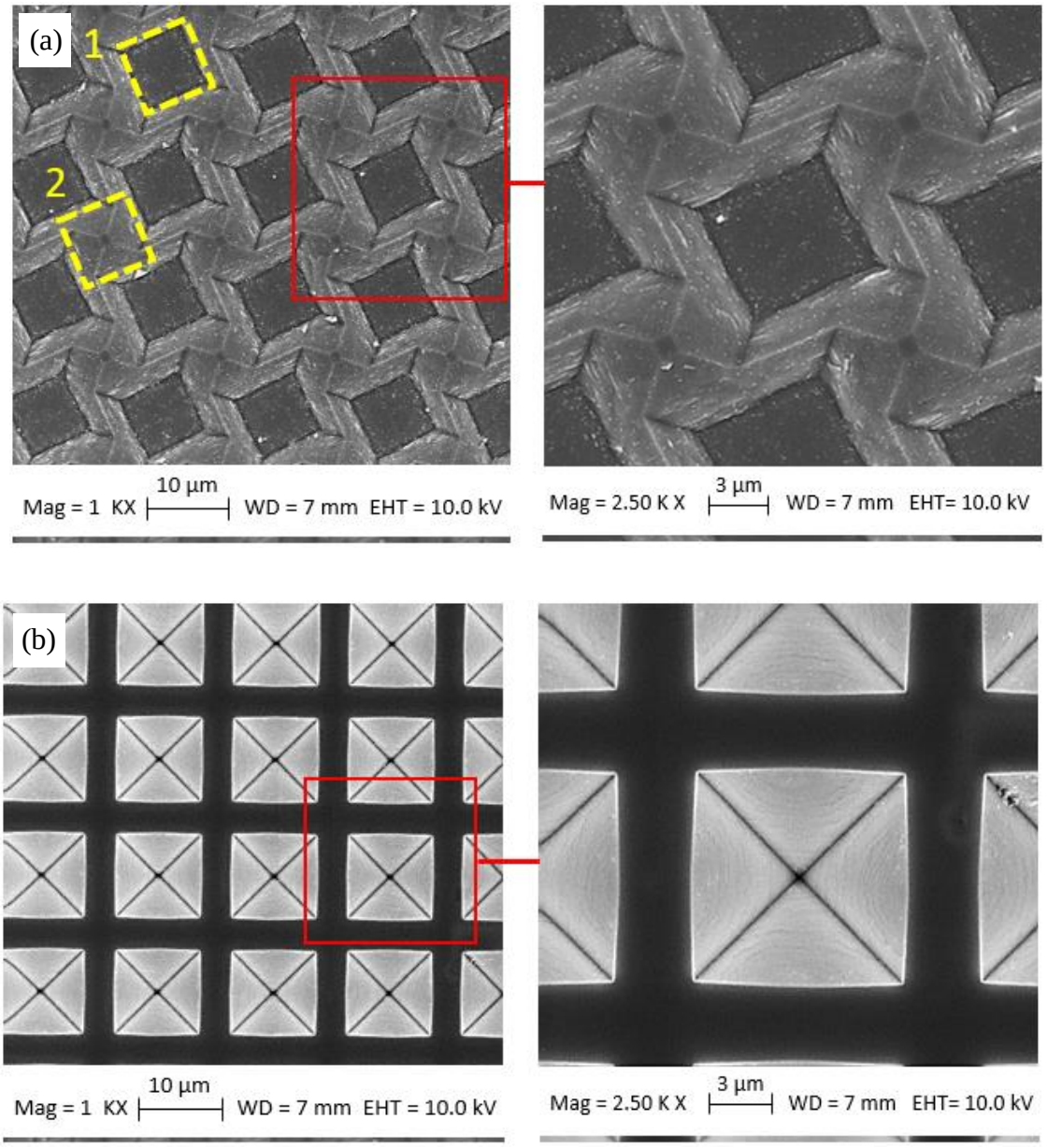

Figure 5.6: SEM image of a Si wafer after KOH etching showing the effect of alignment of the photomask with the crystallographic direction of the Si wafer during UV exposure. (a) Misalignment of the photomask reduced the distance between the openings in SiO_2 and caused sufficient time for KOH to remove the SiO_2 layer. This prevented formation of a full inverted pyramid (the dashed square (1) shows where the inverted pyramid was meant to be). An upright pyramidal shape appeared where neighbouring squares met (indicated by the dashed square (2)). (b) Alignment of the photomask resulted in inverted pyramids with the same pattern as that of the photomask.

The fabricated structure on the PDMS layers after each step of the double casting process were visualised using SEM images (Figure 5.7).

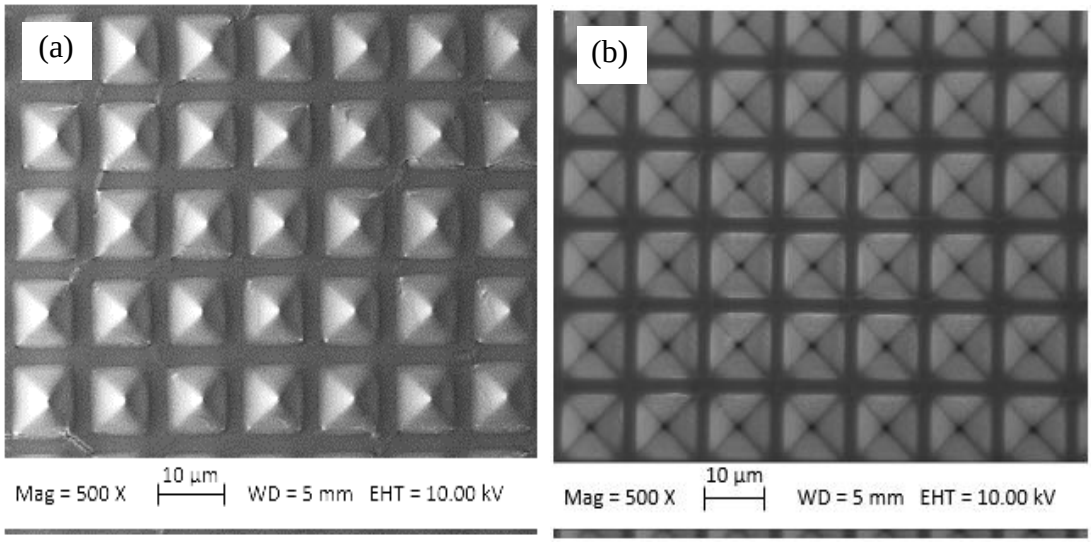

Figure 5.7. SEM images of the fabricated structure at each step of PDMS using the double casting process with a Si master mold containing an inverted pyramidal structure: (a) PDMS master mold containing upright pyramids resulted from the first step of casting which was used as the template for the second step of casting, (b) PDMS master mold containing inverted pyramids resulted from the second step of casting. Magnification of 500X.

SEM images of the TiO_2 patterned with upright pyramids using a polymer-based (Figure 5.8) and an alcohol-based paste (Figure 5.9) were taken before and after annealing. Due to a low percentage of TiO_2 (10 vol%) in the polymer-based structure, burning the polymer and sintering the TiO_2 caused shrinkage of the structure while keeping the pyramidal shape. This issue could be solved by increasing the TiO_2 concentration. However, at higher concentrations of TiO_2, the amount of polymer used was not enough to link between the particles during the UV curing process.

Minimal shrinkage was observed in the alcohol-based structure containing 30 vol% TiO_2. Due to the softness of the PDMS master mold, imprint lithography was performed by application of slight pressure that did not cause structure deformation. This resulted in a very thick continuous layer of

TiO_2 (approx. 10 µm) being formed under the pyramids. In contrast, when using the polymeric paste, the Si wafer was under vacuum during imprinting and as a result the polymeric structure was thinner. Although a thick TiO_2 layer enhances light absorption, if the thickness is higher than the effective UV absorption depth, the excited electron-hole pair undergo volume charge recombination. An absorption depth of 15 µm was reported for P25 TiO_2 coated on an ITO glass substrate using doctor blading and sintered at 450°C for 1 h [386]. However, the effective absorption depth can be much smaller than this value. An optimum thickness of 5 µm was found for photocatalytic activity of a porous film of P25 TiO_2 [387]. The effective absorption of TiO_2 film depends on several parameters such as the size, distribution, crystallinity and abundance of the particles [388].

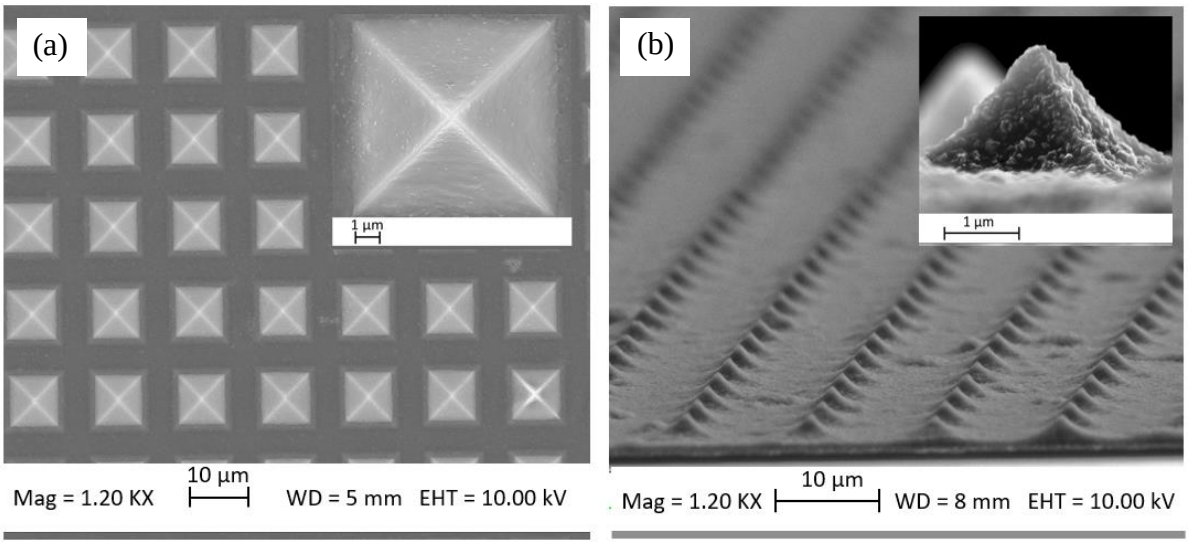

Figure 5.8. SEM image of the upright pyramidal structure fabricated into the polymer-based TiO_2 paste using a Si master mold: (a) before sintering (horizontal substrate), and (b) after sintering (tilted substrate). Magnification of 1200X.

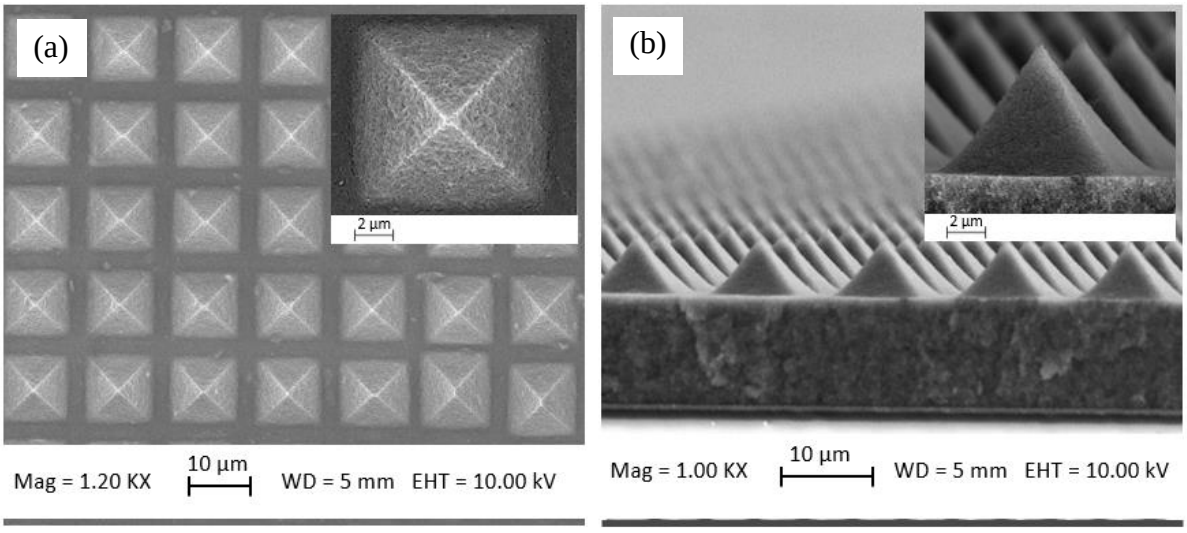

Figure 5.9. SEM image of the upright pyramidal structure fabricated into the alcohol-based TiO_2 paste using PDMS master mold: (a) before sintering (horizontal substrate), and (b) after sintering (tilted substrate). Magnification of 1200X.

5.3.2 Characterisation of patterned FTO coated with TiO_2

The SEM image of the patterned FTO layer showed circular holes with a diameter of 5 µm and depth of 300 nm (Figure 5.10). The patterned FTO was successfully coated with a layer of TiO_2 nanorods with a diameter of less than 0.1 µm (Figure 5.11). The vertically aligned TiO_2 nanorods on the non-etched area of the substrate were denser than those grown in random directions on the etched area. The alignment of TiO_2 nanorods could have a significant effect on light scattering behaviour.

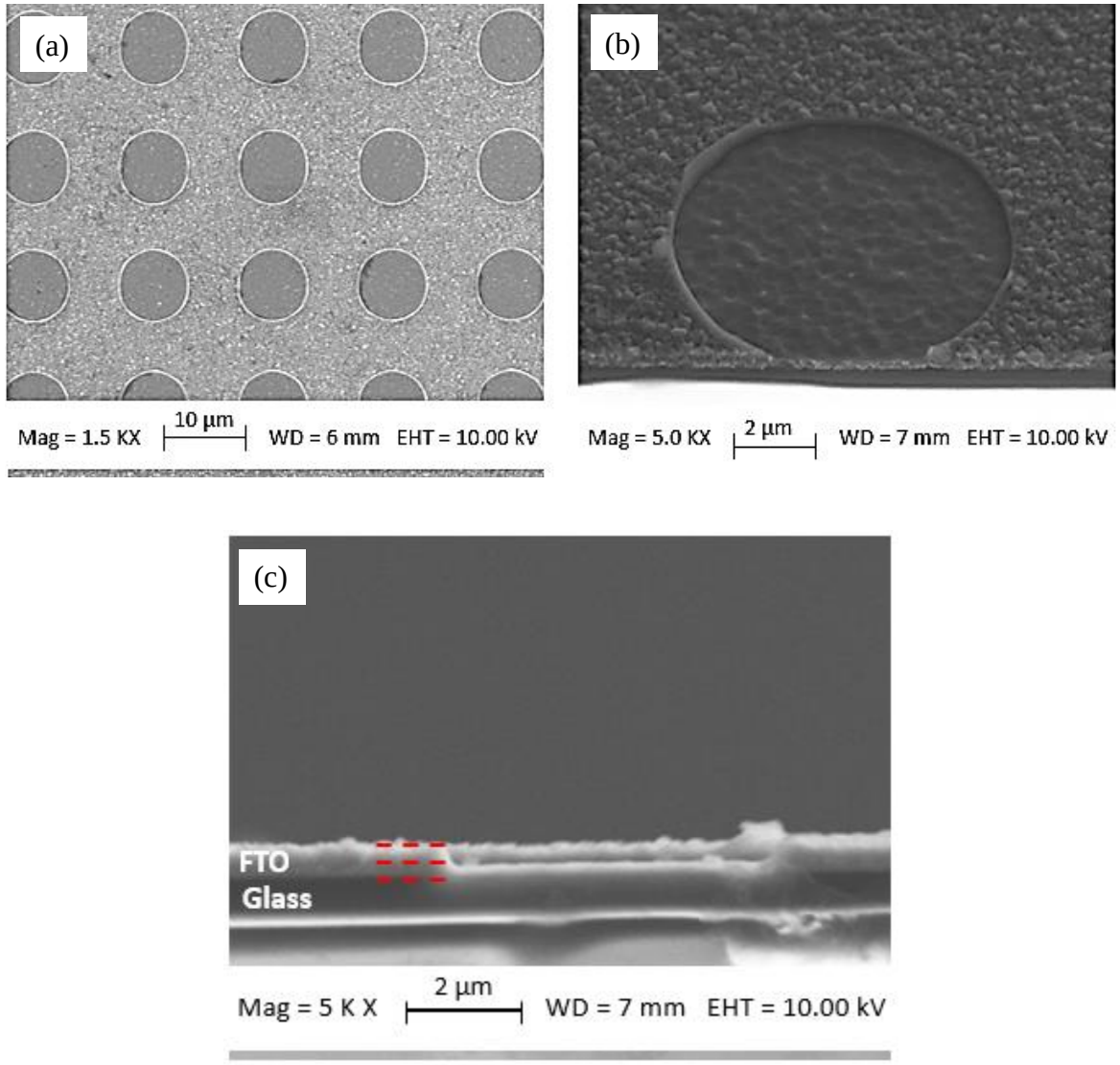

Figure 5.10. SEM images of the FTO substrate patterned by nanoholes using ICP: (a) horizontal substrate at magnification of 1500X, (b) tilted substrate at magnification of 5000X, (c) cross-sectional of substrate at magnification of 5000X showing the thickness of the etched and non-etched part of the FTO using dashed lines.

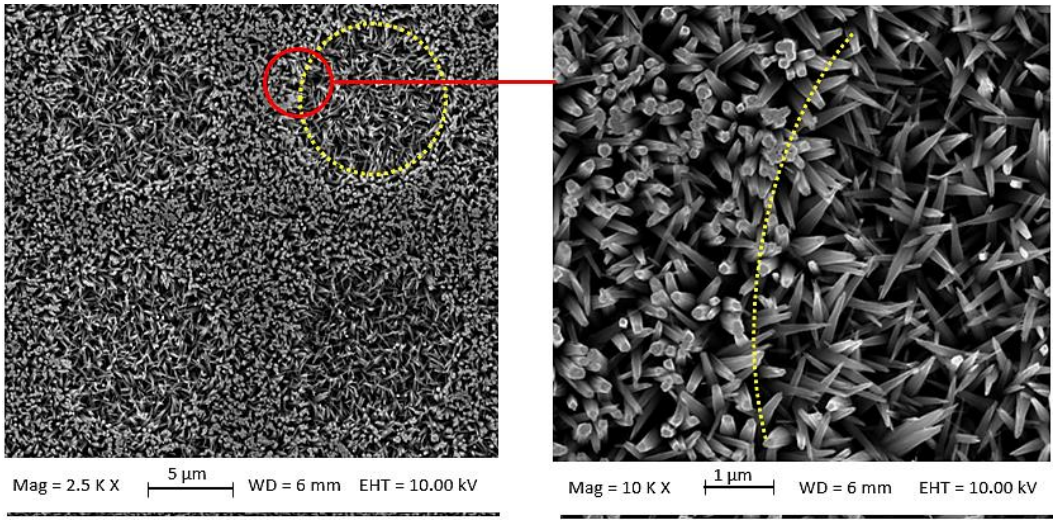

Figure 5.11. SEM image of the TiO_2 nanorods formed on the patterned FTO layer using a hydrothermal method at magnifications of 2500X (left) and 10000X (right). The dashed yellow lines show the border between the etched holes and non-etched part. TiO_2 nanorods were denser on the non-etched part of FTO.

The XRD patterns of the etched and non-etched FTO layers coated by TiO_2 nanorods exhibited strong diffraction peaks at 26°, 36° and 51° from the FTO substrate which has a rutile crystal structure (Figure 5.12) [130, 389]. The small peak at 27° in the patterned substrate could belong to the (110) phase of rutile TiO_2.

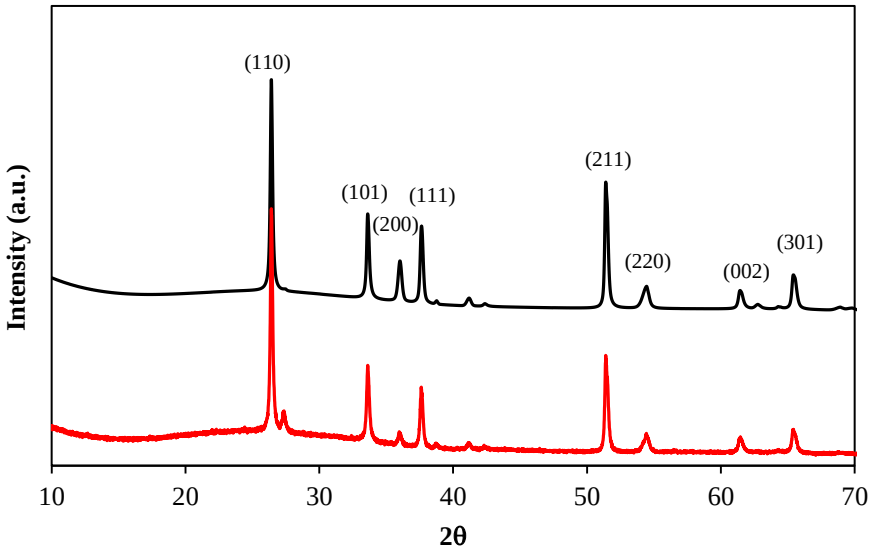

Figure 5.12. XRD diffraction of TiO_2 on FTO for a patterned ━ and flat ━ substrate. The majority of the peaks come from the FTO substrate. The small peak at 27° is from the (110) phase of rutile TiO_2.

5.3.3 Photoelectrochemical behaviour of the patterned photoelectrode

There were some challenges in the study of the photoactivity of photoelectrodes with a patterned semiconductor layer produced using nanoimprint lithography. Reproducibility of the fabricated structure was a major challenge. Photoactivity depended on the thickness of TiO_2. By changing the pressure applied to the master mold during imprint lithography, TiO_2 layers of different thickness were produced. Also, the amount of TiO_2 coated on the surface was not controllable. These reproducibility issues meant that the photoanodic response (which is known to depend on the TiO_2 layer thickness [387]) will be prone to misinterpretations. Therefore, the photoelectrochemical tests were conducted only on photoelectrodes with a patterned FTO layer coated by TiO_2 nanorods using the hydrothermal method. However, the size of the fabricated structure was not large enough to affect the concentration profile of the redox species. Fabrication of larger scale structures required greater thickness of FTO. Efforts were made to increase the thickness of the FTO layer by coating the substrates with further FTO using sol gel and sputtering. These methods failed due to low conductivity of the coatings.

By patterning the FTO layer using ICP etching, some of the conductive material was removed, and this reduced the conductivity of the FTO layer. Therefore, the photoelectrochemical behaviour of the patterned photoelectrode was compared with two flat photoelectrodes with different thicknesses of the FTO layer. The as-received FTO substrates were used as the "flat" surface with a 600 nm FTO layer thickness (flat-600) and a FTO substrate which had half the FTO layer removed by etching – leaving behind a 300 nm thick layer of FTO (flat-300). The thickness of 300 nm was selected as this is the FTO thickness in the region under the patterned TiO_2 (Figure 5.10) and 600 nm is the thickness of the FTO at the non-etched part of the patterned FTO.

Before growing the TiO_2 nanorods, the resistivity of the three FTO glass substrates (patterned, flat-300 and flat-600) were measured by using a four-point probe device and running a linear sweep voltammetry (Figure 5.13). The substrate with the thinnest FTO layer (flat-300) had the highest resistance (43.24 Ω/square), and the substrate with the thickest FTO layer (flat-600) had the lowest resistance (18.54 Ω/square). The resistance of the patterned substrate, which was mostly coated by 600 nm layer of FTO but in some regions was etched to the thickness of 300 nm, lay in between these limits (24.26 Ω/square).

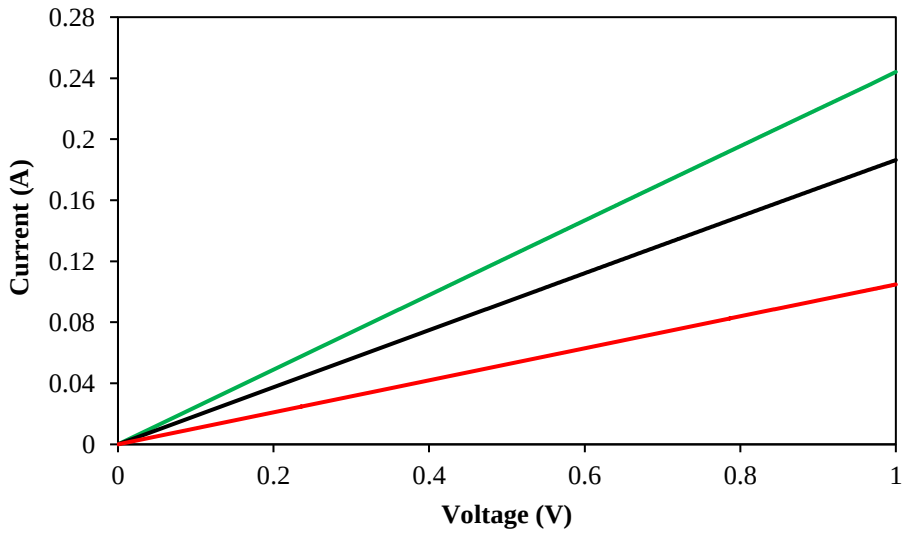

Figure 5.13. Linear sweep voltammetry on a four-point probe device with a potential sweep rate of 0.1 V s^{-1} used to measure the resistivity ($\frac{\text{Voltage}}{\text{Current}}$) of FTO substrates: ━ patterned, ━ flat-300, and ━ flat-600.

The diffraction pattern caused by the periodic microstructure was visualised by illuminating the substrate with laser light with a wavelength of 532 nm (Figure 5.14). As the periodicity of the structure was much larger than light wavelengths in both the visible and UV spectrums, the diffraction pattern would be the same at all wavelengths. Light diffraction affected the path of photons within the semiconductor material. However, the effect of light diffraction on photoelectrochemical behaviour of the fabricated photoelectrode was not evaluated.

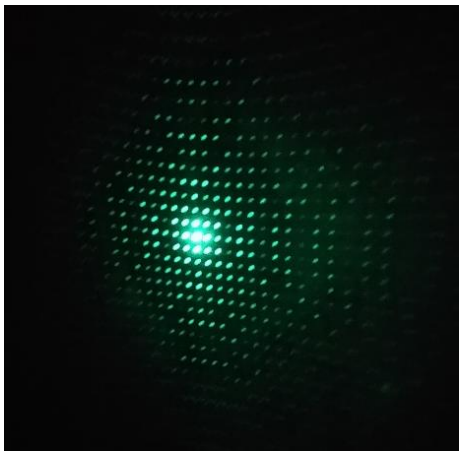

Figure 5.14. Diffracted maxima when the patterned FTO glass was illuminated by laser light ($\lambda = 532$ nm) at a normal angle of incidence.

The photo-response of the patterned photoelectrode was compared with that of a flat-300 (Figure 5.15-a) and a flat-600 (Figure 5.15-b) in a three-electrode setup using linear sweep voltammetry in the presence of V^{4+} ions at a potential sweep rate of 0.5 mV s^{-1} under chopped illumination (20 s dark, 20 s light). In this arrangement, the intention is to photochemically oxidise the V^{4+} when the photoelectrode is illuminated:

$$V^{4+} + \text{hole} \rightarrow V^{5+}$$

By applying a potential higher than the TiO_2 flat band potential, the light-induced electron-hole pairs will drive the photooxidation of V^{4+} to V^{5+} [118]. The flat band potential of rutile and anatase at pH = 0 are respectively -0.155 V and -0.355 V vs. Ag|AgCl [390]. Thus, over the potential range

examined here, an anodic current is expected to occur under light illumination due to photooxidation of V^{4+}, which is what is observed on all electrodes tested above 0.2 V (Figure 5.15).

In addition to this light-induced reaction, the V^{4+} can also undergo a series of electrochemical reactions:

1) $V^{4+} + e^- \rightarrow V^{3+}$ $\quad E^0 = 0.143$ V vs. Ag|AgCl
2) $V^{5+} + e^- \rightarrow V^{4+}$ $\quad E^0 = 0.803$ V vs. Ag|AgCl

The negative current below 0.2 V vs. Ag|AgCl is believed to be the net effect of two redox reaction proceeded in parallel: 1) the reduction of V^{4+} to V^{3+} which is thermodynamically possible below 0.143 V vs. Ag|AgCl, and 2) the photoelectrochemical oxidation of V^{4+} to V^{5+}.

When the photoelectrode is suddenly illuminated, an anodic photocurrent spike attributed to bulk separation of photogenerated electron-hole pairs appeared. Immediately, a photocurrent decay due to surface recombination and/or band-bending decrease occurred until a stationary photocurrent was attained. When the light was switched off, a cathodic spike occurred due to the back reaction of the conduction band electrons with the holes trapped at the surface of the photoelectrode. The sharper spike of patterned photoanode is a sign of higher electron-hole surface recombination and/or decrease in band bending. In this regard, two well-defined regions can be distinguished: 1) below 0.43 V vs. Ag|AgCl, where the small spikes could be attributed to the band-bending decrease due to charge carrier accumulation at the electrode–electrolyte, and 2) at potentials above 0.43 V vs. Ag|AgCl, where sharp spikes could be resulted from surface recombination [391].

Etching the conductive layer reduced the photoactivity of the TiO_2 film. The lowest photoactivity was observed for the electrode with higher etched area (flat-300). There are several parameters that could cause this behaviour such as lower surface concentration of TiO_2 nanorods at the etched area, increased ohmic resistance, and higher charge recombination. Patterning the photoelectrode caused the formation of charge trapping sites which in dark condition improved the electrochemical reaction of the redox species (V^{3+} and V^{5+}) and enhanced the rate of surface charge recombination.

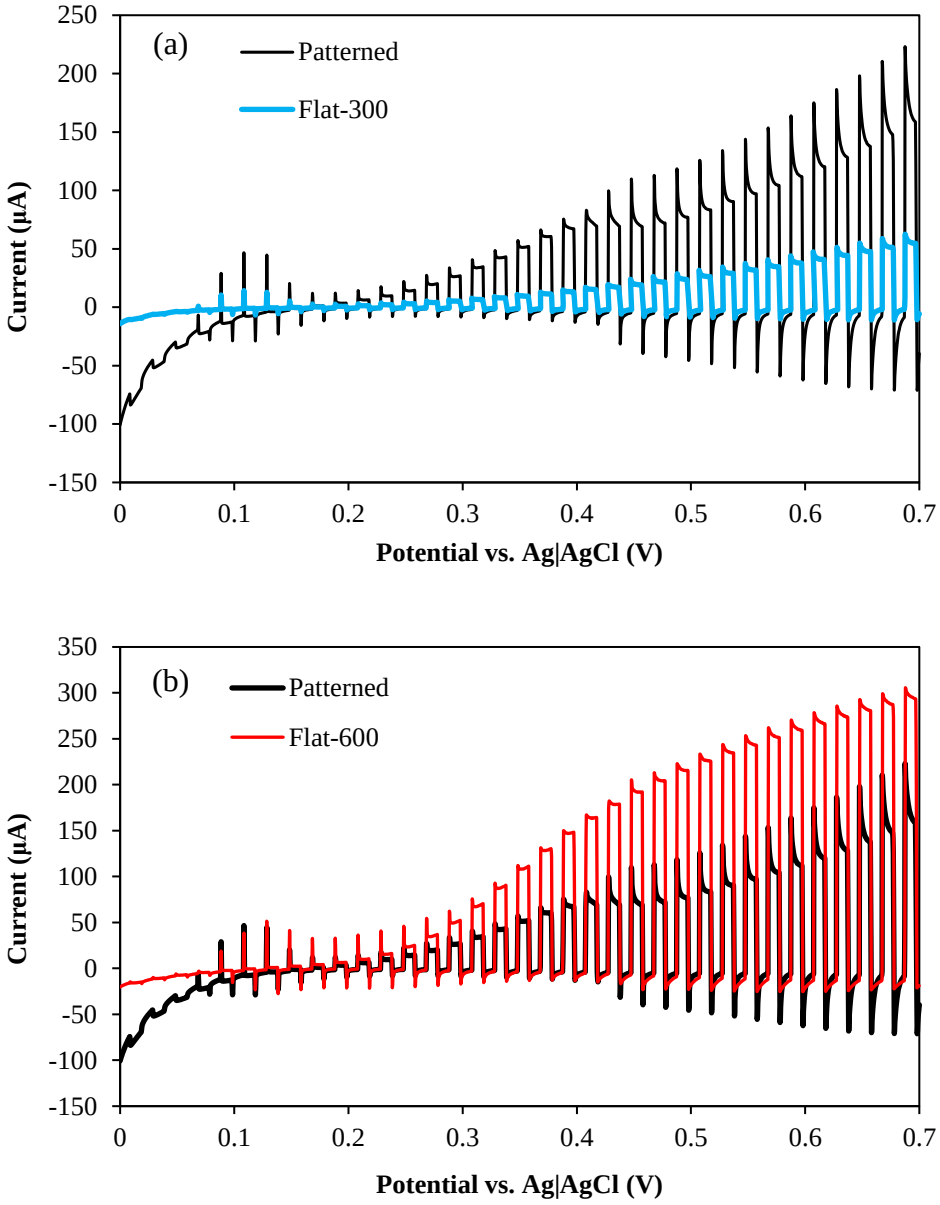

Figure 5.15. Linear sweep voltammetry of a patterned photoelectrode in comparison with: (a) flat-300 photoelectrode, and (b) flat-600 photoelectrode, at a potential sweep rate of 0.5 mV s^{-1} under chopped illumination (20 s dark and light intervals) using a solar simulator at 100 mW/cm^2.

5.4 Conclusion

The semiconductor side of the photoelectrode was patterned by 1) fabrication of a structure into the TiO_2 layer, and 2) coating the TiO_2 layer on a patterned substrate. A pyramidal structure was formed into the TiO_2 layer using imprint lithography on both alcohol-based and polymer-based pastes.

The polymer-based paste was a solution containing 10 vol% TiO_2 dispersed into a UV curable (Ormostamp). The paste was patterned using a Si master mold and was cured by UV light exposure. Due to low concentration of TiO_2, annealing caused the structure to greatly shrink whilst still maintaining the pyramidal form. At higher concentrations of TiO_2, the polymer molecule could not link between TiO_2 particles. The alcohol-based polymer was made by dispersing TiO_2 into α-terpineol. Imprint lithography was performed using a gas permeable master mold (PDMS) that let the alcohol evaporate. In this approach, a solution with a concentration of 30 vol% TiO_2 produced a pyramidal structure with minimal shrinkage during the annealing process. Imprinting the alcohol-based paste required precise control of temperature and pressure to prevent bubble formation (Figure 5.16), therefore, it was much slower to imprint using the alcohol than the polymer-based paste. The alcohol-based structure was 10 times thicker than that based on polymer. This is because the soft PDMS master mold was not exposed to high external pressure as it could cause structural deformation, while for the polymeric paste, the Si wafer was under a vacuum during the imprinting process.

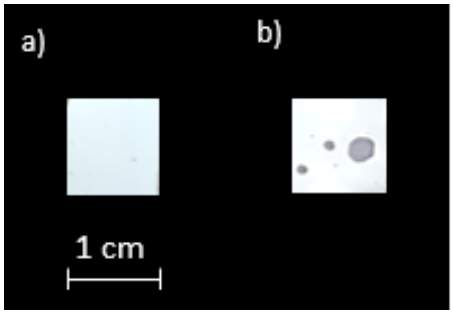

Figure 5.16. Patterned TiO_2 layer coated over 1 cm^2 of an FTO glass substrate using: (a) polymer-based solvent, (b) alcohol-based solvent. The polymer-based paste resulted in a uniform layer over the substrate whilst the alcohol-based film was damaged due to bubble formation during solvent evaporation. A black background has been placed around the photographs of the TiO_2 films for clarity purposes.

To coat the TiO_2 layer on a patterned substrate, the FTO layer of a commercially available FTO glass substrate was patterned with an array of holes (diameter 5 μm, pitch 10 μm, depth 300 nm) using photolithography followed by ICP etching in the presence of argon gas. The FTO substrate was then coated by a layer of TiO_2 by hydrothermal deposition. The TiO_2 nanorods on the non-etched area of the substrate were vertically aligned and had a denser structure than those grown in random directions on the etched area. The alignment of TiO_2 nanorods could have a significant effect on light scattering behaviour.

Due to a reproducibility issue of patterning the TiO_2 layer by imprint lithography, the photoelectrochemical study of the patterned electrode was only conducted on the photoelectrode with a patterned FTO layer. The photoactivity of the patterned photoelectrode was studied during photo-oxidation of V^{4+} in a three-electrode setup while linear sweep voltammetry was performed at a potential sweep rate of 0.5 mV s^{-1} under chopped illumination (20 s dark, 20 s light) using a solar simulator at 100 mW/cm^2. The photo-response of the patterned photoelectrode was compared with two flat photoelectrodes, one with a 300 nm thick FTO layer (equal to the thickness of patterned FTO in the etched part) and the other with 600 nm thick FTO layer (equal to the thickness of patterned FTO in the non-etched part). Patterning the conductive layer affected the photoelectrode in several ways:

1) The periodicity of the fabricated structure was greater than the light wavelength and, as a result, it diffracted light into several beams. Therefore, the path length of photons was changed within the semiconductor layer of the patterned photoelectrode.
2) Removing FTO by etching increased the electrical resistivity of the current collector (FTO) which, as a consequence, increased the ohmic overpotential of the substrate.
3) Etching the FTO affected the alignment and the concentration of TiO_2 nanorods, and this affected the photoactivity of the TiO_2 layer.

The measured photocurrent was affected by all of these factors but the contribution of each was not studied. Overall, etching the FTO layer had a negative effect on the photoactivity of the fabricated electrodes and, by increasing the etched area lower photocurrents were obtained. In addition, patterning the FTO layer caused the formation of charge trapping sites and enhanced the charge recombination rate.

6 Conclusion and recommendations

The integration of a TiO_2 photoelectrode into a redox flow battery (RFB) for a direct solar charging of the battery requires overcoming the challenges of: 1) large band gap of TiO_2 which requires the absorption of ultraviolet photons ($\lambda < 400$ nm), and 2) rapid recombination of photo-generated charge carriers within the TiO_2 layer. This study has focused on improving the photoactivity of a TiO_2 photoelectrode in the UV spectrum using controlled nano-/micro-structures. The TiO_2 photoelectrode consisted of three layers: a glass base, a conductive fluorine-doped tin-oxide (FTO) layer, and a photoactive TiO_2 layer. Each of these layers was patterned with a periodic nano-/micro-structure and its effects on the photoactivity of TiO_2 were described.

This chapter presents the main conclusions of the experimental and numerical studies. Some suggestions are presented to direct future research in this field.

Main outcomes

The behaviour of photoelectrodes can be improved by reducing the losses of light due to: 1) reflection from the surface, 2) absorption within the inactive layers, and 3) transmission through the photoactive layer. By adding surface patterning to the photoelectrode, the behaviour of the light within the photoelectrode can be altered to reduce these losses.

Light behaviour was studied on a glass substrate patterned by a periodic pyramidal nanostructure with a periodicity of 670 nm. The pyramidal structure was initially fabricated onto a Si wafer using LIL followed by a multi-step etching. Then, nanoimprint lithography was employed to transfer the pattern to a glass-like UV curable polymer coated on a glass substrate. The light behaviour was evaluated by a numerical study based on the Finite-Difference Time-Domain method.

The effect of the periodic nanostructure on light behaviour was wavelength dependant. At wavelengths smaller than the periodicity of the structure ($\lambda < 670$ nm), the light was diffracted, while at wavelengths higher than the periodicity ($\lambda > 670$ nm), the structure acted as a homogenous medium without causing light diffraction. Light diffraction increased the light path length within the substrate, which consequently caused more light absorption. The photoactivity of the

photoelectrode was improved by reducing the light absorption within the inactive layers and maximising the absorption within the TiO_2 layer.

Over the whole wavelength range, the periodic nanostructure reduced light reflection from the glass surface by causing a gradual change of refractive index from the air to the substrate. Higher anti-reflection behaviour was observed at wavelengths greater than the periodicity of the structure. Considerable light was also reflected from the glass-FTO and FTO-TiO_2 interfaces. The light reflected from these interfaces were in different phases which, at some wavelengths, resulted in destructive interference leading to fluctuations in reflection and transmission. At some wavelengths, the periodic nanostructure resulted in greater overall reflection. Therefore, fabrication of nanostructure at the other interfaces can improve light harvesting. However, patterning each of the interfaces requires a trade-off between reduced light reflection and increased light absorption within the inactive layers. To study the effect of a patterned optical window on TiO_2 photoactivity, a patterned FTO glass was coated by a layer of TiO_2. The photoactivity of TiO_2 was assessed by measuring photodecomposition of MB at a wavelength of 365 nm. The rate of MB photodecomposition on the patterned substrate was 1.75 times higher than that on the flat substrate. This difference was due to reduced light reflection and prolongation of the path of photons within the TiO_2 layer. The path length was affected by light diffraction caused by the periodic structure and by light scattering from the surface of the TiO_2 particles, but the effects of diffraction and scattering could not be distinguished.

There is a very short period in which photo-generated charge carriers can undergo the electron transfer reaction before charge recombination. Therefore, effective photon absorption within the TiO_2 layer occurs at the vicinity of the electrode-electrolyte interface. This limits the thickness of the TiO_2 layer and the absorption of photons. This issue can be addressed by patterning the TiO_2 with a structure that provides a long dimension for light absorption while requiring the charge carriers to cover a short distance to the acceptor species. This patterning would also influence the transport phenomena at the electrode-electrolyte interface. A model system was developed to separate the influence of patterning on the light/charge carrier behaviour in the photoelectrode material from the influence of the pattern on the transport of redox species at the electrode-electrolyte interface. This involved using both numerical and experimental cyclic voltammetry (CV) on a patterned gold electrode to investigate how patterning the electrode-electrolyte interface

affects the kinetics of a redox couple in the electrolyte. To prepare a patterned gold electrode, a pyramidal structure with a height of 5 μm was initially fabricated onto a Si wafer using photolithography followed by KOH etching. This pattern was then imprinted into a UV curable polymer coated on a glass substrate. After curing, this was coated by a 120 nm layer of gold. During CV, the fabricated structure affected the electrochemical reaction by providing more electroactive surface area (EASA) and changing the mass transfer rate of the redox species towards the electrode. These effects were dependant on the applied potential sweep rate which defines the thickness of the diffusion layer and the reversibility state of the reaction. The effect of EASA was evaluated by measuring the peak separation of the cyclic voltammogram. In a reversible state, the rate of electron transfer reaction is limited by mass transfer and higher EASA does not affect the CV. Low potential sweep rate up to 0.02 V s^{-1} resulted in a reversible condition and the CV did not give any information regarding the electrode's surface roughness. Therefore, slight roughness resulting from poor polishing can give a peak separation similar to that of a flat electrode.

In the quasi-reversible state, surface roughness affected the electron transfer reaction by providing more EASA and changing the redox species mass transfer. The patterned structure caused a nonuniform current density over the electrode surface. The tips of the structure caused a convergent mass transport, and hence much higher current density, while the base of the structure was less accessible for the redox species which resulted in a low current density. Therefore, maximising the number of tips could be a way to promote an electrochemical reaction and also a photoelectrochemical reaction, but the tips need to be sufficiently distant from each other to promote convergent mass transport. The enhanced mass transport caused by the tips could also be a useful method to facilitate the measurement of the rate constant of fast reactions.

The effect of patterning the electrode-electrolyte interface on the mass transfer rate of redox species was specified by numerical study of structures with the same EASA but with different ratios of height to diffusion layer thickness. At high ratios, the surface roughness had more effect on the electrochemical reaction, and higher deviation from the flat electrode was observed. The deviation from the flat electrode occurred because of the patterned structure affecting the diffusion layer. Surface roughness causes the area through which the redox couple diffuses to change as a function of distance from the electrode. It becomes larger closer to the electrode's surface. Regardless of the structure's size, there was a potential sweep rate above which the behaviour of

a patterned electrode started to approach that of a flat electrode. For all structures, this potential sweep rate occurred at the same ratio (h/δ =0.25).

Understanding the effect of surface roughness on redox species concentration profile within the diffusion layer is important when using cyclic voltammetry to extract kinetic information from rough electrodes. The standard Nicholson method is only applicable for a one-dimensional diffusion of redox species towards a planar electrode and clearly cannot be used at a low ratio of height to diffusion layer thickness where the diffusion of redox species is convergent. At high h/δ, the base of the structure would be more accessible for the redox species and the behaviour of a patterned electrode becomes very close to that of a flat electrode with an extended area. This result could be useful to optimise the shape and scale of a rough electrode.

Two approaches were employed to pattern the photoelectrode-electrolyte interface: 1) direct fabrication of the pattern into the TiO_2 layer using imprint lithography, and 2) coating the TiO_2 layer onto a patterned FTO glass. Imprint lithography was employed to fabricate a pyramidal structure into both alcohol-based and polymer-based pastes. The polymer-based paste was a solution containing 10 vol% TiO_2 dispersed into a UV curable polymer. The paste was patterned using a Si master mold and was cured by UV light exposure. Due to low concentration of TiO_2, annealing caused the structure to greatly shrink. At higher concentrations of TiO_2, the polymer molecule could not link between TiO_2 particles. The alcohol-based polymer was made by dispersing TiO_2 into α-terpineol. Imprint lithography was performed using a gas permeable PDMS master mold that let the alcohol evaporate while the mold was held in place. In this approach, a solution with the concentration of 30 vol% TiO_2 produced a pyramidal structure with minimal shrinkage during the annealing process. Imprinting the alcohol paste was much slower than that of the polymer-based paste and required precise control of temperature and pressure to prevent bubble formation. The overall thickness of the alcohol-based structure was 10 times greater than the polymer-based structure. This is because the soft PDMS master mold was not exposed to high external pressure as this could have caused structure deformation, while for the polymeric paste, the Si wafer was under vacuum during imprinting. Imprinting lithography on the polymer-based paste resulted in a higher throughput and a more uniform layer over the whole area of the substrate. In addition, after curing, the polymer formed a strong bond between the particles which is beneficial for the fabrication of a variety of structures with different height and aspect ratio.

To coat the TiO_2 layer on a patterned substrate, a commercially available FTO glass substrate was patterned with an array of holes (diameter 5 μm, pitch 10 μm, depth 300 nm) using photolithography followed by ICP etching in the presence of argon gas. The FTO substrate was then coated with a layer of TiO_2 using hydrothermal deposition.

Due to difficulties with reproducibility when patterning the TiO_2 layer using imprint lithography, the photoelectrochemical study of the patterned electrode was conducted only on the photoelectrode with a patterned FTO layer. The photoactivity of the patterned photoelectrode was studied during photo-oxidation of V^{4+} in a three-electrode setup during linear sweep voltammetry under chopped illumination using a solar simulator at 100 mW/cm^2. Patterning the conductive layer affected the photoelectrochemical results in different ways. The fabricated structure had a periodicity greater than the light wavelength, and hence affected the scattering behaviour of light within the substrate. In addition, removing FTO by etching increased the ohmic resistivity of the substrate. Etching the FTO layer also affected the morphology of the TiO_2 nanorods. On the non-etched area of the substrate, these were vertically aligned and had a denser structure than those grown in random directions on the etched area. The photocurrent was affected by all these factors. Overall, etching the FTO layer had a negative effect on the photoactivity of the fabricated electrodes, and an increased area of etching reduced the photocurrent. In addition, patterning the FTO layer caused the formation of charge trapping sites and enhanced the charge recombination rate.

Recommendations

The results of this study suggest the following recommendations for direction of future research on the application of surface patterning for improvement of photoelectrode performance.

- The effect of a nanostructured surface in improving the optical behaviour of TiO_2 photoelectrodes could be investigated further by studies on optimisation of periodicity of structures for a maximised photon absorption within the TiO_2 layer. A periodic nanostructure could also be applied at the other interfaces (glass-FTO and FTO-TiO_2) to reduce the back reflection by causing a gradual refractive index change between the layers.

Achieving optimal light harvest requires consideration of the light absorption within the inactive layers.

- To maximise photon absorption within the TiO_2 layer, it would be useful to investigate the effect of coating the TiO_2-electrolyte interface with a scattering layer that reflects the non-absorbed photons back to the TiO_2 layer.

- The periodic pyramidal structure could be used for further electrochemical studies such as impedance analysis on a patterned electrode which would provide information about ohmic resistance of the electrolyte solution, double layer capacitance and electron transfer resistance [392]. The patterned electrode could also be studied in a rotating disk electrode system. This would limit the diffusion layer thickness and provide well-defined flow conditions along the disk surface. This method enables to distinguish between the influences of charge and mass transfer on the electrochemical reaction [393].

- The tips of the pyramids caused a high current density due to a convergent mass transport of redox species towards the electrode. Further study could aim to optimise the number of tips and their periodicity for a fast electrochemical reaction. Enhanced mass transport on the tips could be a way to promote a photoelectrochemical reaction.

- Patterning the conductive layer with microstructures combines the advantages of light diffraction, gradual change of refractive index, and structuring the electrode-electrolyte interface. Further studies could investigate the effects of structures of different shape and size. Structures with different height and aspect ratio could be obtained using photolithography [378]. The height of the structure could be adjusted by forming a thick layer of FTO using techniques such as sputtering and sol-gel. The effect of geometrical features and the amount of conductive material could be distinguished by comparing the patterned FTO with a flat electrode that has the same resistivity. Patterning a periodic nanostructure that requires minimal etching of the FTO would result in a small change in the resistivity of the conductive layer and would enable the study of the effect of patterning the FTO-TiO_2 layer on light behaviour and photon absorption within the TiO_2 layer.

- Although the periodic pyramidal microstructure was successfully formed on the surface of the semiconductor layer, a reproducible fabrication method is required to conduct validated photoelectrochemical tests. Imprinting a polymer-based paste using a hard Si master mold under a controlled pressure would provide more control on the thickness of the structure resulting in a higher reproducibility. In this method, the paste could be made by dispersing TiO_2 into a conductive UV/thermal curable polymer that provides intimate contact between the photo-active particles. This conductive polymer could function in the charge-collection phase and facilitate movement of electrons towards the external circuit [394].

- Having a large-scale pyramidal pattern on the semiconductor that can affect the redox species mass transfer rate would increase the thickness of the semiconductor layer and cause high volume charge recombination rate. To benefit from an extended surface area while preventing increase of the layer thickness, the TiO_2 layer could be coated on an FTO layer patterned with a pyramidal microstructure.

Completion of these suggested investigations could result in greatly improved efficiency of TiO_2 photoelectrodes for the application in redox flow batteries which could contribute to reduction in carbon dioxide emissions from use of fossil fuels.

7 References

1. Kannan, N.; Vakeesan, D. Solar energy for future world: - A review. *Renewable and Sustainable Energy Reviews*, **2016**, *62*, 1092–1105.

2. Liang, Y.; Zhao, C.; Yuan, H.; Chen, Y.; Zhang, W. A review of rechargeable batteries for portable electronic devices. *InfoMat*, **2019**, *1*, 6–32.

3. Dunn, B.; Kamath, H.; Tarascon, J. M. Electrical Energy Storage for the Grid: A Battery of Choices. *Science*, **2011**, *334*(6058), 928–935.

4. Poullikkas, A. A comparative overview of large-scale battery systems for electricity storage. *Renewable and Sustainable Energy Reviews*, **2013**, *27*, 778–788.

5. Rugolo, J.; Aziz, M. J. Electricity storage for intermittent renewable sources. *Energy & Environmental Science*, **2012**, *5*, 7151.

6. Chakrabarti, M. H.; Roberts, E. P. L.; Bae, C. Ruthenium based redox flow battery for solar energy storage. *Energy Conversion and Management*, **2011**, *52*, 2501–2508.

7. Kamat, P. V.; Schanze, K. S.; Buriak, J. M. Redox flow batteries. *ACS Energy Letters*, **2017**, *2*, 1368–1369.

8. Liu, P.; Cao, Y. L.; Li, G. R.; Gao, X. P.; Ai, X. P. A solar rechargeable flow battery based on photoregeneration of two soluble redox couples. *ChemSusChem*, **2013**, *6*(5), 802–806.

9. Li, W. Fu; H.-C.; Li, L.; Cabán-Acevedo, M. Integrated photoelectrochemical solar energy conversion and organic redox flow battery devices. *Angewandte Chemie*, **2016**, *128*(42), 13298–13302.

10. Yu, M.; McCulloch, W. D.; Huang, Z.; Trang, B. B.; Lu, J.; Amine, K. Solar-powered

electrochemical energy storage: an alternative to solar fuels. *Jornal of Materials Chemistry A*, **2016**, *4*(8), 2766–2782.

11. McCulloch, W. D.; Yu, M.; Wu, Y. PH-tuning a solar redox flow battery for integrated energy conversion and storage. *ACS Energy Letters*, **2016**, *1*, 578–582.

12. Wedege, K.; Bae, D.; Smith, W. A.; Mendes, A.; Bentien, A. Solar redox flow batteries with organic redox couples in aqueous electrolytes: A minireview. *Journal of Physical Chemistry C*, **2018**, *122*, 25729–25740.

13. Ma, W.; Xie, C.; Wang, X.; Wang, H.; Jiang, X.; Zhang, H. High-performance solar redox flow battery toward efficient overall splitting of hydrogen sulfide. *ACS Energy Letters*, **2020**, *5*, 597–603.

14. Yu, M.; McCulloch, W. D.; Beauchamp, D. R.; Huang, Z. Aqueous lithium-iodine solar flow battery for the simultaneous conversion and storage of solar energy. *Journal of the American Chemical Society*, **2015**, *137*, 8332–8335.

15. Khataee, A.; Azevedo, J.; Dias, P.; Ivanou, D. Integrated design of hematite and dye-sensitized solar cell for unbiased solar charging of an organic-inorganic redox flow battery. *Nano Energy*, **2019**, *62*, 832–843.

16. Fan, L.; Jia, C.; Zhu, Y. G.; Wang, Q. Redox targeting of prussian blue: Toward low-cost and high energy density redox flow battery and solar rechargeable battery. *ACS Energy Letters*, **2017**, *2*, 615–621.

17. Wedege, K.; Bae, D.; Dražević, E.; Mendes, A. Unbiased, complete solar charging of a neutral flow battery by a single Si photocathode. *RSC Advances*, **2018**, *8*, 6331–6340.

18. Russo, P.; Liang, R.; He, R. X.; Zhou, Y. N. Phase transformation of TiO_2 nanoparticles by femtosecond laser ablation in aqueous solutions and deposition on conductive substrates. *Nanoscale*, **2017**, *9*, 6167–6177.

19. Tada, H.; Hattori, A.; Tokihisa, Y.; Imai, K.; Tohge, N.; Ito, S. A patterned-TiO_2/SnO_2

bilayer type photocatalyst. *Journal of Physical Chemistry B*, **2000**, *104*(19), 4586–4587.

20. Zhang, J.; Zhou, P.; Liu, J.; Yu, J. New understanding of the difference of photocatalytic activity among anatase, rutile and brookite TiO_2. *Physical Chemistry Chemical Physics*, **2014**, *16*(38), 20382–20386.

21. Bella, F.; Verna, A.; Gerbaldi, C. Patterning dye-sensitized solar cell photoanodes through a polymeric approach: A perspective. *Materials Science in Semiconductor Processing*, **2018**, *73*, 92–98.

22. Kang, S. M.; Jang, S.; Lee, J. K.; Yoon, J. Moth-eye TiO_2 layer for improving light harvesting efficiency in perovskite solar cells. *Small*, **2016**, *12*(18), 2443–2449.

23. Park, J. T.; Roh, D. K.; Patel, R.; Son, K. J.; Koh, W. G. Fabrication of hole-patterned TiO_2 photoelectrodes for solid-state dye-sensitized solar cells. *Electrochimica Acta*, **2010**, *56*, 68–73.

24. Kong, S. M.; Xiao, Y.; Kim, K. H.; Lee, W. I. Performance improvement of dye-sensitized solar cells by surface patterning of fluorine-doped tin oxide transparent electrodes. *Thin Solid Films*, **2011**, *519*(10), 3173–3176.

25. Chua, J.; Mathews, N.; Jennings, J. R.; Yang, G.; Wang, Q. Patterned 3-dimensional metal grid electrodes as alternative electron collectors in dye-sensitized solar cells. *Physical Chemistry Chemical Physics*, **2011**, *13*(43), 19314–19317.

26. Yoo, B.; Lim, M. K.; Kim, K. J. Application of Pt sputter-deposited counter electrodes based on micro-patterned ITO glass to quasi-solid state dye-sensitized solar cells. *Current Applied Physics*, **2012**, *12*(5), 1302–1306.

27. Shao, W.; Gu, F.; Gai, L.; Li, C. Planar scattering from hierarchical anatase TiO_2 nanoplates with variable shells to improve light harvesting in dye-sensitized solar cells. *Chemical Communications*, **2011**, *47*(17), 5046–5048.

28. Zhang, Q.; Myers, D.; Lan, J.; Jenekhe, S. A. Applications of light scattering in dye-

sensitized solar cells. *Physical Chemistry Chemical Physics*, **2012**, *14*(43), 14982–14998.

29. Šúri, M.; Huld, T. A.; Dunlop, E. D.; Ossenbrink, H. A. Potential of solar electricity generation in the European Union member states and candidate countries. *Solar Energy*, **2007**, *81*(10), 1295–1305.

30. Cox, P. M.; Betts, R. a; Jones, C. D. Acceleration of global warming due to carbon-cycle feedbacks in a coupled climate model. *Nature*, **2000**, *408*(6813), 750.

31. Pehnt, M. Dynamic life cycle assessment (LCA) of renewable energy technologies. *Renewable Energy*, **2006**, *31*(1), 55–71.

32. Hofman, K.; Li, X. Canada's energy perspectives and policies for sustainable development. *Applied Energy*, **2009**, *86*(4), 407–415.

33. Liu, W.; Lund, H.; Mathiesen, B. V.; Zhang, X. Potential of renewable energy systems in China. *Applied Energy*, **2011**, *88*(2), 518–525.

34. Lewis, N. S. Toward Cost-Effective Solar Energy Use, *Science*, **2007**, 798–802.

35. Rehman, S.; Al-Hadhrami, L. M.; Alam, M. M. Pumped hydro energy storage system: A technological review. *Renewable and Sustainable Energy Reviews*, **2015**, *44*, 586–598.

36. Joselin Herbert, G. M.; Iniyan, S.; Sreevalsan, E.; Rajapandian, S. A review of wind energy technologies. *Renewable and Sustainable Energy Reviews*, **2007**, *11*(6), 1117–1145.

37. Barbier, E. Geothermal energy technology and current status: An overview. *Renewable and Sustainable Energy Reviews*, **2002**, *6*(1–2), 3–65.

38. Klass, D. L. *Biomass for renewable energy, fuels, and chemicals*, Elsevier, **1998**.

39. Hoffert, M. I.; Caldeira, K.; Benford, G.; Criswell, D. R.; Green, C. Engineering: Advanced technology paths to global climate stability: Energy for a greenhouse planet. *Science*, **2002**, *298*, 981–987.

40. Azevedo, J.; Seipp, T.; Burfeind, J.; Sousa, C. Unbiased solar energy storage: Photoelectrochemical redox flow battery. *Nano Energy*, **2016**, *22*, 396–405.

41. Li, Q.; Liu, Y.; Guo, S.; Zhou, H. Solar energy storage in the rechargeable batteries. *Nano Today*, **2017**, *16*, 46–60.

42. Hou, Y.; Vidu, R.; Stroeve, P. Solar energy storage methods. *Industrial and Engineering Chemistry Research*, **2011**, *50*, 8954–8964.

43. Winter, M.; Brodd, R. J. What are batteries, fuel cells, and supercapacitors? *Chemical Reviews*, **2004**, *104*, 4245–4269.

44. Scrosati, B. Recent advances in lithium ion battery materials. *Electrochimica Acta*, **2000**, *45*, 2461–2466.

45. Bogno, B.; Sawicki, J. P.; Salame, T.; Aillerie, M. Improvement of safety, longevity and performance of lead acid battery in off-grid PV systems. *International Journal of Hydrogen Energy*, **2017**, *42*, 3466–3478.

46. Wang, Y. X.; Zhang, B.; Lai, W.; Xu, Y.; Chou, S. L.; Liu, H. K. Room-temperature sodium-sulfur batteries: A comprehensive review on research progress and cell chemistry. *Advanced Energy Materials*, **2017**, *7*, 1–17.

47. Fetcenko, M. A.; Ovshinsky, S. R.; Reichman, B.; Young, K. Recent advances in NiMH battery technology. *Journal of Power Sources*, **2007**, *165*, 544–551.

48. Yan, N. F.; Li, G. R.; Gao, X. P. Solar rechargeable redox flow battery based on Li_2WO_4/LiI couples in dual-phase electrolytes. *Journal of Materials Chemistry A*, **2013**, *1*, 7012.

49. Alotto, P.; Guarnieri, M.; Moro, F. Redox flow batteries for the storage of renewable energy: A review. *Renewable and Sustainable Energy Reviews*, **2014**, *29*, 325–335.

50. Fan, X.; Liu, B.; Liu, J.; Ding, J.; Han, X. Battery technologies for grid-level large-scale electrical energy storage. *Transactions of Tianjin University*, **2020**, *26*(2), 92–103.

51. Benato, R.; Cosciani, N.; Crugnola, G. Sodium nickel chloride battery technology for large-scale stationary storage in the high voltage network. *Journal of Power Sources*, **2015**, *293*, 127–136.

52. Ehnberg, J.; Liu, Y.; Grahn, M.; Steen, D. Grid and storage. *Systems erspectives on renewable power* (Publisher: Chalmers univeristy of Technology), **2014**, 46–59.

53. Fujimoto, C.; Kim, S.; Stains, R.; Wei, X. Vanadium redox flow battery efficiency and durability studies of sulfonated Diels Alder poly(phenylene)s. *Electrochemistry Communications*, **2012**, *20*(1), 48–51.

54. Weber, A. Z.; Mench, M. M.; Meyers, J. P.; Ross, P. N. Redox flow batteries: A review. *Journal of Applied Electrochemistry*, **2011**, *41*(10), 1137–1164.

55. Skyllas-Kazacos, M. *Encyclopedia of Electrochemical Power Sources*, Elsevier, **2009**, 444–453.

56. Kisch, H. Semiconductor photocatalysis - Mechanistic and synthetic aspects. *Angewandte Chemie - International Edition*, **2013**, *52*(3), 812–847.

57. Kubacka, A.; Fernández-García, M.; Colón, G. Advanced nanoarchitectures for solar photocatalytic applications. *Chemical Reviews*, **2012**, *112*(3), 1555–1614.

58. Leung, P. K.; Ponce-De-Leon C.; Low, C. T. J.; Shah, A. A. Characterization of a zinc-cerium flow battery. *Journal of Power Sources*, **2011**, *196*(11), 5174–5185.

59. Wills, R. G. A.; Collins, J.; Stratton-Campbell, D.; Low, C. T. J.; Pletcher, D. Developments in the soluble lead-acid flow battery. *Journal of Applied Electrochemistry*, **2010**, *40*(5), 955–965.

60. Bartolozzi, M. Development of redox flow batteries. A historical bibliography. *Journal of Power Sources*, **1989**, *27*(3), 219–234.

61. Elgrishi, N.; Rountree, K. J.; McCarthy, B. D.; Rountree, E. S. A Practical Beginner's Guide

to Cyclic Voltammetry. *Journal of Chemical Education*, **2018**, *95*(2), 197–206.

62. Rychcik, M.; Skyllas-Kazacos, M. Characteristics of a new all-vanadium redox flow battery. *Journal of Power Sources*, **1988**, *22*(1), 59–67.

63. Chang, T. C.; Zhang, J. P.; Fuh, Y. K. Electrical, mechanical and morphological properties of compressed carbon felt electrodes in vanadium redox flow battery. *Journal of Power Sources*, **2014**, *245*, 66–75.

64. Skyllas-Kazacos, M.; Chakrabarti, M. H.; Hajimolana, S. A. Progress in flow battery research and development. *Journal of The Electrochemical Society*, **2011**, *158*(8), R55.

65. Skyllas-Kazacos, M.; Rychick, M.; Robins, R. All-vanadium redox battery, *United States of America Patent*, **1988**.

66. Hruska, L. W. Investigation of factors affecting performance of the iron-redox battery. *Journal of The Electrochemical Society*, **1981**, *128*(1), 18.

67. Sum, E.; Skyllas-Kazacos, M. A study of the V(II)/V(III) redox couple for redox flow cell applications. *Journal of Power Sources*, **1985**, *15*(2–3), 179–190.

68. Sum, E., Rychcik, M., & Skyllas-Kazacos, M. Investigation of the V(V)/V(IV) system for use in the positive half-cell of a redox battery. *Journal of Power Sources*, **1985**, *16*, 85–95.

69. Rychcik, M.; Robins, R. G.; Fane, A. G. The new all-vanadium redox flow cell. *Journal of The Electrochemical Society*, **1986**, *133*(5), 1057–1058.

70. Lopez-Atalaya, A.; Codina, G.; Perez, J. Optimization studies on a Fe/Cr redox flow battery. *Journal of Power Sources*, **1992**, *39*(2), 147–154.

71. Nguyen, T.; Savinell, R. F. Flow batteries. *Electrochemical Society Interface*, **2010**, *19*, 54–56.

72. Fabjan, C.; Garche, J.; Harrer, B. The vanadium redox-battery: An efficient storage unit for photovoltaic systems. *Electrochimica Acta*, **2001**, *47*(5), 825–831.

73. Cedzynska, K. Properties of modified electrolyte for zinc-bromine cells. *Electrochimica Acta*, **1995**, *40*(8), 971–976.

74. Li, B.; Gu, M.; Nie, Z.; Wei, X.; Wang, C. Nanorod niobium oxide as powerful catalysts for an all vanadium redox flow battery. *Nano Letters*, **2014**, *14*(1), 158–165.

75. Zeng, Y. K.; Zhao, T. S.; An, L.; Zhou, X. L. A comparative study of all-vanadium and iron-chromium redox flow batteries for large-scale energy storage. *Journal of Power Sources*, **2015**, *300*, 438–443.

76. Zeng, Y. K.; Zhou, X. L.; An, L.; Wei, L.; Zhao, T. S. A high-performance flow-field structured iron-chromium redox flow battery. *Journal of Power Sources*, **2016**, *324*, 738–744.

77. Zhao, P.; Zhang, H.; Zhou, H.; Yi, B. Nickel foam and carbon felt applications for sodium polysulfide/bromine redox flow battery electrodes. *Electrochimica Acta*, **2005**, *51*(6), 1091–1098.

78. Zhang, L.; Zhang, H.; Lai, Q.; Li, X.; Cheng, Y. Development of carbon coated membrane for zinc/bromine flow battery with high power density. *Journal of Power Sources*, **2013**, *227*, 41–47.

79. Lai, Q.; Zhang, H.; Li, X.; Zhang, L.; Cheng, Y. A novel single flow zinc-bromine battery with improved energy density. *Journal of Power Sources*, **2013**, *235*, 1–4.

80. Wu, M. C.; Zhao, T. S.; Jiang, H. R.; Zeng, Y. K. High-performance zinc bromine flow battery via improved design of electrolyte and electrode. *Journal of Power Sources*, **2017**, *355*, 62–68.

81. Leung, P. K.; Ponce De León, C.; Walsh, F. C. An undivided zinc-cerium redox flow battery operating at room temperature (295 K). *Electrochemistry Communications*, **2011**, *13*(8), 770–773.

82. Pletcher, D.; Wills, R. A novel flow battery - A lead acid battery based on an electrolyte

with soluble lead(II): III. The influence of conditions on battery performance. *Journal of Power Sources*, **2005**, *149*(1–2), 96–102.

83. Hawthorne, K. L.; Wainright, J. S.; Savinell, R. F. Studies of iron-ligand complexes for an all-iron flow battery application. *Journal of The Electrochemical Society*, **2014**, *161*(10), A1662–A1671.

84. Gong, K.; Xu, F.; Grunewald, J. B.; Ma, X. All-soluble all-iron aqueous redox-flow battery. *ACS Energy Letters*, **2016**, *1*(1), 89–93.

85. Jayathilake, B. S.; Plichta, E. J.; Hendrickson, M. A.; Narayanan, S. R. Improvements to the coulombic efficiency of the iron electrode for an all-iron redox-flow battery. *Journal of The Electrochemical Society*, **2018**, *165*(9), A1630–A1638.

86. Li, X.; Hui, D.; Lai, X. Battery energy storage station (BESS)-based smoothing control of photovoltaic (PV) and wind power generation fluctuations. *IEEE Transactions on Sustainable Energy*, **2013**, *4*(2), 464–473.

87. Gibson, T. L.; Kelly, N. A. Solar photovoltaic charging of lithium-ion batteries. *Journal of Power Sources*, **2010**, *195*(12), 3928–3932.

88. Kelly, N. A.; Gibson, T. L. Solar photovoltaic charging of high voltage nickel metal hydride batteries using DC power conversion. *Journal of Power Sources*, **2011**, *196*(23), 10430–10441.

89. Urbain, F.; Murcia-López, S.; Nembhard, N. Solar vanadium redox-flow battery powered by thin-film silicon photovoltaics for efficient photoelectrochemical energy storage. *Journal of Physics D: Applied Physics*, **2019**, *52*(4), 044001.

90. Williams, C. J. C.; Binder, J. O.; Kelm, T. Demand side management through heat pumps, thermal storage and battery storage to increase local self-consumption and grid compatibility of PV systems. *IEEE PES Innovative Smart Grid Technologies Conference Europe*, **2012**, 1–6.

91. Purvins, A.; Sumner, M. Optimal management of stationary lithium-ion battery system in electricity distribution grids. *Journal of Power Sources*, **2013**, *242*, 742–755.

92. Tan, C. W.; Green, T. C.; Hernandez-Aramburo, C. A. A stochastic method for battery sizing with uninterruptible-power and demand shift capabilities in PV (photovoltaic) systems. *Energy*, **2010**, *35*, 5082–5092.

93. Bhattacharjee, A.; Samanta, H.; Banerjee, N.; Saha, H. Development and validation of a real time flow control integrated MPPT charger for solar PV applications of vanadium redox flow battery. *Energy Conversion and Management*, **2018**, *171*, 1449–1462.

94. Liu, J.; Pang, W. K.; Zhou, T.; Chen, L. Li_2TiSiO_5: A low potential and large capacity Ti-based anode material for Li-ion batteries. *Energy and Environmental Science*, **2017**, *10*(6), 1456–1464.

95. Huang, Q.; Yang, J.; Ng, C. B.; Jia, C.; Wang, Q. A redox flow lithium battery based on the redox targeting reactions between LiFePO4 and iodide. *Energy and Environmental Science*, **2016**, *9*(3), 917–921.

96. Schmidt, D.; Hager, M. D.; Schubert, U. S. Photo-Rechargeable Electric Energy Storage Systems. *Advanced Energy Materials*, **2016**, *6*(1), 1–11.

97. Luo, B.; Ye, D.; Wang, L. Recent Progress on Integrated Energy Conversion and Storage Systems. *Advanced Science*, **2017**, *4*(9), 1–15.

98. Guo, W.; Xue, X.; Wang, S.; Lin, C.; Wang, Z. L. An integrated power pack of dye-sensitized solar cell and Li battery based on double-sided TiO_2 nanotube arrays. *Nano Letters*, **2012**, *12*(5), 2520–2523.

99. Paolella, A.; Faure, C.; Bertoni, G.; Marras, S. Light-assisted delithiation of lithium iron phosphate nanocrystals towards photo-rechargeable lithium ion batteries. *Nature Communications*, **2017**, *8*(1),1–10.

100. Li, Q.; Li, N.; Ishida, M.; Zhou, H. Saving electric energy by integrating a photoelectrode

into a Li-ion battery. *Journal of Materials Chemistry A*, **2015**, *3*, 20903–20907.

101. Yu, M.; Ren, X.; Ma, L.; Wu, Y. Integrating a redox-coupled dye-sensitized photoelectrode into a lithium-oxygen battery for photoassisted charging. *Nature Communications*, **2014**, *5*(1), 1–6.

102. Liu, Y.; Li, N.; Liao, K.; Li, Q.; Ishida, M. Lowering the charge voltage of Li-O_2 batteries via an unmediated photoelectrochemical oxidation approach. *Journal of Materials Chemistry A*, **2016**, *4*, 12411–12415.

103. Li, N.; Wang, Y.; Tang, D.; Zhou, H. Integrating a photocatalyst into a hybrid lithium-sulfur battery for direct storage of solar energy. *Angewandte Chemie*, **2015**, *127*(32), 9403–9406.

104. Nikiforidis, G.; Tajima, K.; Byon, H. R. High energy efficiency and stability for photoassisted aqueous lithium-iodine redox batteries. *ACS Energy Letters*, **2016**, *1*(4), 806–813.

105. Wei, Z.; Liu, D.; Hsu, C.; Liu, F. All-vanadium redox photoelectrochemical cell: An approach to store solar energy. *Electrochemistry Communications*, **2014**, *45*, 79–82.

106. Wedege, K.; Azevedo, J.; Khataee, A.; Bentien, A. Direct solar charging of an organic–inorganic, stable, and aqueous alkaline redox flow battery with a hematite photoanode. *Angewandte Chemie - International Edition*, **2016**, *55*(25), 7142–7147.

107. Liao, S.; Zong, X.; Seger, B.; Pedersen, T. Integrating a dual-silicon photoelectrochemical cell into a redox flow battery for unassisted photocharging. *Nature Communications*, **2016**, *7*(1),1–8.

108. Li, W.; Fu, H. C.; Li, L.; Cabán-Acevedo, M. Integrated photoelectrochemical solar energy conversion and organic redox flow battery devices. *Angewandte Chemie*, **2016**, *128*(42), 13298–13302.

109. Lei, B.; Li, G. R.; Chen, P.; Gao, X. P. A solar rechargeable battery based on hydrogen storage mechanism in dual-phase electrolyte. *Nano Energy*, **2017**, *38*, 257–262.

110. Mahmoudzadeh, M. A.; Usgaocar, A. R.; Giorgio, J. A high energy density solar rechargeable redox battery. *Journal of Materials Chemistry A*, **2016**, *4*, 3446–3452.

111. Li, Q.; Li, N.; Liu, Y.; Wang, Y.; Zhou, H. High-safety and low-cost photoassisted chargeable aqueous sodium-ion batteries with 90% input electric energy savings. *Advanced Energy Materials*, **2016**, *6*(18), 1–6.

112. Wei, Z.; Liu, D.; Hsu, C.; Liu, F. All-vanadium redox photoelectrochemical cell: An approach to store solar energy. *Electrochemistry Communications*, **2014**, *45, 79–82*.

113. Feng, H.; Jiao, X.; Chen, R. A microfluidic all-vanadium photoelectrochemical cell with multi-nanostructured TiO_2 photoanode. *Journal of Power Sources*, **2018**, *404*, 1–6.

114. Yong, X.; Schoonen, M. A. A. The absolute energy positions of conduction and valence bands of selected semiconducting minerals. *American Mineralogist*, **2000**, *85*(3–4), 543–556.

115. Khan, S. U. M.; Kainthla, R. C.; Bockris, J. O. M. The redox potential and the Fermi level in solution. *Journal of Physical Chemistry*, **1987**, *91*(23), 5974–5977.

116. Decker, F.; Cattarin, S. Photoelectrochemical cells | Overview. In *Encyclopedia of Electrochemical Power Sources*, Elsevier, **2009**, 1–9

117. Linsebigler, A. L.; Lu, G.; Yates, J. T. Photocatalysis on TiO_2 surfaces: Principles, mechanisms, and selected results. *Chemical Reviews*, **1995**, *95*(3), 735–758.

118. Haber, J.; Nowak, P. A ratalysis related electrochemical study of the V_2O_5/TiO_2(rutile) system. *Langmuir*, **1995**, *11*(3), 1024–1032.

119. Gratzel, M. Photoelectrochemical cells. *Thin Film Solar Cells*, **1983**, *414*, 457–481.

120. Gelderman, K.; Lee, L.; Donne, S. W. Flat-band potential of a semiconductor: Using the Mott-Schottky equation. *Journal of Chemical Education*, **2007**, *84*(4), 685–688.

121. Russo, B.; Cao, G. Z. Fabrication and characterization of fluorine-doped thin oxide thin

films and nanorod arrays via spray pyrolysis. *Applied Physics A: Materials Science and Processing*, **2008**, *90*(2), 311–315.

122. Fukano, T.; Motohiro, T. Low-temperature growth of highly crystallized transparent conductive fluorine-doped tin oxide films by intermittent spray pyrolysis deposition. *Solar Energy Materials and Solar Cells*, **2004**, *82*(4), 567–575.

123. Amanullah, F. M.; Pratap, K. J.; Hari Babu, V. Compositional analysis and depth profile studies on undoped and doped tin oxide films prepared by spray technique. *Materials Science and Engineering: B*, **1998**, *52*(2–3), 93–98.

124. Samad, W. Z.; Salleh, M. M.; Shafiee, A.; Yarmo, M. A. Structural, optical and electrical properties of fluorine doped tin oxide thin films deposited using inkjet printing technique. *Sains Malaysiana*, **2011**, *40*(3), 251–257.

125. Banerjee, A. N.; Kundoo, S.; Saha, P.; Chattopadhyay, K. K. Synthesis and characterization of nano-crystalline fluorine-doped tin oxide thin films by sol-gel method. *Journal of Sol-Gel Science and Technology*, **2003**, *28*(1), 105–110.

126. Bisht, H.; Eun, H. T.; Mehrtens, A.; Aegerter, M. A. Comparison of spray pyrolyzed FTO, ATO and ITO coatings for flat and bent glass substrates. *Thin Solid Films*, **1999**, *351*(1–2), 109–114.

127. Kim, H.; Kushto, G. P.; Auyeung, R. C. Y.; Piqué, A. Optimization of F-doped SnO_2 electrodes for organic photovoltaic devices. *Applied Physics A: Materials Science and Processing*, **2008**, *93*(2), 521–526.

128. Xu, M.; Gao, Y.; Moreno, E. M.; Kunst, M. Photocatalytic activity of bulk TiO_2 anatase and rutile single crystals using infrared absorption spectroscopy. *Physical Review Letters*, **2011**, *106*(13), 1–4.

129. Li, J.; Ishigaki, T.; Sun, X. Anatase , brookite , and rutile nanocrystals via redox reactions under mild hydrothermal conditions : phase-selective synthesis and physicochemical properties. *The Journal of Physical Chemistry C,* **2007**, 4969–4976.

130. Hanaor, D. A. H.; Sorrell, C. C. Review of the anatase to rutile phase transformation. *Journal of Materials Science*, **2011**, *46*(4), 855–874.

131. Sclafani, A.; En, V.; No, C. Comparison of the photoelectronic and photocatalytic activities of various anatase and rutile forms of titania in pure liquid organic phases and in aqueous solutions, **1996**, *100*(32), 13655–13661.

132. Zhang, Q.; Gao, L.; Guo, J. Effects of calcination on the photocatalytic properties of nanosized TiO_2 powders prepared by $TiCl_4$ hydrolysis. *Applied Catalysis B: Environmental*, **2000**, *26*(3), 207–215.

133. Zhang, Z.; Wang, C.; Zakaria, R.; Ying, J. Y. Role of particle size in nanocrystalline TiO_2-based photocatalysts, *The Journal of Physical Chemistry* B, **1998**, *102*(52), 10871–10878.

134. Simonsen, M. E. Heterogeneous Photocatalysis. *Chemistry of Advanced Environmental Purification Processes of Water: Fundamentals and Applications*. Newnes, **2014**, 135–170.

135. Kesselman, J. M.; Shreve, G. A.; Hoffmann, M. R.; Lewis, N. S. Flux-matching conditions at TiO_2 photoelectrodes: Is interfacial electron transfer to O_2 rate-limiting in the TiO_2-catalyzed photochemical degradation of organics? *Journal of Physical Chemistry*, **1994**, *98*(50), 13385–13395.

136. Siah, W. R.; Lintang, H. O.; Shamsuddin, M.; Yuliati, L. High photocatalytic activity of mixed anatase-rutile phases on commercial TiO_2 nanoparticles. *IOP Conference Series: Materials Science and Engineering*, **2016**, *107*(1), 012005.

137. Liu, N.; Chen, X.; Zhang, J.; Schwank, J. W. A review on TiO_2-based nanotubes synthesized via hydrothermal method: Formation mechanism, structure modification, and photocatalytic applications. *Catalysis Today*, **2014**, *225*, 34–51.

138. Hanaor, D.; Michelazzi, M.; Veronesi, P.; Leonelli, C. Anodic aqueous electrophoretic deposition of titanium dioxide using carboxylic acids as dispersing agents. *Journal of the European Ceramic Society*, **2011**, *31*(6), 1041–1047.

139. Roy, P.; Berger, S.; Schmuki, P. TiO_2 nanotubes: Synthesis and applications. *Angewandte Chemie - International Edition*, **2011**, *50*(13), 2904–2939.

140. Wang, F. X.; Hwangbo, C. K.; Jung, B. Y.; Lee, J. H. Optical and structural properties of TiO_2 films deposited from Ti_3O_5 by electron beam. *Surface and Coatings Technology*, **2007**, *201*, 5367–5370.

141. Duyar, Ö.; Placido, F.; Zafer Durusoy, H. Optimization of TiO_2 films prepared by reactive electron beam evaporation of Ti_3O_5. *Journal of Physics D: Applied Physics*, **2008**, *41*(9), 095307.

142. Yang, C.; Fan, H.; Xi, Y.; Chen, J. Effects of depositing temperatures on structure and optical properties of TiO_2 film deposited by ion beam assisted electron beam evaporation. *Applied Surface Science*, **2008**, *254*(9), 2685–2689.

143. Ohsaki, H.; Tachibana, Y.; Hayashi, A.; Mitsui, A. High rate sputter deposition of TiO2 from TiO_{2-x} target. *Thin Solid Films*, **1999**, *351*, 57–60.

144. Tachibana, Y.; Ohsaki, H.; Hayashi, A.; Mitsui, A. TiO_{2-x} sputter for high rate deposition of TiO_2. *Vacuum*, **2000**, *59*, 836–843.

145. Cevro, M.; Carter, G. Ion beam sputtering and dual ion beam sputtering of titanium oxide films. *Journal of Physics D: Applied Physics*, **1995**, *28*(9), 1962–1976.

146. Siefering, K. L.; Griffin, G. L. Kinetics of low-pressure chemical vapor deposition of TiO2 from titanium tetraisopropoxide. *Journal of The Electrochemical Society*, **1990**, *137*(3), 814–818.

147. Rausch, N.; Burte, E. P. Thin TiO_2 films prepared by low pressure chemical vapor deposition. *Journal of The Electrochemical Society*, **1993**, *140*(1), 145–149.

148. Byun, D.; Jin, Y.; Kim, B. Photocatalytic TiO_2 deposition by chemical vapor deposition. *Journal of Hazardous Materials*, **2000**, *73*(2), 199–206.

149. Ismail, W. N. W. Sol–gel technology for innovative fabric finishing—A Review. *Journal of Sol-Gel Science and Technology*, **2016**, *78*(3), 698–707.

150. Vorotilov, K. A.; Orlova, E. V.; Petrovsky, V. I. Sol-gel TiO_2 films on silicon substrates. *Thin Solid Films*, **1992**, *207*(1–2), 180–184.

151. Nair, A. S.; Jose, R.; Shengyuan, Y.; Ramakrishna, S. A simple recipe for an efficient TiO_2 nanofiber-based dye-sensitized solar cell. *Journal of Colloid and Interface Science*, **2011**, *353*(1), 39–45.

152. Aduda, B. O.; Ravirajan, P.; Choy, K. L.; Nelson, J. Effect of morphology on electron drift mobility in porous TiO_2. *International Journal of Photoenergy*, **2004**, *6*(3), 141–147.

153. Xi Xi, J.; Dahoudi, N. A.; Zhang, Q. Effect of annealing temperature on the performances and electrochemical properties of TiO_2 dye-sensitized solar cells. *Science of Advanced Materials*, **2012**, *4*(7), 727–733.

154. Ito, S.; Chen, P.; Comte, P.; Nazeeruddin, M. K. Fabrication of Screen-Printing Pastes From TiO_2 Powders for Dye-Sensitised Solar Cells. *Progress in Photovoltaics: Research and Applications*, **2007**, *15*, 603–612.

155. Marcos, P. S.; Marto, J.; Trindade, T.; Labrincha, J. A. Screen-printing of TiO_2 photocatalytic layers on glazed ceramic tiles. *Journal of Photochemistry and Photobiology A: Chemistry*, **2008**, *197*, 125–131.

156. Bendoni, R.; Sangiorgi, N.; Sangiorgi, A.; Sanson, A. Role of water in TiO_2 screen-printing inks for dye-sensitized solar cells. *Solar Energy*, **2015**, *122*, 497–507.

157. Senevirathne, A. M. C.; Seneviratne, V. A.; Ileperuma, O. A. Novel quasi-solid-state electrolyte based on γ-butyrolactone and tetrapropylammonium iodide for dye-sensitized solar cells using fumed silica as the gelling agent. *Procedia Engineering*, **2016**, *139*, 87–92.

158. Lin, C. P.; Chen, H.; Nakaruk, A.; Koshy, P. Effect of annealing temperature on the photocatalytic activity of TiO 2 thin films. *Energy Procedia*, **2013**, *34*, 627–636.

159. Mamat, M. H.; Amizam, S.; Rafaie, H. A.; Hashim, H. Effect of annealing temperature on the surface morphology and electrical properties of aluminum doped zinc oxide thin films prepared by sol-gel spin-coating method. *AIP Conference Proceeding*, **2008**, *1017*(1), 139–143.

160. John, B. M.; Mugo, S. W.; Ngaruiya, J. M. Effect of annealing rates on surface roughness of TiO_2 thin films, *Journal of Materials Physics and Chemistry*, **2018**, 6(2), 43-46.

161. Masakazu, A. Second-generation titanium dioxide photocatalysts prepared by the application of an advanced metal ion-implantation method. *Pure and Applied Chemistry*, **2000**, *72*, 1787–1792.

162. Fuerte, A.; Hernández-Alonso, M. D.; Maira, A. J.; Martínez-Arias, A. Visible light-activated nanosized doped-TiO_2 photocatalysts. *Chemical Communications*, **2001**, *1*(24), 2718–2719.

163. Yamashita, H.; Harada, M.; Misaka, J.; Takeuchi, M. Application of ion beam techniques for preparation of metal ion-implanted TiO_2 thin film photocatalyst available under visible light irradiation: Metal ion-implantation and ionized cluster beam method. *Journal of Synchrotron Radiation*, **2001**, *8*(2), 569–571.

164. Zaleska, A. Doped-TiO_2: A review. *Recent Patents on Engineering*, **2008**, *2*(3), 157–164.

165. Basavarajappa, P. S.; Patil, S. B.; Ganganagappa, N.; Reddy, K. R. Recent progress in metal-doped TiO2, non-metal doped/codoped TiO_2 and TiO_2 nanostructured hybrids for enhanced photocatalysis. *International Journal of Hydrogen Energy*, **2020**, *45*(13), 7764–7778.

166. Venieri, D.; Fraggedaki, A.; Kostadima, M.; Chatzisymeon, E. Solar light and metal-doped TiO2 to eliminate water-transmitted bacterial pathogens: Photocatalyst characterization and disinfection performance. *Applied Catalysis B: Environmental*, **2014**, *154*, 93–101.

167. Cong, Y., Zhang, J., Chen, F., & Anpo, M. Synthesis and characterization of nitrogen-doped TiO2 nanophotocatalyst with high visible light activity. *Journal of Physical Chemistry C*,

2007, *111*(19), 6976–6982.

168. Patil, S. B; Basavarajappa, P. S.; Ganganagappa, N.; Jyothi, M. S. Recent advances in non-metals-doped TiO_2 nanostructured photocatalysts for visible-light driven hydrogen production, CO_2 reduction and air purification. *International Journal of Hydrogen Energy*, **2019**, *44*(26), 13022–13039.

169. Yu, J. C.; Zhang, L.; Zheng, Z.; Zhao, J. Synthesis and characterization of phosphated mesoporous titanium dioxide with high photocatalytic activity. *Chemistry of Materials*, **2003**, *15*(11), 2280–2286.

170. Ohno, T.; Mitsui, T.; Matsumura, M. Photocatalytic activity of S-doped TiO_2 photocatalyst under visible light. *Chemistry letters*, **2003**, *32*, 364–365.

171. Liu, Y.; Chen, X.; Li, J.; Burda, C. Photocatalytic degradation of azo dyes by nitrogen-doped TiO2 nanocatalysts. *Chemosphere*, **2005**, *61*(1), 11–18.

172. Zangeneh, H.; Zinatizadeh, A. A.; Feyzi, M.; Zinadini, S.; Bahnemann, D. W. Application of a novel triple metal-nonmetal doped TiO_2 (KBN-TiO_2) for photocatalytic degradation of Linear Alkyl Benzene (LAB) industrial wastewater under visible light. *Materials Science in Semiconductor Processing*, **2018**, *75*, 193–205.

173. Ihara, T.; Miyoshi, M.; Ando, M.; Sugihara, S.; Iriyama, Y. Preparation of a visible-light-active TiO_2 photocatalyst by RF plasma treatment. *Journal of Materials Science*, **2001**, *36*(17), 4201–4207.

174. Koji, T.; Isao, N.; Osamu, M.; Shinichi, S.; Masazumi, A. Preparation of visible-light-responsive titanium oxide photocatalysts by plasma treatment. *Chemistry Letters*, **2000**, *29*, 1354–1355.

175. Naldoni, A.; Altomare, M.; Zoppellaro, G.; Liu, N. Photocatalysis with reduced TiO_2 : From Black TiO_2 to cocatalyst-free hydrogen production. *ACS Catalysis*, **2019**, *9*(1), 345–364.

176. Tian, J.; Hu, X.; Yang, H.; Zhou, Y. High yield production of reduced TiO_2 with enhanced

photocatalytic activity. *Applied Surface Science*, **2016**, *360*, 738–743.

177. Wang, X.; Wang, X.; Song, J.; Li, Y. A highly efficient TiO_X (X = N and P) photocatalyst for inactivation of Microcystis aeruginosa under visible light irradiation. *Separation and Purification Technology*, **2019**, *222*, 99–108.

178. Yang, Z.; Gao, S.; Li, W.; Vlasko-Vlasov, V. Three-dimensional photonic crystal fluorinated tin oxide (FTO) electrodes: Synthesis and optical and electrical properties. *ACS Applied Materials & Interfaces*, **2011**, *3*(4), 1101–1108.

179. Baia, L.; Orbán, E.; Fodor, S.; Hampel, B. Preparation of TiO_2/WO_3 composite photocatalysts by the adjustment of the semiconductors' surface charge. *Materials Science in Semiconductor Processing*, **2016**, *42*, 66–71.

180. Hirai, T.; Suzuki, K.; Komasawa, I. Preparation and photocatalytic properties of composite CdS nanoparticles-titanium dioxide particles. *Journal of Colloid and Interface Science*, **2001**, *244*(2), 262–265.

181. Liu, X.; Xing, Z.; Zhang, H.; Wang, W. Fabrication of 3D mesoporous black $TiO_2/MoS_2/TiO_2$ nanosheets for visible-light-driven photocatalysis. *ChemSusChem*, **2016**, *9*(10), 1118–1124.

182. Chatterjee, D.; Mahata, A. Demineralization of organic pollutants on the dye modified TiO_2 semiconductor particulate system using visible light. *Applied Catalysis B: Environmental*, **2001**, *33*(2), 119–125.

183. Jiang, D.; Xu, Y.; Wu, D.; Sun, Y. Visible-light responsive dye-modified TiO_2 photocatalyst. *Journal of Solid State Chemistry*, **2008**, *181*(3), 593–602.

184. Yao, K. S.; Cheng, T. C.; Li, S. J.; Yang, L. Y. Comparison of photocatalytic activities of various dye-modified TiO_2 thin films under visible light. *Surface and Coatings Technology*, **2008**, *203*(5–7), 922–924.

185. Wang, J.; Ma, T.; Zhang, G.; Zhang, Z. Preparation of novel nanometer TiO_2 catalyst doped

with upconversion luminescence agent and investigation on degradation of acid red B dye using visible light. *Catalysis Communications*, **2007**, *8*(3), 607–611.

186. Zhou, W.; Zheng, Y. Novel luminescent RE/TiO_2 (RE = Eu, Gd) catalysts prepared by in-situation sol-gel approach construction of multi-functional precursors and their photo or photocatalytic oxidation properties. *Applied Surface Science*, **2006**, *253*(3), 1387–1392.

187. Bard, A. J.; Shea, T. V.; Crayston, J. A.; Kittlesen, G. P. Digital simulation of the measured electrochemical response of reversible redox couples at microelectrode arrays: Consequences arising from closely spaced ultramicroelectrodes. *Analytical Chemistry*, **1986**, *58*(11), 2321–2331.

188. Kayes, B. M.; Atwater, H. A.; Lewis, N. S. Comparison of the device physics principles of planar and radial p-n junction nanorod solar cells. *Journal of Applied Physics*, **2005**, *97*(11), 114302.

189. Sajedi Alvar, M.; Javadi, M.; Abdi, Y.; Arzi, E. Enhancing the electron lifetime and diffusion coefficient in dye-sensitized solar cells by patterning the layer of TiO_2 nanoparticles. *Journal of Applied Physics*, **2016**, *119*(11), 114302.

190. Kwak, E. S.; Lee, W.; Park, N. C.; Kim, J. Compact inverse-opal electrode using non-aggregated TiO2 nanoparticles for dye-sensitized solar cells. *Advanced Functional Materials*, **2009**, *19*(7), 1093–1099.

191. Safriani, L.; Cai, B.; Komatsu, K.; Sugihara, O.; Kaino, T. Fabrication of inverse opal TiO_2 waveguide structure. *Japanese Journal of Applied Physics*, **2008**, *47*, 1208–1210.

192. Seo, Y. G.; Woo, K.; Kim, J.; Lee, H.; Lee, W. Rapid fabrication of an inverse opal TiO_2 photoelectrode for DSSC using a binary mixture of TiO_2 nanoparticles and polymer microspheres. *Advanced Functional Materials*, **2011**, *21*(16), 3094–3103.

193. Li, Q.; Shang, J. K. Inverse opal structure of nitrogen-doped titanium oxide with enhanced visible-light photocatalytic activity. *Journal of the American Ceramic Society*, **2008**, *91*(2), 660–663.

194. Gitlin, L.; Schulze, P.; Belder, D. Rapid replication of master structures by double casting with PDMS. *Lab on a Chip*, **2009**, *9*(20), 3000–3002.

195. Jang, S.; Yoon, J.; Ha, K. Facile fabrication of three-dimensional TiO_2 structures for highly efficient perovskite solar cells. *Nano Energy*, **2016**, *22*, 499–506.

196. Kim, J.; Koh, J. K.; Kim, B.; Kim, J. H.; Kim, E. Nanopatterning of mesoporous inorganic oxide films for efficient light harvesting of dye-sensitized solar cells. *Angewandte Chemie*, **2012**, *124*(28), 6970–6975.

197. Dong, L.; Cheng, K.; Weng, W.; Song, C.; Du, P. Hydrothermal growth of rutile TiO_2 nanorod films on titanium substrates. *Thin Solid Films*, **2011**, *519*(15), 4634–4640.

198. Huang, H.; Pan, L.; Lim, C. K.; Gong, H. Hydrothermal growth of TiO_2 nanorod arrays and in situ conversion to nanotube arrays for highly efficient quantum dot-sensitized solar cells. *Small*, **2013**, *9*(18), 3153–3160.

199. Feng, X.; Shankar, K.; Varghese, O. K.; Paulose, M. Vertically aligned single crystal TiO_2 nanowire arrays grown directly on transparent conducting oxide coated glass: Synthesis details and applications. *Nano Letters*, **2008**, *8*(11), 3781–3786.

200. Liu, B.; Aydil, E. S. Growth of oriented single-crystalline rutile TiO_2 nanorods on transparent conducting substrates for dye-sensitized solar cells. *Journal of the American Chemical Society*, **2009**, *131*(11), 3985–3990.

201. Fujishima, A.; Zhang, X.; Tryk, D. A. TiO_2 photocatalysis and related surface phenomena. *Surface Science Reports*, **2008**, *63*(12), 515–582.

202. Yoshihara, T.; Katoh, R.; Furube, A.; Tamaki, Y. Identification of reactive species in photoexcited nanocrystalline TiO_2 films by wide-wavelength-range (400-2500 nm) transient absorption spectroscopy. *Journal of Physical Chemistry B*, **2004**, *108*(12), 3817–3823.

203. Peiró, A. M.; Colombo, C.; Doyle, G.; Nelson, J. Photochemical reduction of oxygen

adsorbed to nanocrystalline TiO_2 films: A transient absorption and oxygen scavenging study of different TiO_2 preparations. *Journal of Physical Chemistry B*, **2006**, *110*(46), 23255–23263.

204. Emeline, A. V.; Ryabchuk, V. K.; Serpone, N. Dogmas and misconceptions in heterogeneous photocatalysis. Some enlightened reflections. *Journal of Physical Chemistry B*, **2005**, *109*(39), 18515–18521.

205. Wang, Y.; Hang, K.; Anderson, N. A.; Lian, T. Comparison of electron transfer dynamics in molecule-to-nanoparticle and intramolecular charge transfer complexes. *Journal of Physical Chemistry B*, **2003**, *107*(35), 9434–9440.

206. Esfandyarpour, M.; Garnett, E. C.; Cui, Y.; McGehee, M. D. Metamaterial mirrors in optoelectronic devices. *Nature Nanotechnology*, **2014**, *9*(7), 542–547.

207. Leung, S. F.; Zhang, Q.; Xiu, F.; Yu, D. Light management with nanostructures for optoelectronic devices. *Journal of Physical Chemistry Letters*, **2014**, *5*(8), 1479–1495.

208. Mateus, C. F. R.; Huang, M. C. Y.; Deng, Y.; Neureuther, A. R. Ultrabroadband mirror using low-index cladded subwavelength grating. *IEEE Photonics Technology Letters*, **2004**, *16*(2), 518–520.

209. Lee, Y. T.; Song, Y. M.; Jang, S. J.; Yu, J. S. Bioinspired parabola subwavelength structures for improved broadband antireflection. *Small*, **2010**, *6*(9), 984–987.

210. Sahoo, K. C.; Lin, M. K.; Chang, E. Y.; Lu, Y. Y. Fabrication of antireflective sub-wavelength structures on silicon nitride using nano cluster mask for solar cell application. *Nanoscale Research Letters*, **2009**, *4*(7), 680–683.

211. Lei, Z.; Qing-Dong, O.; Jing-De, C.; Su, S. Light manipulation for organic optoelectronics using bio-inspired moth's eye nanostructures. *Sientific Reports*, **2014**, *4*(1), 1–8.

212. Peter Amalathas, A.; Alkaisi, M. M. Efficient light trapping nanopyramid structures for solar cells patterned using UV nanoimprint lithography. *Materials Science in*

Semiconductor Processing, **2017**, *57*, 54–58.

213. Prasad, A. Porous Silicon Oxide anti-reflection coating for solar cells. *Journal of The Electrochemical Society*, **1982**, *129*(3), 596.

214. Li, Y.; Zhang, J.; Yang, B. Antireflective surfaces based on biomimetic nanopillared arrays. *Nano Today*, **2010**, *5*(2), 117–127.

215. Ko, D. H.; Tumbleston, J. R.; Gadisa, A. Light-trapping nano-structures in organic photovoltaic cells. *Journal of Materials Chemistry*, **2011**, *21*(41), 16293–16303.

216. Sai, H.; Fujii, H.; Arafune, K.; Ohshita, Y.; Kanamori, Y. Wide-angle antireflection effect of subwavelength structures for solar cells. *Japanese Journal of Applied Physics, Part 1: Regular Papers and Short Notes and Review Papers*, **2007**, *46*, 3333–3336.

217. Sahoo, K. C.; Li, Y.; Chang, E. Y. Shape effect of silicon nitride subwavelength structure on reflectance for silicon solar cells. *IEEE Transactions on Electron Devices*, **2010**, *57*(10), 2427–2433.

218. Chen, J. Y.; Sun, K. W. Enhancement of the light conversion efficiency of silicon solar cells by using nanoimprint anti-reflection layer. *Solar Energy Materials and Solar Cells*, **2010**, *94*(3), 629–633.

219. Boden, S. A.; Bagnall, D. M. Optimization of moth-eye antireflection schemes for silicon solar cells. *Progress in Photovoltaics: Research and Applications*, **2010**, *18*(3), 195–203.

220. Nishioka, K.; Horita, S.; Ohdaira, K.; Matsumura, H. Antireflection subwavelength structure of silicon surface formed by wet process using catalysis of single nano-sized gold particle. *Solar Energy Materials and Solar Cells*, **2008**, *92*(8), 919–922.

221. Eisele, C.; Nebel, C. E.; Stutzmann, M. Periodic light coupler gratings in amorphous thin film solar cells. *Journal of Applied Physics*, **2001**, *89*(12), 7722–7726.

222. Chattopadhyay, S.; Huang, Y. F.; Jen, Y. J. Anti-reflecting and photonic nanostructures.

Materials Science and Engineering R: Reports, **2010**, *69*(1–3), 1–35.

223. Wilson, S. J.; Hutley, M. C. The optical properties of 'moth eye' antireflection surfaces. *Optica Acta*, **1982**, *29*(7), 993–1009.

224. Schulz, U. Wideband antireflection coatings by combining interference multilayers with structured top layers. *Optics Express*, **2009**, *17*(11), 8704.

225. Halir, R.; Bock, P. J.; Cheben, P.; Ortega-Moñux, A.; Alonso-Ramos, C. Waveguide sub-wavelength structures: A review of principles and applications. *Laser and Photonics Reviews*, **2015**, *9*(1), 25–49.

226. Bell, J. M.; Derrick, G. H.; Bell, J. M.; McPhedran, R. C. Diffraction gratings in the quasi-static limit. *Optica Acta*, **1982**, *29*(11), 1475–1489.

227. Shalin, A. S. Progress In Electromagnetics Research B. *Encyclopedia of Electrochemical Power Sources*, **2013**, *47*, 127–144.

228. Trespidi, F.; Timò, G.; Galeotti, F.; Pasini, M. PDMS antireflection nano-coating for glass substrates. *Microelectronic Engineering*, **2014**, *126*, 13–18.

229. Sun, C. H.; Ho, B. J.; Jiang, B.; Jiang, P. Biomimetic subwavelength antireflective gratings on GaAs. *Optics letters*, **2008**, *33*(19), 2224–2226.

230. Lin, Q.; Leung, S. F.; Lu, L.; Chen, X.; Chen, Z. Inverted nanocone-based thin film photovoltaics with omnidirectionally enhanced performance. *ACS Nano*, **2014**, *8*(6), 6484–6490.

231. Cheben, P.; Bock, P. J.; Schmid, J. H.; Lapointe, J. Refractive index engineering with subwavelength gratings for efficient microphotonic couplers and planar waveguide multiplexers. *Optics Letters*, **2010**, *35*(15), 2526.

232. Lin, H.; Xiu, F.; Fang, M.; Yip, S. Rational design of inverted nanopencil arrays for cost-effective , broadband , **2014**, *8*(4), 3752–3760.

233. Song, Y. M.; Jeong, Y.; Yeo, C. I.; Lee, Y. T. Enhanced power generation in concentrated photovoltaics using broadband antireflective coverglasses with moth eye structures. *Optics Express*, **2012**, *20*(106), A916.

234. Han, K. S.; Shin, J. H.; Lee, H. Enhanced transmittance of glass plates for solar cells using nano-imprint lithography. *Solar Energy Materials and Solar Cells*, **2010**, *94*(3), 583–587.

235. Forberich, K.; Dennler, G.; Scharber, M. C.; Hingerl, K. Performance improvement of organic solar cells with moth eye anti-reflection coating. *Thin Solid Films*, **2008**, *516*(20), 7167–7170.

236. Sivasubramaniam, S.; Alkaisi, M. M. Inverted nanopyramid texturing for silicon solar cells using interference lithography. *Microelectronic Engineering*, **2014**, *119*, 146–150.

237. Amalathas, A. P.; Alkaisi, M. M. Upright nanopyramid structured cover glass with light harvesting and self-cleaning effects for solar cell applications. *Journal of Physics D: Applied Physics*, **2016**, *49*(46), 465601.

238. Lee, Y.; Lee, Y.; Ruby, D. S.; Ruby, D. S. ZnO Nanostructures as Effcient Antire ection Layers in Solar Cells. *Nano*, **2008**, 8(5), 1501–1505.

239. Chen, J. Y.; Sun, K. W. Nanostructured thin films for anti-reflection applications. *Thin Solid Films*, **2011**, *519*(15), 5194–5198.

240. Spinelli, P.; Verschuuren, M. A.; Polman, A. Broadband omnidirectional antireflection coating based on subwavelength surface Mie resonators. *Nature Communications*, **2012**, *3*, 692–695.

241. Zhu, J.; Yu, Z.; Burkhard, G. F.; Hsu, C. M. Optical Absorption Enhancement in Amorphous Silicon Nanowire and Nanocone Arrays. *Nano Letters*, **2009**, *9*(1), 279–282.

242. Kanamori, Y.; Sasaki, M.; Hane, K. Broadband antireflection gratings fabricated upon silicon substrates. *Optics Letters*, **1999**, *24*(20), 1422.

243. Amalathas, A. P.; Alkaisi, M. M. Enhanced light scattering and hydrophobicity of glass with upright nanopyramid structure for solar cells using UV nanoimprint lithography, In *Proceedings of the 32nd European Photovoltaic Solar Energy Conference and Exhibition, EU PVSEC*, **2016**, pp. 245-248.

244. Kang, S. H.; Kim, J. Y.; Kim, H. S.; Koh, H. D. Influence of light scattering particles in the TiO2 photoelectrode for solid-state dye-sensitized solar cell. *Journal of Photochemistry and Photobiology A: Chemistry*, **2008**, *200*(2–3), 294–300.

245. Durán-Ramírez, V. M.; Martínez-Ríos, A.; Guerrero-Viramontes, J. A. Measurement of the refractive index by using a rectangular cell with a fs-laser engraved diffraction grating inner wall. *Optics Express*, **2014**, *22*(24), 29899.

246. Palmer, C. H. Diffraction Grating Anomalies II Coarse Gratings. *Journal of the Optical Society of America*, **1956**, *46*(1), 50.

247. Popov, E. Introduction to diffraction gratings: Summary of applications. *Gratings: theory and numeric applications*, **2012**, 1–21.

248. Bock, J. P.; Robison, J. R.; Sharma, R.; Zhang, J.; Mazumder, M. K. An efficient power management approach for self-cleaning solar panels with integrated electrodynamic screens. *Proceedings of the ESA Annual Meeting on Electrostatics*, **2008**, *Paper O2*.

249. Sutha, S.; Suresh, S.; Raj, B.; Ravi, K. R. Transparent alumina based superhydrophobic self–cleaning coatings for solar cell cover glass applications. *Solar Energy Materials and Solar Cells*, **2017**, *165*, 128–137.

250. Mazumder, M.; Sharma, R.; Biris, A.; Horenstein, M. Electrostatic removal of particles and its applications to self-cleaning solar panels and solar concentrators. In *Developments in Surface Contamination and Cleaning*, Elsevier, **2011**, 149–199.

251. Mazumder, M. K.; Sharma, R.; Biris, A. S.; Zhang, J. Self-cleaning transparent dust shields for protecting solar panels and other devices. *Particulate Science and Technology*, **2007**, *25*(1), 5–20.

252. Tavakoli, M. M.; Tsui, K. H.; Zhang, Q.; He, J. Highly efficient flexible perovskite solar cells with antireflection and self-cleaning nanostructures. *ACS Nano*, **2015**, *9*(10), 10287–10295.

253. Syafiq, A.; Pandey, A. K.; Adzman, N. N.; Rahim, N. A. Advances in approaches and methods for self-cleaning of solar photovoltaic panels. *Solar Energy*, **2018**, *162*, 597–619.

254. He, G.; Zhou, C.; Li, Z. Review of self-cleaning method for solar cell array. *Procedia Engineering*, **2011**, *16*, 640–645.

255. Gould, P. Smart, clean surfaces. *Materials Today*, **2003**, *6*(11), 44–48.

256. Parkin, I. P.; Palgrave, R. G. Self-cleaning coatings. *Journal of Materials Chemistry*, **2005**, *15*(17), 1689–1695.

257. Cheng, Y. T.; Rodak, D. E.; Wong, C. A.; Hayden, C. A. Effects of micro- and nano-structures on the self-cleaning behaviour of lotus leaves. *Nanotechnology*, **2006**, *17*(5), 1359–1362.

258. Blossey, R. Self-cleaning surfaces — virtual realities. *Nature materials*, **2003**, *2*(5), 301–306.

259. Tanaka, K.; Capule, M.; Hisanga, T. Effect of crystallinity of TiO_2 on its photocatalytic action. *Chemical Physics Letters*, **1991**, *187*, 73–76.

260. Saadoun, L.; Ayllón, J. A.; Jiménez-Becerril, J.; Peral, J. 1,2-Diolates of titanium as suitable precursors for the preparation of photoactive high surface titania. *Applied Catalysis B: Environmental*, **1999**, *21*(4), 269–277.

261. Colombo, D. P.; Bowman, R. M. Does interfacial charge transfer compete with charge carrier recombination? A femtosecond diffuse reflectance investigation of TiO_2 nanoparticles. *The Journal of Physical Chemistry*, **1996**, *100*(47), 18445–18449.

262. Carp, O.; Huisman, C. L.; Reller, A. Photoinduced reactivity of titanium dioxide. *Progress*

in Solid State Chemistry, **2004**, *32*, 33–177.

263. Yang, Y.; Hoffmann, M. R. Synthesis and stabilization of blue-black TiO_2 nanotube arrays for electrochemical oxidant generation and wastewater treatment. *Environmental Science and Technology*, **2016**, *50*(21), 11888–11894.

264. Liu, J.; Liu, H.; Zuo, X.; Wen, F. Micro-patterned TiO_2 films for photocatalysis. *Materials Letters*, **2019**, *254*, 448–451.

265. Numthuam, S.; Kakegawa, T.; Anada, T.; Khademhosseini, A. Synergistic effects of micro/nano modifications on electrodes for microfluidic electrochemical ELISA. *Sensors and Actuators, B: Chemical*, **2011**, *156*(2), 637–644.

266. Fojt, L.; Hasoň, S. Sensitive determination of oligodeoxynucleotides by anodic adsorptive stripping voltammetry at surface-roughened glassy carbon electrode in the presence of copper. *Journal of Electroanalytical Chemistry*, **2006**, *586*(1), 136–143.

267. La O, G. J.; In, H. J.; Crumlin, E.; Barbastathis, G. Recent advances in microdevices for electrochemical energy conversion and storage. *International Journal of Energy Research*, **2007**, *31*, 548–575.

268. Wieckowski, A. *Fuel cell catalysis: a surface science approach* (Vol. 1), John Wiley & Sons, **2009**.

269. Aricò, A. S.; Bruce, P.; Scrosati, B.; Tarascon, J. M.; Van Schalkwijk, W. Nanostructured materials for advanced energy conversion and storage devices. *Nature Materials*, **2005**, *4*(5), 366–377.

270. Kato, H.; Asakura, K.; Kudo, A. Highly efficient water splitting into H_2 and O_2 over lanthanum-doped $NaTaO_3$ photocatalysts with high crystallinity and surface nanostructure. *Journal of the American Chemical Society*, **2003**, *125*(10), 3082–3089.

271. Marković, N. M.; Ross, P. N. Surface science studies of model fuel cell electrocatalysts. *Surface Science Reports*, **2002**, *45*(4–6), 117–229.

272. Sherigara, B. S.; Kutner, W.; D'Souza, F. Electrocatalytic properties and sensor applications of fullerenes and carbon nanotubes. *Electroanalysis*, **2003**, *15*(9), 753–772.

273. Pei, Y.; Hu, M.; Xia, Y.; Huang, W.; Li, Z.; Chen, S. Electrochemical preparation of Pt nanoparticles modified nanoporous gold electrode with highly rough surface for efficient determination of hydrazine. *Sensors and Actuators, B: Chemical*, **2020**, *304*, 127416.

274. Lee, I.; Morales, R.; Albiter, M. A.; Zaera, F. Synthesis of heterogeneous catalysts with well shaped platinum particles to control reaction selectivity. *Proceedings of the National Academy of Sciences of the United States of America*, **2008**, *105*(40), 15241–15246.

275. Al Sulaiman, D.; Shapiro, S. J.; Gomez-Marquez, J.; Doyle, P. S. High-resolution patterning of hydrogel sensing motifs within fibrous substrates for sensitive and multiplexed detection of biomarkers. *ACS Sensors*, **2021**, *6*(1), 203–211.

276. Kim, S. R.; Kim, J. H.; Park, J. W. Wearable and transparent capacitive strain sensor with high sensitivity based on patterned Ag nanowire Networks. *ACS Applied Materials and Interfaces*, **2017**, *9*(31), 26407–26416.

277. Cedeño, C. C.; Seekamp, J.; Kam, A. P.; Hoffmann, T. Nanoimprint lithography for organic electronics. *Microelectronic Engineering*, **2002**, *61*, 25–31.

278. Defranco, J. A.; Schmidt, B. S.; Lipson, M.; Malliaras, G. G. Photolithographic patterning of organic electronic materials. *Organic Electronics*, **2006**, *7*(1), 22–28.

279. Lee, H.; Jung, G. Y. Wafer to wafer nano-imprinting lithography with monomer based thermally curable resin. *Microelectronic Engineering*, **2005**, *77*(2), 168–174.

280. Segalman, R. A. Patterning with block copolymer thin films. *Materials Science and Engineering R: Reports*, **2005**, *48*(6), 191–226.

281. Xia, Y.; Whitesides, G. M. Soft lithography. *Angewandte Chemie - International Edition*, **1998**, *37*(5), 550–575.

282. Pimpin, A.; Srituravanich, W. Reviews on micro- and nanolithography techniques and their applications. *Engineering Journal*, **2012**, *16*(1), 37–55.

283. Tong, H. D.; Jansen, H. V.; Gadgil, V. J.; Bostan, C. G. Silicon nitride nanosieve membrane. *Nano Letters*, **2004**, *4*(2), 283–287.

284. Sandison, M. E.; Anicet, N.; Glidle, A.; Cooper, J. M. Optimization of the geometry and porosity of microelectrode arrays for sensor design. *Analytical Chemistry*, **2002**, *74*(22), 5717–5725.

285. Khodagholy, D.; Doublet, T.; Gurfinkel, M.; Quilichini, P. Highly conformable conducting polymer electrodes for in vivo recordings. *Advanced Materials*, **2011**, *23*(36), 268–272.

286. Hsu, C. W.; Su, F. C.; Peng, P. Y.; Young, H. T. Highly sensitive non-enzymatic electrochemical glucose biosensor using a photolithography fabricated micro/nano hybrid structured electrode. *Sensors and Actuators, B: Chemical*, **2016**, *230*, 559–565.

287. Koep, E.; Compson, C.; Liu, M.; Zhou, Z. A photolithographic process for investigation of electrode reaction sites in solid oxide fuel cells. *Solid State Ionics*, **2005**, *176*(1–2), 1–8.

288. Van Wolferen, H.; Abelmann, L. Laser interference lithography. *Lithography: Principles, processes and materials*. **2011**, 133–148.

289. Campbell, P.; Green, M. A. Light trapping properties of pyramidally textured surfaces. *Journal of Applied Physics*, **1987**, *62*(1), 243–249.

290. Brady, B.; Wang, P. H.; Steenhoff, V.; Brolo, A. G. *Nanostructuring solar cells using metallic nanoparticles*, pp. 197–221, Elsevier, **2019**.

291. Hulteen, J. C.; Van Duyne, R. P. Nanosphere lithography: A materials general fabrication process for periodic particle array surfaces. *Journal of Vacuum Science & Technology A: Vacuum, Surfaces, and Films*, **1995**, *13*(3), 1553–1558.

292. Cheng, J. Y.; Ross, C. A.; Thomas, E. L.; Smith, H. I.; Vancso, G. J. Fabrication of

nanostructures with long-range order using block copolymer lithography. *Applied Physics Letters*, **2002**, *81*(19), 3657–3659.

293. Bates, C. M.; Maher, M. J.; Janes, D. W.; Ellison, C. J.; Willson, C. G. Block copolymer lithography. *Macromolecules*, **2014**, *47*, 2–12.

294. Altissimo, M. E-beam lithography for micro-/nanofabrication. *Biomicrofluidics*, **2010**, *4*(2), 2–7.

295. Gates, B. D.; Xu, Q.; Stewart, M.; Ryan, D.; Willson, C. G. New approaches to nanofabrication: Molding, printing, and other techniques. *Chemical Reviews*, **2005**, *105*(4), 1171–1196.

296. Madou, M. J. *Fundamentals of microfabrication: the science of miniaturization*. CRC press, **2018**.

297. Liu, L.; Luo, Y.; Zhao, Z.; Zhang, W.; Gao, G. Large area and deep sub-wavelength interference lithography employing odd surface plasmon modes. *Scientific Reports*, **2016**, *6*, 1–8.

298. Yang, H. F.; He, H. D.; Zhao, E. L.; Han, J.; Hao, J. B. Simulation and fabrication of nanostructures with laser interference lithography. *Laser Physics*, **2014**, *24*(6), 065901.

299. Murukeshan, V. M.; Sreekanth, K. V.; Chua, J. K. Metal Particle-Surface System for Plasmonic Lithography. Retrieved from *Lithography* (pp. 598–614). Editor: M. Wang, IntechOpen, **2010**.

300. Haynes, C. L.; McFarland, A. D.; Smith, M. T.; Hulteen, J. C.; Van Duyne, R. P. Angle-resolved nanosphere lithography: Manipulation of nanoparticle size, shape, and interparticle spacing. *Journal of Physical Chemistry B*, **2002**, *106*(8), 1898–1902.

301. Chou, S.; Krauss, P.; Renstrom, P. Imprint of sub-25nm vias and trenches in polymers. *Applied Physics Letter*, **1995**, *67*, 3114–3116.

302. 301. Paetzold, U. W.; Qiu, W.; Finger, F.; Poortmans, J.; Cheyns, D. Nanophotonic front electrodes for perovskite solar cells. *Applied Physics Letters*, **2015**, *106*(17), 173101.

303. Padeste, C.; Bellini, S.; Siewert, D.; Schift, H. Anti-sticking layers for nickel-based nanoreplication tools. *Microelectronic Engineering*, **2014**, *123*, 23–27.

304. Yang, Y. K.; Wu, Y. X.; Lin, T. H.; Yu, C. W. Improve large area uniformity and production capacity of laser interference lithography with beam flattening device, *Laser-based Micro- and Nanoprocessing X*, vol. 9736, p. 97360Y. International Society for Optics and Photonics, **2016**.

305. Leem, J. W.; Su Yu, J.; Jun, D. H.; Heo, J. Efficiency improvement of III-V GaAs solar cells using biomimetic TiO_2 subwavelength structures with wide-angle and broadband antireflection properties. *Solar Energy Materials and Solar Cells*, **2014**, *127*, 43–49.

306. Brunner, R.; Sandfuchs, O.; Pacholski, C.; Morhard, C.; Spatz, J. Lessons from nature: Biomimetic subwavelength structures for high-performance optics. *Laser and Photonics Reviews*, **2012**, *6*(5), 641–659.

307. Arbabi, A.; Horie, Y.; Ball, A. J.; Bagheri, M.; Faraon, A. Subwavelength-thick lenses with high numerical apertures and large efficiency based on high-contrast transmitarrays. *Nature Communications*, **2015**, *6*, 2–7.

308. Yu, Z.; Gao, H.; Wu, W.; Ge, H.; Chou, S. Y. Fabrication of large area subwavelength antireflection structures on Si using trilayer resist nanoimprint lithography and liftoff. *Journal of Vacuum Science and Technology B: Microelectronics and Nanometer Structures*, **2003**, *21*(6), 2874–2877.

309. Lee, H.; Bhushan, B. Fabrication and characterization of hierarchical nanostructured smart adhesion surfaces. *Journal of Colloid and Interface Science*, **2012**, *372*(1), 231–238.

310. Leem, J. W.; Yeh, Y.; Yu, J. S. Enhanced transmittance and hydrophilicity of nanostructured glass substrates with antireflective properties using disordered gold nanopatterns. *Optics Express*, **2012**, *20*(4), 4056–4066.

311. Zhou, D.; Biswas, R. Photonic crystal enhanced light-trapping in thin film solar cells. *Journal of Applied Physics*, **2008**, *103*(9), 093102.

312. Zaidi, S. H.; Gee, J. M.; Ruby, D. S. Diffraction grating structures in solar cells. *Conference Record of the IEEE Photovoltaic Specialists Conference*-2000, *(Cat. No. 00CH37036)*, pp. 395–398. IEEE, **2000**.

313. Hore, S.; Vetter, C.; Kern, R.; Smit, H.; Hinsch, A. Influence of scattering layers on efficiency of dye-sensitized solar cells. *Solar Energy Materials and Solar Cells*, **2006**, *90*(9), 1176–1188.

314. Dudem, B.; Leem, J. W.; Lim, J. H.; Lee, S. H.; Yu, J. S. Multifunctional polymers with biomimetic compound architectures via nanoporous AAO films for efficient solar energy harvesting in dye-sensitized solar cells. *RSC Advances*, **2015**, *5*(109), 90103–90110.

315. Janthong, B.; Moriya, Y.; Hongsingthong, A.; Sichanugrist, P.; Konagai, M. Management of light-trapping effect for a-Si:H/μc-Si:H tandem solar cells using novel substrates, based on MOCVD ZnO and etched white glass. *Solar Energy Materials and Solar Cells*, **2013**, *119*, 209–213.

316. Ho, C. H.; Lien, D. H.; Chang, H. C.; Lin, C. A.; Kang, C. F. Hierarchical structures consisting of SiO2 nanorods and p-GaN microdomes for efficiently harvesting solar energy for InGaN quantum well photovoltaic cells. *Nanoscale*, **2012**, *4*(23), 7346–7349.

317. Sheng, P.; Bloch, A. N.; Stepleman, R. S. Wavelength-selective absorption enhancement in thin-film solar cells. *Applied Physics Letters*, **1983**, *43*(6), 579–581.

318. Lakshmi, S.; Renganathan, R.; Fujita, S. Study on TiO_2-mediated photocatalytic degradation of methylene blue. *Journal of Photochemistry and Photobiology, A: Chemistry*, **1995**, *88*(2–3), 163–167.

319. Houas, A.; Lachheb, H.; Ksibi, M.; Elaloui, E. Photocatalytic degradation pathway of methylene blue in water. *Applied Catalysis B: Environmental*, **2001**, *31*(2), 145–157.

320. Hou, C.; Hu, B.; Zhu, J. Photocatalytic degradation of methylene blue over TiO_2 pretreated with varying concentrations of NaOH. *Catalysts*, **2018**, *8*(12), 575.

321. Trandafilović, L. V.; Jovanović, D. J.; Zhang, X. Enhanced photocatalytic degradation of methylene blue and methyl orange by ZnO:Eu nanoparticles. *Applied Catalysis B: Environmental*, **2017**, *203*, 740–752.

322. Wu, C. H.; Chern, J. M. Kinetics of photocatalytic decomposition of methylene blue. *Industrial and Engineering Chemistry Research*, **2006**, *45*(19), 6450–6457.

323. Xu, N.; Shi, Z.; Fan, Y.; Dong, J. Effects of particle size of TiO_2 on photocatalytic degradation of methylene blue in aqueous suspensions. *Industrial and Engineering Chemistry Research*, **1999**, *38*(2), 373–379.

324. Xiao, Q.; Zhang, J.; Xiao, C.; Si, Z.; Tan, X. Solar photocatalytic degradation of methylene blue in carbon-doped TiO_2 nanoparticles suspension. *Solar Energy*, **2008**, *82*(8), 706–713.

325. Swinehart, D. F. The Beer-Lambert law. *Journal of Chemical Education*, **1962**, *39*(7), 333–335.

326. Dariani, R. S.; Esmaeili, A.; Mortezaali, A.; Dehghanpour, S. Photocatalytic reaction and degradation of methylene blue on TiO_2 nano-sized particles. *Optik*, **2016**, *127*(18), 7143–7154.

327. Ushkov, A. A.; Verrier, I.; Kampfe, T.; Jourlin, Y. Subwavelength diffraction gratings with macroscopic moiré patterns generated via laser interference lithography. *Optics Express*, **2020**, *28*(11), 16453.

328. Seidel, H. Anisotropic etching of crystalline silicon in alkaline solutions: I. Orientation dependence and behavior of passivation layers. *Journal of The Electrochemical Society*, **1990**, *137*(11), 3626.

329. Zubel, I.; Barycka, I. Silicon anisotropic etching in alkaline solutions I. The geometric description of figures developed under etching Si (100) various solutions, **1998**, *70*, 250–

259.

330. Fan, Y.; Han, P.; Liang, P.; Xing, Y. Differences in etching characteristics of TMAH and KOH on preparing inverted pyramids for silicon solar cells. *Applied Surface Science*, **2013**, *264*, 761–766.

331. Zubel, I. Silicon anisotropic etching in alkaline solutions III : On the possibility of spatial structures forming in the course of Si (100) anisotropic etching in KOH and KOH+IPA solutions, *Sensors and Actuators A: Physical*, **2000**, *84*(1–2), 116–125.

332. Milošević, M. D.; Logar, M. M.; Poharc-Logar, A. V.; Jakšić, N. L. Orientation and optical polarized spectra (380–900 nm) of methylene blue crystals on a glass surface. *International Journal of Spectroscopy*, **2013**.

333. Salehi, M.; Hashemipour, H.; Mirzaee, M. Experimental study of influencing factors and kinetics in catalytic removal of methylene blue with TiO_2 nanopowder. *American Journal of Environmental Engineering*, **2012**, *2*(1), 1–7.

334. Rakhshani, A. E.; Makdisi, Y.; Ramazaniyan, H. A. Electronic and optical properties of fluorine-doped tin oxide films. *Journal of Applied Physics*, **1998**, *83*(2), 1049–1057.

335. Siefke, T.; Kroker, S.; Pfeiffer, K.; Puffky, O. Materials pushing the application limits of wire grid polarizers further into the deep ultraviolet spectral range. *Advanced Optical Materials*, **2016**, *4*(11), 1780–1786.

336. Pajkossy, T. Impedance spectroscopy at interfaces of metals and aqueous solutions - Surface roughness, CPE and related issues. *Solid State Ionics*, **2005**, *176*(25–28), 1997–2003.

337. Aaronson, B. D. B.; Chen, C. H.; Li, H.; Koper, M. T. M. Pseudo-single-crystal electrochemistry on polycrystalline electrodes: Visualizing activity at grains and grain boundaries on platinum for the Fe^{2+}/Fe^{3+} redox reaction. *Journal of the American Chemical Society*, **2013**, *135*(10), 3873–3880.

338. Afshar, A.; Dolati, A. G.; Ghorbani, M. Electrochemical characterization of the Ni-Fe alloy

electrodeposition from chloride-citrate-glycolic acid solutions. *Materials Chemistry and Physics*, **2003**, *77*(2), 352–358.

339. Wang, C. C.; Liu, Y. C. Strategy for obtaining improved surface-enhanced Raman scattering by combining electrochemical and plasmas technologies. *Electrochemistry Communications*, **2005**, *7*(12), 1199–1204.

340. Liu, Y. C.; Hwang, B. J.; Jian, W. J. Effect of preparation conditions for roughening gold substrate by oxidation-reduction cycle on the surface-enhanced Raman spectroscopy of polypyrrole. *Materials Chemistry and Physics*, **2002**, *73*(2–3), 129–134.

341. Hoogvliet, J. C.; Dijksma, M.; Kamp, B.; Van Bennekom, W. P. Electrochemical pretreatment of polycrystalline gold electrodes to produce a reproducible surface roughness for self-assembly: A study in phosphate buffer pH 7.4. *Analytical Chemistry*, **2000**, *72*(9), 2016–2021.

342. Liu, Z.; Yang, Z. L.; Cui, L.; Ren, B.; Tian, Z. Q. Electrochemically roughened palladium electrodes for surface-enhanced Raman spectroscopy: Methodology, mechanism, and application. *Journal of Physical Chemistry C*, **2007**, *111*(4), 1770–1775.

343. Çakir, O.; Temel, H.; Kiyak, M. Chemical etching of Cu-ETP copper. *Journal of Materials Processing Technology*, **2005**, *162*, 275–279.

344. Smythe, E. J.; Dickey, M. D.; Jiming, B.; Whitesides, G. M. Optical antenna arrays on a fiber facet for in Situ surface-enhanced Raman scattering detection. *Nano Letters*, **2009**, *9*(3), 1132–1138.

345. Stromme, M.; Niklasson, G. A.; Granqvist, C. G. Voltammetry on fractals. *Solid State Communications*, **1995**, *96*, 151–154.

346. Kant, R. Diffusion-limited reaction rates on self-affine fractals. *Journal of Physical Chemistry B*, **1997**, *101*(19), 3781–3787.

347. Go, J. Y.; Pyun, S. I.; Hahn, Y. D. A study on ionic diffusion towards self-affine fractal

electrode by cyclic voltammetry and atomic force microscopy. *Journal of Electroanalytical Chemistry*, **2003**, *549*, 49–59.

348. Nyikos, L.; Pajkossy, T. Diffusion to fractal surfaces. *Electrochimica Acta*, **1986**, *31*(10), 1347–1350.

349. Pajkossy, T.; Nyikos, L. Diffusion to fractal surfaces—II. Verification of theory. *Electrochimica acta*, **1989**, *34*, 171–179.

350. Pajkossy, T.; Nyikos, L. Diffusion to fractal surfaces—III. Linear sweep and cyclic voltammograms. *Electrochimica Acta*, **1989**, *34*, 181–186.

351. Stromme, M.; Niklasson, G. A.; Granqvist, C. G. Determination of fractal dimension by cyclic I-V studies: The Laplace-transform method. *Physical Review B*, **1995**, *52*(19), 14192–14197.

352. Dassas, Y.; Duby, P. Diffusion toward fractal interfaces: potentiostatic, galvanostatic, and linear sweep voltammetric techniques. *Journal of The Electrochemical Society*, **2019**, *142*(12), 4175–4180.

353. Kozaderov, O. A.; Vvedenskii, A. V. Diffusion problem in chronopotentio- and chronoamperometry for electrode with rough surface. *Russian Journal of Electrochemistry*, **2001**, *37*(8), 798–802.

354. Kant, R.; Rangarajan, S. K. Effect of surface roughness on diffusion-limited charge transfer. *Journal of Electroanalytical Chemistry*, **1994**, *368*(1–2), 1–21.

355. Atighilorestani, M.; Brolo, A. G. Recessed gold nanoring-ring microarray electrodes. *Analytical Chemistry*, **2017**, *89*(18), 9870–9876.

356. Atighilorestani, M.; Brolo, A. G. Comparing the electrochemical response of nanostructured electrode arrays. *Analytical Chemistry*, **2017**, *89*(11), 6129–6135.

357. Prehn, R.; Abad, L.; Sánchez-Molas, D.; Duch, M.; Sabaté, N. Microfabrication and

characterization of cylinder micropillar array electrodes. *Journal of Electroanalytical Chemistry*, **2011**, *662*(2), 361–370.

358. Molina, A.; González, J.; Laborda, E.; Compton, R. G. On the meaning of the diffusion layer thickness for slow electrode reactions. *Physical Chemistry Chemical Physics*, **2013**, *15*(7), 2381–2388.

359. Amatore, C.; Szunerits, S.; Thouin, L.; Warkocz, J. S. The real meaning of Nernst's steady diffusion layer concept under non-forced hydrodynamic conditions. A simple model based on Levich's seminal view of convection. *Journal of Electroanalytical Chemistry*, **2001**, *500*(1–2), 62–70.

360. Velasco, J. G. On the dependence of the Nernst diffusion layer thickness on potential and sweep rate for reversible and of the thickness of the charge transfer layer for irreversible processes studied by application of the linear potential sweep method. *Electrochimica Acta*, **2006**, *51*(14), 2971–2976.

361. Nicholson, R. S. Theory and Application of Cyclic Voltammetry for Measurement of Electrode Reaction Kinetics. *Analytical Chemistry*, **1965**, *37*(11), 1351–1355.

362. Ward, K. R.; Gara, M.; Lawrence, N. S.; Hartshorne, R. S.; Compton, R. G. Nanoparticle modified electrodes can show an apparent increase in electrode kinetics due solely to altered surface geometry: The effective electrochemical rate constant for non-flat and non-uniform electrode surfaces. *Journal of Electroanalytical Chemistry*, **2013**, *695*, 1–9.

363. Mabbott, G. A. An introduction to cyclic voltammetry. *Journal of Chemical Education*, **1983**, *60*(9), 697–702.

364. Pletcher, D.; Greef, R.; Peat, R.; Peter, L. M.; Robinson, J. *Instrumental methods in electrochemistry.* Elsevier, **2001**.

365. Dickinson, E. J. F.; Wain, A. J. The Butler-Volmer equation in electrochemical theory: Origins, value, and practical application. *Journal of Electroanalytical Chemistry*, **2020**, *872*, 114145.

366. Ward, K. R.; Gara, M.; Lawrence, N. S.; Hartshorne, R. S.; Compton, R. G. Nanoparticle modified electrodes can show an apparent increase in electrode kinetics due solely to altered surface geometry: The effective electrochemical rate constant for non-flat and non-uniform electrode surfaces. *Journal of Electroanalytical Chemistry*, **2013**, *695*, 1–9.

367. Hamelin, A.; Martins, A. M. Cyclic voltammetry at gold single-crystal surfaces. Part 1. Behavior of high-index faces. *Journal of Electroanalytical Chemistry*, **1996**, *407*, 13–21.

368. Tremiliosi-Filho, G.; Dall'Antonia, L. H.; Jerkiewicz, G. Limit to extent of formation of the quasi-two-dimensional oxide state on Au electrodes. *Journal of Electroanalytical Chemistry*, **1997**, *422*(1–2), 149–159.

369. Schmid, G. M.; Hackerman, N. Double layer capacities of single crystals of gold in perchloric acid solutions. *Journal of The Electrochemical Society*, **1962**, *109*(3), 243.

370. Tobias, R. F.; Nobe, K. Electrochemical behavior of rotating iron disks: Effect of Fe(III). *Journal of The Electrochemical Society*, **1975**, *122*(1), 65–70.

371. Bard, A. J.; Faulkner, L. R. *Electrochemical Methods: Fudamentals and applications*, John Wiley & Sons, **2001**.

372. Wipf, D. O.; Kristensen, E. W.; Deakin, M. R.; Wightman, R. M. Fast-scan cyclic voltammetry as a method to measure rapid , heterogeneous electron-transfer kinetics, *Analytical Chemistry*, **1988**, *60*(4), 306–310.

373. Sun, P.; Mirkin, M. V. Kinetics of electron-transfer reactions at nanoelectrodes. *Analytical Chemistry*, **2006**, *78*(18), 6526–6534.

374. Wang, F.; Subbaiyan, N. K.; Wang, Q.; Rochford, C. Development of nanopatterned fluorine-doped tin oxide electrodes for dye-sensitized solar cells with improved light trapping. *ACS Applied Materials & Interfaces*, **2012**, *4*(3), 1565–1572.

375. Wei, Q.; Zheng, H.; Huang, Y. Direct patterning ITO transparent conductive coatings. *Solar Energy Materials and Solar Cells*, **2001**, *68*(3–4), 383–390.

376. Chowdhury, F. I.; Blaine, T.; Gougam, A. B. Optical transmission enhancement of fluorine doped tin oxide (FTO) on glass for thin film photovoltaic applications. *Energy Procedia*, **2013**, *42*, 660–669.

377. Kim, K.; Kim, I. H.; Lee, J. Y.; Jang, J.-H. α-Fe_2O_3 on patterned fluorine doped tin oxide for efficient photoelectrochemical water splitting. *Journal of Materials Chemistry A*, **2015**, *3*(35), 7706–7709.

378. Lee, K.; Kim, A. Y.; Park, J. H.; Jung, H. G. Effect of micro-patterned fluorine-doped tin oxide films on electrochromic properties of Prussian blue films. *Applied Surface Science*, **2014**, *313*, 864–869.

379. Lee, K.; Kim, A. Y.; Park, J. H.; Jung, H. G. Effect of micro-patterned fluorine-doped tin oxide films on electrochromic properties of Prussian blue films. *Applied Surface Science*, **2014**, *313*, 864–869.

380. Wang, Y. C.; Cho, C. P. Improved performance of dye-sensitized solar cells with patterned fluorine-doped tin oxide electrodes. *Energy*, **2015**, *89*, 277–282.

381. Vasudev, A. P.; Schuller, J. A.; Brongersma, M. L. Nanophotonic light trapping with patterned transparent conductive oxides. *Optics Express*, **2012**, *20*(103), A385–A394.

382. Narasimha Rao, A. V.; Swarnalatha, V.; Pandey, A. K.; Pal, P. Determination of precise crystallographic directions on Si{111} wafers using self-aligning pre-etched pattern. *Micro and Nano Systems Letters*, **2018**, *6*(1), 1–9.

383. Yang, L.; Hao, X.; Wang, C.; Zhang, B.; Wang, W. Rapid and low cost replication of complex microfluidic structures with PDMS double casting technology. *Microsystem Technologies*, **2014**, *20*(10–11), 1933–1940.

384. Shao, G.; Wu, J.; Cai, Z.; Wang, W. Fabrication of elastomeric high-aspect-ratio microstructures using polydimethylsiloxane (PDMS) double casting technique. *Sensors and Actuators, A: Physical*, **2012**, *178*, 230–236.

385. Smits, F. M. Measurement of Sheet Resistivities with the Four-Point Probe. *Bell System Technical Journal*, **1958**, *37*(3), 711–718.

386. Hossain, M. K.; Mortuza, A. A.; Sen, S. K.; Basher, M. K. A comparative study on the influence of pure anatase and Degussa-P25 TiO_2 nanomaterials on the structural and optical properties of dye sensitized solar cell (DSSC) photoanode. *Optik*, **2018**, *171*, 507–516.

387. Carbonell, E.; Ramiro-Manzano, F.; Rodríguez, I.; Corma, A. Enhancement of TiO_2 photocatalytic activity by structuring the photocatalyst film as photonic sponge. *Photochemical and Photobiological Sciences*, **2008**, *7*(8), 931–935.

388. Egerton, T. A. Uv-absorption-the primary process in photocatalysis and some practical consequences. *Molecules*, **2014**, *19*(11), 18192–18214.

389. Han, C. H.; Han, S. D.; Gwak, J.; Khatkar, S. P. Synthesis of indium tin oxide (ITO) and fluorine-doped tin oxide (FTO) nano-powder by sol-gel combustion hybrid method. *Materials Letters*, **2007**, *61*(8–9), 1701–1703.

390. Kalyanasundaram, K.; Gratzel, M. Applications of functionalized transition metal complexes in photonic and optoelectronic devices. *Coordination chemistry reviews*, **1998**, *177*, 347–414.

391. Tafalla, D.; Salvador, P.; Benito, R. M. Kinetic approach to the photocurrent transients in water photoelectrolysis at n-TiO_2 electrodes: II. Analysis of the photocurrent-time dependence. *Journal of The Electrochemical Society*, **1990**, *137*(6), 1810–1815.

392. Dhillon, S.; Kant, R. Theory for electrochemical impedance spectroscopy of heterogeneous electrode with distributed capacitance and charge transfer resistance. *Journal of Chemical Sciences*, **2017**, *129*(8), 1277–1292.

393. Pajkossy, T.; Borosy, A. P.; Imre, A.; Martemyanov, S. A. Diffusion kinetics at fractal electrodes. *Journal of Electroanalytical Chemistry*, **1994**, *366*(1–2), 69–73.

394. Lewis, N. S. A perspective on forward research and development paths for cost-effective

solar energy utilization. *ChemSusChem*, **2009**, *2*(5), 383–386.